Alma Mater Studiorum - Università di Bologna

DOTTORATO DI RICERCA IN

GEOFISICA

Ciclo XXIX

Settore Concorsuale di afferenza: 02/C1
Settore Scientifico Disciplinare: FIS/06

Challenges and critical aspects in stable boundary layer representation in numerical weather prediction modeling: diagnostic analyses and proposals for improvement

Presentata da: Ines Cerenzia

Coordinatore Dottorato:
Prof. Nadia Pinardi

Supervisore:
Prof. Rolando Rizzi

Relatore:
Dr. Tiziana Paccagnella

Esame finale anno 2017

Contents

Overview

This thesis explores the use of a lower limit to turbulent diffusivity (long-tail) in operational numerical weather prediction modelling. Its introduction in the 90's was advocated by a better simulation of the synoptic scale dynamics, but led to inaccurate representation of the scarcely diffusive stable boundary layer. After 20 years, a clear alternative to long-tail formulations in operational forecast does not exist yet. Several critical points emerging from the stable boundary layer observations, theoretical knowledge and modelling can be at the base of such alternate formulations. Among them, this dissertation develops the hypothesis that the parametrization of processes occurring at the unresolved scale, and currently neglected, can increase the cross-isobaric flow as much as the long-tail formulations.
The topic is investigated by using a specific limited area model, COSMO, operational at several European weather services.
First, the turbulence and transfer schemes operational in the COSMO model are described. An inter-comparison between COSMO and a state-of-the-art model, not using long-tail formulations, highlights the detrimental consequences of turbulence enhancing in the stable boundary layer. Then the long-tail formulations applied in the COSMO turbulence scheme are described, their influence on the stable boundary layer is investigated, alternative formulations are proposed in case the turbulence-enhancing effect is an undesired side effect and finally their influence on the operational transfer scheme is explored.
Finally, the potential role of two neglected subgrid scale processes, to overcome the operational need of turbulence-enhancing formulations in the stable boundary layer, is evaluated: i) the kinetic energy transfer from circulations induced by subgrid scale orography to turbulence, ii) the modification on the stable boundary layer structure induced by subgrid thermal heterogeneity of the surface. Results show that the parametrization of the first process, already in COSMO, gives a more physical but still partial answer to the operational need, with respect to the long tail approach. The second process is described by the tile approach, whose behaviour under stable stratification has not been fully investigated yet. The approach has been explored by idealized numerical experiments, also combining it with different order turbulence schemes. Results indicate that the tile method manages to represent, at least partially, the modifications induced by the thermal heterogeneous terrain and has the potential to produce a positive feedback on large scale dynamics.

Chapter 1

Introduction

1.1 Introduction

This dissertation deals with the issues in the operational representation of the stable boundary layer by state-of-the-art numerical weather models. Despite these issues affect only a fraction of the troposphere (i.e. the boundary layer) in specific conditions (i.e. thermal stability), they are relevant for the weather forecast at the level of human life in about % of the real atmospheric state in average on the Earth and during one year. The origin of these issues sites in the connection between the processes occurring in the stable boundary layer and the large scale synoptic flow. Given that a high performance in the forecast of the latter is the first need of the operational weather prediction, the former is adapted to this necessity, going to the detriment of its correspondence with reality. The gap between operational necessity and observations can be explained by several open challenges in the SBL study: some of them refer to the uncertainties in the observative data sampling, some other to the multitude of processes at work and their mutual interactions for which a complete physical understanding and theoretical framework still misses, and finally some others regard the intrinsic gap between the model resolution and the scale of the phenomena of the stable boundary layer. This section examines in depth all these concepts. At first, some useful concepts about the SBL physics and about the numerical weather prediction models are given (section 1.2). Section 1.3 analyses the interconnection between the local processes occurring in the stable boundary layer and the large scale synoptic circulation, while section 1.4 deepens the several open questions related to the stable boundary layer representation in operational models.

1.2 The role of the Stable Boundary Layer in Numerical Weather Prediction

1.2.1 Stable Boundary Layer

The Planetary Boundary Layer (PBL) is the atmospheric layer in direct contact with the Earth' surface, which is strongly influenced by the effects of the daily cycle and of the surface friction (Stull, 1988). In the PBL, heat, moisture, momentum and passive tracers (as pollution) are transported by turbulent eddies, which are irregular swirls of the flow. The size of turbulent eddies ranges between few millimetres and the PBL height. Indeed, they exert energy from the mean flow and transport it from larger to smaller eddies, until they dissipate it by molecular viscosity. These turbulent motions are driven by mechanical forcing and buoyancy. The first is caused by the friction that the surface imposes to an adjacent moving flow, for which the surface roughness (e.g. due to obstacles like grass, trees, buildings) plays a relevant role. By this, the generated wind shear feeds the turbulence. On the other side the buoyancy force originates from a density difference between a warm air fluid parcel and a colder surrounding environment, leading to an upward displacement. This mechanism is a source of turbulence. During daytime, in particular over land where the surface quickly responds to the daily insolation, the buoyancy generated by heating from the ground surface is the major driver of turbulence. The boundary layer rapidly grows in the morning, and large convective eddies provide vigorous vertical mixing over typically 1-2 km depth. The PBL is then called unstable or convective. The buoyancy force can suppress turbulence as well, i.e. in case an upward moving air parcel is colder than the environment and sinks. In this case, vertical motions are dampened and the turbulence is only sustained by the mechanical forcing. In this case, the PBL is then called stable (SBL). Turbulent eddies are small, vertical exchange is low and the PBL becomes shallow, with depths of 100-200 m. Due to the low level of turbulent mixing, other small scale processes influence the SBL transport: divergence of radiation, fog and dew formation, topographical slope effects, intermittent turbulence, internal gravity waves (orographically induced and not) and meandering motions as well as surface heterogeneities.

The multiplicity of physical processes, their mutual interaction and their site-dependence hampered ambiguity in the interpretation of the observations in SBL. Despite the large effort of the scientific community, many processes lack a complete understanding, which prevents the adequate representation of the SBL in numerical weather prediction (NWP) models.

In term of weather prediction, the main responsibility of the boundary layer simulation is the representation of the transport of the dynamical variables (e.g. temperature, wind, humidity, ..) from the surface to the free atmosphere. The energy budget at the surface defines the surface heat fluxes, which are the source of energy at the lower boundary of the PBL. Away from the surface, turbulence together with the other mentioned non-turbulent processes mixes the PBL, thus influencing the temporal evolution of the vertical profiles of temperature and humidity. Friction at the surface, leading to

shear stress, slows down the wind, generating a vertical wind gradient and a consequent downward turbulent transport of momentum.

The correct representation of the SBL evolution is relevant mainly for nocturnal forecasts over land, as the occurrence frequency is high in these cases. Indeed, the SBL develops in response to surface cooling by infrared (longwave) upwelling radiation emission. In particular, the absence of clouds strengthens the thermal stratification, as clouds emit longwave that warms the surface up and, similarly, weak winds intensify stability, due to the low shear production of turbulence. Moreover, the SBL occurs also daytime during winter in mid-latitude or over polar regions , as well as in case of warm advection over a cold sea surface. First applications regard the near surface temperature and humidity, and in particular minimum temperature as nocturnal situations are mostly involved. In transport and aviation for instance, the warnings of road-ice or fog or haze are based on these variables. Similarly, for agricultural purpose, the forecast of near surface frost can help to plan protection for plants and yields. The PBL depth is needed in air quality modelling, as it determines the layer where the pollutants emitted at the surface are diluted. When the PBL is shallow, pollutions stay stagnant close to the surface, increasing the pollutant concentration. Finally, the accurate forecast of wind profile in SBL is determinant for the estimate of wind energy production. For these, wind forecast is required at 100-200m above the ground, where the wind inertial oscillation may play a large role. The wind strength at this level is highly influenced by the velocity and intensity of the surface-to-atmosphere decoupling.

In the SBL, the potential temperature θ increases with the altitude. In case also the temperature increases with the altitude, the layer experiences a thermal inversion. In the vicinity of the SBL top, a layer of supergeostrophic wind, called Low-Level Jet (LLJ), may develop during night while subgeostrophic wind occurs during daytime due to the large turbulent mixing. Indeed, after sunset, the stable layer at the surface reduces the drag to only the lowest tens of meters, allowing the air flow aloft to accelerate. Fig. 1.1 reports an illustrative profile of a SBL.

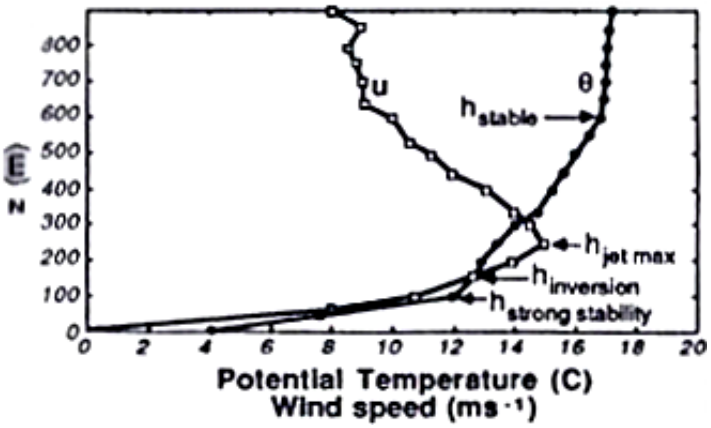

Figure 1.1: Typical vertical profiles of potential temperature and wind speed in a SBL

Often the SBL is classified in two regimes (Mahrt, 1998). In the so called *weakly stable regime*, the turbulence is the dominant transport mechanism, in which the vertical turbulent heat flux increases monotonically with the stratification intensification. In the *very stable boundary layer*, the stratification drastically alters the turbulence structure: buoyancy suppression of the vertical turbulent motion is such that the turbulent heat flux decreases for any further straightening of stratification. If the buoyancy effects and viscous dissipation overcomes the shear production, turbulence may also vanish. However, the cessation of turbulence is not an on-off process, as it is frequently broken by significant local turbulence episodes, which identify the intermittent behaviour of turbulence in the very stable regime (Mahrt, 2010).
Beyond turbulence, other processes are at work. The most relevant are here introduced.

Radiation

Because the SBL is mainly a nocturnal phenomenon, principally longwave radiation is of interest in the SBL. The main roles of infrared radiation in SBL are in the surface energy budget and in the radiation divergence (i.e. radiative cooling) of the atmosphere. The former is linked to the net irradiance (difference between up- and down-welling fluxes) at surface. Whilst the surface temperature governs the surface upwelling emission (spectrally integrated longwave radiation is a function of the forth power of temperature), the profile of temperature and also the profiles of moisture, carbon dioxide and methane dominate the radiative exchange within the atmosphere and towards the surface (due to their longwave absorptivity). Especially in the SBL, the temperature gradients near the surface can become extremely large, and consequently the net irradiance differs strongly between the different layers. The vertical divergence of the net irradiance in an atmospheric layer defines the radiative cooling rate of that layer.

Moist processes

The radiative cooling of the surface can lead the adjacent air to saturation, allowing condensation and radiative fog development. As the fog grows, the initial stable stratification is destabilized, partly because of the condensational heat release within the fog layer and partly (and this is the largest contribute) due to the cooling at the top of the fog layer where the upwelling longwave radiation is emitted to space. A mixed layer gradually develops below the top of the fog, leading, in final stage, to a saturated-adiabatic lapse rate.

Land surface

In the nocturnal SBL, the (upwelling) soil heat flux is one of the terms of the surface energy budget, together with the net radiative flux and the sensible and latent heat fluxes. It is determined by the soil thermal profile and the thermal conductivity, where the latter depends on the soil moisture and on the soil type. Moreover, the snow cover

and the presence of vegetation, as well as the freezing of the soil moisture, increase the soil isolation. Another connection to SBL is through the surface momentum and heat fluxes by means of the surface roughness: the more complex the flow is through the surface obstacles (e.g. buildings, vegetation, sea waves, small topography), the more flux is exerted.

1.2.2 Numerical Weather Prediction models

The models in our interest are mathematical representations of a part of the atmosphere through equations that relate variables thought to be important to describe it. Numerical models resolve these equations numerically. Weather prediction models numerically resolve the following set of non-linear differential equations:

- conservation of momentum: simplification of Navier-Stokes equations representing the fluid flow in the rotating atmosphere and assuming that the atmosphere is in hydrostatic equilibrium (hydrostatic models) or not (non-hydrostatic models)
- continuity equation, i.e. conservation of mass
- thermal energy budget, considering heat sink and sources
- conservation of water mass (in various phases)

Dynamical prognostic variables are the wind components u, v, w, the potential temperature θ, the specific humidity q (differentiating between the water phases in operational state-of-the-art models), the air density ρ and the pressure p.
NWP models discretize the atmosphere by a 3-dimensional grid and resolve the governing equations in every grid point. Global models represent the full Earth's atmosphere up to the top of stratosphere and higher, while limited area (or regional) models consider a reduced domain, generally at higher resolution, and need to be fed at the boundaries with the incoming phenomena.
Some processes can not be explicitly simulated, either due to their relatively small scales (unresolved for the model), the ignorance of the fundamental equations of the processes, the high complexity of their solutions, or the impossibility to write the equations in a closed form. Therefore they need special parametrizations that mimic the processes without coming from basic principles. Current NWP models include specific schemes for radiation, gravity wave drag, vertical turbulence, convection (despite deep convection is resolved by finer resolution models), clouds and surface interaction.

1.3 Critical aspects of the Stable Boundary Layer simulation

A large intercomparison in the framework of the GEWEX [1] Atmospheric Boundary Layer Study (GABLS) evidenced the lower skilfulness of the operational NWP models in reproducing SBL compared to research NWP models and to the reference, given by an ensemble of Large Eddy Simulations (LES, i.e. fluid-dynamics models that describe the largest flow eddies by resolving the Navier-Stokes equations together with a low-pass filter). As it will explained later in this section, the requirements of the operational forecast are detrimental to the SBL simulation. For instance, in the idealized simulation of a weakly stratified boundary layer in homogeneous terrain (experiment GABLS1), the operational models produced significantly deeper SBL, with small wind turning between the surface and the PBL top, weaker stratification and too high and weak LLJ (Beare et al., 2006; Cuxart, 2006; Svensson and Holtslag, 2009), see Figure 1.2.

Regarding the operational forecast, the same mismatch of the SBL structure is visible through biases in the nocturnal temperature and humidity forecast over land in wintertime, as cold continental regions offer favourable conditions to the SBL development. As an example, Figure 1.3 illustrates the broader mean absolute error in the nocturnal temperature at 2m in the Northern Hemisphere during winter, compared to the summer scores in the Southern Hemisphere, produced by the leading European Centre for Medium-Range Weather Forecasts (ECMWF) numerical weather prediction model. Atlaskin and Vihma (2012) showed an increase of the 2m temperature bias with decreasing temperature and strengthening thermal inversion in four NWP models (the global model developed by ECMWF, the regional model developed by an european consortium, the the regional model developed by Météo -France and the global model of the US National Center for Environmental Predictions, NCEP), despite the model differences in data assimilation, forecast initialization and configuration, physical parametrizations and dynamical cores. The same models simulate too weak thermal inversions in case the observed stratification was very stable. In term of wind, the directional turning across the boundary layer in short-range forecasts was identified as systematically underestimated by two independent NWP models (ECMWF model and the regional model developed by UK Met Office) in a verification performed over the North-Atlantic (Brown et al., 2005). A large fraction of the cases with the largest errors resulted in stable boundary layers. In these cases the modelled boundary layers were typically too deep.

The clear difficulty of operational NWP models in the SBL representation originates in the introduction of measures that enhance turbulent diffusion beyond the micrometeorological observational evidence. These measures were implemented in the 90's and were called "long tail" as they introduced a non-zero turbulent mixing at large Richard-

[1] The Global Energy and Water Cycle Experiment (GEWEX) is a core project in the World Climate Research Programme (WCRP) pertaining to the dynamics and thermodynamics of the atmosphere and interactions with the Earth's surface

Figure 1.2: Profiles of (a) potential temperature (K), (b) total horizontal wind speed (m s1), and (c) boundary layer wind turning simulated by. operational NWP models (red lines), research NWP models (blue lines), and LES models (solid black lines). From Holtslag et al. (2013)

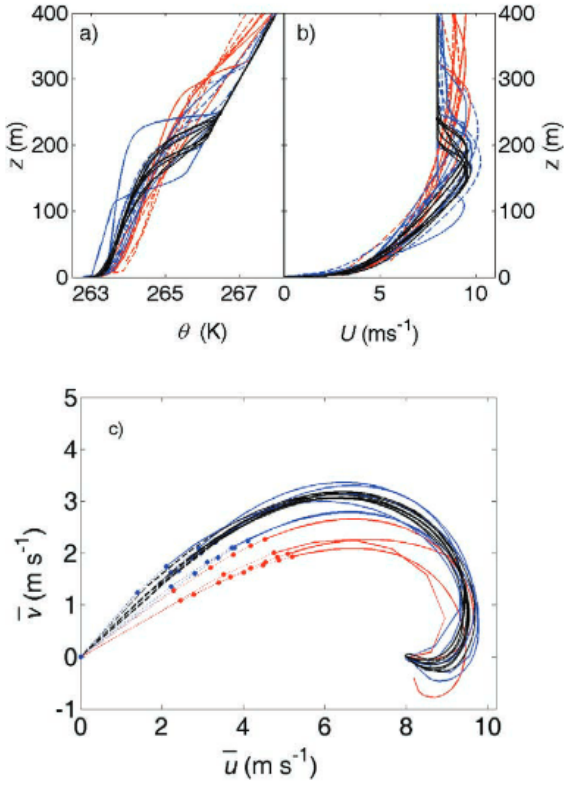

son (Ri) numbers (Louis, 1979; Viterbo et al., 1999; Beare, 2007). A first explanation was the prevention of the severe numerical issues and consequent model crash due to the occurrence of unrealistic surface decoupling from the atmosphere causing a sudden surface cooling, the so-called "run away surface cooling" (e.g. Basu and Holtslag, 2012). However, the main reason sites in the sensitivity that large scale scores show to the SBL diffusion and that historically leads the SBL simulation to be more based on model performance than on physical reality. In the 90's, many large scale operational NWP models suffered from insufficient cyclone filling, i.e. the forecast low pressure systems were too deep and too long-lasting compared to observations (Viterbo et al., 1999; Beljaars and Viterbo, 1998; Holtslag et al., 2013). It was apparent that additional drag was required to dampen the large-scale "activity". This was finally obtained by enhancing turbulent diffusion and drag by long tail formulation. Despite the synoptic flow was better reproduced, these measures were not physically justified in term of boundary layer simulation (Beare, 2007; Sinclair et al., 2010), leading to the inconsistent operational representation of boundary layer structure under stable stratification. The bridge between large scale processes, as low pressure systems evolution, and a

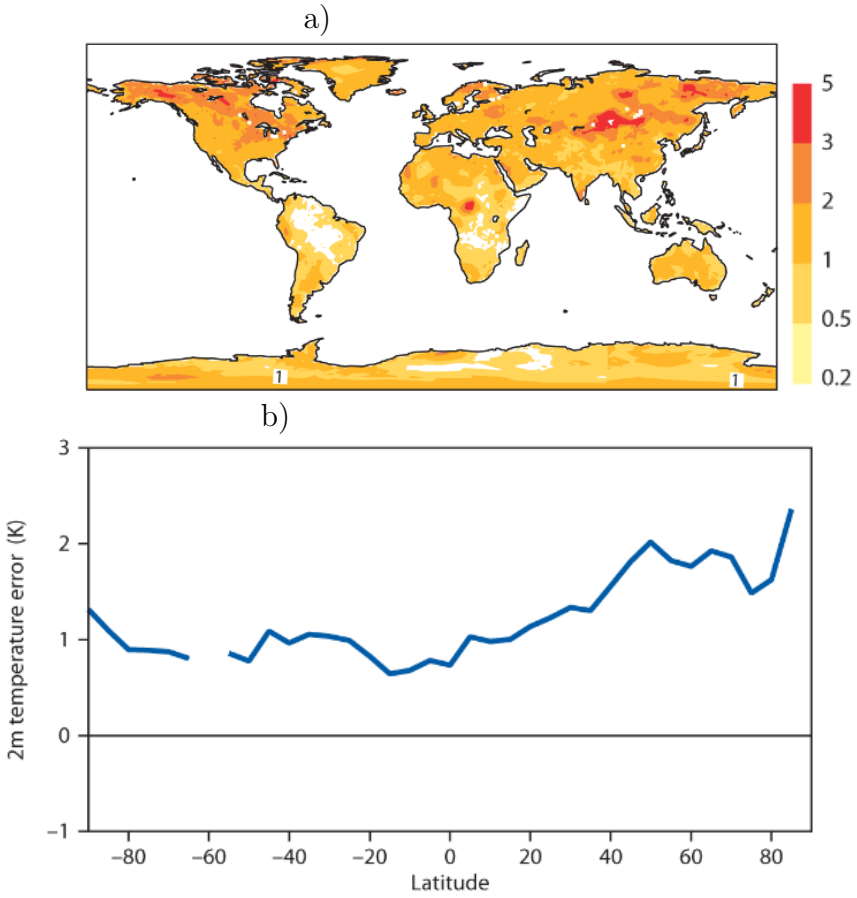

Figure 1.3: Mean absolute error (a) and its zonal average over land (b) of the nocturnal 2m temperature of the operational ECMWF system against the analyses for January 2011. Analysis draws well to the SYNOP observations of 2m temperature except in areas with very few or no SYNOP stations. From Beljaars (2011)

local process such as turbulent diffusion is arguably mainly based on the momentum budget (Holtslag et al., 2013; Beljaars, 2011; Svensson and Holtslag, 2009). Within the boundary layer, the cross-isobaric (ageostrophic) flow is produced by the friction at the surface in the direction of geostrophic wind. In particular, the vertical integral of the cross-isobaric flow is equal to the surface momentum stress along the geostrophic wind direction, under the assumption of flow stationariety and homogeneity (Svensson and Holtslag, 2009). If it is assumed that the geostrophic wind blows in u-direction, this relation can be formulated as:

$$f \int_0^\infty \overline{v} dz = -\overline{u'w'_0} \tag{1.1}$$

where f is Coriolis parameter ($f = 2\Omega sin\sigma$, with Ω the rotation rate of the Earth and σ the latitude), v is the cross-wind component (i.e. wind normally oriented to the geostrophic wind) and $\overline{u'w'_0}$ is the surface stress in the geostrophic direction. Integrating

along the vertical eq. 1.1, the averaged cross-wind component $< v >$ within the PBL is directly related to the surface stress itself, while it is inversely related to PBL depth h_{PBL}:

$$< v >= \frac{\overline{u'w'_0}}{fh_{PBL}}$$

Eddy diffusivity influences all these three components in SBL (Svensson and Holtslag, 2009; Grisigono, 2011), thus justifying its role for large scale systems forecast, as for example the cyclone filling.

1.4 Challenges in Stable Boundary Layer simulation

The gap between operational necessity and observations can be described by several open challenges in SBL study.

1.4.1 Observational and theoretical challenges

The micro-meteorological observations may be more inaccurate at low diffusivity due to limits of the instruments to record the very low fluxes typical of very stable regime. Moreover, with increasing stability flow becomes more horizontal and observation footprints enlarge, thus disturbances located several hundred meters away may affect measurements.
Another relevant issue is in the observation elaborations, which may be affected by self-correlation (i.e. when one dimensionless group of variables is plotted against another, and both the groups are dependent on some common variables, e.g. Hicks, 1978). Self-correlation affects the derivation of the empirical functions at the base of the Monin-Obukhov similarity theory (Monin and Obukhov, 1954), the well accepted and validated theory expressing the flux-gradient relation in the surface layer (Stull, 1988) and, on a local sense, in the whole SBL, via the local similarity theory from Nieuwstadt (1984, 1985). The empirical dimensionless lapse rate ϕ_h and the dimensionless shear ϕ_m define the ratio between the vertical gradients of momentum and heat and their respective fluxes. Self-correlation arises in the traditional plot of ϕ_m and ϕ_h as a function of the dimensionless stability parameter $\xi = z/L_{MO}$ (Baas et al., 2006), where z is the distance from the surface and L_{MO} is Monin-Obukhov length dependent on momentum stress τ and buoyancy flux $\overline{w'\theta'}$:

$$L_{MO} = -\frac{\theta_0(\tau/\rho)^{3/2}}{kg\overline{w'\theta'}|_0}$$

In this representation, the momentum and heat fluxes are common variables in x and y axes. In particular in stable conditions, self-correlation leads to an asymmetric behaviour of the data scatter, which is much large in ϕ_h than in ϕ_m (Baas et al., 2006).

It should be noted that the same issue is valid also for unstable stratification, but with inverted asymmetry (the scatter is larger in ϕ_m and is suppressed in ϕ_h) and with lower extent. Indeed, the stability parameter ξ includes high power of the fluxes, which are very large in unstable stratification and very small in stable cases (for instance u_* is at the third power). Therefore, the uncertainty associated to ξ is much smaller in unstable cases than in stable ones. The solution is to raise the most uncertain variables (for SBL the turbulent fluxes) to the lowest power in order to minimize the influence of their high relative error (Baas et al., 2006). Given that under stable stratification the gradients are much larger than the fluxes and their relative error is much smaller, Klipp and Mahrt (2004) suggested to substitute ξ with the Richardson gradient number, which is:

$$Ri_g = \frac{\frac{g}{\overline{\theta}}\frac{\partial \overline{\theta}}{\partial z}}{(\frac{\partial \overline{u}}{\partial z})^2}$$

Based on this arguments, it can be stated that Monin-Obukhov similarity theory is much more suitable for unstable than for stable conditions. It can be regarded as a flux-based scaling approach, while for the SBL a gradient-based scaling might be more suitable (Baas et al., 2006). Development along this line are in Sorbjan (2006, 2010).
One of the most challenging issue connected to the SBL representation is the lack of a general framework incorporating the very stable regime (e.g. Mahrt, 2010). Nieuwstadt (1984, 1985) theory of local similarity in the SBL has been largely validated in the limit of weak stability (e.g. Sorbjan, 2006), but it tends to fail when wind slows down and stratification increases (e.g Grachev et al., 2005; Mahrt, 2010). From atmospheric observations, it is still unclear if stratification can become strong enough to suppress totally turbulence (Mauritsen and Svensson, 2007; Mahrt and Vickers, 2006), and even the definition of a turbulent or non-turbulent regime may be locally difficult in a very stable boundary layer. However, it is a well-accepted hypothesis that the cessation of turbulence is not an on-off process, but rather an intermittent local transition from the absence of turbulence to turbulent occurrences. This behaviour of turbulence is referred to as global intermittency (Mahrt, 1998). This intermittency has been observed concurrently at different disturbances of the flow, like orographic obstacles (Acevedo and Fitzjarrald, 2003), density current passage (Sun et al., 2002), solitary and internal gravity waves (Sun et al., 2004) and non-turbulent wind oscillation (e.g. in the LLJ, Sun et al., 2012). Moreover, it has been recently proved that global intermittency can occur also in absence of these local perturbations (Ansorge and Mellado, 2014), thus resulting an intrinsic feature of the stratified atmosphere. In this sense, flow perturbations are simply triggers of the turbulent episodes and determine the spatio-temporal distribution of intermittency, coherently with the site dependency observed in turbulence intermittency (Mahrt, 2010).
A hypothesis of the mechanism behind turbulence intermittency in absence of trigger is based on the existence of a maximum amount of turbulent heat that can be transported downwards, limited by the available mechanical forcing (i.e. wind shear, de Wiel et al., 2012a; Donda et al., 2016). In the case of weak winds and high radiation divergence, this maximum can be significantly smaller than the net radiative loss minus soil heat

transport. This imbalance in the surface energy budget generates a rapid surface cooling that further suppresses the turbulent heat transport, so that eventually turbulence largely ceases. However, cessation of turbulence reduces the turbulent friction and leads, on a long-term, to a flow acceleration, which provides enough shear to turbulence generation. The interplay between these regimes is driven by the time scale for boundary layer diffusion (typically on the order on tenth of minutes) and the time scale for flow acceleration (i.e. $f^{-1}s^{-1} \approx 10^4 s$ at midlatitude). The former time scale limits the available momentum that can be used for surface heat extraction and the fact that it is much smaller compared to the acceleration time scale can explain the several hours-duration of turbulence cessation observed (Sun et al., 2004). A first parametrization of this mechanism, refereed to as "maximum sustainable heat flux", was suggested by (de Wiel et al., 2012b) and it is currently under test with the use of direct numerical simulations (Holdsworth et al., 2016; Donda et al., 2016).

1.4.2 Modelling challenges

The first modelistic challenge is the adaptation of the observative evidences and derived theory to the model needs. On a side, observations represent the state of the atmosphere in a specific location. Moreover, due to the complexity of boundary layer processes, the theory is based on measurements collected on near flat, homogeneous terrain. Indeed the widely used similarity theory is valid under the assumptions of flow homogeneity and stationariety (Monin and Obukhov, 1954). On the other side, operational models need to describe the global behaviour of the atmosphere inside a grid-cell, which size may vary between 1 and $\approx 10^2$km. Traditionally it is argued that two main peaks do exist in the wide spectrum of atmospheric motions spanning from 10^{-3} to 10^8 m, and they are at the micro scale (i.e. turbulent motions, $\leq 10^3 m$) and at the synoptic scale ($\geq 1000km$). The spectrum gap between these peaks motivated the effort in representing the turbulence scale, where the bulk of unresolved energy sites. However, in the stably stratified flow this gap is not observed. Indeed the small extent of large-scale forcings gives relevance to intermediate-scale (so called meso-scale) low-energetic processes. Universal spectra of these motions are not observed but rather the energy distribution varies substantially between sites (Vickers and Mahrt, 2007; Mahrt, 2009, 2010). Moreover, their energy is generally greater in complex terrain, with the exception of drainage flows where mesoscale motions tends to be weaker than in flat terrain (Mahrt, 2007). Surface heterogeneities, e.g. in topography, land use or soil type are a first source of mesoscale motions. They are introduced in the following paragraphs. Other sources of mesoscale instability are the interaction turbulence-wave (an extended description in Sun et al., 2015) and in the flow instability (e.g. vertical directional shear, Mahrt (2007), jet streaks Koch et al. (2005)).

Unresolved orography in SBL Unresolved orography can interact with the mean flow in several ways (Lott and Miller, 1997) i) an additional drag due to low-level-flow passage along the orography flanks (blocking or form drag), ii) an additional drag due

to the breaking of vertical propagating gravity waves generated by stably stratified flow passing over the sub-grid scale orography, iii) wave stress generated by vertically propagating or trapped gravity waves in the lee of the orography.
For strong flow and/or weak stability, a large part of the flow passes over the orography, then the amplitude of the vertically propagating gravity wave is large and the depth over which blocking is effective is small. Vice versa for weak flow and very stable stratification, air sticks to the orography flanks, thus the gravity wave amplitude is small and the blocking height large. Different parametrizations of the combination of these processes (e.g. McFarlane, 1987; Lott and Miller, 1997; Webster et al., 2003; Brown and Webster, 2004) are included in NWP models with forecast quality improvement (Palmer et al., 1986), especially in the Northern Hemisphere during winter. However, normally only orography on horizontal scales larger than 5 km (Beljaars et al., 2004) is considered, as smaller scales can excite only evanescent (non-vertically propagating) gravity waves. However, on one hand this is not a constraint for the blocking effect, which should be considered also at smaller scales and, on the other hand this may be correct for typical free-tropospheric stratification, but is not a priori correct for the SBL, where smaller horizontal scales may influence gravity wave generation (Steeneveld et al., 2008).
Regarding the first point, a representation of the form drag due to orography on scales smaller than 5km is usually included in models as a contribute on surface momentum flux. A specific parametrization of this contribute was developed by Beljaars et al. (2004). It evidenced improvements in the simulation of winter months in the Northern Hemisphere in term of geopotential height at 1000hPa and in large-scale scores (in IFS model of ECMWF Sandu et al., 2013), and at the local scale in near-surface winds especially in SBL but with some negative feedbacks on winds during daytime (in WRF model Lorente-Plazas et al., 2016). Other models (e.g., the UM of the MetOffice) do not have a special parametrization for turbulent orographic contribute to drag, but represent it by artificially enhancing the surface roughness length over orography, so that the orographic form drag is implicitly represented by surface fluxes parametrization.
Regarding the wave stress due to orography on scales smaller than 5km, it has been theoretically shown (Nappo, 2002; Chimonas and Nappo, 1989) and observed (Steeneveld et al., 2009) that it can be as large as the turbulent stress in SBL during weak wind; neglecting it in NWP models can be a possible explanation for the need for long-tail mixing functions. A preliminary study evidenced that a parametrization of the wave stress in SBL gives similar cross-isobaric mass flow (a measure of the cyclone filling) of the long-tail formulation, and at the same time a smaller (more realistic) boundary layer height, as well as a better representation of the LLJ (Steeneveld et al., 2008). However, a validation of the scheme is still necessary before any application in NWP models.
Several other processes related to terrain slopes may affect the SBL, for instance the shear increase due to the drainage flow along the orography flanks (Mahrt, 1982), the cold pools formation in topography depression due to the larger surface at the interface with air compared to flat terrain (e.g Jiménez et al., 2008), or the valley-mountain

breeze. However, a generally accepted framework in case they occur at the subgrid scale is not available for NWP applications.

Unresolved land use or soil type heterogeneity in SBL Land use or soil type are determinant features of the surface energy budget. Moreover, the subscale differences in temperature can generate small scale baroclinicities, which can induce sub grid circulations, increasing the wind shear and as a consequence the turbulent mixing. Furthermore, land cover determines the roughness length, which influences the momentum and heat fluxes. Depending on the scope, the resolution of a NWP model can vary from 1 to more than 50km, thus every grid cell includes a large variety of land and soil features. In general, the predominant coverage and soil type in the grid cell are extended to the full cell (so called "dominant approach"), but the results can be very different from the reality (e.g. Mahrt, 1987; Mason, 1988). An alternative approach estimates the effective parameters over the grid cell for the land surface properties (Sellers et al., 1986; Mason, 1988; Beljaars and Holtslag, 1991; Bou-Zeid et al., 2004). However, it resulted adequate only in cases of roughness variability, while the large nonlinearity due to thermal heterogeneity can not be described (e.g. Mahrt, 1987). Other approaches suggest to compute the surface energy balance for homogeneous (in term of soil and land cover features) sub-areas inside every grid cell (Avissar and Pielke, 1989). They are the "mosaic" and "tile" approaches, which differ in the sub-cell breaking up: mosaic considers a defined number of sub-area equally dividing the cell, while tile considers homogeneous sub-cell fractions of any size. The vertical fluxes over each patch are aggregated for every cell at the lowermost model level, where they are needed for vertical diffusion computation. These methods assume that vertical fluxes over each patch are much larger than advection effects between patches. Blyth et al. (1993); Blyth (1995); Arola (1999); Ament and Simmer (2006) recommend extending the tile model to heterogeneous flows at which this assumption fails, i.e. at a vertical height scale called the "blending height". The implicit assumption is that vertical homogeneity occurs below the model lowermost level. However, this hypothesis break down in case of high thermal contrast between the patches, especially with the current vertical resolution of NWP models (typically the lowermost level ranges between 10 and 20 m above the surface). Therefore, the issue of subgrid advections between the patches is not well addressed by none of the available approaches, and would require an additional parametrization. Finally, the failure of the assumption of constant fluxes in the surface layer in the SBL (see above) increases uncertainties in the heterogeneous cases. (Stoll and Porté-Agel, 2009) shown that in thermally heterogeneous terrain the introduction of Niewstadt's local scaling hypothesis (Nieuwstadt, 1984, 1985) over stable individual patches has the potential to largely improve the traditional tile approach.

A second modelling challenge is in the interdependency of processes, by which the enhanced turbulent mixing may be required to dampen the near surface response to errors elsewhere in the surface energy budget.
The representation of ground heat flux includes several degrees of uncertainty, first of

all in the temperature and moisture profiles. Due to lack of direct observations, they are often retrieved for NWP initialization from other observations (e.g. soil moisture analysis Mahfouf, 1991) or from the model itself after a long-period simulation continuously assimilating atmospheric measurements. Moreover, soil conductivity depends on local features as soil texture, density and water content. In particular in NWP models, the latter is often assumed constant in depth and equal to a medium wetness value. During night, this leads in very dry soil to too high soil conductivity with systematic overestimation of the upward ground heat flux and excessive warming of the surface (e.g. in the COSMO model Schulz et al., 2016). Another example of the feedback between soil properties and SBL simulation is in the soil moisture freezing, which increases the soil heat capacity close to the freezing point, slowing down the soil cooling (Viterbo et al., 1999). Its parametrization showed in the ECMWF model similar effects of the turbulent enhanced mixing, and their combined introduction reduced a large cold bias at 2m present over land wintertime (Viterbo et al., 1999). The soil-atmosphere transfer is also influenced by several additional processes, which need to be realistically parametrized. For instance the heat transfer in the snow cover or in the vegetation layer, with the introduction of a multiplicity of new parameters: e.g. depth, density and fractional cover of snow or type, height, activity and fractional cover of vegetation. Thermodynamic interaction of the stable boundary layer with the low heat capacity vegetation can contribute to intermittency.

Also the representation of radiation in SBL evidenced large uncertainties. For example, different radiation schemes largely underestimate the radiative cooling associated with clear sky calm nights (Steeneveld et al., 2010). This is particularly detrimental after the evening transition, when the radiative divergence is the primary contributor to the formation of the nocturnal surface inversion (Ha and Mahrt, 2003), and in very stable PBL, due to the low turbulent fluxes. It is still not clear if the problem arises from poor input to the radiation scheme (e.g. cloud cover and aerosol concentration), from its formulation, from the fact that it is not executed at every timestep or from the coarse vertical resolution. However, the latter is certainly a key point, as the strongest radiation divergence is observed with the concave curvature of the temperature profile, quite often observed in the nocturnal SBL in the surface vicinity. By this, radiative flux divergence decreases with the height, showing a stabilizing effect on the air near surface (Ha and Mahrt, 2003). Given the small vertical extent of this structure, a vertical resolution coarser than approximately 1m near the surface would linearise the temperature profile, thus underestimating the radiative cooling, and even leading to an erroneous radiative warming near the surface (Ha and Mahrt, 2003). Unfortunately, such resolution is far to be affordable by NWP models at the current state. Despite this error seems to produce similar effects of the enhanced turbulent mixing (e.g. destabilize the SBL), it may cause the neglect of other processes: for instance a very intense inversion at the surface may intensify the downwards radiation flux in the lowest few cm of atmosphere, leading to a surface net radiative flux to 0, which prevents further cooling of the surface (Edwards, 2011). This process can avoid the *run-a-way cooling* of the surface, which is one of the justifications of the introduction of the enhanced

turbulent mixing in NWP models.

1.5 Objective and plan of the thesis

Considering the above described challenges, the overall aim of the thesis can be summarized as:
to investigate the critical points in the SBL representation in specific long-tailed turbulence and transfer schemes operationally applied in a numerical weather prediction model, and to formulate and evaluate potential solutions to them
This will be achieved by pursuing the more specific aims:

1. to evaluate the performance of a specific operational NWP model in simulating real SBL conditions, compared to a short tail NWP model
2. to identify the turbulence-enhancing (or long-tail) formulations applied in the turbulence and transfer scheme, focusing on their impacts in different atmospheric and topographic conditions, to consider the consequences of their weakening/removal and to propose alternatives to the specific cases in which the limit to low diffusivity is an unmeant side effect
3. to assess the potential role of the neglected subgrid scale processes to overcome the operational need of turbulence-enhancing formulation in the SBL, and in particular considering parametrizations of :
   A. the kinetic energy transfer from circulations induced by subgrid scale orography to turbulence
   B. the modification on the SBL structure induced by subgrid thermal heterogeneity of the surface

This thesis treats the topic using the Italian reference model for limited area forecast, i.e. the COSMO (Consortium for Small-Scale Modelling) model. Chapter 2 gives at first an overview of the COSMO model, and of the operational turbulence and transfer schemes, and secondly deals with the first aim in the specific COSMO case. The aim is addressed by an inter-comparison between high resolution simulations of the SBL over a homogeneous terrain site in the Po Valley (Italy) performed by the long-tailed COSMO model and a state-of-the-art short-tailed NWP model.
Chapter 3 and chapter 4 are dedicated to the second and third aims. In particular, chapter 3 pursues point 2 in the turbulence scheme operational in the COSMO model: for each turbulence enhancing recipe, a physical description is reported followed by an investigation aimed at identifying the regions and conditions more affected by it and an analysis of the potential weakening/removing alternatives. Chapter 4 addresses point 2 in the transfer scheme, reporting the diagnostics of the problem that prevents the surface flux decays at high stability in the COSMO operational model, which thus acts

as transfer-enhancing formulation.
Chapter 5 and chapter 6 tackle the issue of the long-tail operational necessity in a broader sense, dealing with points 3A and 3B respectively. Indeed, a likely reason for the long-tail formulations is the neglect of the complexity within grid boxes (see previous section 1.4.2). Chapter 5 gives a physical description of the parametrization of the interaction between subgrid scale orography and turbulence, as introduced in the COSMO model. Moreover, the effect in a real SBL case is investigated, as well as the parametrization role to overcome the long-tail operational need. Chapter 6 deals with the representation of the impact of terrain thermal heterogeneity at the subgrid scale on the turbulence on the SBL. The COSMO model already includes a parametrization to address this effect as a part of the turbulence scheme, but it will be demonstrated affected by several problems (sections 3.1). Chapter 6 evaluates the performance in idealized COSMO simulations of an alternative approach (tile approach), which effects are well known for convective PBL, but not enough investigated for stable PBL.

Chapter 2

The COSMO model performance in the stable boundary layer

2.1 The COSMO model

The COSMO model was developed by the Consortium for Small-Scale Modelling to provide operational high-resolution weather forecasts and is the Italian reference model for limited-area forecast. At ARPAE-Emilia Romagna weather service (hereafter referred as SIMC), it runs operationally with horizontal resolutions of 7 and 2.8km in deterministic mode and of 7km in ensemble mode. The passage to finer resolutions (respectively 5 and 2.2km in deterministic mode and one more system at 2.2km in ensemble mode) is foreseen for 2017. The integration domains of the mentioned setup are in Figure 2.1. The COSMO model makes use of three-dimensional non hydrostatic, compressible hydro-thermodynamic equations in advective form (see 1.2.2), which are solved numerically with a 2nd or 3rd order Runge-Kutta split-explicit scheme (Wicker and Skamarock, 2002). The grid structure is based on Arakawa C-grid with Lorenz vertical grid staggering in a rotated (lat/lon) coordinate system. The vertical coordinate is terrain-following, in particular the Gal-Chen height coordinate (Gal-Chen and Sommerville, 1975) is applied in SIMC configuration.
The initial conditions are produced operationally at SIMC by means of a data assimilation stream based on the nudging technique (Schraff, 1997), but optionally can be an interpolated analysis from a coarser-grid model (e.g. IFS, ICON [1]). Lateral boundary conditions are always introduced with a one-way nesting from coarser-grid models.
The physical package includes: a δ - two stream radiation scheme after (Ritter and Geleyn, 1992), a grid scale cloud and precipitation scheme (optionally a 2 or 3 categories ice scheme) and a statistical scheme for sub-grid clouds (Sommeria and Deardorff, 1977), a moist convection scheme (based optionally on Tiedtke (1989) or on Bechtold et al. (2001)) applied only in the configuration with 7km grid spacing, a shallow con-

[1]ICON is the general circulation model developed by the German Weather Service (DWD) and Max-Planck-Institute for the Meteorology

Figure 2.1: Integration domains of the COSMO model at SIMC for the configuration with 7km and 2.8km grid spacing

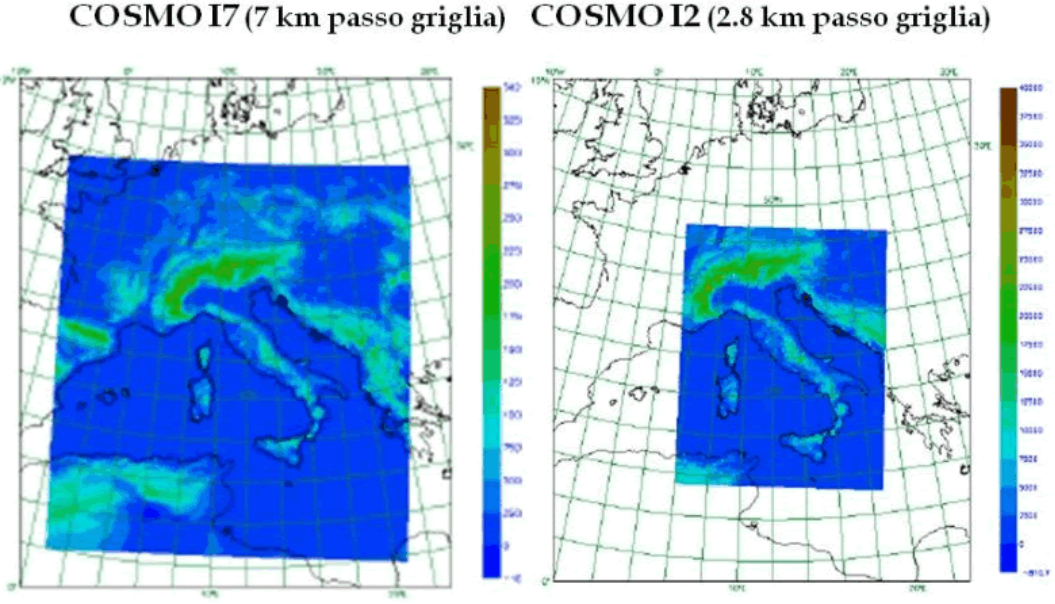

vection scheme (a reduction from Tiedtke, 1989), a turbulence scheme based on Mellor and Yamada (1982) optionally at the 2.0 or 2.5 level of their truncation hierarchy, a multi layer transfer scheme (Doms et al., 2011), a subgrid scale orography scheme (Lott and Miller, 1997) applied only in the configuration with 7km grid spacing, a multi-level soil scheme after Jacobsen and Heise (1982) based on the direct numerical solution of the heat conduction equation, a sea-ice scheme (Mironov and Ritter, 2004) and a lake scheme (Mironov et al., 2010).
Despite the SBL structure depends on the interplay of several subgrid processes (see ch 1.2.1), this thesis focuses on critical aspects of the turbulence and surface-to-atmosphere exchange. Therefore, the respective schemes (turbulence and transfer schemes) operational in the COSMO model are described in the following section.

2.2 Turbulence and transfer schemes in the COSMO model

The operational turbulence and transfer schemes were developed by Matthias Raschendorfer of the Deutscher Wetter Dienst (DWD) and have been introduced in 2001. Unfortunately, their complete description is still not available. Some aspects of the turbulence scheme are treated in unpublished works by the developer (Raschendorfer, 2001, 2009) and in the published papers from Wacker et al. (2005); Buzzi (2008); Baldauf et al. (2011). Fewer studies have dealt with the transfer scheme of COSMO, thus the only reference is Buzzi (2008). The most salient aspects of the turbulence and transfer

schemes for the present dissertation are herein reported. Their extended description is given in the Appendix.

2.2.1 Turbulence scheme

In the operational COSMO setting, the turbulence scheme uses a reduced 2-nd order closure with a prognostic equation for the Turbulent Kinetic Energy ($TKE = 0.5(\overline{u'^2} + \overline{v'^2} + \overline{w'^2})$), whereas transport and local time tendency terms in all the other 2-nd order momentum equations are neglected and the vertical turbulent fluxes are diagnostically derived. The scheme is based on Mellor and Yamada (1982) at Level 2.5, a scheme widely applied in numerical models for geophysical flow.
The time tendency of TKE, expressed in term of the turbulent velocity scale q ($q = \sqrt{2TKE}$), prescribes the balance between different forcings (first three terms r.h.s), the dissipation and its vertical diffusion (4th and 5th terms), while advection and horizontal diffusion can be optionally activated in the code but are neglected in the present thesis:

$$\frac{\partial q}{\partial t} = -\frac{1}{q}\overline{u'w'}\frac{\partial \overline{u}}{\partial z} + \frac{1}{q}\frac{g}{\theta_v}\overline{w'\theta'_v} + f^C - \frac{\epsilon}{q} - \frac{1}{\overline{\rho} q}\frac{\partial}{\partial z}\left[\frac{1}{2}\overline{\rho q^2 w'}\right] \tag{2.1}$$

Besides the forcings due to wind shear and buoyancy (the first and second terms r.h.s., later called f_m and f_h), some additional contribute to TKE is given by the interaction between turbulence and mesosocale circulations (f_C). The latter includes the treatment of some subgrid scale flow patterns generated by subgrid scale heterogeneities (e.g. orography, surface thermal heterogeneity, convection plumes). These formulations address the model need of higher complexity in large grid boxes, which is especially relevant in stable stratification (see section 1.4.2). This is an extension to the original Mellor and Yamada (1982) scheme and it arises from an applied scale separation of small scale turbulence from larger, but still subgrid scale circulations (Separated Turbulence Interacting with Circulation, STIC approach Raschendorfer, 2007, 2011). Under the hypothesis of STIC approach, the kinetic energy produced at the mesoscale is transferred to the turbulence scale, and it is thus considered as a source for TKE. New scale-interaction terms (i.e. f_C) result from this procedure, and they are introduced in the TKE equation. Among the scale interaction terms, the one accounting for the shallow thermal circulation induced by surface thermal inhomogeneities such as nocturnal downhill density flow is operational in all COSMO members. The term results proportional to the vertical variation of the product between a length scale (representative of the subgrid scale surface thermal pattern) and the buoyancy forcing: $f_C \propto \frac{\partial}{\partial z}[L_{therm}\,(-f_h)]$. This length scale is estimated from average grid size dynamic variables, external settings (horizontal resolution and a configuration parameter) and the subgrid scale clouds coverage. However, the parametrization of this term is still quite rough, as in absence of subgrid scale clouds, L_{therm} in independent on any subgrid scale features (Cerenzia et al., 2014). A dependency on the standard deviation of the subgrid scale orography has been recently developed (G. Zangl, pers. commun.) and its application on the global model ICON (using the same turbulence code of COSMO)

shows promising results.
Other scale interaction terms optionally available in COSMO are: the wake production of TKE by blocking due to subgrid scale orography, which is derived by scalar multiplication of the horizontal wind vector with its tendencies generated by subgrid scale orography and the wake production of TKE by convective plume.

The vertical turbulent fluxes are computed by the down-gradient approach:

$$\overline{\psi' w'} = -K^M \frac{\partial \overline{\psi}}{\partial z} = -qlS^M \frac{\partial \overline{\psi}}{\partial z}, \quad \text{for } \psi = u, v \tag{2.2}$$

$$\overline{\psi' w'} = -K^H \frac{\partial \overline{\psi}}{\partial z} = -qlS^H \frac{\partial \overline{\psi}}{\partial z}, \quad \text{for } \psi = \theta_w, q_w \tag{2.3}$$

K^M and K^H are the eddy diffusion coefficients for momentum and scalars respectively. They are the product of q, l denoting the master (or mixing) length scale, and, respectively, of the stability functions for momentum S^M and heat S^H.
The master length scale is based on Blackadar (1962)'s formulation plus an optional additional correction for stability from Deardorff (1976), third term r.h.s. in the following formulation:

$$\frac{1}{l(z)} = \frac{1}{\kappa z} + \frac{1}{l_{scal}} + a_{stab} \frac{\sqrt{f_h}}{q} \tag{2.4}$$

In the surface vicinity, $l(z)$ is $\approx kz$, where z is the geometric distance from the rigid surface detracted from a certain displacement height of the roughness layer, and $\kappa = 0.4$ is the von Karman constant. At higher altitude, the length scale is limited by

$$l_{scal} = min(l_{max}, \Delta_g) \tag{2.5}$$

which depends on the coefficient l_{max} and on the horizontal grid scale Δ_g. l_{scal} corresponds to the ratio between the asymptotic length scale from Blackadar (1962), l_{inf} and κ, where l_{inf} represents the maximum size of turbulent eddies. If the stability correction is active, it can limit the length scale for increasing stable stratification. In case the additional correction for stability is enabled (when a_stab parameter is equal to 1), the mixing length is limited by stability (represented by f_h), thus the stronger is the stability, the smaller is the length scale.
The computation of the stability functions S^M and S^H follows Mellor and Yamada (1982) at Level 2.5 only for stable and neutral stratification, since the solution has a singularity for unstable stratification; this point is discussed by (Mellor and Yamada, 1982) and illustrated in their Figure 3. To avoid this singularity, $S^{M,H}$ are calculated in the COSMO scheme for unstable stratification by a modification of Mellor and Yamada (1982) at Level 2.5: essentially, it extends the derivation of $S^{M,H}$ done by Mellor and Yamada (1982) at 2.0 Level by introducing a non-zero time tendency term in the q equation there considered (an extended description is in Wacker et al., 2005; Buzzi, 2008).

2.2.2 Transfer scheme

In contrast with traditional NWP operational models, the COSMO model applies a transfer scheme neither explicitly employing Monin-Obukhov similarity theory (MOST) nor any empirically derived stability correction function. Rather, it is based on the decomposition of the surface layer in sub-layers, treated in terms of aerodynamic resistances. Specific assumptions and interpolations are used to calculate the sub-layers transfer resistances, while information about the turbulence state are inferred from the turbulence scheme. The aim of this unconventional scheme is firstly to enhance the consistency between the transfer and the turbulence schemes, and secondly to introduce the additional physics held onto the turbulence scheme (e.g. subgrid mesoscale processes) in the surface layer description.
The surface fluxes of momentum τ , sensible heat SH and latent heat LH are written in the traditional bulk formulation as:

$$\tau = \rho C_{SA}^{M} |\boldsymbol{v_A}|^2 \tag{2.6}$$
$$SH = -\rho c_p C_{SA}^{H} |\boldsymbol{v_A}| (\theta_A - \theta_S) \tag{2.7}$$
$$LH = -\rho L_e C_{SA}^{H} |\boldsymbol{v_A}| (q_A - q_S) \tag{2.8}$$

Here $\boldsymbol{v_A}$ is the grid cell average of horizontal wind speed. The suffixes S and A mark the surface level and the mid-level of the lowest atmospheric model layer, with $\boldsymbol{v_S} = 0$ due the non-slip condition at the surface. Further, ρ is the mean air density in the surface layer, while c_p and L_e are the specific heat capacity for constant pressure and the latent heat of vaporization. Finally, C^M and C^H are the dimensionless transfer coefficients for momentum (M) and heat (H). In the schemes based on MOST, the latters are usually derived directly from the empirical functions, while in the transfer scheme of the COSMO model, they are calculated according the following formula:

$$C_{SA}^{\varphi} = \frac{1}{r_{SA}^{\varphi} |\boldsymbol{v_A}|} \tag{2.9}$$

valid for any prognostic grid scale averaged variable φ, and where r_{SA}^{φ} is the total aerodynamic transfer resistance. r_{SA}^{φ} is the sum of the resistances of two sub-layers by which the surface layer consists in COSMO formulation.

$$r_{SA}^{\varphi} = r_{0A}^{\varphi} + r_{S0}^{\varphi} \tag{2.10}$$

The first term r.h.s. relates to the constant-flux (or inertial) sub-layer, which spans from the level z_A to the roughness length z_0, while the second term refers to the roughness sub-layer, located underneath the former, thus extending from the rigid surface level z_S to z_0 (Figure 2.2). The constant-flux sub-layer corresponds to the layer usually described by MOST. The roughness sub-layer features the processes that occur in the vicinity of the roughness elements, such as rough flow or molecular diffusion adjacent to the canopy top. The roughness sub-layer resistance for scalar r_{S0}^{H} substitutes the traditional use in MOST based schemes of a roughness length for scalars z_0^H lower than

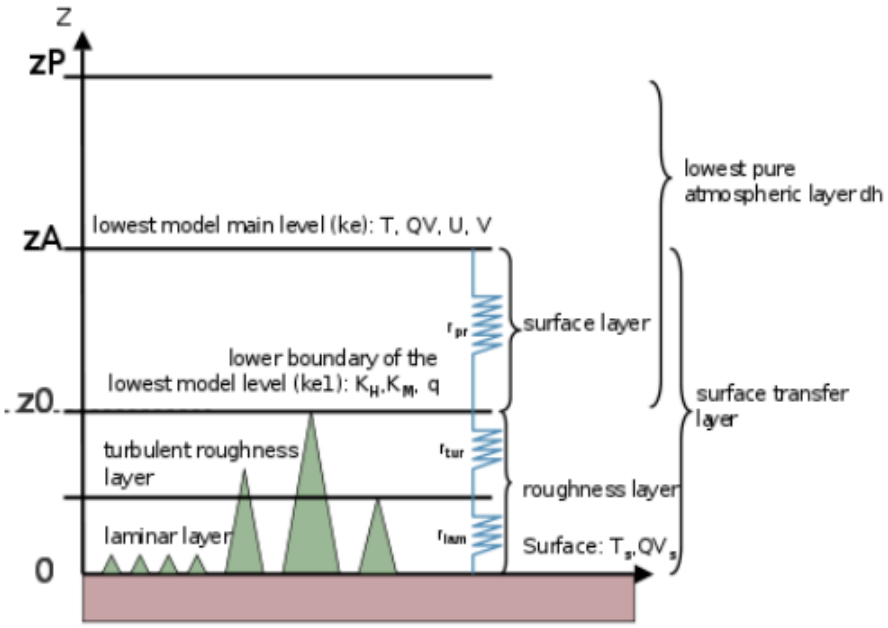

Figure 2.2: Schematic representation of the vertical levels in the transfer scheme of the COSMO model (the labelled "laminar and roughness sub-layers" correspond in their associated form to the roughness sub-layer, while the labelled "surface layer" corresponds to the inertial sub-layer). Sketch modified from Buzzi (2008)

z_0. Vice versa, the roughness sub-layer is neglected for momentum exchange ($r_{S0}^M = 0$), meaning that the roughness length for momentum z_0^M is assumed equal to z_0.
The inertial resistance represents the opposition to the transfer offered by air within the constant-flux layer, thus it can be expressed in the integral form:

$$r_{0A}^{\varphi} = \int_{z_0}^{z_A} \frac{dz}{K_{0A}^{\varphi}(z)} \tag{2.11}$$

where the specific turbulent coefficient $K_{0A}^{\varphi}(z)$ is assumed as the product of a turbulent length scale $l(z)$ and a turbulent velocity scale $u^{\varphi}(z)$:

$$K_{0A}^{\varphi}(z) = l(z)u^{\varphi}(z) \tag{2.12}$$

The turbulent length scale is defined as $l(z) = \kappa z$, while $u^{\varphi}(z)$ derives from the turbulence scheme, under provision of its functional dependence on z. Since the full turbulence scheme is applied at the upper boundary level $z = z_P$ of the lowest model layer and additionally (in a reduced mode) at level $z = z_0$, the turbulent velocity scale u^{φ} is provided at these two levels of the vertical profile and the resistance integrals can be solved via an interpolation function for u^{φ} between those two nodes.

$$\begin{aligned} K_{0A}^{\varphi}(z = z_P) &= K_P^{\varphi} \\ K_{0A}^{\varphi}(z = z_0) &= K_0^{\varphi} \end{aligned}$$

wherein K_P^φ and K_0^φ are the turbulent diffusion coefficients derived at level z_P and z_0 respectively. The interpolation function for u^φ between those two nodes is assumed linear with z, in order to ensure the accordance with the log-low based formulations at least in the specific case of neutral stratification. In the latter case $u_P^\varphi = u_0^\varphi$ and particularly $u_0^M = u_*$, in which $u_* = \sqrt{|\frac{\tau}{\rho}|}$ is the friction velocity, and:

$$K_{0A}^\varphi(z) = K_{MOST}^\varphi(z) = zku_* \tag{2.13}$$

The final formula of r_{0A}^φ and r_{S0}^φ applied in COSMO code and their derivations are reported in Appendix B.1. Through the same resistance reasoning, the diagnostic formula for the temperature and humidity at 2m and the wind components at 10m are derived (as reported in Appendix B.2).

2.3 Long-term verification

A very favourable region for the SBL development is the Po Valley in North-Italy, a large flat area extended about 400Km in W-E direction and 100Km in the N-S direction and shaded from the main westerly winds by the Alps Mountains. Thus, weak winds are very common and in case of fair weather, the nocturnal cooling yields to intense stratifications in the surface vicinity. In conditions of clear sky and weak winds, the operational verification of the near surface variables in COSMO evidences:

- an underestimation of the amplitude of the daily cycle of temperature at 2m. The difference is greater in absolute value at night when the overestimation of the minima is about 1.5-2°C on average (but peak errors can be as large as 5-8°C), whereas in the daytime the average underestimation of the maxima is about 0.5-1°C (see Figure 2.3),

- an overestimation of the wind speed at 10m above the surface, but the largest errors being found during daytime (Figure 2.4).

Figures 2.3-2.4 refers to Spring 2012, but similar scores are still actual, with worse performance during winter, when the stratification conditions are stronger. In the same conditions, the PBL height is overestimated as well as the thermal vertical gradient within the SBL is underestimated. The case shown in Figure 2.5 is not uncommon in the night time in absence of cloud cover and strong wind. In the reported case, the observed thermal difference between the lowest measurement (2m) and the top at the thermal inversion was about 10°C, in contrast with the 2-3°C foreseen by COSMO.
In this sense, the operational COSMO model shows difficulties in the forecast of SBL intensity and structure, in agreement with other NWP operational models (see chapter 1.3).

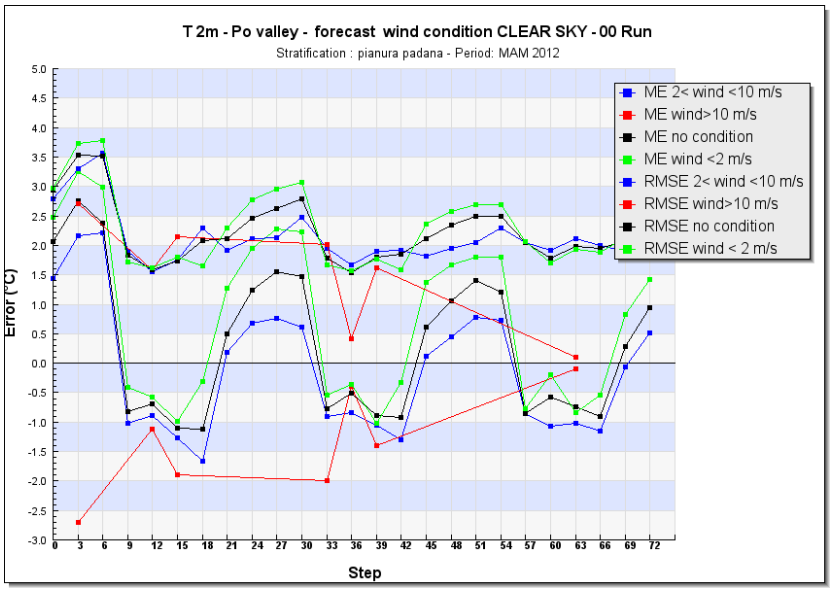

Figure 2.3: Average trend of the errors of temperature at 2m produced by the operational COSMO-I7 at SIMC in the spring months of 2012 in conditions of clear sky during the forecast, considering all the Po Valley stations. Different colours refer to wind strength conditions (red to $Ws \geq 10m/s$, blue to $2m/s \leq Ws \leq 10m/s$, green to $Ws \leq 2m/s$, black to no wind discrimination). Red curve is not statistically significant due to the low amount of data.

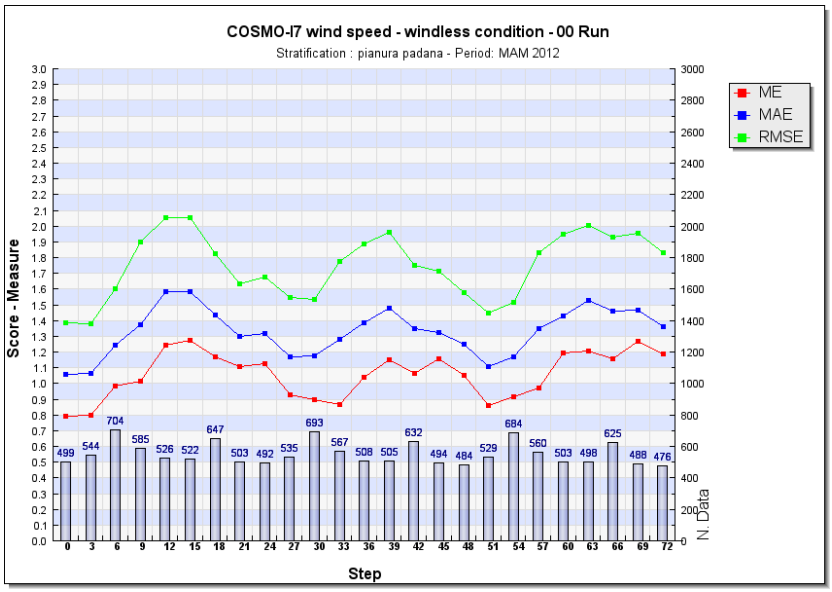

Figure 2.4: Average trend of the errors of wind speed at 10m produced by the operational COSMO-I7 at SIMC in the spring months of 2012 in conditions of clear sky adn wind speed lower than $2m/s$ during the forecast.

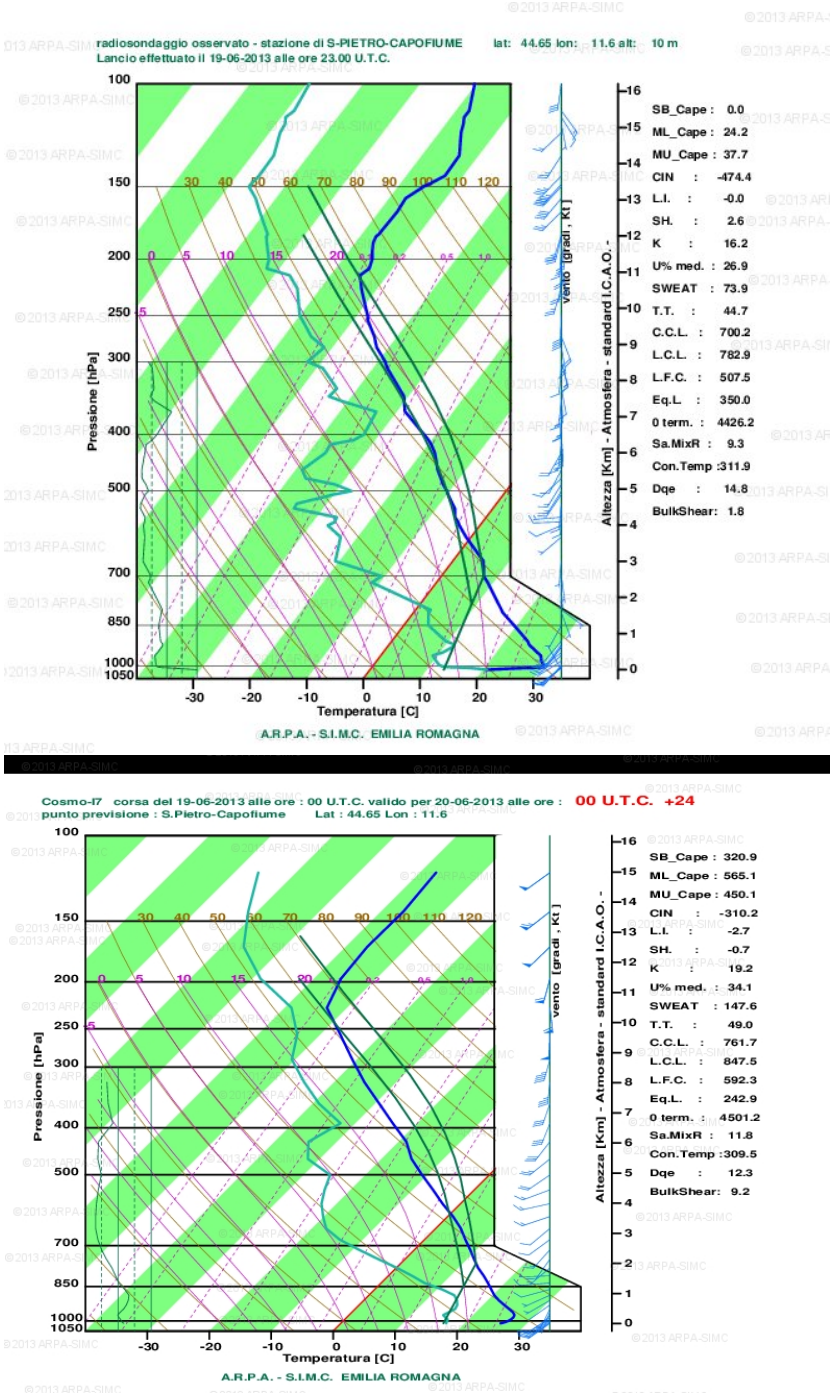

Figure 2.5: Forecasted (top) and observed (bottom) profiles of temperature and dew point temperature at San Pietro Capofiume station in the Po Valley at 00 UTC of 20/06/2013

2.4 Intercomparison of COSMO and WRF in a real case study simulation

The first step to study the COSMO model performance in SBL is to test it in a specific real case. The simulation is compared with observations collected at a specific location, and additionally, with the performance of another state-of-the-art mesoscale NWP model. For this purpose the Weather Research and Forecasting WRF model (textithttp://www.wrf-model.org/index.php) is selected, being similar in its architecture to COSMO. A three day synoptically quiescent period is considered and a dataset collected at the San Pietro Capofiume station in the middle of the Po Valley, Northern-Italy, is used as a reference. Both models are nested in ECMWF operational analysis (initial and boundary conditions) and their configurations in terms of grid size, domain, warm-up time are chosen in order to minimize differences. The spatio-temporal evolution and various simulated statistics of the very stable boundary layer are compared with a focus on the turbulence modelling. In order to highlight the role of the long-tail formulation, the COSMO model applies the operational long tail turbulence scheme (adaptation from Mellor and Yamada (1982) scheme at Level 2.5), while WRF uses a short tail scheme (Yonsei University scheme version 3.4.1). The impacts due to the different transfer, radiation and land surface modelling are tackled as well. Section 2.4.1 describes the observational site and dataset, while the WRF model and its components relevant for the present analysis are introduced in section 2.4.2. In section 2.4.3, the experimental setup is illustrated and the results are presented in section 2.4.4.

2.4.1 The observational array

The observational dataset is collected at the observatory of San Pietro Capofiume (N 44.65, E 11.62). It is a grassland site surrounded by crop, laying in a flat area about 60km away from both the sea and the first hills of the Appenines (Figure 2.6) The

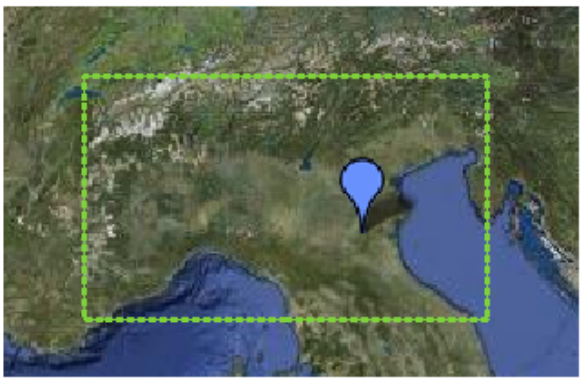

Figure 2.6: Geographical location of San Pietro Capofiume station (blue arrow) in Northern Italy (green box)

surface features a low heterogeneity level essentially due to land use: a small bunch of trees and some buildings are within 200m distance to the instrument field, mainly in directions North and East (see Figure 2.7). The surface patchiness due to crops, bare soil and grass is extended for several km in every direction. However, during the night and in absence of fog, the thermal heterogeneity of this kind of surface is quite small (approximately $O(10^{-1}K)$ [2]) and, aside from the vegetative season, also the roughness variation is scarce.
Measurements of surface fluxes for momentum and heat are provided by an eddy-covariance instrumentation located 3.6m above ground and they are used for our purpose as 60-min averages. Vertical sampling of wind, temperature and humidity is performed daily by a radiosonde launch at 00UTC. Besides the near-surface measurements of wind at 10m, as well as temperature and humidity at 2m, observations of radiation and the soil states are also available (Bonafé, 2010). Instrument positions are reported in Figure 2.7.

Figure 2.7: Aereal photo of the measurement field at San Pietro Capofiume, from Bonafé (2010)

The meteorological situation in the selected period (07-10 January 2012) was dominated by a large anticyclonic system located in the North-East Atlantic, with its eastern part extended over North Italy (Figure 2.8). In the Po Valley, the weather was very stable and characterized by clear sky and absence of significant weather phenomena. At the surface, large daily thermal excursions of $15°C$ were observed and winds were generally weak with values on average about 2-3 m/s coming from West, North-West.

[2]determined by very high resolution numerical simulation performed by COSMO over Po Valley region away from inland water basins or rivers

Dry soil and relative humidity always below 80%, but the night of the 9th of January, created conditions unfavourable to fog developing during the night (see later).

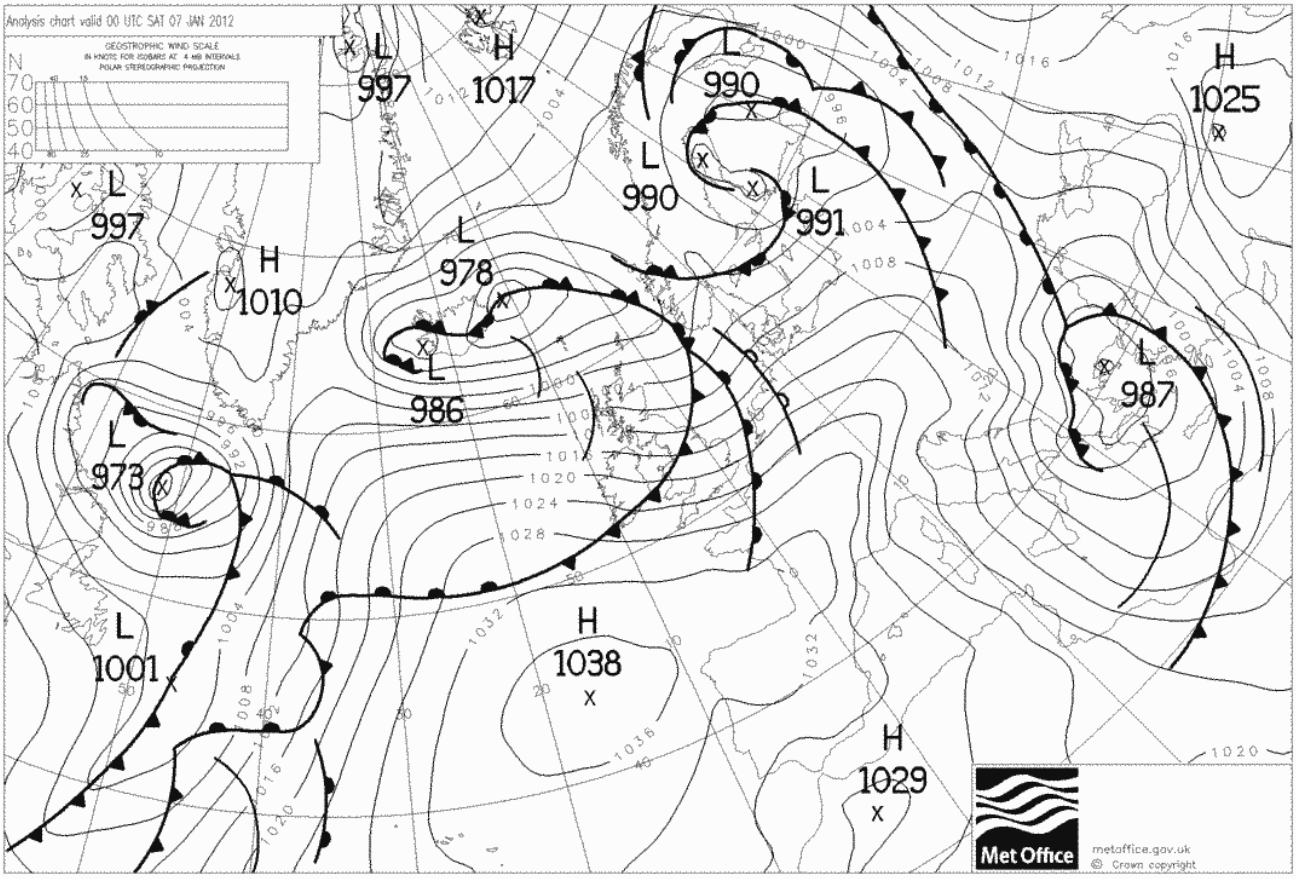

Figure 2.8: Surface pressure field over Europe at the 07/01/2012 00UTC

Spatial representativeness of the dataset

In order to ensure the spatial representativeness of San Pietro Capofiume station, the hourly anomaly correlation of the near surface parameters (temperature and relative humidity at $2m$ and wind speed at $10m$) collected at the site is computed with respect to the data sampled by other stations in Po Valley. The anomaly is calculated with respect to the monthly average day of the period 2009-2013. Figure 2.9,left illustrates how San Pietro Capofiume station is representative of an area of $50 - 100km$ (values of correlation R larger than 0.8) for the temperature and relative humidity at $2m$, while the spatial correlation of wind speed at $10m$ is lower ($R \approx 0.5 - 0.7$) within the same ray. In absence of strong synoptic forcings, the wind is particularly sensitive to local processes, explaining its high temporal variability and its low spatial correlation. The influence of local processes is more evident during the night when stability is more intense. Moreover, they affect with a smaller extent the temperature and humidity as

well. Indeed during the selected period, the variability of the stations correlated to San Pietro Capofiume (i.e. with $R \geq 0.9$ in the hourly anomaly of temperature at $2m$) is larger in the night time than daytime for both the scalar parameters (Figure 2.9,right). During the night, San Pietro Capofiume tends to be colder and consequently with larger relative humidity than the surrounding. Nevertheless, the data fall in the interquartile area with only few exceptions. Despite wind speed has a lower spatial representativeness, in general the order of magnitude and the time evolution is coherent with the more correlated stations.

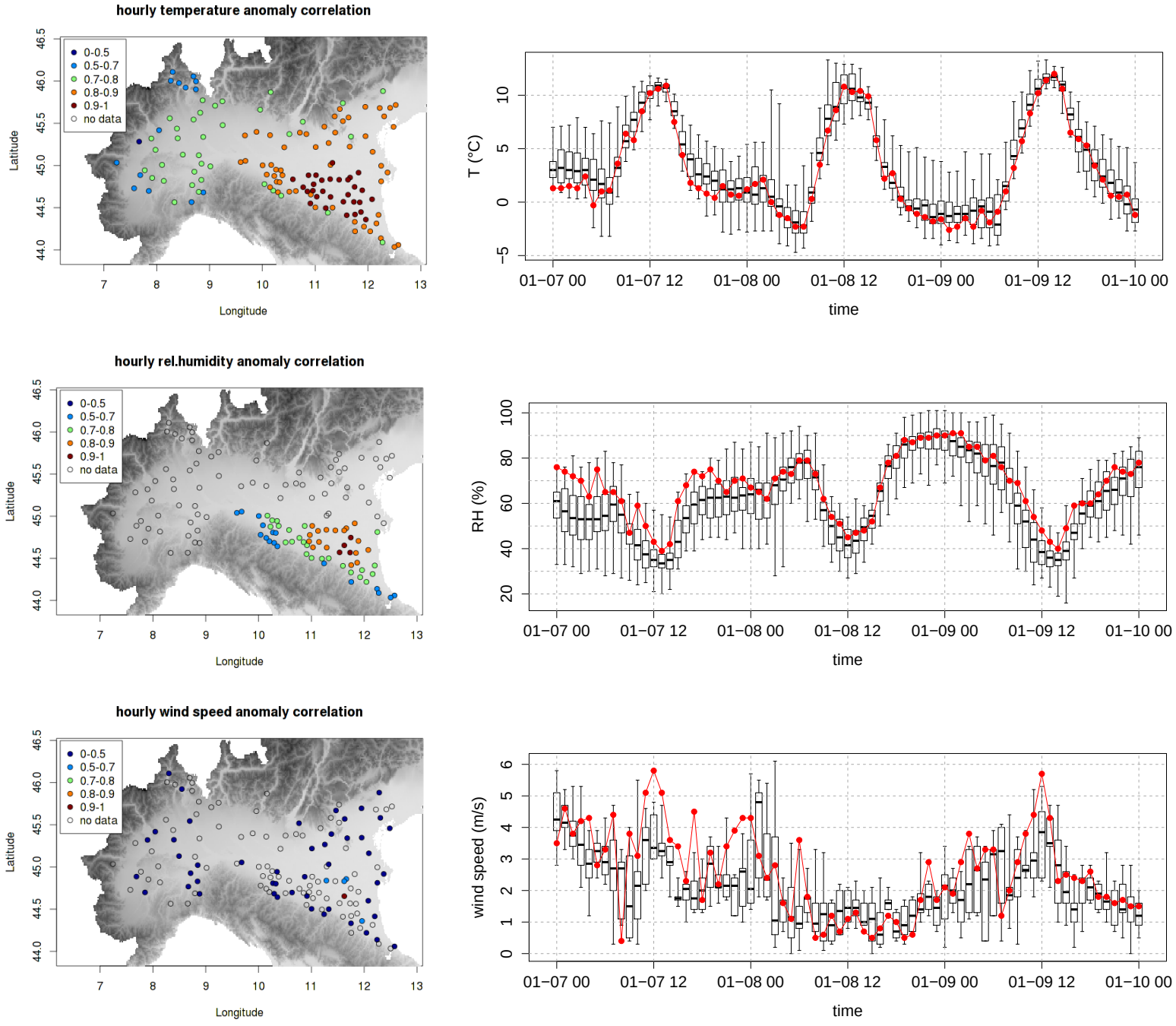

Figure 2.9: Left columns: spatial representation of the hourly anomaly correlation of temperature at 2m (top row), relative humidity at 2m (middle row) and wind speed at 10m (bottom row) collected at San Pietro Capofiume station during the case study against other stations in Po Valley. Right column: time series of temperature at 2m (top row), relative humidity at 2m (middle row) and wind speed at 10m (bottom row) collected at San Pietro Capofiume station during the case study over a box plot of the time series of the same variables recorded in a high-correlated subset of stations.

2.4.2 Model configurations

As the COSMO model, also the WRF model is a fully compressible and nonhydrostatic model, using the terrain-following hydrostatic pressure coordinate in vertical and the Arakawa C-grid grid staggering in horizontal. As well as COSMO, WRF can use the Runge-Kutta 2nd or 3rd order time integration schemes, and 2nd to 6th order advection schemes in both the horizontal and vertical. Moreover, being a free software, the physical package includes a wide range of options. The land-surface scheme used by the WRF model in the present experiment is the Unified Noah Land Surface Model (Chen and Dudhia, 2001). Similarly to the scheme applied in the COSMO model (TERRA-ML, Doms et al., 2011), it is a multi-level scheme, solving the soil temperature and water content equations. Differences between the two formulations refer mainly to bare soil evaporation, evapotranspiration and canopy conductance treatments (Grasselt et al., 2008). All these issues have a small impact over grass in the wintertime period under consideration.
The radiation scheme applied in WRF, RRTMG (Mlawer et al., 1997), is quite sophisticated with respect to the one applied in COSMO (δ two-streams, Ritter and Geleyn, 1992). The first calculates the fluxes and heating rates over 14 contiguous bands in the shortwave and 16 in the longwave regime, while the latter solves the radiative transfer equation for 3 solar and 5 thermal spectral intervals. Other different approaches in terms of the optical properties of water and ice clouds, the droplet effective radius and distribution, the cloud fraction overlap are relevant only for the night in part cloudy (9 January) in the period studied.
The Yonsei University (YSU) scheme, version 3.4.1, (Hong and Pan, 2006) is a lower order scheme with respect to the operational one in COSMO, being a first-order PBL model (i.e. all second order moments are diagnostically derived). It is characterized by a counter-gradient term and an explicit entrainment term in the turbulence flux equation, particularly useful to describe daily large convective eddies and entrainment flux. Indeed, the YSU PBL scheme results to realistically capture the vertical structure of the daytime convective PBL (Hu et al., 2012). In the SBL, the non-local fluxes are zero and the eddy diffusivity is computed from a nocturnal boundary layer depth h_{YSU} (based on a non-local Richardson bulk Ri_b number) via:

$$K^{H,M} = kw_s z\left(1 - \frac{z}{h_{YSU}}\right)^2$$

where w_s is a scale velocity, equal in the v3.4.1 version herein used to:

$$w_s = \frac{u_*}{1 + 5z/L_{MO}}$$

This scheme is short tail (e.g. Tsiringakis et al., 2016). In nocturnal SBL, the stratification accounted for in the w_s formulation produces fairly accurate simulation of the vertical profiles of eddy diffusivity and in general of the SBL structure, at least in moderate windy cases (LeMone et al., 2014; Hong, 2010; X.-M.Hu et al., 2013).

The surface layer formulation applied in teh WRF model is based on the similarity theory, contrary to the COSMO model. The version herein applied is a revision of the MM5 scheme (Chen and Dudhia, 2001), developed by Jimenez et al. (2011) with the aim to better capture the surface layer evolution under strongly stable/unstable conditions. With respect to a traditional similarity based scheme, the similarity functions are revised and the limits preventing low diffusivity (e.g., lower limit of u_*) are reduced or removed. The use of the combination of the YSU v3.4.1 scheme for the PBL with the revised MM5 scheme for the surface layer is meant to produce a reference model scarcely affected by long tail problems.

2.4.3 Experiment setup

The models are configured in order to minimize the differences non-related to the PBL physics. The horizontal resolution is set to 3km in WRF and 2.8km in COSMO. Both the simulations uses 50 vertical levels, but the vertical discretization is higher in WRF in the lowest 1000m (18 levels) than in COSMO (10 levels). The integration domain is equal in the two cases and quite broad (Figure 2.1,left), in order to ensure the balance of the lateral conditions. The simulations are one-way nested in the ECMWF analysis, both the initial state and the boundary conditions. The latter are introduced every 6 hours at the domain borders. Horizontal resolution of ECMWF dataset is 16km, but whereas COSMO uses a highly vertical resolved ECMWF analysis (91 levels), WRF uses only a 21 pressure levels. A spin-up time of 24h is used, in order to allow the generation of mesoscale structures (S. Basu, pers. comm.). Regarding the physiographic fields, there are few differences, e.g. the fact that the COSMO model uses GLOBCOVER2000 dataset (European Commission, Joint Research Center; see http://www-gvm.jrc.it/glc2000), while the WRF model uses USGS (Survey, 2016). The most relevant difference for the present aim is in the roughness length, being in the closest point to San Pietro Capofiume equal to $z_0 = 0.16m$ for the COSMO model and to $z_0 = 0.05m$ for the WRF model.

2.4.4 Results

Classification of observed nocturnal SBL

To support the comparison with the NWP models it is useful, as a first step, to classify the observed nocturnal SBL into 5 classes: continuous turbulent, intermittent turbulent, radiative, cloudy and transient. Here the qualitative classification based on the magnitude and behaviours of the surface fluxes after de Wiel et al. (2002) and de Wiel et al. (2003) is followed.
In the nights of 7 and 8 January, the surface sensible heat flux SH is on average intense with values of about $-40Wm^2$ with large fluctuations lasting from 1 hour (the minimum of the averaging period used) to 3-4 hours. There are also quiet periods especially in the last part of 8 January night, but they need not to result in a total decay of the

flux, as some spikes still appear. In these nights, the SH fluctuations are well correlated to the time variations of the surface momentum flux τ , as can be seen comparing Figure 2.11,b and 2.12 . This correlation is a typical feature of intermittency, due to turbulent burst affecting both the heat and momentum transport. Moreover, the net longwave radiation shows some small deviations from its average nocturnal value. They derive from the temperature variation caused by intermittency episodes like turbulent bursts (de Wiel et al., 2003), which quickly reflects on the radiative surface emission. Therefore, the nights of 7 and 8 Jan are classified as intermittent.
Similar features are experienced in the first part of the night of 9 January. However, few hours before midnight the net longwave radiation decreases (in absolute value) due to an increment of the downward component. Such a quick modification is very likely generated by a cloud passage or by fog formation. The radio-sounding of specific humidity evidences more humid air below 1000m in the night of the 9th of January compared to the other nights, with a peak between 70 and 200m (Figure 2.15). Indeed, at this altitude a fog layer formed as confirmed by the Skew-T diagram at midnight (Figure 2.10). Nevertheless, even after the fog development the correlation between the fluctuations of SH and τ remains good, indicating that the SBL dynamics is not entirely driven by the cloud presence (de Wiel et al., 2003). The night of the 9th of January can be classified as transient given that it is a mixture of the intermittent and cloudy class.
Finally in the night of the 10th of January the SH recorded is weak and with very small fluctuations, while the radiative loss of the surface is still high. This night is classified as radiative. Results are summarized in Table 2.1.

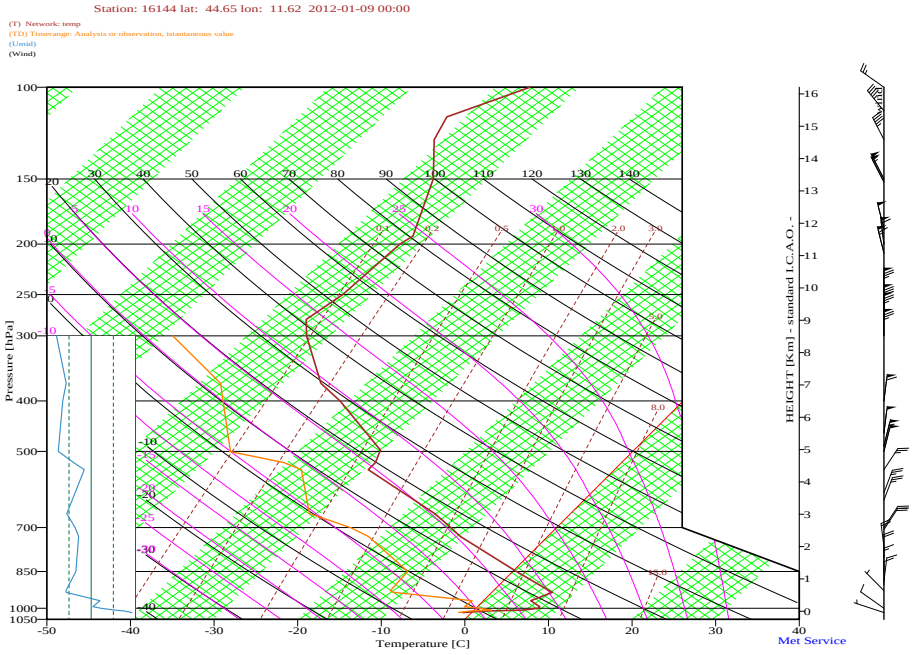

Figure 2.10: Skew-T diagram of the observed profile above San Pietro Capofiume

Day	7 Jan	8-9 Jan	9-10 Jan	10 Jan
Hours	00-08	16-08	16-08	16-00
Class	Intermittent	Intermittent	Transient	Radiative

Table 2.1: Classification of the nocturnal SBL during the case study, according to de Wiel et al. (2002) and de Wiel et al. (2003)

Surface energy budget

At the surface, the energy balances simulated by the COSMO and WRF models lead to similar skin temperatures T_{skin} during the night (see time series in Figure 2.11). However, the terms of the energy balance differ between the two simulations. The terms involved in the nocturnal energy budget at the surface are the sensible heat flux SH, the net long wave radiation NLW and the soil heat flux into the soil G. During the night, SH and NLW are larger of $20 - 40W/M^{-2}$ in absolute value in COSMO simulation than in the WRF one, as visible in Figure 2.11. These discrepancies are neutralised when the terms of the surface balance are summed up, since SH is upward and NLW is downward (upward corresponds to positive sign, while downward corresponds to negative sign in the notation used in Figure 2.11), while the magnitude of the ground heat fluxes is comparable in the two runs. This balance explains the analogy in the simulated T_{skin}.
It is not possible to assess the performance of the two models in terms of the complete surface energy balance, since G was not observed. However, the lower skill of the COSMO model in terms of SH and NLW is evident from Figure 2.11, especially during the night. The net long wave radiation is the difference between an upward and a downward flux. The first comes from the Stephen-Boltzmann law, which essentially expresses the dependence on the forth power of the surface temperature at the net of the emissivity, a multiplicative coefficient dependent on the surface characteristics, and of Stephen-Boltzmann constant. This upward component is similar in the two runs (not shown), thus it can not be the primary contributor to the NLW overestimation (in absolute value) done by COSMO, compared to WRF. It is instead the downward term the main cause of this discrepancy. A different reproduction of this term can be either due to a diverse input to the radiation scheme (e.g. aerosol and gas concentration, vertical lapse rate) or to the formulation of the radiation scheme, or finally to a different vertical resolution (see section 1.4.2). The two models differ in the present experiment in all these three points, being the WRF model favoured by the more sophisticated radiation scheme and the finer vertical discretization at the lowest levels. However, further tests would be necessary to pinpoint the main reason among them. Furthermore, despite WRF reproduces more accurately the radiative budget at the surface, it shows an underestimation of the downward infrared component of 10 to 40 W/m^2 during the night. The downward radiative flux simulated by both the models in the 9th of January at the time of the fog development evidences the miss of this phenomena.
The SH simulated by both the models increases with increasing stability reaching a

maximum at about $\xi = zL_{MO}^{-1} \approx 0.1 - 0.2$ in the weakly stability regime (Figure 2.13). If the stability further intensifies, the SH fluxes reduce in both the simulations. This general behaviour agrees with the observations and with the physics of stable regimes (see section 1.2.1). However compared to the observations, COSMO produces too intense SH fluxes in cases of observed low fluxes (i.e. in very stable regime and in quasi neutral regime), while WRF simulates a too weak heat transfer between the surface and the low atmosphere at every stability regime with $\xi \geq 0$ (Figure 2.13). The same consideration is evidenced by the SH scatterplots shown in Figure 2.14. The formulation of SH used in both the models is given in eq. 2.7. The large negative values seen by the COSMO model in comparison with the WRF model and the observations can be due to: i) a too large heat transfer coefficient, ii) a too large temperature difference between the surface and the lowest model level, iii) a too intense wind speed at the lowest model level. Some clarification comes from the simulations of the surface momentum flux τ (see scatterplots in Figure 2.14). Indeed, COSMO tends to overestimate the observed weaker flux cases, while WRF underestimates τ at every stability regime with $\xi \geq 0$. Given the analogy with the simulation of the SH, it is reasonable to suppose that a common problem influences both the momentum and heat fluxes in both the models. In the bulk formulation (eq. 2.6), τ depends on the wind speed at the lowest model level and on the momentum transfer coefficient (see eq. 2.6). Since these terms are used in SH computation as well, it is probable that one of them or both are incorrectly simulated by the two models, thus discarding the previously mentioned hypothesis of an error in the vertical temperature difference for SH. Unfortunately, no wind observations are available at the heights of the lowest model level in the two models, being $z \approx 7.2m$ and $8.2m$ in WRF and COSMO respectively. This precludes the objective quantification of the potential role of the wind speed at the lowest model level and of the transfer coefficients in causing the flux inaccuracies. At a qualitative level, the stability dependency shown by the error in the COSMO model suggests an origin in the SBL itself, for example among the physical processes influenced by stratification. This hypothesis is investigated and developed in chapter 4, where a more extensive analysis is performed.
Regardless the specific model biases, the surface fluxes are better represented by WRF compared to COSMO, as indicated by the RMSE scores in Figure 2.14.

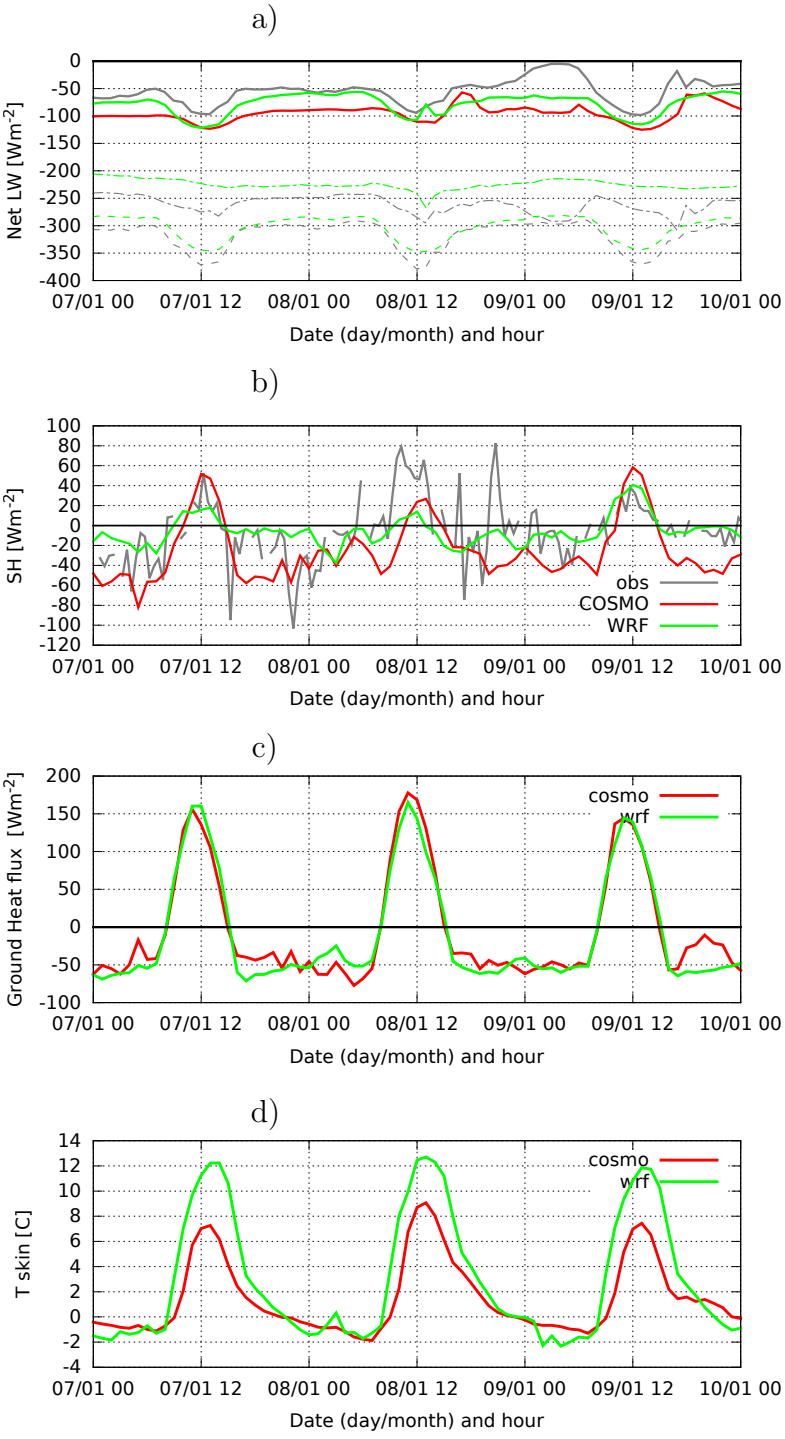

Figure 2.11: Time series of (a) net long wave radiation (solid lines), upward long wave component (dashed lines), downward long wave component (dot-dashed lines), (b) sensible heat flux, (c) ground soil flux and (d) skin temperature observed (grey lines) and simulated by COSMO (red lines) and WRF (green lines) for the case study of the 7th-10th of January at San Pietro Capofiume

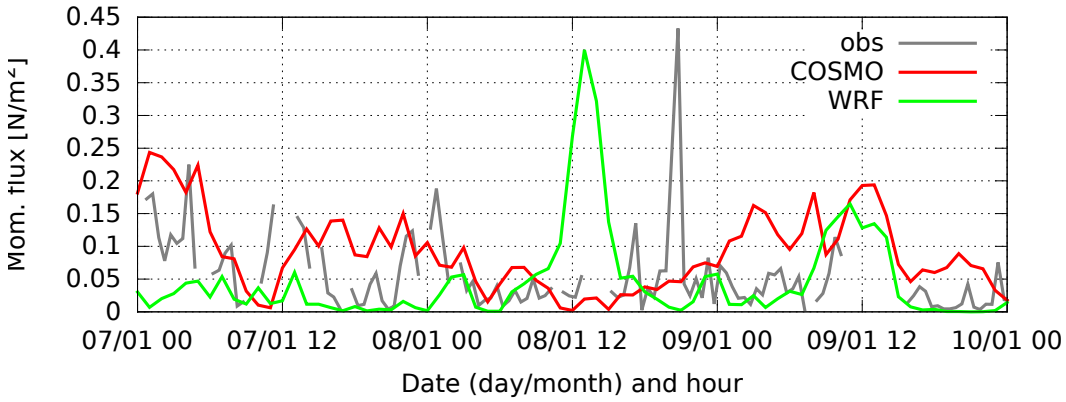

Figure 2.12: Time series of momentum flux observed (if available) and simulated by COSMO and WRF models

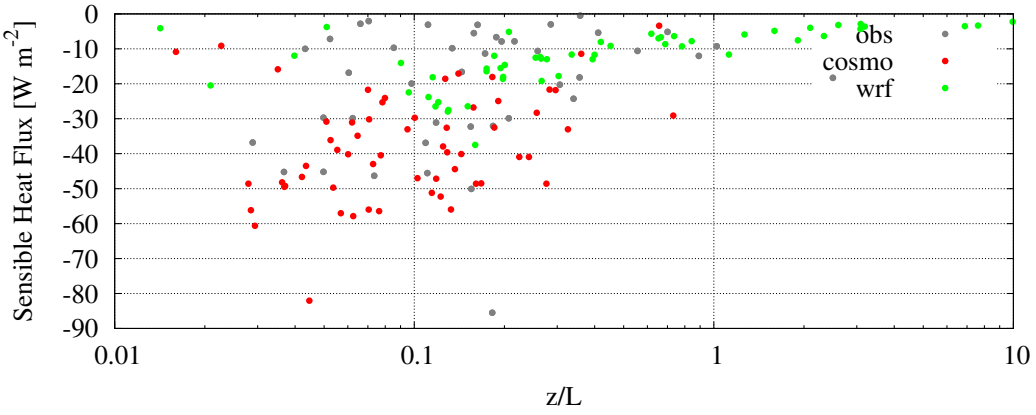

Figure 2.13: Sensible heat fluxes as a function of the stability parameter simulated by COSMO and WRF models and observed

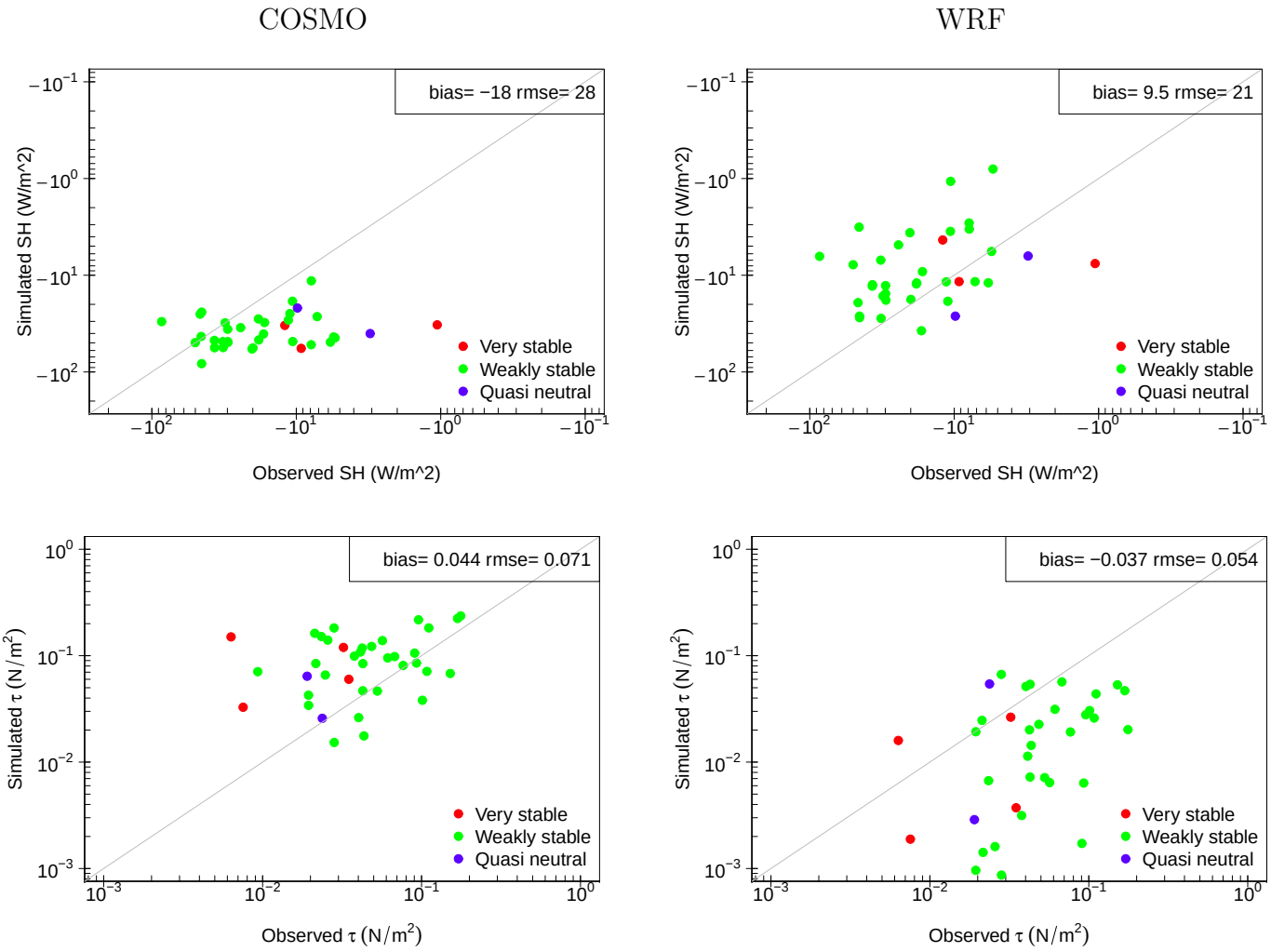

Figure 2.14: Simulated against observed sensible heat flux (top row) and momentum flux (bottom row) for the COSMO model (left) and WRF model (right). Colors indicate the observed stability regime: near neutral ($0 \leq \xi \leq 0.1$), weakly stable ($0.1 \leq \xi \leq 0.6$), very stable ($\xi \geq 0.6$)

	7 Jan	8 Jan	9 Jan	10 Jan
Observations	240	230	160	85
COSMO	400	450	300	270
WRF	100	150	150	160

Table 2.2: PBL depths (m) estimated on the base of $\frac{\partial T}{\partial z} = 0$ criteria (Yamada, 1979) from the radio-sounding profile and from the model simulations

Atmospheric profiles

Compared with the available nocturnal radio-soundings in Figure 2.15, WRF correctly reproduces the vertical thermal gradient in the surface vicinity (lowest 50m), with the exception of midnight in the 8th of January, where the observed profile is particularly homogeneous in the lowest 15m. Indeed, this time corresponds with the occurrence of a turbulent burst, as indicated by the fluxes increase at the surface (Figure 2.11), which is not caught by the model. Above 50m, the WRF model fails the lapse rate simulation, either overestimating it as in the nights of the 7th and 8th of January or underestimating it as in the night of the 10th of January. Likely, this point relates with the turbulent mixing reproduction. In the intermittent SBLs recorded the 7 and 8 January, the overestimated thermal gradient is probably associated to a weak turbulent mixing, while the opposite is likely true in the radiative SBL observed the 10 January, where turbulent mixing appears overpowered. Table 2.2 reports the PBL heights estimated in both the models and in the radio-soundings as the lowest height at which $\frac{\partial T}{\partial z} = 0$, after Yamada (1979). Despite the YSU scheme already produces the PBL height h_{YSU} in output, here the use of the same methodology in both the models and the observations is favoured. The obtained PBL heights are shallower for the WRF model than the one derived from radio-sounding in the nights of 7-8 January. Vice versa the WRF PBL depth is higher in the 10 January night than in the observations, in agreement with the consideration about the under/over-estimation of turbulent mixing. In the night of the 9 of January, the PBL depth simulated by WRF is coherent with the observed one, however it is hard to comment the state of turbulent mixing as the simulated SBL dynamics is different from the one observed (the model misses the fog development).
In Figure 2.15, the vertical profiles of temperature simulated by the COSMO model show the traces of the too high turbulent mixing within the SBL with respect to the observations, likely due to the long tail formulations. Indeed the PBL height is too deep in all the considered nights, and the lapse rate is too close to neutral stratification.

The assessment of the model performances in term of wind profile poses more difficulties. The four midnight radio-soundings do not show low level jet occurrences, while both the models reproduce a jet in the nights of the 7th and 9th of January (despite at different heights). Wind rotation is expected to approximate 35° clockwise in the weakly stable boundary layer (Grisigono, 2011). However, the observed wind turning estimated as the angular difference between the wind direction at the near surface (i.e. $z = 10m$) and at the PBL height (from Table 2.2) is always smaller, and even backs in

	7 Jan	8 Jan	9 Jan	10 Jan
Observations	5	-16	20	-14
COSMO	40	-	80	-30
WRF	22	66	4	39

Table 2.3: Clockwise wind turning from the surface to the PBL depths in the radiosounding and in the model simulations

the nights of 8th and 10th of January (see table 2.3). Regarding the simulations, while the WRF model always sees a clockwise turning within the simulated SBLs ranging from 4 to 66 degrees, the COSMO model shows an even larger variability (rotations ranging from -30 to 80 degrees). This COSMO behaviour is surprising since in general long-tail models underestimate the wind turning in the SBL, as a result of the excessive mixing (Holtslag et al., 2013; Svensson and Holtslag, 2009). The inconsistency of these results for wind can be explained considering the higher spatial variability typical of wind with respect to temperature (e.g. as shown for their near surface values in section 2.4.1). Therefore, the small dataset does not allow statistically based consideration about wind profile simulation.

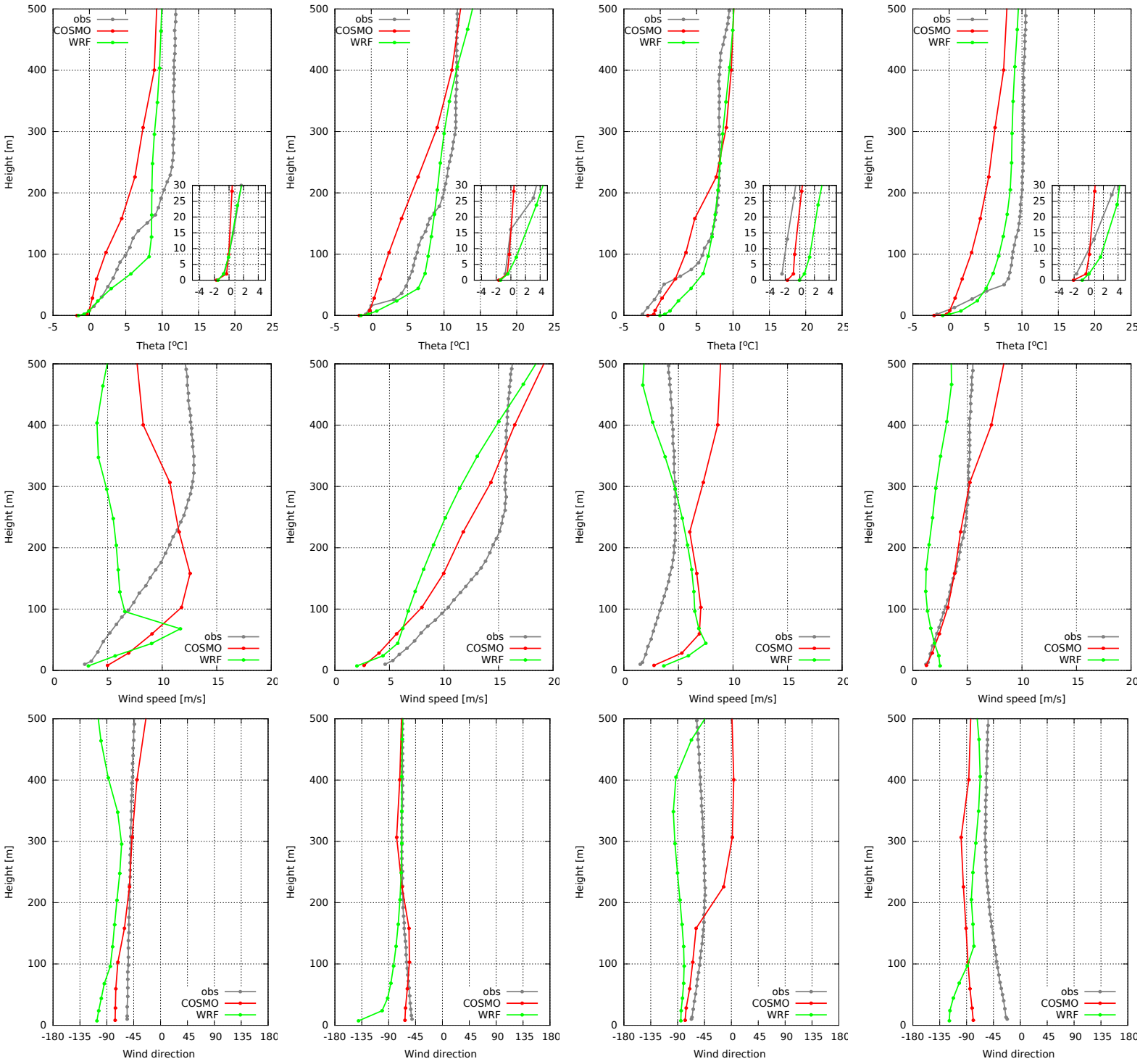

Figure 2.15: Vertical profiles of θ (top row) and wind speed (middle row) and wind direction (bottom row) at 00:00 local time from day 07/01 to 10/01 observed in a radio-sounding and simulated by COSMO and WRF models

Near surface diagnostics

The near surface variables (temperature and relative humidity at 2m, wind at 10m) are diagnosed by the transfer scheme. Their simulated and observed evolutions in the case study are plotted in Figure 2.16, while in Figure 2.17 their simulations during the nocturnal hours (16:00-08:00) are compared to the observations through scatterplots and statistical scores.

The nocturnal temperature at 2m is overestimated by both the models by approximately the same extent. Despite this analogy, the temporal behaviour of their error (WRF shows a too slow cooling after the sunset, while COSMO delays both the evening cooling and the morning warming after the dawn) indicates a possible diverse origin of their errors. In COSMO, a potential explanation of both the overestimation and the delay is an excessive coupling between 2m and the lowest model level, which is evidenced by the underestimated lapse rate in this layer visible in the vertical temperature profiles in Figure 2.15(but the 8th of January, when it was observed a turbulent burst). Indeed, this would motivate a 2m temperature overestimation even in case of a perfect representation of the lowest model level and surface values. The slow reaction to the changes of insolation (at sunrise and sunset) can be related to the too large inertia offered by a too mixed layer between 2m and the lowest model level. WRF does not show the same problem of the lapse rate (the vertical gradients in the surface vicinity are in agreement with the observed profiles, but the turbulent burst at midnight of the 8th of January). In WRF, the overestimation of the nocturnal temperature at 2m appears more associated to a too warm layer close to the surface than to an issue of 2m diagnostics. Indeed, both the profiles in nights 9th and 10th (Figure2.15) evidence a drift of WRF toward warmer temperature between the surface and the first model level compared to observations. A potential explanation may lay in the evidenced underestimation of the radiative cooling of the atmosphere (seen by the too small downwards radiative income at the surface in Figure 2.11,a), which can explain also the too slow cooling at 2m shown after sunset. However, these speculative explanations need additional data for being confirmed.

The relative humidity at 2m is always overestimated by the COSMO model, as a result of the too humid SBL simulated by COSMO (not shown), while WRF simulation is in better agreement with the measurements.

The wind speed at 10m simulated by the models is in general fair agreement with the observations during night (but not during day, especially for the WRF model) as illustrated in Figure 2.16.

In conclusion, the two models appear approximately comparable in terms of near surface variables (e.g. in terms of RMSE). Therefore, the differences between the transfer schemes applied by the two models are somehow compensated by the diagnostics algorithms.

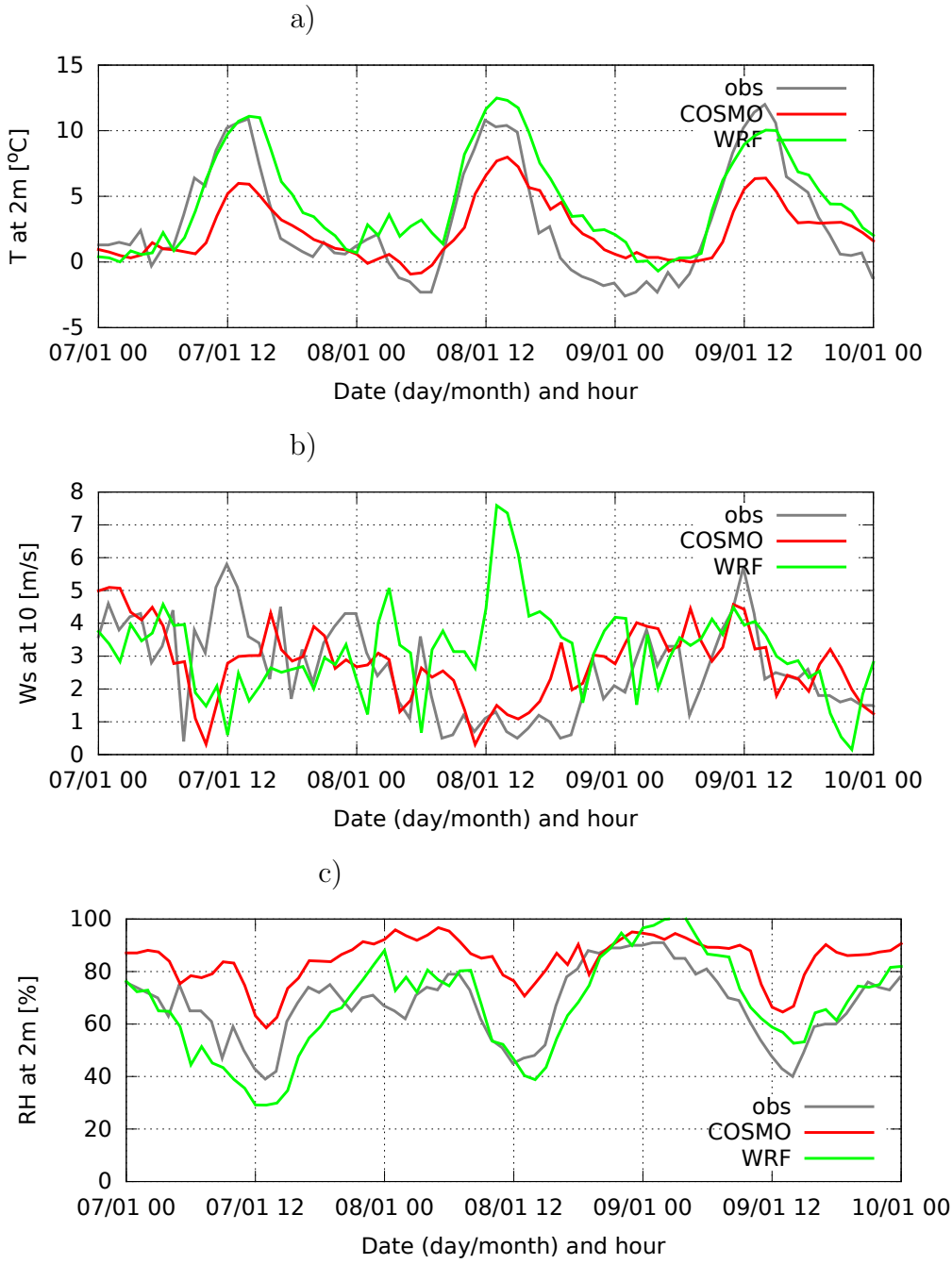

Figure 2.16: Time series of the temperature at 2m, relative humidity at 2m and wind speed at 10m observed and simulated by COSMO and WRF models

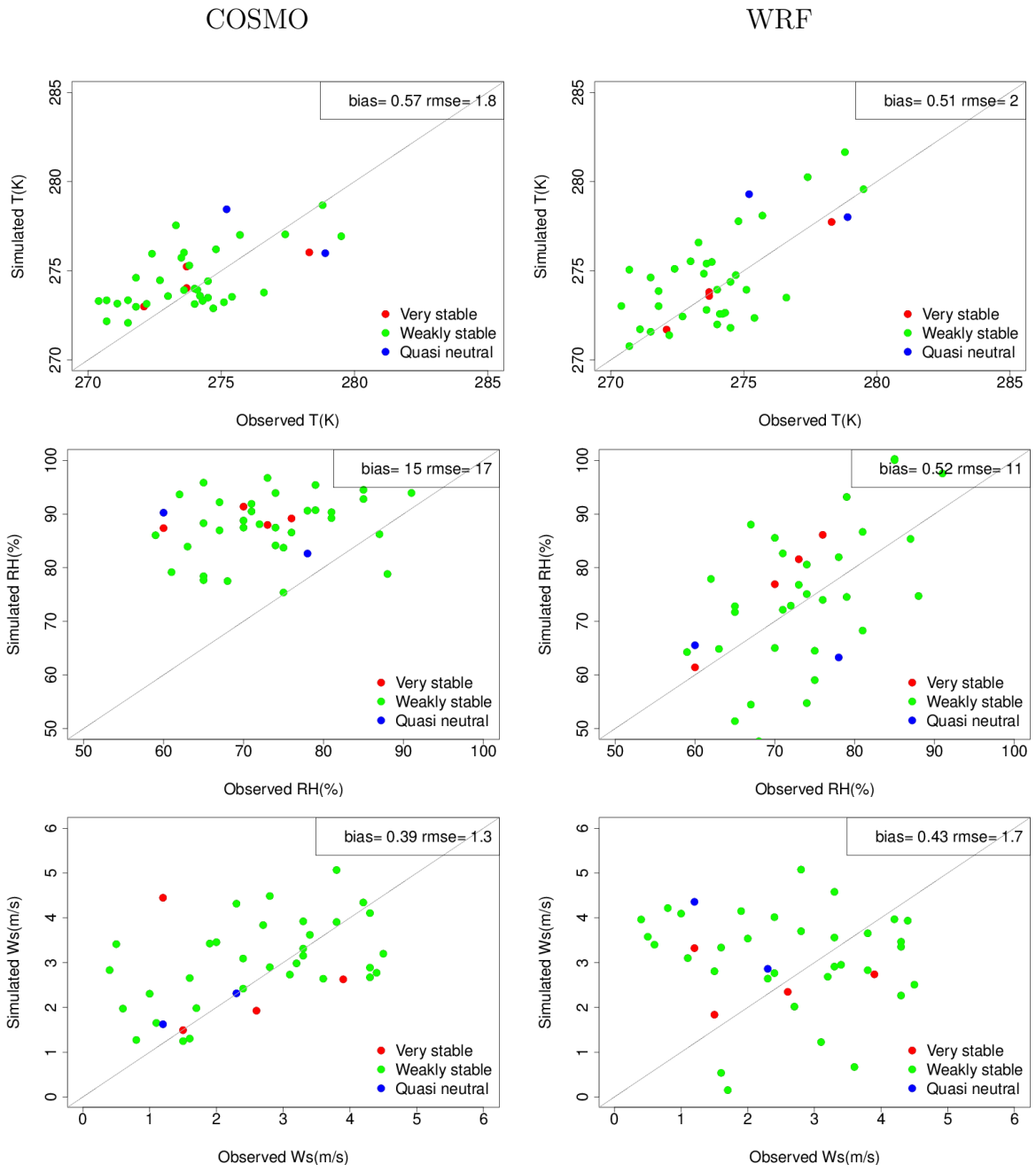

Figure 2.17: Simulated against observed temperature at 2m (top row), relative humidity at 2m (middle row) and wind speed at 10m (bottom row) for the COSMO model (left) and WRF model (right). Colors indicate the observed stability regime: near neutral ($0 \leq \xi \leq 0.1$), weakly stable ($0.1 \leq \xi \leq 0.6$), very stable ($\xi \geq 0.6$)

2.4.5 Conclusions

The period under investigation includes two nights of intermittent SBL (7 and 8 January), one night of transient SBL (partly intermittent and partly foggy, 9 January) and one night classified as radiative SBL (10 January). On the whole, WRF simulates better than COSMO these SBLs. This deviation is mainly imputable to the different turbulent and transfer schemes applied, since errors not directly associated to these schemes (e.g. underestimation of the downward component of the radiative flux at the surface) are common to both the models. The long-tail turbulence scheme applied by the COSMO model strongly affects the turbulent mixing simulation on the thermal vertical profiles. Indeed, independently on the type of SBL observed, the simulated SBLs are always too deep and too close to neutral stratification, confirming the general behaviour of long-tail models (Holtslag et al., 2013; Cuxart, 2006; Beare et al., 2006). Vice versa, WRF (which uses a short tail turbulence scheme) simulates lapse rates in good accordance with the observed ones in the surface vicinity (lowest 50m) and above, the performance depends on the kind of SBL observed (underestimation of turbulent mixing in the intermittent nights, overestimation of it in the radiative night, correct simulation in the transient night), but always with better agreement with the measurement (e.g. in term of PBL height) compared to COSMO. The low amount of available vertical profiles prevent any analysis of the wind speed and direction. The surface fluxes (computed by the transfer scheme) show better scores in WRF than in COSMO simulation at any stability regime for $\xi > 0$ (the only exception is for wind speed at 10 at near neutral and weakly stable regime). Indeed, in the COSMO model, the situation worsens due to a net overestimation of the surface fluxes at the surface at high stratification. The source of this anomaly is not detectable in the present study. Focused experimentation is reported in chapter 4. Despite with a smaller extent, also the WRF model presents inaccurate surface fluxes, which are underestimated in magnitude. Although the near surface variables (temperature and relative humidity at 2m and wind at 10m) are diagnosed by the transfer scheme (as the surface fluxes), differences between the model simulations are less evident.

This experimentation clearly evidences the added value in terms of SBL representation that the use of a short-tail PBL scheme and an optimized transfer scheme can give with respect to the long-tailed turbulence and transfer scheme operationally applied in the COSMO model. It also highlights that state-of-the art short-tail PBL scheme and stability-optimized transfer scheme still require refinements in order to describe flat terrain SBL, especially in terms of intermittent and radiative situations.

Chapter 3

The turbulence-enhancing formulations and their removal

Several formulations have been introduced in the COSMO turbulence code in order to enhance turbulent mixing under stable stratification above the observative evidence. While some of them are well known features of the COSMO model (i.e. the minimum diffusion coefficients for momentum and heat $K_{min}^{M,H}$, e.g. Heise, 2006; Buzzi, 2008; Volker et al., 2009; Köhler et al., 2011) intentionally introduced in the code in order to increase diffusivity, other ones are less documented and their turbulence enhancement effect is accidental, as they are needed to allow turbulence computation. It is the case of the minimum limit to the sum of TKE forcings (i.e. wind shear plus buoyancy) that prevents the TKE equation to deal with cases in which the Ri_f number exceeds the critical value for highly stable stratification $Ri_f^{crit} = 0.19$, and the case of the minimum value of $q(= \sqrt{2TKE})$, associated to the treatment of the realizability criteria and singularity of the turbulence scheme applied in COSMO (Mellor and Yamada, 1982). Other limits like the minimum value of $q = 10^{-6} m/s$ and the second lower limit to the heat and momentum diffusion coefficients equal to their molecular diffusion counterparts are not considered in this list as they only prevent physical unreasonable solutions. As mentioned in section 1.3, the turbulent enhancing formulations deteriorate the representation of stable layers (SBL, entrainment at the PBL top) in favour of the large scale scores. Moreover, they can prevent undesirable numerical instabilities due to the decoupling between the surface and the atmosphere in SBL. The purpose of this section is to analyse the role of each of these formulations in different topography and stability conditions with the use of COSMO simulations in 3D and 1D mode, to evaluate the possibility of their removal/reduction and to assess the potential consequences of this action.

3.1 Minimum diffusion coefficients

The minimum diffusion coefficients for momentum and heat, force the turbulence to continue mixing also when the diffusion coefficients would drop below the prescribed minimum values. The limit to the diffusion coefficients is expressed as:

$$K^{M,H} = lqS^{M,H} \geq K^{M,H}_{min} \tag{3.1}$$

where l is the mixing length and $S^{M,H}$ are the stability functions. Buzzi et al. (2011) performed a sensitivity test on these parameters by progressively reducing their values from 1 m^2/s to 0.001 m^2/s in a ideal simulation of a shear driven SBL using COSMO single column. The overestimation of mixing was evident for limit higher than 0.1 m^2/s, producing a too high and less stable SBL, missing the low level jet. He found an optimal minimum limit equal to $K^{M,H}_{min}$=0.01 m^2/s which does not alter the SBL representation. This threshold broadly agrees with the observative evidence, as rarely data show smaller diffusivity (e.g. Yagüe et al., 2006).
In the present study, the sensitivity to this optimal minimum limit to the vertical diffusion coefficients is tested in a real 3D simulation with the operational setting of the COSMO model at ARPAE-SIMC (in which $K^{H,M}_{min} = 0.4m^2/s$, corresponding to the suggested threshold for COSMO operational applications). A similar test have been already performed some years ago by Volker et al. (2009) highlighting the positive increment of the PBL clouds (as humidity is not lost at the PBL top) and the contrasting results in terms of temperature at 2m (the limit reduction results beneficial over flat homogeneous site, but detrimental over a domain as large as Germany). Among the differences from this previous study [1], the output is required every time step (20s) in order to better visualize turbulence evolution. The operational setting includes the scale interaction term for the thermal circulation, thus allowing considerations about its role. The focus is at first local on SBL over homogeneous terrain and subsequently it is extended over heterogeneous terrains. Finally, a long term verification is performed comparing the COSMO model with and without the minimum diffusion coefficients and the thermal circulation scale-interaction term.

3.1.1 Experiment setup

The case study shown in section 2.4 is selected also for the present analysis. The anticyclonic system extending over the North-Western Europe and Northern Italy yields to favourable conditions to the SBL development over North-Italy. The station of San Pietro Capofiume is the reference for the homogeneous terrain study (details about the meteorological situation, the observational array are in section 2.4.1).
The COSMO model is run with a operational-like configuration. The initial state for both the atmosphere and the soil comes from the ECMWF's analysis, as well as the

[1] the operational base limit is smaller in present analysis ($K^{H,M}_{min} = 0.4m^2/s$ against $1m^2/s$) and the COSMO version applied is newer

boundary conditions introduced at the border of the integration domain by a one-way nesting every 6h. The domain is reported in Figure 2.1,left. Differently from the simulation described in section 2.4, here the horizontal resolution is set to 7km and the vertical axis is discretized in 40 vertical model levels. Moreover, the model output is here collected and plotted at every integration time step (20s). This reference simulation using $K^{M,H}_{min} = 0.4m^2/s$ is compared with a second simulation (in the following called 'Test1') in which $K^{M,H}_{min} = 0.01m^2/s$.

3.1.2 Analysis of results at San Pietro Capofiume

Figure 3.1 reports the vertical profiles of momentum diffusion coefficient, temperature and wind speed simulated by the described experimental configuration (referred to as Test 1 in the plot) and by a second experimental simulation that will be later described (referred to as Test 2 in the plot). The reduction of the minimum limit of $K^{M,H}$ to the optimal value $0.01m^2/s$ yields to lower simulated diffusion coefficients above the SBL ($\approx 850hPa$ in Figure 3.1, scalar coefficient not shown but similar to the momentum one), but not always within the PBL, where turbulence mixing results sustained. Temperature profile indicates a slight strengthening of stratification in Test1 run with colder temperature at the surface and warmer at the top of the inversion (coherently with Volker et al., 2009), while wind speed profile does not show relevant changes.

At the lowest model level, Figure 3.2 illustrates as the momentum diffusion coefficient drops below the reference minimum limit several times along the considered period (the same is valid for the heat coefficient), mainly (but not only) when the Richardson flux Ri_f number is above the critical value 0.19 (i.e. in very stable regime). This is beneficial for the temperature at 2m, which shows a lower overestimation of the nocturnal temperatures in correspondence with the diffusion coefficient drops, coherently with Volker et al. (2009).

The high frequency of COSMO output employed for these visualizations allows to evidence that both the operational and the experimental solutions appear not fully stable when the stratification is stable. Some high frequency oscillations (about 15 timesteps) are excited (Figure 3.2). All turbulence related variables in the surface vicinity (e.g. diffusion coefficients, TKE, wind, temperature, humidity) are involved up to three/four levels above the lowest one (see e.g. the temperature at 2m in Figure 3.2). Vice versa the variables at the surface are unaffected. The oscillations appear sensitive to the reduction of the diffusivity limit: the amplitude is strongly enlarged, the period is approximately doubled and they are less wavy and periodic (Figure 3.2). This kind of oscillation is a numerical artefact and it is not anyhow related to the observed intermittency in stable stratification. Some tests performed to check the numerical origin underlined as the oscillations are sensitive to changes of numerical scheme and integration timestep, but their direct role is discarded. This feature is visible only thanks to the high frequency output selected. However, such oscillations could enlarge the forecast uncertainty because the model output (generally sampled at each hour of sim-

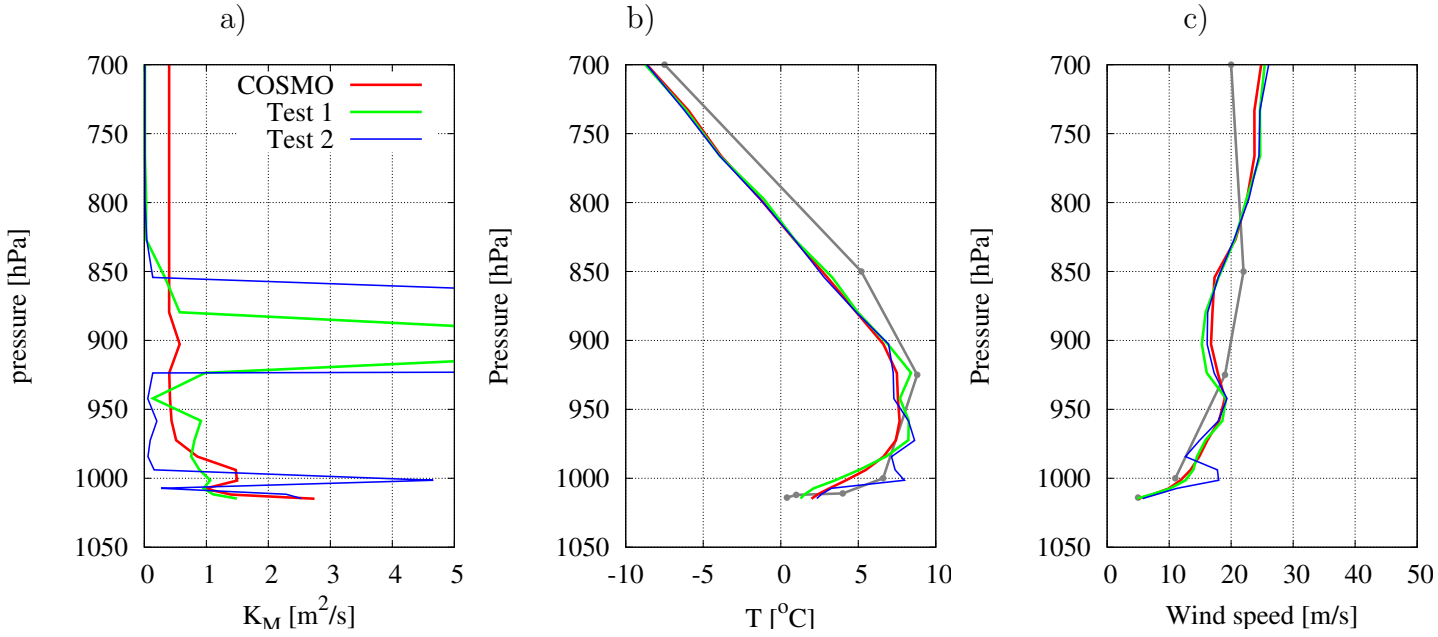

Figure 3.1: Vertical profiles of momentum diffusion coefficient(a), temperature (b), and wind speed (c) at San Pietro Capofiume site, on the 08/01/2012 at 00:00. Grey line represents the radio-sounding observations, when available. Red line is the COSMO simulation using the reference configuration, green line is the experiment in which $K^{M,H} \geq 0.01 m^2/s$ (Test 1) and blue line is the experiment in which $K^{M,H} \geq 0.01 m^2/s$ and the thermal circulation term set equal to 0 (Test 2)

ulation) could fall indifferently on the top or bottom of the oscillation. For this reason, it is important to understand the source and possibly to eliminate it.
Buzzi et al. (2011) detected a similar non-stable behaviour of COSMO in 1D idealized simulation of a shear driven SBL. In that case, the oscillations were visible in the vertical profiles of $K^{M,H}$, showing an analogous sensitive to the lower limit of $K^{M,H}$. Their onset was explained by a physical inconsistency in the stability functions in the Mellor and Yamada (1982) scheme at Level 2.5 (Burchard and Deleersnijder, 2001; Mellor, 2003), and was cured by vertical filtering applied to the turbulent diffusion or to the stability functions. In the present study, despite the vertical profile of $K^{M,H}$ shows some vertical oscillations, the application of Buzzi's filters does not cure neither them nor the previously mentioned temporal oscillation (Cerenzia et al., 2014).
It is useful to consider the behaviour of the oscillation in the temporal evolution of the terms of TKE equation at the lowest model level. They are plotted in Figure 3.3 along few nocturnal hours. The TKE equation (expressed in terms of $q = \sqrt{2TKE}$) read [2]:

$$\frac{\partial q}{\partial t} = frc + f_C - \frac{\epsilon}{q} + q_{diff} \tag{3.2}$$

[2]it expanded form is in equation 2.1

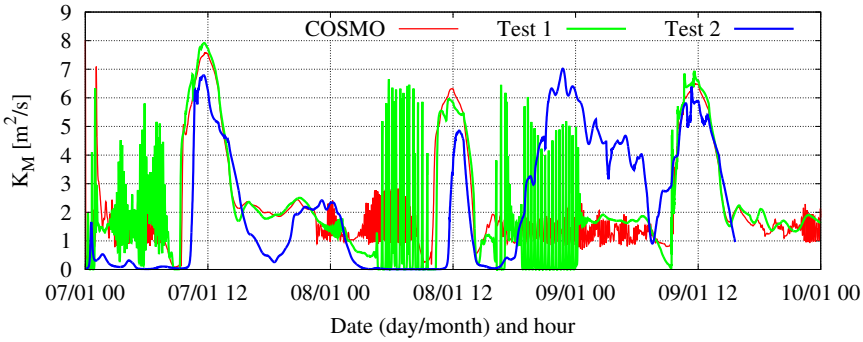

a)

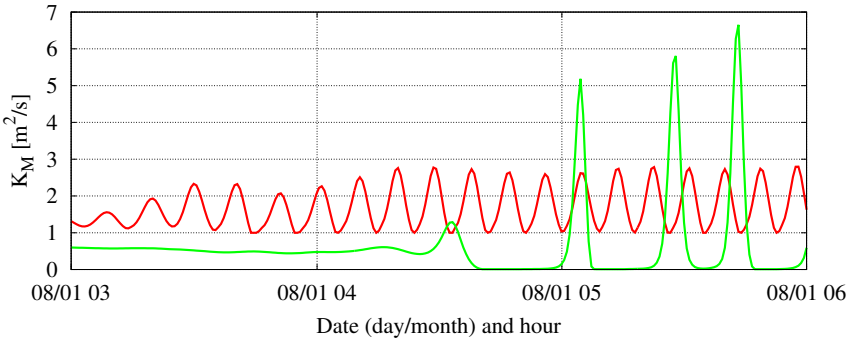

b)

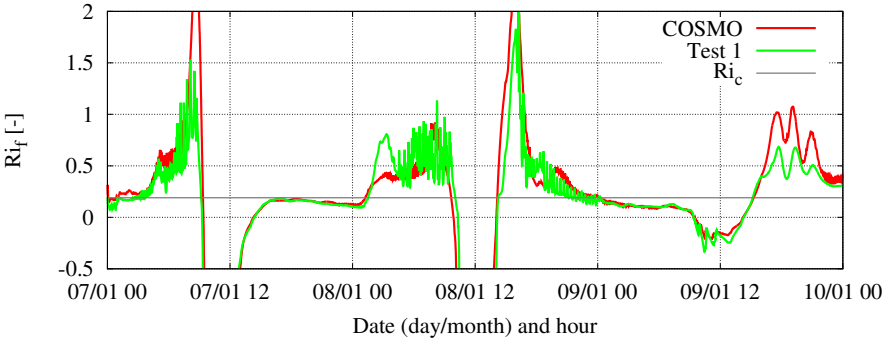

c)

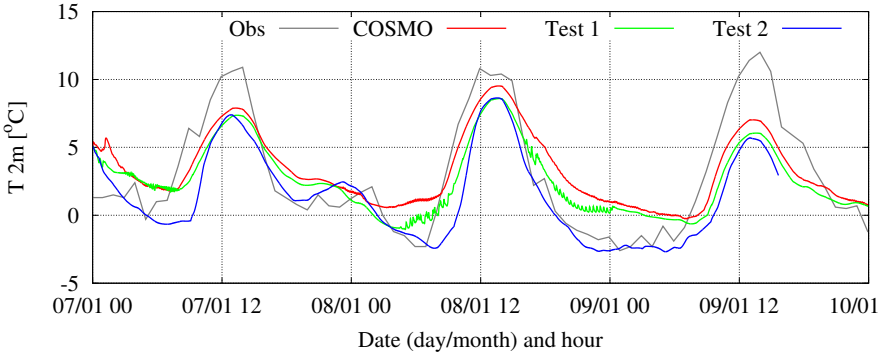

d)

Figure 3.2: Time trend at the lowest main level of (a) the momentum diffusion coefficient, (b) the same in a temporal zoom, (c) the Richardson flux number and (d) the temperature at 2m. Red line represents COSMO default, green line is Test 1 and blue is Test 2. Grey line are observations, if available

Figure 3.3: Temporal evolution of the terms of TKE prognostic equation (eq. 3.2) at the lowest model level during a nocturnal stable period in the proximity of $Ri_f = Ri_c$ simulated by COSMO using the reference configuration. Ri_c is exceeded at around 01:00 when "Ri_c Lim" line is above the "$f_m + f_h$" line

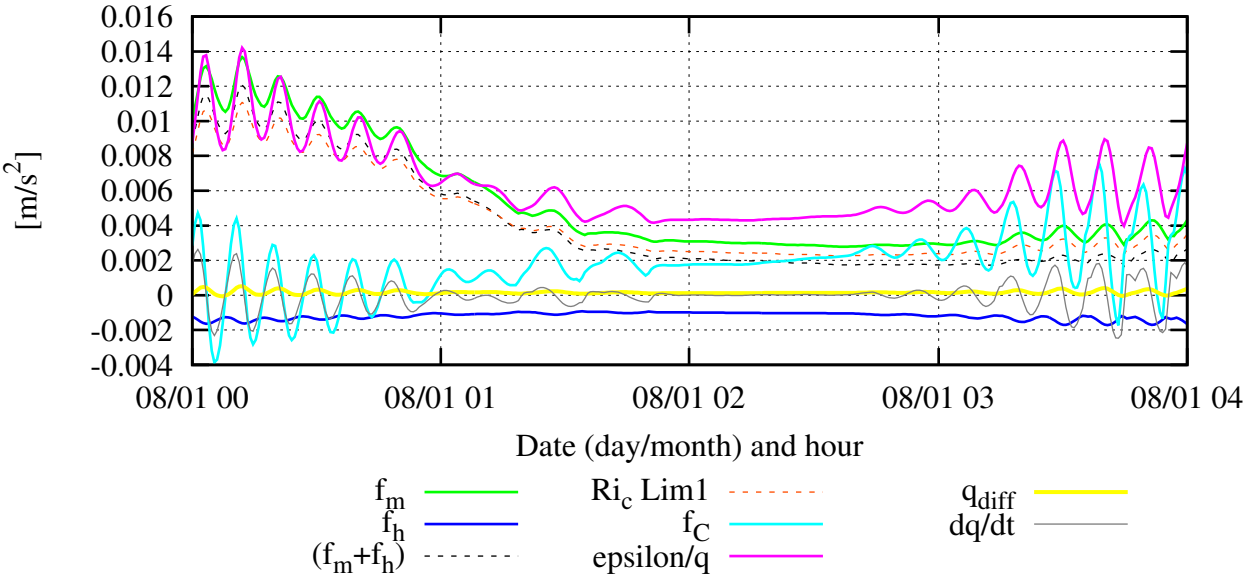

where frc is the sum of the mechanical forcing due to wind shear f_m and of the buoyancy forcing f_h (negative under stable stratification), f_C is the additional forcing associated to subgrid circulation motions (scale-interaction terms, see section 2.2.1), in this experiment including only the thermal circulation, $\frac{\epsilon}{q}$ represents q dissipation and finally q_{diff} the vertical diffusion of q (line labelled as "$Ri_c Lim1$" in Figure 3.3 refers to the limit on the forcing sums frc and it will be described in the following section 3.2). At the lowest model level, the thermal circulation term f_C results a very active source of TKE compared to the forcing sum frc (Figure 3.3). Moreover, it seems to have a correlation with the oscillations since it anticipates the wave of one-two time steps with respect to other TKE-eq. terms.

In order to clarify the role of f_C on the oscillation onset, a third experiment is run turning off the thermal circulation term in TKE budget while keeping the $K^{H,M}_{min} = 0.01 m^2/s$ (experiment later referred to as 'Test 2'). The first result is a complete elimination of time oscillations, as it is visible in the temporal trend of K^M and of temperature at 2m in Figure 3.2. In Test 2, the mixing during stable conditions strongly decreases with respect to Test 1, partially because of the disappearance of the oscillations and partially due to the lack of the additional TKE production. Consequently, the nocturnal temperature shows a stronger inversion at the lower model levels (Figure 3.1, centre), leading to a lower temperature at 2m, in close agreement with the observations (Figure 3.2). Daily maxima are unchanged compared to Test 1.

Along the vertical, the variability of temperature, wind and $K^{M,H}$ increases (Figure 3.1). The reason of this reduced coupling between vertical model levels comes from the fact that practically, the thermal circulation term represents the main interaction between different vertical levels in stable conditions, because it includes a second order vertical derivative ($f_C \propto \frac{\partial}{\partial z}(L_{therm}\frac{K^H}{q}\frac{\theta}{g}\frac{\partial\theta}{\partial z})$, see section 2.2.1) and it largely exceeds in magnitude the same order term in the TKE budget, i.e. the vertical diffusion term q_{diff} [3], as it is shown in Figure 3.3.

[3] $q_{diff} = \frac{1}{\overline{\rho}}\frac{\partial}{\partial z}\left(\overline{\rho}\cdot K_q\frac{\partial q}{\partial z}\right) + \frac{K_q}{q}\left(\frac{\partial q}{\partial z}\right)^2$, full derivation in the appendix A

3.1.3 Analysis over the Northern Italy area

If the minimum diffusivity is reduced (Test 1), the temperature at 2m is either unchanged or cooler (of a maximum $4°C$) on grid points sited in flat and hilly terrains (with some cooling also over sea surface) during the more stable periods (Figure 3.4, top). There is a minor impact over mountains because in general the stronger wind shear keeps high the diffusion coefficients. The effect of time oscillations can be retrieved in the onset of some localized peaks at low levels changing location and intensity in time (graph not shown). They are more visible in TKE and diffusion coefficients, coherently with the larger amplitude recognized also at San Pietro Capofiume, and they appear only over flat or hilly regions.

The disabling of f_C in TKE equation together with the reduction of the diffusivity limit (Test 2) causes a further reduction of mixing in more stable periods yielding to a further cool at 2m (Figure 3.4, bottom). The cooling shows different extents and beneficial or detrimental consequences (illustrated in Figure 3.5) depending on topography, due to the relative impact of the thermal circulation.

- Over flat regions the cooling varies between 1 and 5^oC. In this area, Test 2 is overall in agreement with the majority of stations with some slight underestimation cases (mean error ranging between $+1^oC$ and -2 ^oC, Figure 3.5). The overestimation of the temperature at 2m typical of COSMO operational setting is avoided.

- Over hilly and low mountain area, Test 2 cools of about 5^oC with respect to the reference. However, compared to the observations, it results excessive (Figure 3.5). Given that the resolved topography is generally gentle in these areas, it does not affect the TKE production (via mean-grid wind shear) to the point to produce a significantly more mixed SBL. Thus, the thermal circulation term represents a relevant source of TKE compared to the other terms of TKE budget. Over rough topography, this term appears as a valid complement to the TKE budget in order to treat the additional mixing generated by the subgrid heterogeneity.

- Over high mountains, Test 2 deviates only slightly from the reference. Already the reference catches the higher instability of the low atmosphere and the thermal circulation term has not a leading role in TKE budget.

The current formulation of f_C does not include any information on the subgrid scale pattern of temperature or even orography (in absence of subgrid scale clouds). Obviously, the additional production of TKE due to thermal circulation is not necessary when a subgrid scale heterogeneity is not existing (flat regions), while it is beneficial over rough terrains, prevent that the low troposphere is stable enough.
As a side remark, the horizontal peak-structures variable in time seen in Test1 disappeared in Test 2, demonstrating that they are a manifestation of the temporal instabilities.

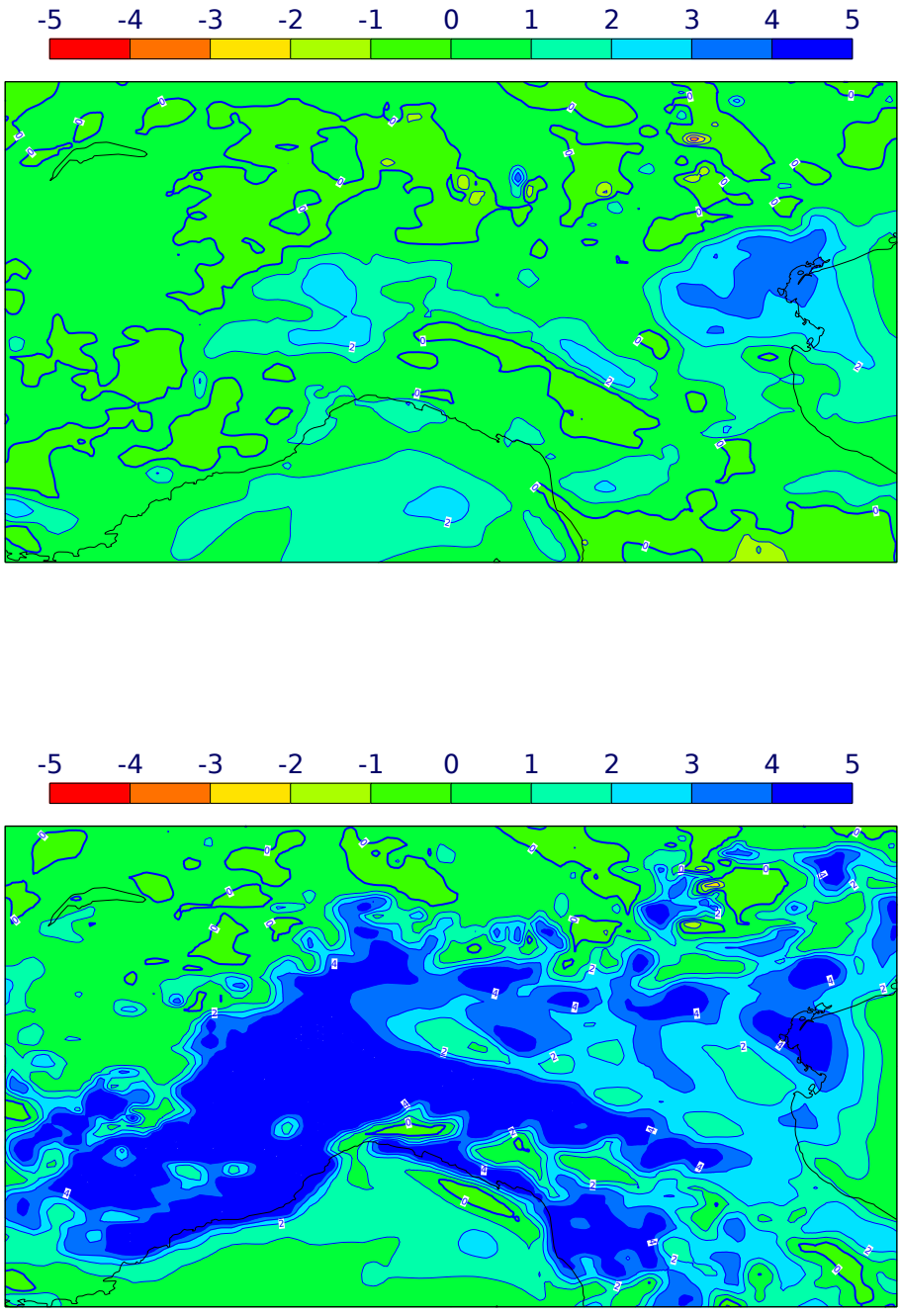

Figure 3.4: Maps of difference in temperature at 2m between COSMO reference simulation and Test 1 (left side) and Test 2 (right side). The scale is in [$^{\circ}C$], with blue colors indicating a cooling and red colors a warming. The maps refer to the output at 08/01/2012-4:00 am

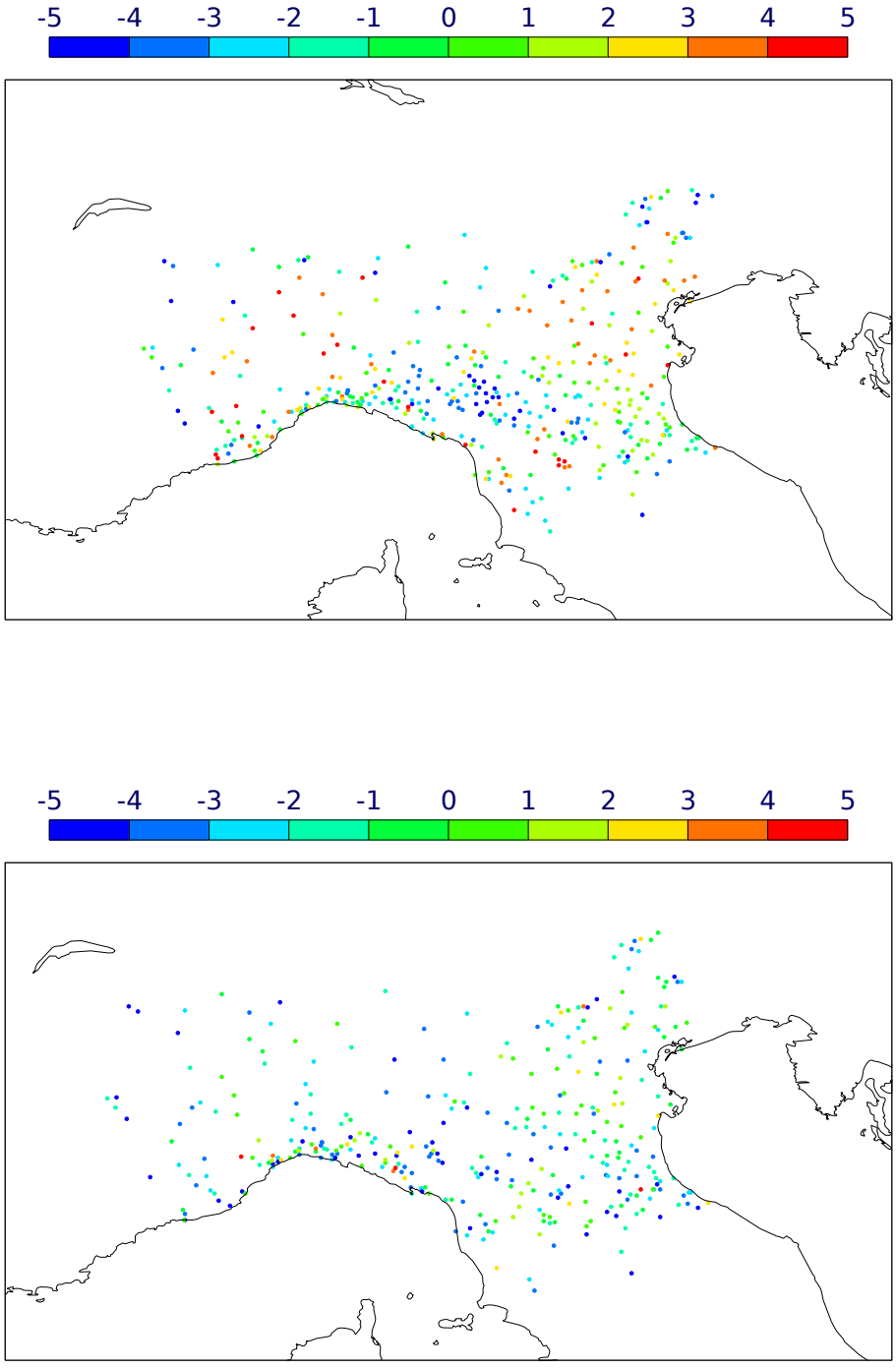

Figure 3.5: Mean error of temperature at 2m in COSMO reference run (top) and in COSMO Test 2 (bottom) against the observations. The scale is in $[°C]$, with red points indicating positive values and blue points negative values. The maps refer to 08/01/2012 at 4:00am

3.1.4 Conclusions

The reduction of $K_{min}^{M,H}$ to a physical reasonable value produces a weak reinforcement of the thermal stratification over homogeneous terrain, with a simulation colder at 2m of about $1°C$ mainly during night. The effect is confined to cases of strongly stratified SBL (no effect over mountains). However, a numerical oscillations is intensified by the turbulent mixing reduction. It can be dangerous to numerical model stability, beyond affecting the physical simulation at the lowest model levels. It is produced by the scale interaction term accounting for the subgrid scale thermal inhomogeneity of the surface added to the TKE budget (f_C). The reduction of $K_{min}^{M,H}$ should then come along with the removal of this term. The case study analysis reveals that the thermal circulation term has an even stronger turbulence-enhancing effect than $K_{min}^{M,H}$: over homogeneous terrains the stable stratification intensifies in the surface vicinity yielding to cooler temperatures at 2m up to $5°C$, more in agreement with the observations. On the contrary, over heterogeneous terrains if the boundary layer is sufficiently stable, the removal of the thermal circulation leads to excessive cooling. Hence, it is desirable a re-formulation of the thermal circulation term on a side accounting for the subgrid scale features (at the current state it is not the case) and on the other side curing the numerical oscillation issue. If and when such formulation will be available, it could be tested as a physical meaningful alternative to the $K_{min}^{M,H}$.

3.2 Minimum sum of TKE forcings

The sum of TKE forcings f_m and f_h is constrained in order to prevent that Ri_f exceeds the critical value of 0.19. The limit is expressed as:

$$frc = MAX(d\, f_m, f_m + f_h) \tag{3.3}$$

with the coefficient $d = 0.81$. Given that Ri_f is defined as:

$$Ri_f = -\frac{f_h}{f_m}$$

the limit in eq. 3.3 can be rewritten as a function of Ri_f by few passages:

$$\begin{aligned} frc &= (f_m + f_h) \cdot MAX(d\frac{f_m}{f_m + f_h}, 1) \\ &= (f_m + f_h) \cdot MAX(d\frac{f_m}{f_m(1 - Ri_f)}, 1) \\ &= (f_m + f_h) \cdot MAX(\frac{d}{(1 - Ri_f)}, 1) \end{aligned}$$

Therefore, when $\frac{d}{1-Ri_f} \geq 1$, or in other words when $Ri_f \geq 0.19$ (i.e. in very stable conditions), the limit is enabled, constraining the forcing sum to non-negative values

(i.e. as f_m is always greater or equal to 0). In this case the buoyancy term f_h (which is negative by definition under stable stratification) is constrained to be larger than $df_m - f_m = (d-1)f_m = -0.19f_m$. Basically, the restriction pumps artificially energy in TKE equation any time that the TKE sink due to buoyancy becomes too intense. By this, the turbulence scheme produces a more diffusive SBL, even when strongly stable temperature profiles are provided to the turbulence scheme. In these cases, TKE equation behaves as the stability is equal to $Ri_f = 0.19$.
Figure 3.6 evidences the high frequency of occurrence of this limit over a flat homogeneous point (San Pietro Capofiume) in the three-day simulation characterized by conditions particularly favourable to the generation of strongly stratified SBL (case study described in section 2.4.1). Another example is shown in Figure 3.3, where the limit activates at 08/01 01:00 and persists for several hours. The removal of this limit

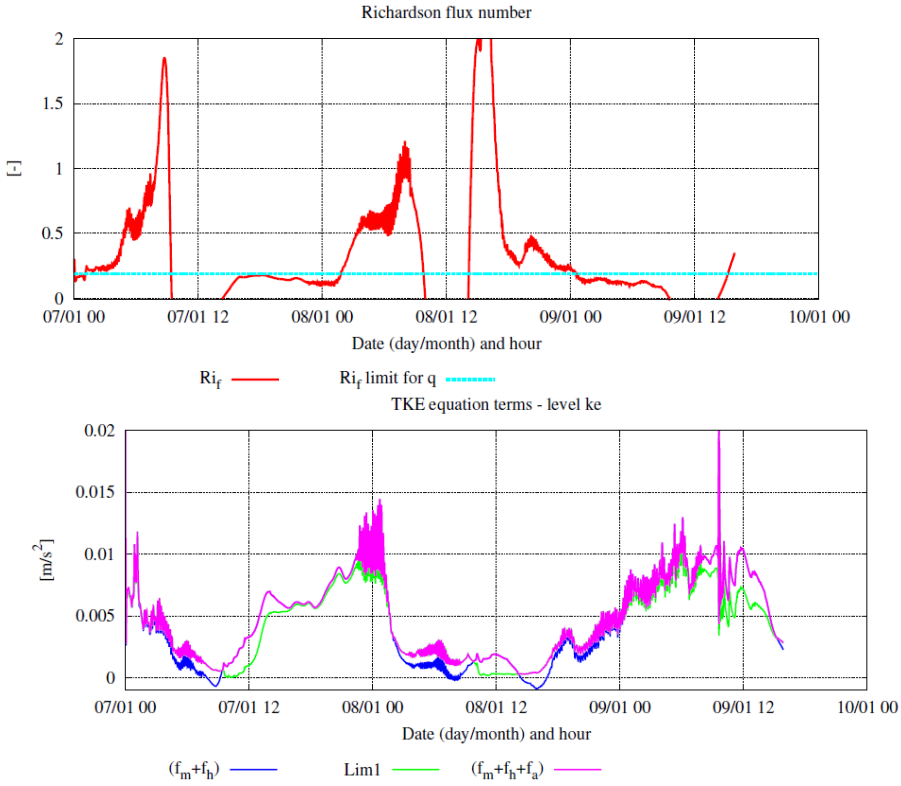

Figure 3.6: Time series of (top) the Ri_f number with in evidence the critical Ri_f number and (bottom) the TKE forcing sum (pink) as well as its original value (blue) and its maximum value (green)

causes a not-a-number error in the solution of TKE equation. However, a sensitivity test to the limit can be performed after a code rearrangement (Raschendorfer, pers. comm.). The constrain removal (obtained by setting $d = -9999$) allows negative value for the TKE forcing sum and thus unbounded solutions of TKE equation in case of high stability.

The simulation of the case study performed by the operational-like model configuration (and described in section 3.1.1) is here repeated by eliminating the constrain.

Over North-Italy domain the differences in temperature at 2m between the simulations using the original code and the modified one vary between $-1°C$ and $-3°C$, mainly during night (Figure 3.7). Apparently in contrast with the connection of the limit to high stability conditions, its influence appears larger over the mountain regions (North-West side of Alps), where stable stratification is weaker, than over the flat Po Valley (Figure 3.7). A possible explanation is that the influence of this forcing sum bounding is masked over flat and hilly terrains by other long-tail formulations, which are more active over flat terrain (e.g. $K_{min}^{M,H}$ and the thermal circulation term hava a large impact on flat regions, Figure 3.4, top).

In conclusion, from a physical point of view, it would be preferable to remove the limit to the TKE forcing. In practice, despite the limit frequent activation, it does not affect temperature in flat terrain. Indeed likely, its action is hidden by more vigorous mixing constrains over these areas. Mainly the less stable mountain regions appear to suffer by this bounding. The verification of temperature at 2m in the reference case study simulation against ground stations indicate an already negative bias of temperature over mountains (Figure 3.5,top), thus the further cooling produced by this limit removal in these regions will be detrimental for the local near surface temperature representation.

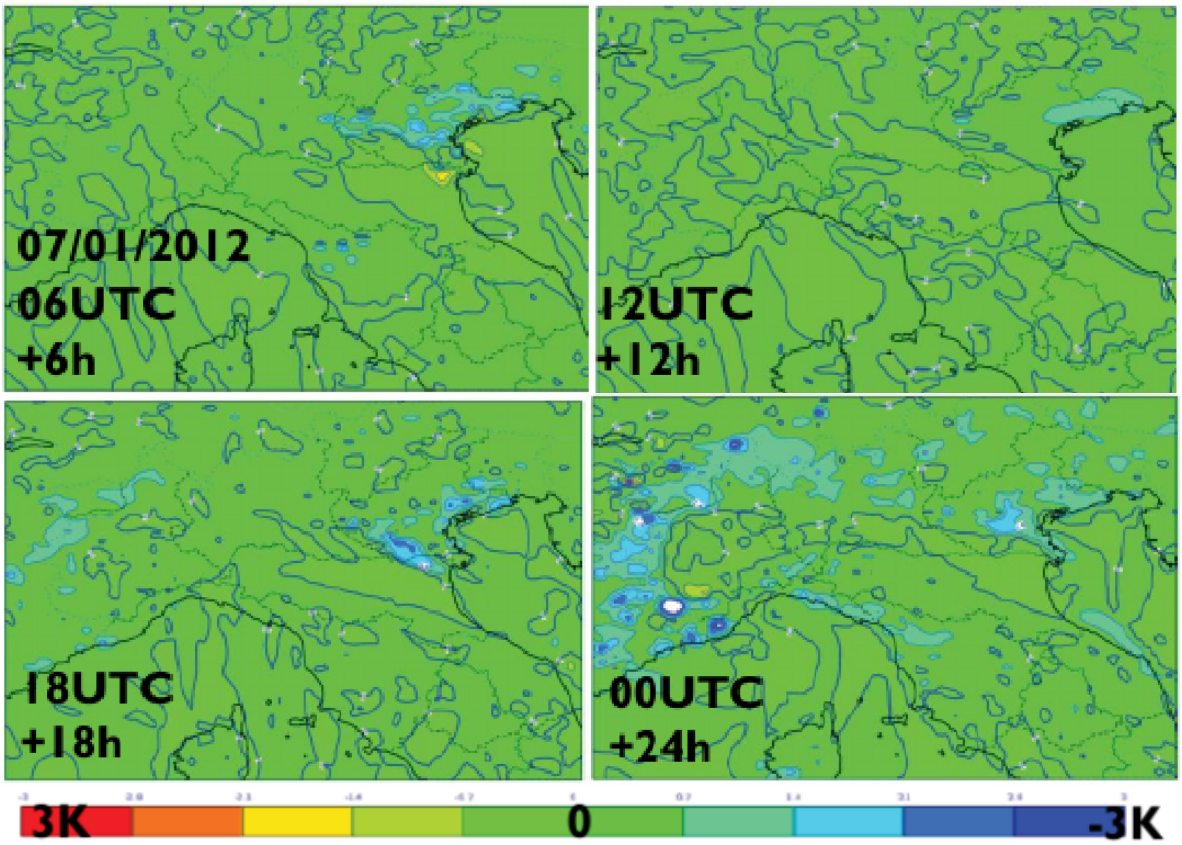

Figure 3.7: Differences of temperature at 2m between the reference configuration and the experiment without the Ri_f limit on TKE forcing sum at different simulation time ranges

3.3 q_{min} avoiding q solutions too distant from the equilibrium value

Mellor and Yamada (1982) scheme in its truncation at Level 2.5 presents a singularity in the stability functions for growing turbulence under unstable stratification ($Ri \leq 0$), which mainly occurs in the transition between nocturnal stable stratification to daily unstable condition. The singularity takes origin from the violation of the hypothesis of near-isotropic turbulence at the base of the Level 2.5 derivation, which happens as soon as turbulence begins to be driven by convective vertical eddies (Helfand and Labraga, 1988). The singularity was originally identified by Mellor and Yamada (1982) and several solutions have been suggested to cure it (Mellor and Yamada, 1982; Hassid and Galperin, 1983; Helfand and Labraga, 1988; Janjic, 2002). In the turbulence scheme introduced in COSMO, the singularity is avoided by using a modified formulation of the original Level 2.5 for $Ri \leq 0$ (extended description in Wacker et al., 2005) and a minimum limit for q. In this limit lays the interest in term of SBL, as it acts in both unstable and stable stratification. In order to explain the COSMO code behaviour and to investigate possible alternatives, some theory concepts about the singularity are given in the following.

The realizability criteria require firstly that model integration ensures non-negative values of the potential temperature variance $\overline{\theta'^2}$ and momentum variances $\overline{u'^2}$,$\overline{v'^2}$, $\overline{w'^2}$, and secondly that Schwarz inequality are fulfilled (Schumann, 1977). Mellor and Yamada (1982) suggested even more stringent criteria than non-negative variances for their model, on the base of experimental data. The full set of criteria can be expressed as:

$$0.12 \leq \frac{\overline{u'^2}}{q^2}, \frac{\overline{v'^2}}{q^2}, \frac{\overline{w'^2}}{q^2} \leq 0.76 \tag{3.4}$$

$$0 \leq S^H \leq 6.08 \tag{3.5}$$

$$S_M^2 G_M \leq 0.44. \tag{3.6}$$

where S^M and S^H are the stability functions for momentum and heat respectively, defined as:

$$S^M = -\frac{\overline{u'w'}}{lq}\frac{\partial \overline{u}}{\partial z} \tag{3.7}$$

$$S^H = -\frac{\overline{\theta'w'}}{lq}\frac{\partial \overline{\theta}}{\partial z} \tag{3.8}$$

and G^M is the dimensionless square of the shear, defined as:

$$G^M = \frac{l^2}{q^2}\left[\left(\frac{\partial \overline{u}}{\partial z}\right)^2 + \left(\frac{\partial \overline{u}}{\partial z}\right)^2\right] \tag{3.9}$$

Furthermore, the Mellor and Yamada (1982) scheme at Level 2.5 presents some singularities associated to fast growing turbulence, which would lead to so quickly increasing

S^M, S^H and momentum variances that they become physically non-realizable (Helfand and Labraga, 1988). The set of criteria in eq. 3.4-3.6 is violated before the occurrence of the singularities of Mellor and Yamada (1982) scheme at Level 2.5, thus their fulfillment ensures the scheme stability. As an example, Figure 3.8,a reports the singular behaviour of S^H (divergence to infinite, indicated by the contour line labelled as "∞") and its upper realizability limit (denoted by the dashed line) on the plane $Rixq^2/q_{eq}^2$. In the y-axis of the plane, q^2/q_{eq}^2 indicates the squared ratio between q ($q = \sqrt{2TKE}$) and its solution at equilibrium q_{eq}, which is derived from the balance between TKE production (i.e. the sum of wind shear and buoyancy forcings, $frc = f_m + f_h$) and dissipation ϵ, as follow:

$$0 = frc - \epsilon = frc - \frac{q_{eq}^2}{ld_{mom}} \rightarrow q_{eq} = \sqrt{ld_{mom}frc} \tag{3.10}$$

where it has been used ϵ definition and the negative root of q_{eq} is neglected, as q is positive defined (moreover, l refers to the mixing length, see eq. 2.2.1 and $d_{mom} = 16.6$ to a parameter). It can be demonstrated that $q/q_{eq} \geq 1$ corresponds to decaying turbulence, $q/q_{eq} \leq 1$ to growing turbulence and $q/q_{eq} = 1$ indeed to the special case in which production and dissipation balance each other (Helfand and Labraga, 1988). By this, the visualization of the scheme realizability on the plane $Rixq^2/q_{eq}^2$ is quite useful, as the plane is divided in four quadrants indicating stable/unstable regime and growing/decaying turbulence. Figure 3.8,a visualizes that the critical issues of the scheme at Level 2.5 for S^H occur in case of growing turbulence under unstable stratification. The other criteria affect the same region of the space and additionally a small fraction of the $Ri \geq 0$ plane in growing turbulence conditions close to plane origin (see Figure 7 in Helfand and Labraga (1988)).
In order to highlight the behaviour of the solution applied by COSMO turbulence scheme (description in Wacker et al., 2005), the same visualization of Figure 3.8,a is reproduced for the COSMO code in Figure 3.8,b. The contour lines are indicated by color transition produced by the S^H in output of COSMO in 1D mode with an every time step frequency, in a three-day simulation. In the COSMO turbulence code, the application of a modified version of the Mellor and Yamada (1982) scheme at 2.5 Level (only under unstable stratification) produces small differences in S^H from the original version, for negative-Ri sector of the plane $Rixq^2/q_{eq}^2$. In contrast, a main difference consists in the application of a lower limit to the q^2/q_{eq}^2 ratio in COSMO scheme, affecting cases of growing turbulence for both stable and unstable regimes. The limit is defined in the code as:

$$q \geq \sqrt{7.14lfrc} \tag{3.11}$$

and, using eq. 3.3, it can be expressed as:

$$q^2 \geq 0.43q_{eq}^2 \tag{3.12}$$

Despite the realizability of the turbulence scheme is ensured in COSMO, the scheme does not describe any case of strongly growing turbulence $\frac{q^2}{q_{eq}^2} \leq 0.43$, for any stable

stratification intensity. The relevance of this limit can be understood by plotting the same visualization in a COSMO version using a reduced applicability of q limit to only $Ri \leq 0$ (Figure 3.8,c). In this case, a large number of solutions of the turbulence scheme fall below the $\frac{q^2}{q_{eq}^2} \leq 0.43$ threshold for stable stratification (right bottom corner of the $\frac{q^2}{q_{eq}^2} x Ri$ plane in Figure 3.8,c). Unfortunately, when the code with this less-stringent limit is used in a 3D mode simulation, it often leads to a model crash (mainly with issues started in stable layers), which motivates the need of such strict constrain.

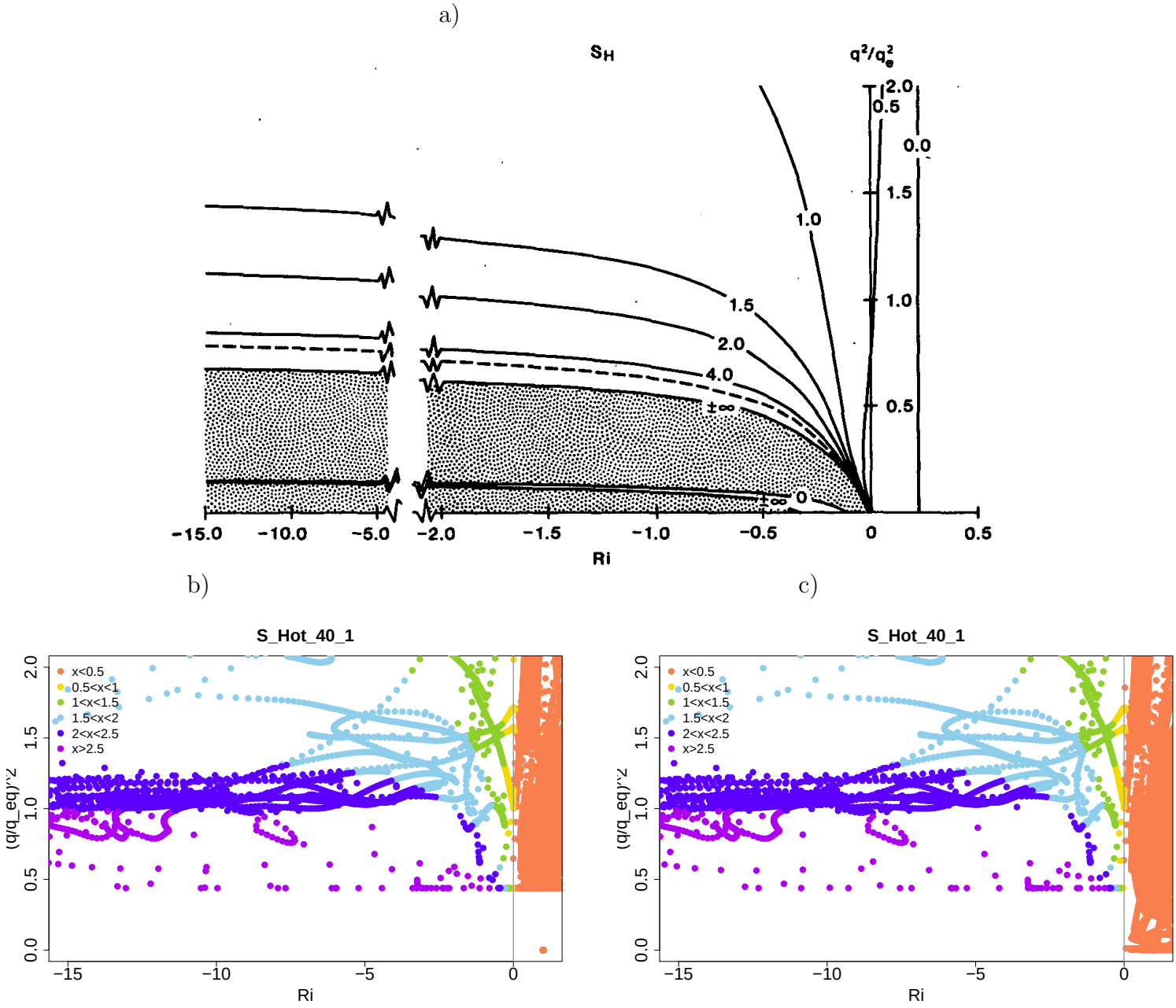

Figure 3.8: Contour plots of the stability function S^H (indicated as 'x' in legend) in the plane $\frac{q^2}{q_{eq}^2} x Ri$ in (a) Mellor-Yamada Level 2.5 scheme (shaded areas indicate the regions where the realizability conditions are violated) from Helfand and Labraga (1988), (b) the turbulence scheme applied in COSMO, (c) the modified turbulence scheme applied in COSMO model with q limit constraining only ($Ri \leq 0$)

Different alternatives to the approach applied in COSMO turbulence scheme are now considered in order to treat the singularity, aimed at reducing the constrains on q.

1. A first alternative to remove the singularity is to apply the Mellor-Yamada scheme at Level 2.0 for $q^2/q_{eq}^2 \leq 1$ (as suggested by Helfand and Labraga, 1988). Mellor and Yamada (1982) scheme at level 2.0 assumes the exact balance between production and dissipation for all the second-order moments, TKE included. Therefore, differently from Level 2.5, in Level 2.0 the diagnostic eq. 3.3 is used in spite of the prognostic TKE equation 2.1. This solution requires that TKE and all other second-order turbulent moments adjust immediately to the local equilibrium for growing turbulence. This, basically, precludes any solution for values of q^2/q_{eq}^2 lower than 1. At the matter of fact, this solution is an even stricter limit on q than the one in COSMO turbulence scheme (plot not shown).

2. A compromise mentioned in Helfand and Labraga (1988) is to apply the Level 2.0 scheme only in the calculation of $S^{M,H}$, while TKE is forecast for growing turbulence by the Level 2.5 scheme. The advantage is that the diffusion coefficients $K^{M,H} = qlS^{M,H}$ describe better the transient effects than those based on Level 2.0 scheme only, as they depend on the prognostic value of q rather than on its equilibrium value. In addition to Helfand and Labraga (1988), in the present analysis this compromise is applied only to unstable layers, in order to keep the highest degree of freedom of the Level 2.5 scheme at least for $Ri \geq 0$. The results are shown by looking at the time evolution of S^H at different vertical levels at about the sunrise, i.e. when turbulence is growing at the transition between stable and unstable stratification (Figure 3.9). While COSMO turbulence scheme shows some oscillations in the night-to-day transition, this modification produces a smooth passage. However, not always the $S^{M,H}$ daily asymptotic values are equal in the two schemes (Figure 3.9, right). Indeed, this second option de-potentates all the 2-nd order turbulent moments in unstable layers. In the plotted case, the difference is given by the weakening of the thermal circulation term (computed as a vertical diffusion term), which is maximum close to the surface.

3. The last alternative considered is the optimum approach proposed in Helfand and Labraga (1988), which attempts a physical manner to treat the singularity. They suggest to give an estimate to the anisotropy in the temperature variance equation in growing turbulence in the Level 2.5 scheme (and in particular assuming that it behaves like the one of TKE equation), as the failure appears in the treatment of the anisotropy in second-order moment equations. The implementation in COSMO turbulence scheme consists in the use of the Helfand-Labraga scheme for $\frac{q^2}{q_{eq}^2} \leq 1$ and of Mellor-Yamada (1982) Level 2.5 original scheme in the other case. The limit on q and the use of the modified Mellor and Yamada (1982) scheme (applied in COSMO for $Ri \leq 0$) is unnecessary. Figure 3.10 shows the good agreement between the implementation of Helfand-Labraga modification

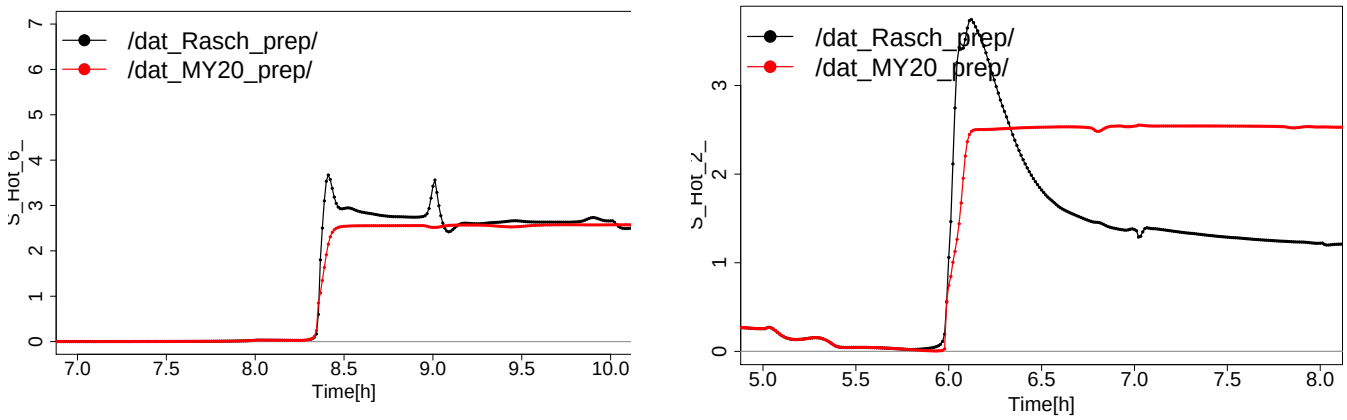

Figure 3.9: Time series of the stability function S^H at 300m (left) and 10m (right) above the surface for the numerical simulations of the PBL using the COSMO turbulence scheme (black line) and the COSMO turbulence scheme integrating the calculation of the stability functions from Mellor-Yamada Level 2.0 scheme for $Ri \leq 0$ (red line).

in COSMO turbulence scheme (in 1D mode) and their theoretical scheme. The length of the period of transition from stable to unstable stratification at sunrise is longer applying this third option with respect to the COSMO turbulence scheme (Figure 3.11), looking more realistic and in agreement with the Helfand-Labraga theoretical model. However, the kinked contours at $\frac{q^2}{q^2_{eq}} = 1$ (see Figure 3.10) produce a rough transition between the Helfand and Labraga (1988) formulation (for $\frac{q^2}{q^2_{eq}} \leq 1$) and Mellor and Yamada (1982) scheme (for $\frac{q^2}{q^2_{eq}} \geq 1$), which manifests not only at the sunrise (as already observed by Helfand and Labraga (1988)), but also at other hours (see deep oscillations in S^H in Figure fig:SH HL88 singularity,right). Any further test with COSMO 3D is thus precluded. Further work would be necessary to evaluate the possible improvements.

In conclusion, at the current state the only alternative avoiding on a side the singularity for growing turbulence in unstable layers and on the other side the q constrain limiting the distance from the equilibrium solution under stable stratification consists in a partial integration of the Level 2.0 scheme in the Level 2.5 scheme only for $Ri \leq 0$. Promising results are obtained by the implementation of Helfand-Labraga modification of Level 2.5 scheme for $\frac{q^2}{q^2_{eq}} \leq 1$, but some additional effort would be necessary to rectify its behaviour in COSMO turbulence scheme.

3.4 Conclusions

In the present chapter, several turbulence enhancing recipes introduced in COSMO operational model are described from a physical point of view. The meteorological and topographical conditions which make the COSMO model sensitive to them are investigated through simulations in 1D and 3D mode. In the same way, their reduction or removal is also investigated. Results for each of them are summarized in the following.

1. The minimum limit of the diffusion coefficients for momentum and scalar $K^{M,H}$ equal to a value higher than observational evidence ($K^{M,H}_{min} = 0.4m^2/s$ in the operational COSMO code at SIMC) is the most known turbulence enhancing option introduced in COSMO and its action is well documented at the near surface in SBL, on the SBL structure and on the PBL clouds (Buzzi, 2008; Volker et al., 2009; Heise, 2006; Köhler et al., 2011). In the present study, the reduction to a value non-influencing the turbulence scheme computation ($K^{M,H}_{min} = 0.01m^2/s$, from Buzzi, 2008) is tested over a 3D domain. At the near surface, a cooling of $\approx 1°C$ of the diagnostic temperature at 2m and stronger thermal inversion are observed over flat terrain (where stable stratification is stronger), fitting better observations, coherently with previous similar tests (Volker et al., 2009). The originality of this experiment consists in the use of a every time step (20s) output, which allows the detection of numerical oscillations with a ≈ 20 time steps period which affect turbulence-related and dynamical variables at the lowest model levels in the SBL. They result associated with the scale interaction term in charge for the description of the influence of the subgrid surface thermal heterogeneity on TKE (see next point) and they enlarge the forecast uncertainties, since the model output could fall indifferently at the oscillation trough or peak.

2. The scale interaction term introduced in the TKE equation in order to account for the influence of the subgrid surface thermal heterogeneity on TKE does not include at the current state any dependence on subgrid surface features (in absence of subgrid clouds). Moreover, it has a strong turbulent mixing effect at the lowest model levels (beyond causing the deep oscillations previously mentioned). For these two reasons, it can be listed among the long-tail formulations introduced in COSMO. Its deactivation, associated with the reduced diffusivity limit ($K^{M,H}_{min} = 0.01m^2/s$), leads to a strong cooling at 2m (between 1 and $5°C$) affecting flat and hilly terrains (and to the disappearance of the numerical oscillations). From the case study analysis, the near surface cooling results beneficial over flat regions and deleterious over rough terrain regions (where thermal heterogeneity are most likely present). However, the test of the same configuration in parallel with the operational chain for several months shows a worsening of rmse errors at 2m.
   Currently, the global NWP model ICON runs operationally using the COSMO turbulence scheme with a modified thermal circulation term, in which a dependence on subgrid scale orography is included (G. Zängl, pers. communication). A

similar choice in COSMO would improve the physical meaningfulness of the term and at least reduce its long-tail action.

3. The limit on the TKE forcing sum is a less known long-tail formulation, despite its TKE enhancing effect acts at every model level. It avoids the turbulence scheme to describe cases in which the stratification exceeds the very stable threshold $Ri_f \geq 0.19$ (and in these cases, the negative sink of TKE due to the buoyancy forcing is limited). At the moment, any modification to it should be performed in the hard code. The removal of the limit produces a cooling at the near surface over mountains (stressing the model deficiencies in these areas), while the impact on very SBL in flat regions results only marginal (likely because the presence of large $K_{min}^{M,H}$ masks it).

4. Another less known lower limit to TKE enhancing turbulent mixing is associated to the treatment of the singularities and realizability constrains of the Mellor and Yamada (1982) scheme at Level 2.5 applied in the COSMO model (a description in Wacker et al., 2005). It is formulated as $q^2/q_{eq}^2 \geq 0.43$ and, under stable stratification, it avoids the turbulence scheme to describe cases of growing turbulence (e.g. at the sunset). Several alternatives to the COSMO treatment of the singularities and realizability constrains are tested in order to remove/reduce the limit for stable stratification. The only working option consists in a partial integration of the Mellor and Yamada (1982) scheme at Level 2.0 (i.e. only in terms of stability function computations) in the Level 2.5 scheme for $Ri \leq 0$. Despite this solution weakens the vertical exchange terms in the TKE budget equation (e.g. triple terms and thermal circulation term), its application can be considered in COSMO in 3D mode. However, it has not yet been tested in operational runs. Promising results are obtained also by the implementation of Helfand and Labraga (1988) modified version of Level 2.5 scheme for $\frac{q^2}{q_{eq}^2} \leq 1$ in COSMO in 1D mode, but some additional effort is necessary to rectify its behaviour in COSMO turbulence scheme.

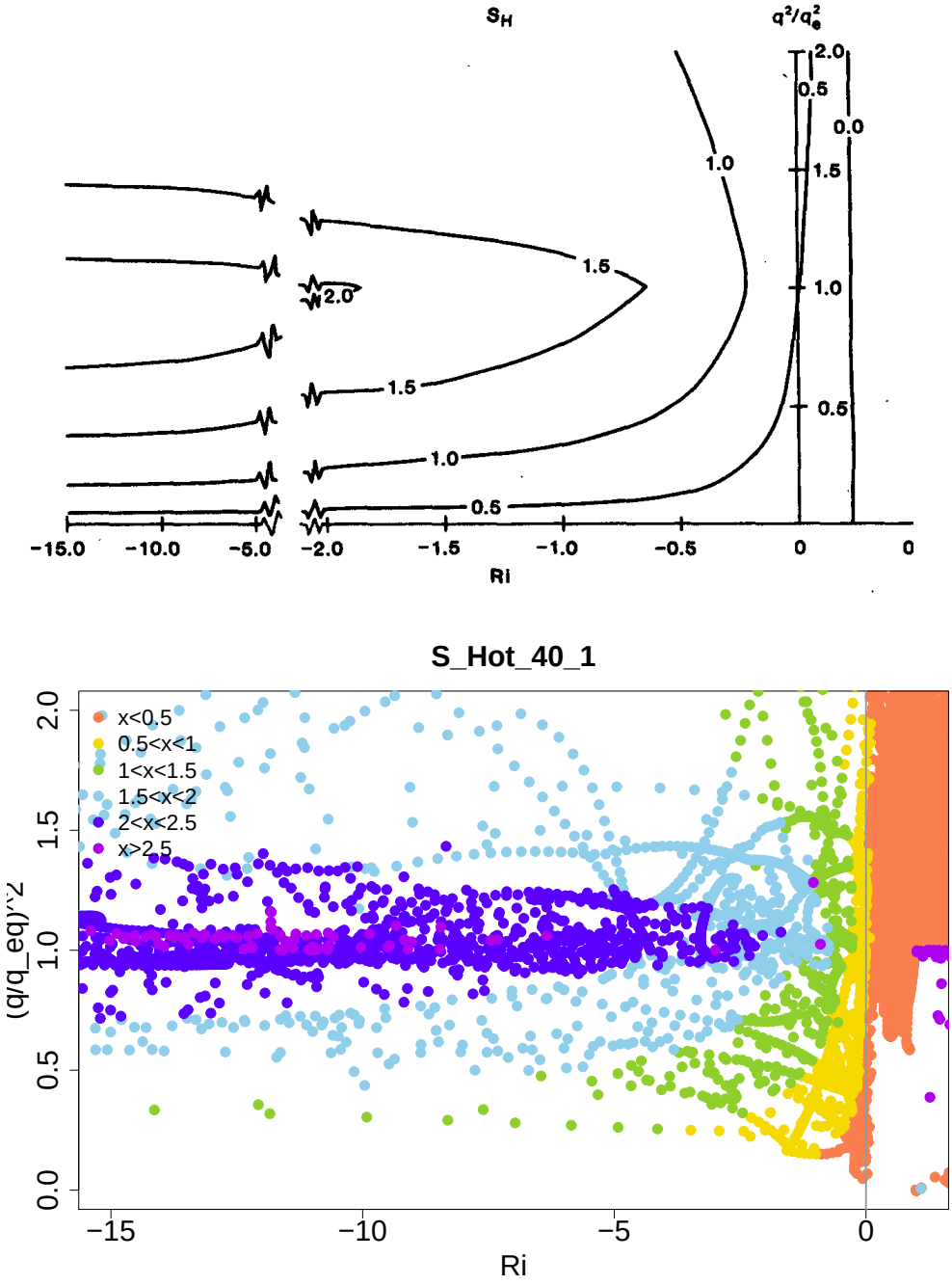

Figure 3.10: Contour plots of the stability function S^H in the plane $\frac{q^2}{q^2_{eq}} x Ri$ in Helfand and Labraga (1988) modified scheme (top, from their paper) and the implementation of their modification in COSMO turbulence scheme (bottom). Simulation with single column version of COSMO

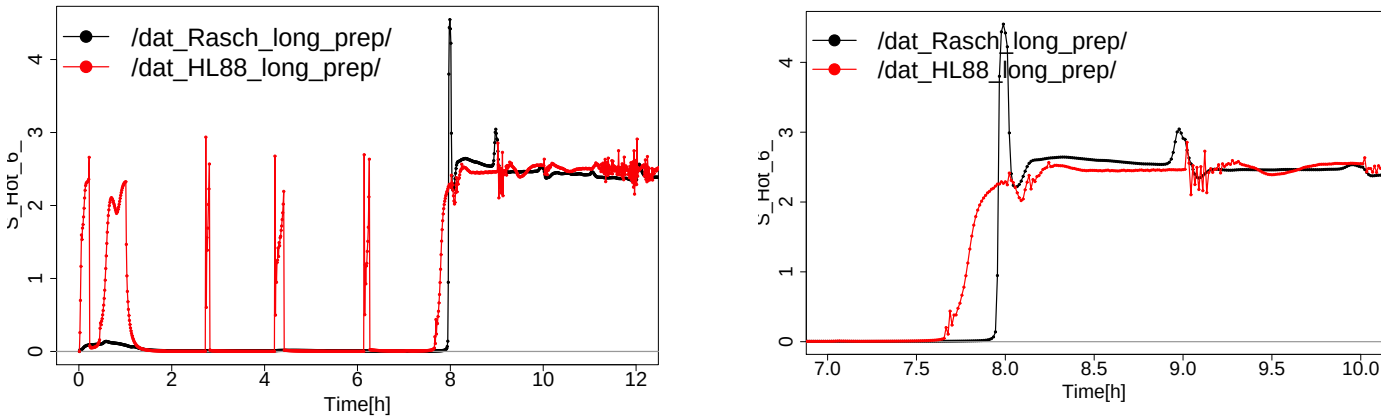

Figure 3.11: Time series of the stability function S^H at 300m above the surface (left) and its temporal zoom (right) for the numerical simulations of the PBL using the COSMO turbulence scheme (black line) and the COSMO turbulence scheme integrating Helfand-Labraga modification (red line).

Chapter 4

Diagnostics of the transfer scheme

4.1 Introduction

The analysis of the case study in section 2.4 evidenced that COSMO overestimates (in absolute value) the sensible heat and momentum fluxes at the surface with the strengthening of the stable stratification (latent heat flux was not considered in that study as the measurements were not usable). The dependence of the errors on stability allowed to draw the hypothesis that the model issue originates within the representation of the processes relevant for the SBL.
The computation of the surface fluxes is part of the transfer scheme. In the latter the transfer coefficients for momentum and scalar (i.e. temperature and humidity) are estimated. Other relevant terms for the surface fluxes calculation are the difference in temperature between the surface and the lowest model level and the wind at the lowest model level (see bulk formulation in eq. 2.7,2.6). The case study showed the flux errors are most likely related to the transfer coefficients and/or to the lowest level wind speed, but the short period under investigation, the experiment setup and the several feedback mechanisms within the SBL prevented a clear understanding of the error source.
In order to investigate the above question, tests of each possible component were performed using the the single column (SC) version of COSMO. The SC model is run over a one month period with all the variables defining the surface fluxes (profiles and surface values of temperature, pressure, humidity and wind) prescribed by observations. Thus, only the transfer scheme formulation is tested independently by feedbacks with other model errors. The observational data belong to the Lindenberg super-site (Germany), located in a quite homogeneous terrain. Given that in this simple terrain case the validity of the Monin-Obukhov similarity theory (MOST) is well documented (at least up to weak stability), the performance of the COSMO transfer scheme is compared with two MOST based formulations: an empirical and a semi-empirical formulations. Empirical formulations are the ones in which the non-dimensional gradients of the mean wind speed ϕ_m and of the mean virtual potential temperature ϕ_h in the surface layer (expressing the proportionality between vertical gradients and fluxes) are purely empirically derived as universal functions of the stability parameter $\xi = zL^{-1}$.

A wide variety of different empirical formulations is available for stable stratification in literature (see Luhar et al., 2009, for a review). In the present analysis, Cheng and Brutsaert (2005, hereafter referred to as CB05) is selected as a recent example of pure empirical formulation. On the other side, the semi-empirical formulations originate from the compromise between observational evidence and NWP applications. In these formulations, the dimensionless functions are modified in order to describe a slower decay for increasing thermal stability or a differential behaviour between heat and momentum transport. Moreover, the stability parameter ξ (function of the surface fluxes) is substituted by the Ri_b number (function of the vertical gradient), thus avoiding the implicit computation of the surface fluxes. The schemes of Louis-Tiedke-Geleyn (Louis et al., 1982) and its revision (Viterbo et al., 1999) are examples of these semi-empirical MOST based schemes. The formulation from Louis et al. (1982, hereafter referred to as LTG) is herein considered as an example of a semi-empirical approach.
In a second experiment, the performance of COSMO transfer scheme is compared with the one of the best performing MOST based formulation (in the SC study) by 3D simulations over a one month period. The results are compared with data collected at the super-site station of San Pietro Capofiume in the Po Valley (Italy) focusing on cases of stable stratification in the low atmosphere. In contrast to the previous experiment, this latter analysis includes the feedbacks by the internal coupling of all the other model components with the transfer scheme.

4.2 Surface flux formulation

The surface fluxes are derived via the bulk formulations in eqs. 2.6-2.7 in all the three transfer schemes under consideration (COSMO, empirical MOST based CB05, semi-empirical MOST based LTG). The formulations of the transfer coefficients in these transfer schemes is reported below.

4.2.1 COSMO formulation

As mentioned in section 2.2.2, the inertial sub-layer of COSMO transfer scheme corresponds to the constant-flux layer described by MOST based formulations, i.e. to the layer between the roughness length z_0 and the lowest model level z_A. The aerodynamic resistance of the inertial sub-layer is derived by integrating vertically the inverse of a lenght scale and turbulent velocity scale u^φ (see eq. 2.11-2.12, where the superimposed φ stands for M, H, respectively momentum and scalar variables), under the assumption of a linear interpolation function of u^φ between the levels z_0 and z_P (i.e. lower and upper boundary of the lowest model level centred in z_A; at z_0 and z_P levels the turbulence scheme is solved)[1]:

$$r_{0A}^{\varphi} = \frac{1}{k u_0^{\varphi}(1-\gamma)} \ln \frac{z_A}{z_0 + \gamma(z_A - z_0)} \tag{4.1}$$

[1]Complete derivation of r_{0A}^{φ} is reported in appendix B.1

with

$$\gamma = \frac{z_0}{z_P - z_0} \frac{u_P^{\varphi} - u_0^{\varphi}}{u_0^{\varphi}} \tag{4.2}$$

varying in the range:

$$-z_0[2(z_P - z_0)]^{-1} \leq \gamma \leq 2z_0(z_P - z_0)^{-1} \tag{4.3}$$

in order to improve the model numeric stability. When $\gamma \to 1$, the singularity in eq. 4.1 is avoided by using the function:

$$r_{0A}^{\varphi} = \frac{1}{k u_0^{\varphi}} \frac{z_A}{z_0 + z_A} \tag{4.4}$$

The linear interpolation function of u^{φ} ensures that in case of neutral stratification $u_0^{\varphi} = u_P^{\varphi}$ and that, in particular for momentum, these turbulent velocity scales correspond to the friction velocity $u_0^M = u_P^M = u_*$. By this, eq. 4.1 turns to the logarithmic relation in accordance with MOST:

$$r_{0A}^{\varphi} = \frac{1}{k u_0^{\varphi}} \ln\left(\frac{z_A}{z_0}\right) \tag{4.5}$$

The total resistance of the surface layer is the sum of the inertial sub-layer and roughness sub-layer contributions. If the roughness sub-layer is neglected, then its respective resistance is set equal to 0. In this case, the transfer coefficients for heat and momentum are obtained introducing eq. 4.1 in the C_{SA}^{φ} formula as follow:

$$C_{SA}^{\varphi} = \frac{1}{r_{SA}^{\varphi} |\boldsymbol{v_A}|} = \frac{1}{r_{0A}^{\varphi} |\boldsymbol{v_A}|} = C_{0A}^{\varphi} = \frac{k u_0^{\varphi} (1 - \gamma)}{|\boldsymbol{v_A}|} \frac{1}{\ln \frac{z_A}{z_0 + \gamma(z_A - z_0)}} \tag{4.6}$$

If the roughness sub-layer contribution is not neglected, the transfer coefficients C_{SA}^{φ} are obtained by eq. 2.9, with the resistance of the roughness sub-layer given by the integration of eq. 2.11 between level z_S and z_0, under the assumption of a constant turbulent velocity scale $u^{\varphi} = u_0^{\varphi}$ and a lenght scale following the function:

$$\frac{dl}{dz} = \frac{k}{S_0} \tag{4.7}$$

S_0 is a surface parameter that expresses the roughness element density. At the surface, it is assumed $l(z_S) = \nu u_0^{-1}$, with ν the kinematic viscosity. By this, the roughness sub-layer resistance for heat exchange is:

$$r_{S0}^{H} = \frac{1}{k S_0 u_0^{H}} \ln \frac{K_0^M}{\nu} \tag{4.8}$$

while the roughness sub-layer resistance for momentum exchange is equal to 0 in the operational setup. Moreover, another contribution is introduced in eq. 4.8, in order to account for the laminar heat transfer. Thus the roughness sub-layer resistance becomes:

$$r_{S0}^{H} = \frac{1}{k S_0 u_0^{H}} \ln \frac{K_0^M}{\nu} + \frac{\varsigma}{k S_0 u_0^{M}} \frac{\nu}{\mu} \tag{4.9}$$

with ς a function of the land/water coverage ratio in the grid box, meant to increase the laminar contribute over water surface, and μ the kinematic conductivity. Complete derivation of r_{S0}^{H} is reported in appendix B.1.

4.2.2 MOST based formulations

Following MOST, the drag coefficient and bulk transfer coefficient for scalar for the constant-flux layer may be written as:

$$C_{0A}^{M} = \kappa^2 \qquad [ln(\tfrac{z_A}{z_0}) - \phi^M(\tfrac{z_A}{L}) + \phi^M(\tfrac{z_0}{L})]^{-2} \tag{4.10}$$

$$C_{0A}^{H} = \kappa^2 \quad \left[[ln(\tfrac{z_A}{z_0}) - \phi^M(\tfrac{z_A}{L}) + \phi^M(\tfrac{z_0}{L})][ln(\tfrac{z_A}{z_0}) - \phi^H(\tfrac{z_A}{L}) + \phi^H(\tfrac{z_0}{L})]\right]^{-1} \tag{4.11}$$

where κ is von Karman constant. The empirical functions proposed by CB05 read like:

$$\phi^M\left(\frac{z}{L}\right) = -a \cdot ln\left[\frac{z}{L} + \left[1 + \left(\frac{z}{L}\right)^b\right]^{1/b}\right] \tag{4.12}$$

$$\phi^H\left(\frac{z}{L}\right) = -c \cdot ln\left[\frac{z}{L} + \left[1 + \left(\frac{z}{L}\right)^d\right]^{1/d}\right] \tag{4.13}$$

Where $a = 6.1$, $b = 2.5$, $c = 5.3$ and $d = 1.1$. Their validity extends to the full stable range (see CB05 for details). For the purpose of the present analysis, the CB05 formulation has been implemented as a test version into the COSMO model, being enabled only in case the surface layer is statically stable ($Ri_b \geq 0$). A smooth transition with the operational solution is achieved by a linear weighting function in the range $0 \leq \xi \leq 0.1$, where differences between the two schemes are marginal.
In the LTG formulation, the drag and bulk transfer coefficients are defined as:

$$C_{0A}^{\varphi} = \frac{\kappa^2}{ln\frac{z_A}{z_0} ln\frac{z_A}{z_x}} f^{\varphi} \tag{4.14}$$

where $z_x = z_0$ and $z_x = z_h$ are the roughness length values for momentum and for scalars respectively. z_h is set to the minimum between z_0 and $0.1m$. The semi-empirical stability functions f_{0A}^{φ} employed when $Ri \geq 0$ are:

$$f^M = \frac{1}{1 + 10Ri_b(1 + 5Ri_b)^{-1/2}} \tag{4.15}$$

$$f^H = \frac{1}{1 + 15Ri_b(1 + 5Ri_b)^{+1/2}} \tag{4.16}$$

The LTG formulation had been run operationally until 2001 in the COSMO model and it can still be optionally enabled for comparison purposes (Doms et al., 2011).

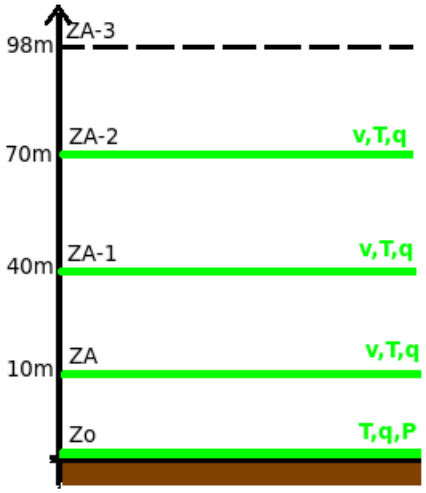

Figure 4.1: Schematic representation of the vertical levels in the SC experiment. The letters in green are the measured variables that are introduced as forcing at the respective levels (v, T, q, P stand respectively for wind vector, potential temperature, specific humidity and surface pressure).

4.3 Single Column experiment

4.3.1 Experimental set up and data

The single column (SC) mode of the COSMO model enables to set up "forced" model-runs, meaning that the vertical and temporal interpolations of selected measurements replace the model variables at specified vertical levels for each timestep of the computation. This facility allows to test the characteristic of specific model components compared to measurements, as the main influencing variables of such components can be prescribed (independently on feedbacks with other potentially erroneous parts of the model).
For that purpose, the SC model is forced by measured estimates of the following model variables: $\mathbf{v}$, θ and q at the levels z_0 and z_A. Additionally, the model is forced by these variables also at the two model levels above z_A (see Figure 4.1), where they are required by the turbulence scheme for the calculation of the turbulent velocity scale at level z_P. Apart from the setting $\mathbf{v}(z_0) = 0$, estimates of θ and q at the z_0 level are derived (through a methodology explained in the next) at the canopy top (assuming negligible variation between the values at z_0 and the canopy top, which should be on the order of cm since the canopy is a grass cover).
The transfer and turbulence schemes are guided by such estimated variables in order to derive the surface fluxes for momentum and heat. Finally they are directly compared with their respective observed values.

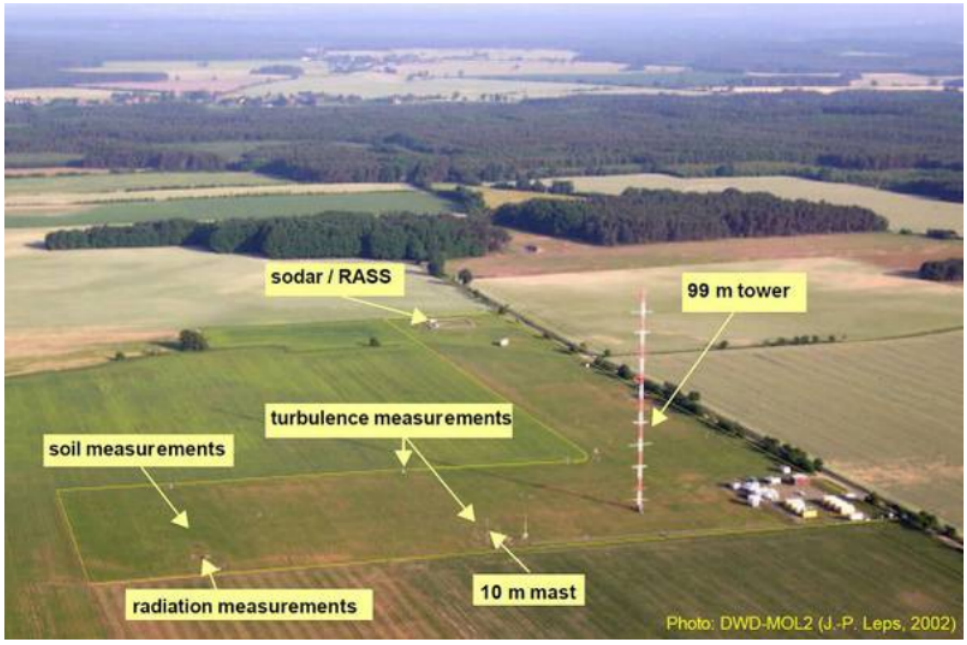

Figure 4.2: Lindenberg supersite measurement field

The measurements from the Lindenberg supersite station, located at 52.21 N, 14.12 E in a flat grassy area are selected for this SC experiment. The station is provided with mast-mounted instrumentation for sampling wind, temperature and humidity at 10, 20, 40, 60, 80 and 98 m every 10 minutes (Figure 4.2). Traditional near-surface measurements of temperature and humidity at 2m are provided at the same rate, as well as radiation observations close to the surface. Moreover, two sonic anemometers (together with high frequency registrations of temperature and humidity), located at 2.4m height have been used for eddy-correlation measurements of turbulent flux densities. These instruments are sited at the eastern and western edge of the uniform grassland area, in order to record data representative both for westerly and easterly wind directions. The sampling time for eddy correlation was 30-min, while 60-min averages of the flux densities are later performed for comparison with the simulated fluxes. Data covering the whole July 2013 are used. This period was characterized by anticyclonic conditions interrupted by few frontal passages. The analysis of the Obukhov stability parameter ξ derived from the eddy-correlation data has indicated that 17% of the full-applicable dataset belongs to moderately stable stratification ($0.02 \leq \xi \leq 0.6$) and about 24% to very stable stratification ($\xi \geq 0.6$), following the stability classification of Sorbjan and Grachev (2010).
The roughness length z_0 is derived several times during July 2013, by wind-profile regression in neutral conditions. Values range between 0.01m and 0.04m, depending on the grass height. In the present analysis, the constant value equal to the mean value from the full dataset ($z_0 = 0.025m$) is used along the whole month .

The lowest SC levels are chosen at 10m, 40m and 70m in order to minimize when comparing with observations. An additional not forced level at 98m height is included in order to avoid high vertical gradients at the model top, as non-penetrative upper boundary conditions (i.e. fluid velocity normal to the wall is set to 0, but the fluid velocity parallel to the wall is unrestricted) are set. At the surface, the forcing temperature is derived from infrared radiation measurements, by assuming an emissivity of $\epsilon = 0.96$, providing a top-of-the-canopy temperature estimate associated to the level z_0. As surface humidity is not measured directly, it is estimated by inverting the bulk flux-gradient relationships, using the measured values of sensible and latent heat fluxes, surface temperature as well as temperature and humidity at 2m as input. In order to avoid undesirable self-correlation effects for the flux verification, the latent heat flux, being highly dependent on skin moisture, was not included in the verification. Vice versa, the sensible heat flux is directly influenced by near surface moisture only through its modulation of virtual temperature (used for the calculation of air density or buoyancy forcing of turbulence), and indeed, sensitivity tests on the sensible heat flux with varying skin moisture evidenced only a marginal impact (not shown).
Forced SC runs in the described manner are performed using the transfer and turbulence schemes of the COSMO model (the turbulence scheme is necessary to compute the transfer velocity scale values at z_0 and z_P), as well as the LTG semi-empirical formulation and the CB05 empirical formulation. Since the lowermost measurements are associated with the z_0 level (assumed negligible differences between z_0 and the canopy top), rather than with the rigid surface, the effects due to roughness sub-layer are excluded in the observational dataset, thus they do not need to be described by the transfer formulation. Hence, in this experiment $C^{\varphi}_{0A} = C^{\varphi}_{SA}$ (see eq. 4.6).

4.3.2 Single Column experiment results

In the SC experiment the operational configuration includes that:

1. one of the scale interaction terms in the TKE equation is active, i.e. the thermal circulation term

2. all the turbulence enhancing measures are active.

The operational formulation of the transfer scheme of the COSMO model and the two MOST based schemes (LTG and CB05) behave approximately similarly in simulating $\boldsymbol{\tau}$ and SH under near neutral and weakly stable regimes (Figure 4.3). However, large differences are manifest at higher thermal stability, where a marked overprediction of the fluxes by the operational formulation of COSMO is evident.

Since the simulated vertical gradients correspond to the observations by construction of the SC setup, the analysis of the surface fluxes can be recast into an analysis of transfer coefficients (compare with eqs. 2.6-2.8). In this respect, the overestimation of the surface fluxes is highlighted in Figure 4.4, showing C^{φ}_{0A} as a function of the bulk

Richardson number Ri_b:

$$Ri_b = \frac{g}{\theta_0} \frac{(\theta_A - \theta_0)(z_A - z_0)}{|\boldsymbol{v_A}|^2} \tag{4.17}$$

which is completely determined by the observations.

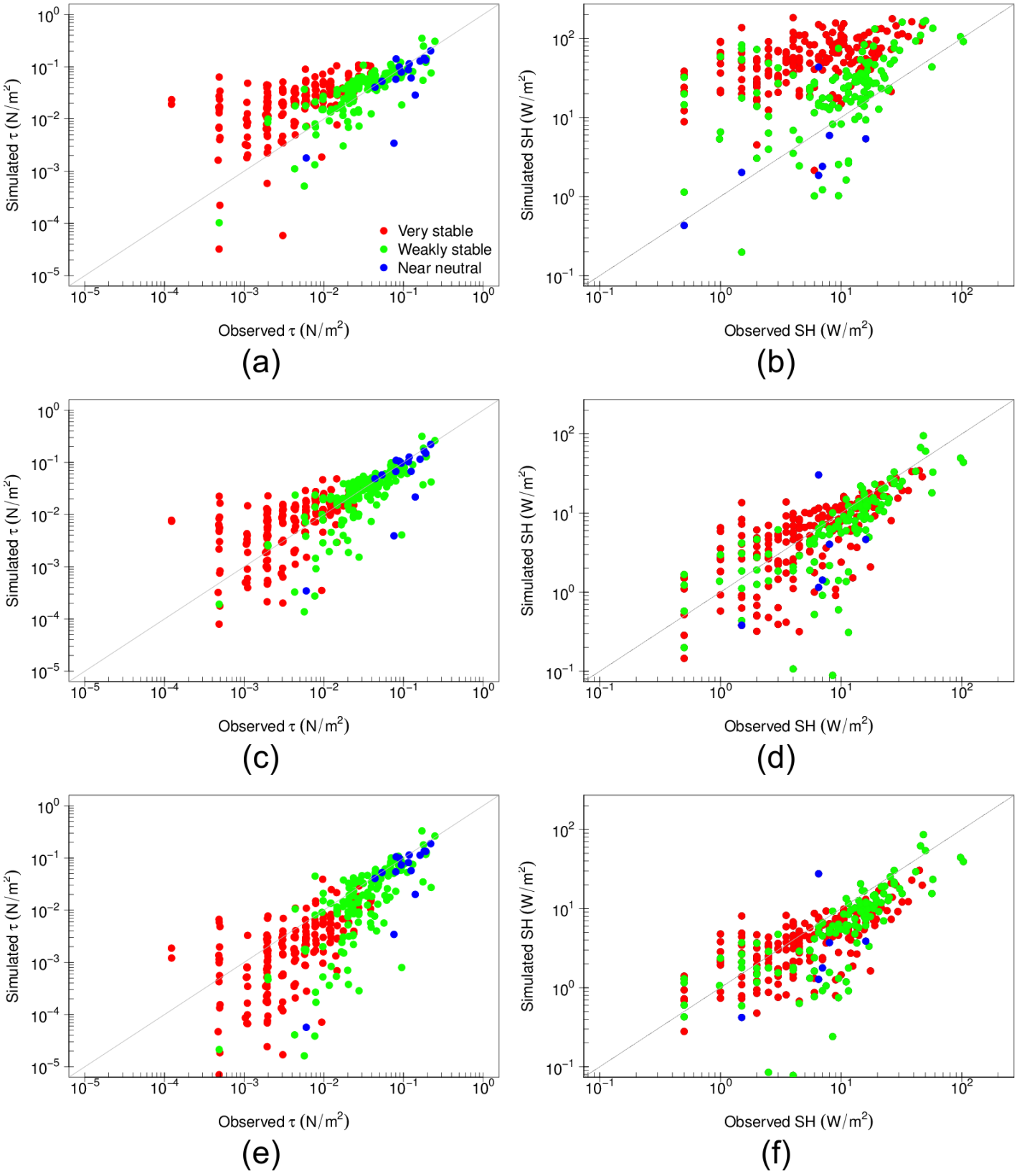

Figure 4.3: Simulated surface momentum stress (left) and sensible heat flux (right) using the SC mode and applying alternatively the operational surface layer scheme (top), the LTG scheme (middle) and the CB05 scheme (bottom) in comparison with the observations. Data are coloured according to the observed stability.

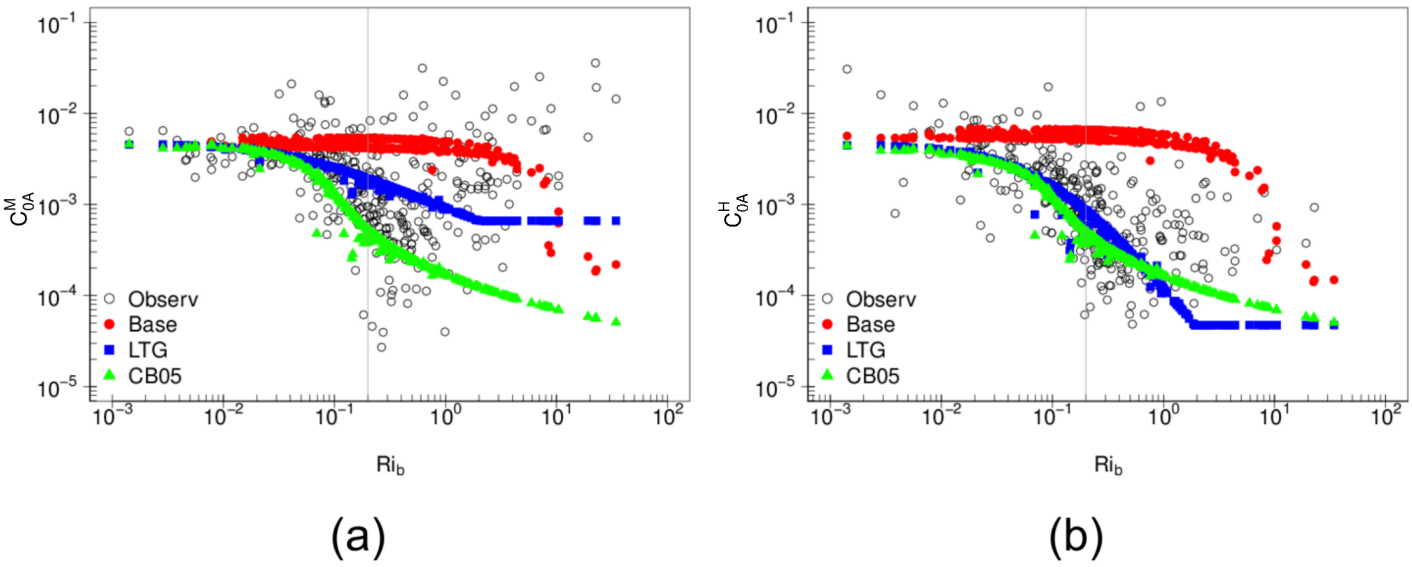

Figure 4.4: Drag (a) and bulk (b) transfer coefficients as a functions of Ri_b, simulated by the SC mode applying the operational surface layer scheme (labelled 'Base'), as well as LTG and CB05. Data derived from the observations by inverting eq. 2.6-2.7 are also plotted. Vertical gray line at Ri_b indicates the critical value of intense stratification

For the stable regime and especially at super-critical Ri_b numbers, the operational formulation leads to exchange coefficients only scarcely dependent on the stability, compared to both data computed by the MOST based reference schemes and those derived directly from the observations. Indeed, the operational version shows C_{0A}^{φ} being constant for $Ri_b \geq 0.5$ until reducing at very high Ri_b values, down to a minimum value of about $C_{0A}^{\varphi} = 10^{-4}$ at $Ri_b = O(10)$. In contrast, both the MOST based schemes drop off at lower Ri_b values and show a stronger asymptotic tendency. In the LTG case, the decrease of the transfer coefficients is limited by a minimum value, preventing the simulation from air-to-surface decoupling. At high Ri_b numbers, LTG also shows a larger transfer coefficient for momentum exchange decreasing proportionally to $Ri_b^{-0.5}$, compared to those for heat exchange declining by $Ri_b^{-1.5}$, see eq. 4.15 and 4.16. This behaviour is a feature of the LTG scheme. It is not compatible with the pure empirical formulation, which rather evidences a similar dependency of the transfer coefficients on Ri_b for both the momentum and heat (Viterbo et al., 1999). Actually, the Lindenberg observations confirm a stronger exchange efficiency for momentum compared to heat above, say, $Ri_b = 1$ (Figure 4.4), coherently with several field, laboratory and LES experiments performed in very stable boundary layers (Luhar et al., 2009; Anderson, 2009; Grachev et al., 2007; Zilitinkevich et al., 2007). This feature is generally associated to non-stationarity submesoscale motions (Mahrt, 2010), such as internal gravity wave bursts (Luhar et al., 2009), which are not accounted for by pure empirical MOST formulations. Hence with regard to the Lindenberg data, turbulent transfer for high

Ri_b number is on average best simulated by the LTG scheme, reducing on the one hand the underprediction of surface momentum stress shown by the CB05 formulation, and avoiding on the other hand the overprediction by the operational scheme (Figure 4.3).

Stability dependency of the operational transfer coefficients

In the operational scheme, the transfer coefficients can be expressed in the following formula by factorizing the diffusion coefficient at z_0 level $K_0^\varphi = \kappa z_0 u_0^\varphi$ in eq. 4.6:

$$C_{0A}^\varphi = \frac{K_0^\varphi}{|\boldsymbol{v_A}|\lambda_{0A}^\varphi} \tag{4.18}$$

In this notation, the function λ_{0A}^φ (called resistance length due to its lenght dimension) contains the stability dependency of the vertical u^φ profile in the inertial resistance:

$$\lambda_{0A}^\varphi = \frac{z_0}{1-\gamma} \ln \frac{z_A}{z_0 + \gamma(z_A - z_0)} \tag{4.19}$$

Figure 4.5 shows the dependency of each component of eq. 4.18 on the stratification expressed as Ri_b number. Interestingly λ_{0A}^φ shows only a marginal dependency on Ri_b, with marked upper and lower boundaries, due to the γ limit in eq. 4.3 (Figure 4.5,a). Regarding the other factors of C_{0A}^φ (Figure 4.5,b-c), the reduction of K_0^φ with increasing Ri_b cancels out in the calculation of C_{0A}^φ to the most part up to approximately $Ri_b \leq 5$, since a drop of the same magnitude is present in the lowest level wind speed $|\boldsymbol{v_A}|$. As a consequence, the operational version of the transfer scheme shows a tiny decay of the transfer fluxes with increasing stability compared to the local measurements. Beyond the limits on γ function, which appear to constrain the resistance lenght (Figure 4.5,a), also the turbulence enhancing measures can play a role in reducing the stability dependency of the transfer coefficients. Indeed the turbulence scheme defines the velocity scales values u_0^φ and u_P^φ, which then enter into the K_0^φ and K_P^φ formulations (see eq. 2.12). Among the measures active in stable stratified conditions (see Chapter 3), the following ones are herein experimentally reduced/removed in order to test the sensitivity of the transfer coefficients:

1. reduction of K_{min}^φ, from 0.4 to 0.001 $m^2 s^{-1}$,
2. removal of the lower limit of TKE forcing sum,
3. switching off the thermal circulation term in the prognostic TKE equation, i.e. the scale interaction term treating the subgrid thermal heterogeneity of the surface[2].

[2]The thermal circulation term is included in this list since currently it is activated independently on the terrain heterogeneity despite meant to account for subgrid surface thermal inhomogeneity. Therefore, it behaves as a turbulence enhancing measure over homogeneous cell (see section 3.1)

All these three measures were enabled only at level z_P, while at z_0 level, TKE equation is solved diagnostically and the computation is less restricted. In addition to them, it is tested the substitution of γ limits in eq. 4.3 by a less restrictive solution, directly avoiding negative arguments of the logarithm function of the inertial resistance (i.e. eq. B.1.1).
The stability dependency of the calculated transfer coefficients is not significantly influenced by any of the tested actions: neither by a singular one, nor by any combination. This is evidenced in Figure 4.6,a showing only those combinations of the tested modifications causing the largest effect. Similarly, u_0^φ is only slightly affected by actions like removing γ limits, reducing K_{min}^φ and switching off the thermal circulation term. Nevertheless, their combination shows a large impact on u_P^φ, which declines a couple of orders in magnitude at high Ri numbers (Figure 4.6,c). The reason is that the TKE equation at z_P level is directly affected by the K_{min}^φ limit and the thermal circulation term (and the sensitivity of the turbulence scheme to them is high, as shown in section 3.1). Clearly, the stability dependency of u_P^φ is not properly integrated in the transfer scheme.

The weakest point in the transfer scheme formulation is the use of a linear interpolation function between the two nodes u_0^φ and u_P^φ, which is justified only in case of neutral stratification. In this case, it ensures the accordance between the operational inertial resistance and the MOST formula in eq. 4.5. Aside from neutrality, the linear assumption can be inaccurate. The turbulent velocity scale based on MOST can be written for all stability regimes as:

$$u_{MOST}^\varphi(z) = \frac{u_*}{\phi^\varphi(\xi)} \tag{4.20}$$

The simplest expressions of $\phi^\varphi(\xi)$ under stable stratification is from Businger et al. (1971) and reads: $\phi^\varphi(\xi) = 1 + \alpha\xi$ with α an empirical coefficient. If it is introduced in eq. 4.20, the turbulence velocity scale features a hyperbolic dependency on z:

$$u_{MOST}^\varphi(z) = \frac{u_*}{1 + \alpha z L^{-1}} \tag{4.21}$$

Hence, assuming a hyperbolic vertical function of u^φ interpolating between the nodes u_0^φ and u_P^φ, it is possible to derive a new inertial resistance for stable stratification, by introducing eq. 4.21 in eq. 2.11 and integrating it. The unknown values u_* and $\alpha \cdot L^{-1}$ are expressed as functions of u_0, u_P, z_0, z_P, which convey the stability information from the turbulence equations (solved at levels z_0 and z_P) to the transfer scheme. The derived formula, valid only for stable stratification, is:

$$r_{0A}^\varphi = \frac{1}{k[u_0 + \frac{u_P - u_0}{1 - u_P z_P (u_0 z_0)^{-1}}]} [ln\frac{z_A}{z_0} + \frac{(u_P - u_0)(z_A - z_0)}{u_0 z_0 - u_P z_P}] \tag{4.22}$$

where the superscript $\varphi = M, H$ is omitted for brevity. When the stratification is neutral, eq. 4.22 corresponds to the logarithm relation in accordance with MOST (eq.

	$\tau[10^{-3}N/m^2]$		$SH[W/m^2]$	
	ME	RMSE	ME	RMSE
Base	15	29	-29	40
LTG	-0.5	20	2	7
CB05	-7	23	3.9	8.5
Test K_{min}+ SGS off $+\gamma$	3	25	-12	23

Table 4.1: Statistical indices of the surface fluxes simulated by the SC using either the operational scheme (labelled 'Base'), LTG, CB05 or the operational version combining: the modified profile function of the velocity scale, a reduced K^{φ}_{min}, the less strict limits on γ and the switching off of the thermal circulation term (labelled 'Test K_{min}+ SGS off $+\gamma$')

4.5). The singularity of eq. 4.22 in $u_0 = u_P z_P z_0^{-1}$ is very unlikely to occur, especially if $z_0 \ll z_P$ as in this experiment (however a treatment valid for all kind of surface needs to be found). The use of Businger et al. (1971)'s functions is further justified by their consistency with the Mellor and Yamada (1982)' scheme (Mellor, 1973), on which the turbulence scheme of COSMO is based.
The previous sensitivity study of the operational transfer scheme to the limits and mixing enhancement options is now replicated using the modified inertial resistance in eq. 4.22 every time the stratification is stable. The transfer coefficients C^{φ}_{0A} experience now a pronounced stability reduction when all the previously mentioned measures are reduced/removed (K^{φ}_{min} reduced, γ limit removed and thermal circulation term switched off), As shown in Figure 4.7. The stability dependency of u^{φ}_P to this combination of options now properly affects the transfer scheme in the case of stable stratification. The large scatter of C^{φ}_{0A} indicates that the transfer coefficients are not pure function of the stability parameter Ri_b, but follow the turbulence evolution as computed by the TKE equation in the turbulence scheme. Actually, the scatter area seems quite realistic compared to the measurements collected at Lindenberg.
Notice that if K^{φ}_{min} and γ limits and the thermal circulation term are kept enabled, then the modified inertial resistance does not show any impact. Apparently, the additional mixing induced by these measures prevents the turbulence decay for increasing Ri_b. This ineffectiveness for operational applications has probably been the reason for not noticing in the past the consequences of the inertial resistance inconsistency in the official COSMO.
The statistical scores analysis in table 4.1 evidences a large improvement of the modified operational formulation (i.e. using the new inertial resistance for stable cases and disabling the subgrid scale thermal term, K^{φ}_{min} and γ limits) compared to the operational scheme in both the surface sensible heat and momentum fluxes. Despite these modifications allow the operational transfer scheme to better describe the case of stable stratification in nearly homogeneous terrain, the model version employing the LTG approach still produces the best performance in this experiment, especially in terms of

SH. CB05 approach shows slightly lower skill than LTG, as fluxes are more underestimated (in absolute value), especially for τ. The relative behaviour of CB05 with respect to LTG can be understood for τ by looking at the faster decay with increasing stability featuring the transfer coefficients in CB05 formulation with respect to LTG (Figure 4.4).

4.4 Full model experiment

4.4.1 Full model experimental set-up

In order to test the behaviour of the different surface layer formulations including all the model feedbacks and applied to the whole model domain with all types of non-homogeneous surfaces, simulations with the full 3D COSMO model are performed at the operational model domain for Italy (741 x 781 grid-points with about 2.8 km horizontal spacing and a depth of the lowest model layer of about 20m). Boundary and initial conditions are provided by ECMWF analysis and the model lead time was always 48 h starting at 00UTC each day, where only the respective second forecast day (free of spin-up effects) is used for comparison.
Verification of surface flux estimates is performed with data from the super-site station of San Pietro Capofiume located in Po valley, by considering the model grid point being nearest to the site (with a distance of 1.1 km).
Measurements of surface fluxes for momentum and heat are provided by an eddy-covariance instrumentation located 3.6m above ground and they are used as 60-min averages. Vertical sampling of wind, temperature and humidity is performed daily by a radiosonde launch at 00UTC. Besides the near-surface measurements of wind at 10m, temperature and humidity at 2m, the observations of radiation and the soil states are also available (Figure 2.7).
The analysis of the stability parameter ξ estimated from eddy-covariance revealed a relatively high occurrence of stable stratification in the surface vicinity during March 2012: 38% of 734 valid hourly data belongs to weakly stable stratification, while 8.4% are associated to very stable stratification.
In the present analysis, simulations using the operational surface layer formulation of COSMO and the best performing alternative formulation (with regard to the SC component tests) are investigated.

4.4.2 Full model experiment results

From the results of the SC test, LTG is selected to be compared to the operational transfer scheme of COSMO. In Chapter 3, it has been shown that the turbulence enhancing measures (and in particular the ones referring to the K^{φ}_{min} and the thermal circulation term) are necessary at the current COSMO model state in order to preserve the large scale scores. Given that the introduction of the modified inertial resistance formulation in the operational transfer scheme without the removal/reduction of the

N=316	$\tau(10^{-3}N/m^2)$		$SH(W/m^2)$		$T_{2m}(^oC)$		$Td_{2m}(^oC)$		$U_{10m}(m/s)$	
	ME	RMSE	ME	RMSE	ME	RMSE	ME	RMSE	ME	RMSE
Base	32	64	-2.4	25	2.4	3.3	3.3	4.3	0.4	1.1
LTG	29	67	-0.35	27	1.8	2.9	1.4	3.0	0.6	1.5

Table 4.2: Statistical indices of the surface fluxes and variables at the synoptic levels under stable observed conditions ($\xi \geq 0.02$) simulated by the 3D hind-cast using the operational scheme (labelled 'Base') and LTG scheme

mixing enhancement measures and the limits in the transfer and turbulence schemes does not change the simulation, it is meaningless at the moment to test the combined effect of all these actions together with the modification of the resistance formulation in a full model experiment.
The analysis of the 3D hind-cast experiments at the grid point associated to San Pietro Capofiume station provides similar results to the SC test in terms of transfer coefficients (Figure 4.8). Indeed, the operational transfer scheme yields to a less pronounced drop of C_{SA}^{φ} at high stability with respect to LTG formulation. The differences already start at $\xi \geq 0.1$, reaching about one order of magnitude and more at $\xi \geq 1$. Here however, in the operational version, C_{SA}^{H} values are smaller than C_{SA}^{M} by about $2 \cdot 10^{-3}$ close to neutral stratification. This is due to the consideration of the roughness sub-layer resistance for scalars r_{S0}^{H} which is added to the inertial resistance r_{0A}^{H}. In LTG scheme, the roughness sub-layer is represented by the use of the specific roughness length for scalars $z_h = 0.1m$ (while for momentum $z_0 = 0.3m$ for this grid point). The difference between the two treatments appears marginal.
Differently from the SC outcome, in terms of surface fluxes the performance of COSMO is roughly independent of the transfer scheme used under stable stratification. Indeed in both cases, the fluxes are overestimated (in absolute value) of the same magnitude (Table 4.2). The only difference is a slightly worse performance by using the operational transfer scheme when the stratification is very intense, as it can be seen by comparing the flux frequency distributions at different observed stabilities in Figure 4.9.

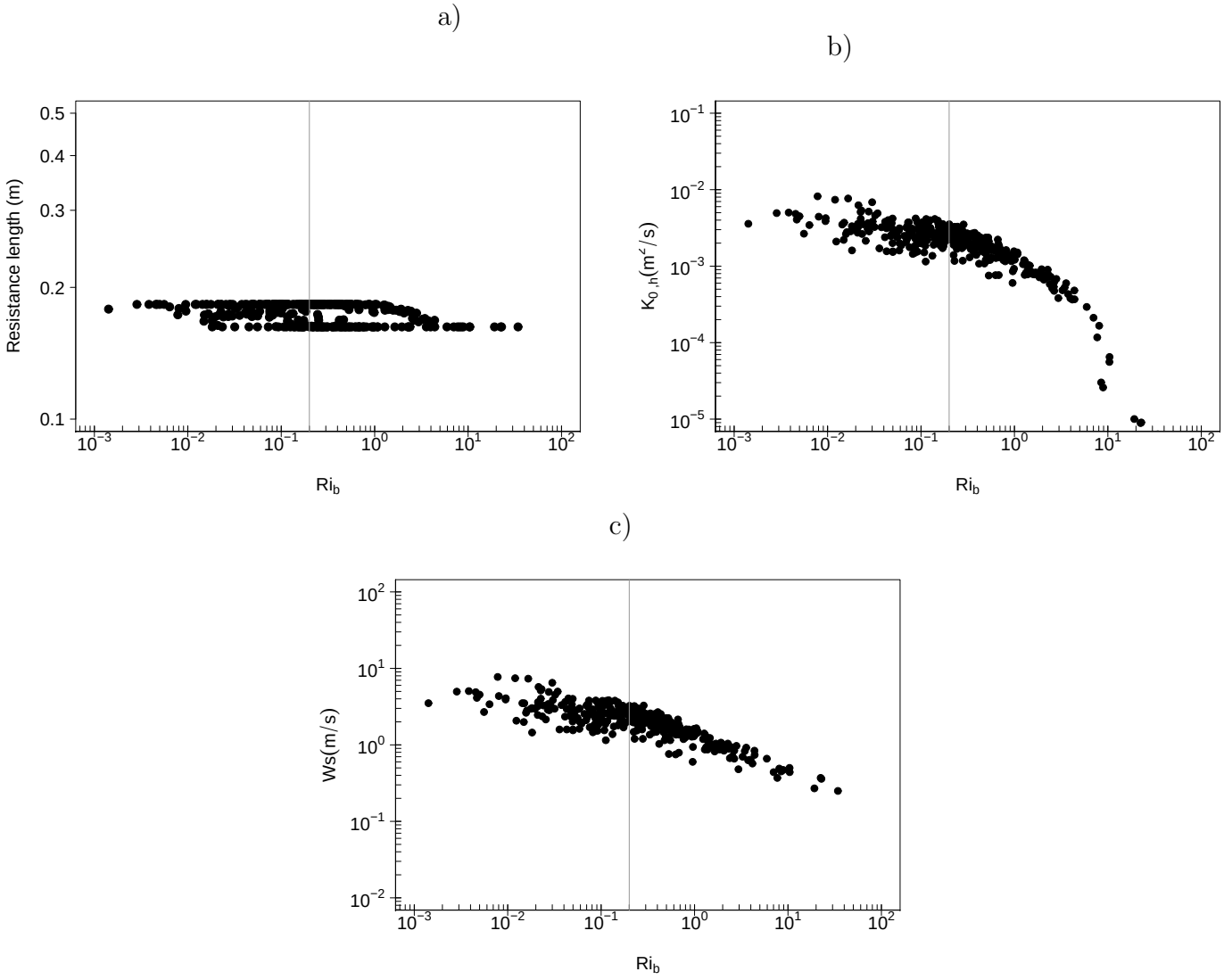

Figure 4.5: Total resistance components: resistance length of the inertial sub-layer (a), turbulent heat diffusion coefficient (b), wind speed at the first model level (c) simulated by the SC component test. Vertical gray line at Ri_b indicates the critical value of intense stratification

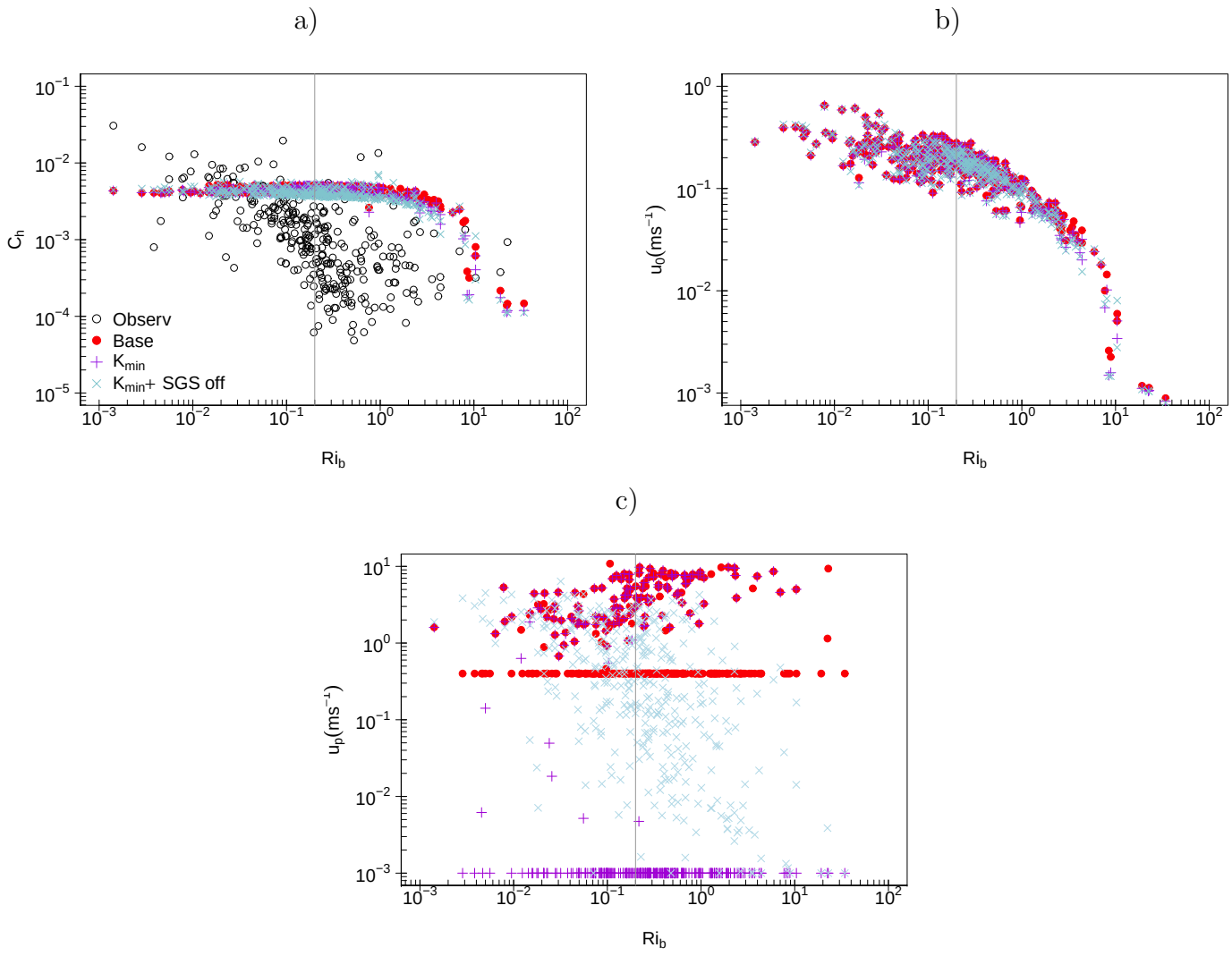

Figure 4.6: Bulk transfer coefficient (a), velocity scales at level z_0 (b) and z_P (c) derived in the SC mode using the operational surface layer scheme (labelled 'Base'), the same scheme modified by reducing $K_{min}^{M,H}$ and removing γ limits (labelled '$K_{min}+\gamma$') and the latter with the removal of the thermal circulation term from TKE equation (labelled 'K_{min}+ SGS off $+\gamma$')

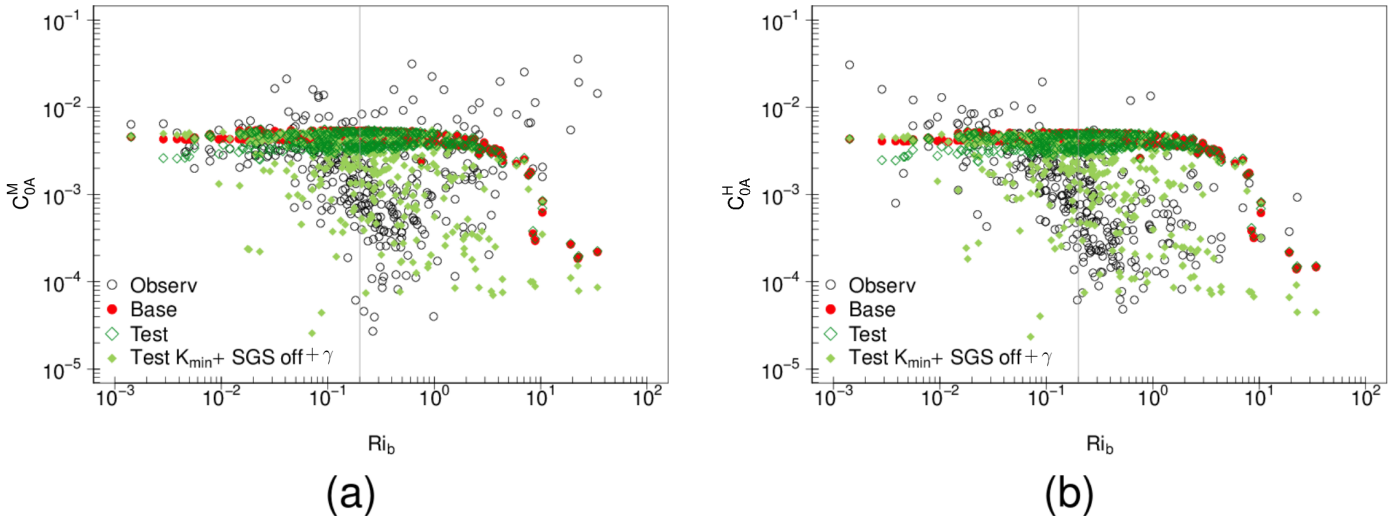

Figure 4.7: As in Figure 4.4, but applying the model version with the modified profile function of the velocity scale (labelled 'Test') or the latter with a reduced K^{φ}_{min} and the removal of γ limits and of the subgrid thermal circulation term (labelled 'K_{min}+ SGS off +γ').

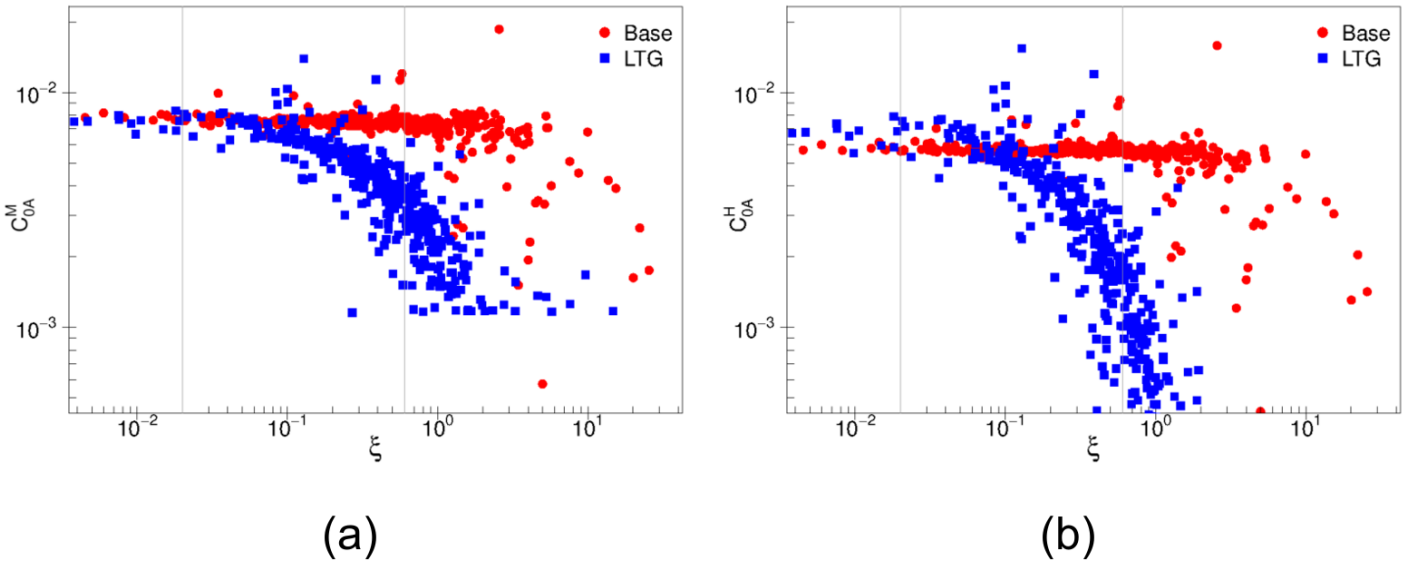

Figure 4.8: Drag (a) and bulk (b) transfer coefficients as a function of the observed ξ simulated by the full model version applying the operational (labelled 'Base') or the LTG transfer scheme, both evaluated for the model grid point closer to the station San Pietro Capofiume. Vertical gray lines indicates the transition between near-neutral, weakly stable and very stable stability

This behaviour is explained by the negative feedback between the surface fluxes and the vertical profiles in the surface layer in a full model run. Originally, the smaller exchange coefficients simulated using the LTG scheme produce more decoupled surface layers, with larger vertical gradients compared to the case of using the operational scheme. By this, the wind speed at the lowest model level and the lapse rate between the surface and the lowest model level increase, as it is verified in Figure 4.10. The larger wind speed lapse rate increase the surface fluxes (in absolute value). Consequently, the better performance in terms of C^{φ}_{SA} by LTG cancels out.

Apart from this feedback, the wind speed at the lowest model level is overestimated independently of the transfer scheme applied. This is a major issue in terms of surface fluxes overestimation, as $\mathbf{v_A}$ is present in both the flux formulations. This error can be related to the stable boundary layer over-mixing.
Table 4.2 reports also the scores of the diagnostics of the near surface parameter. In average under stable stratification, wind speed at 10m is more overestimated by the LTG approach than by the operational scheme. The near surface wind level corresponds to the height of the lowest model level over this grid point. Therefore, the diagnostic algorithm is ineffective and the two wind values correspond. By this, the near surface verification confirms with a larger statistics the consideration about wind speed at the lowest model level. On the other side, the dry-bulb and dew-point temperatures at 2m are better simulated by LTG scheme than by the operational scheme (Table 4.2). In part this is a consequence of the flux-gradient feedback, yielding to smaller lapse rate in the run using the operational scheme, and in part it depends on the specific diagnostic algorithm used in the two transfer scheme (i.e. LGT and the COSMO operational scheme).

4.5 Conclusions

A detailed diagnostics of the surface fluxes simulation by the operational transfer scheme of the COSMO model is presented for the condition of stable thermal stratification above homogeneous surface. This scheme differs from the widely used MOST based formulations, as it provides an intrinsic consistency with the whole vertical diffusion formulation, by a direct integration of the operational turbulence scheme (based on Mellor and Yamada, 1982) and the surface layer scheme. In practice, the integration is performed via a vertical interpolation of the turbulent velocity scale between two supporting vertical levels within the where the turbulence scheme is run. As an advantage, this formulation automatically introduces the generalizations of the turbulence scheme into the transfer formulation, contributing to processes that typically are not considered in traditional schemes (e.g. related to subgrid scale inhomogeneities). The drawback is that the turbulence enhancement measures still present in the turbulence scheme get applied in the surface layer scheme as well.
Since MOST based formulations are valid above homogeneous surfaces, it is herein

tested whether the COSMO approach can be reduced to MOST results for stable stratification, and thus can be regarded as a potential extension of that traditional approach. The performance of the operational transfer scheme is firstly tested in a stand alone mode, employing the single column version of COSMO in combination with observations collected at Lindenberg site (Germany). Secondly, the formulation is examined in the fully coupled model version, evaluating the simulation with measurements at the station of San Pietro Capofiume (Italy). As the measurements at both measurement sites refer to the simplest case of homogeneous surface, the model simulations is expected to be coherent in both the case studies.
The analysis of the transfer scheme in a stand alone mode evidences that the operational transfer scheme of COSMO is only weakly dependent on thermal stratification in stable regime, yielding overestimated momentum and sensible heat fluxes at high Ri_b numbers. Vice versa, both of the empirical and semi-empirical MOST based formulations considered (respectively CB05 and LTG) show a better agreement with the observations. Compared to them, the operational configuration of the COSMO transfer scheme appears unable to describe in a satisfactory manner the stable surface layer above a homogeneous surface. It is demonstrated that this undesired behaviour is due to two circumstances:

1. in the operational transfer scheme, a linear interpolation of the turbulent velocity scale is used for the derivation of the transfer resistance in the inertial sub-layer at all stability regimes. This choice is in accordance with MOST only under neutral stability, while a hyperbolic interpolation is herein demonstrated the correct choice for keeping the agreement with MOST in stably stratified surface layers,

2. some turbulence enhancement measures applied to the turbulence scheme (i.e. the minimal diffusion coefficients and the inaccurately formulated scale interaction term dealing with the effect of thermal surface inhomogeneity) together with a limit in the inertial resistance formulation introduced for numerical reasons (limits to γ function), affect the dependency of the transfer coefficients on thermal stability.

If the first point is not taken into account, the stability dependence information is not conveyed from the turbulence scheme to the transfer scheme, independently of the reduction of turbulent mixing at the lowest model level. If the second point is not fulfilled, the overestimation of turbulent mixing at the lowest model level prevents the decay of the transfer exchange at high stability, independently on the stability consistency of the transfer scheme with the turbulence scheme. Only if both the conditions are fulfilled, then the operational transfer scheme approximates both the MOST based reference schemes for the tested situation. Even in this case however, the operational transfer scheme performs worse than the MOST based schemes in the stable regime over the almost homogeneous terrain case under investigation. In particular, the LTG approach results a bettering alternative to the operational transfer scheme.
In the fully coupled COSMO simulation, the feedback between surface fluxes and vertical profile within the surface layer cancels out the LTG advantage, thus the two schemes

are roughly equivalent in terms of surface fluxes. The most relevant impact is due to the overestimation of the wind speed at the lowest model level, which worsens when LTG scheme is applied. In general, this error can be related to the stable boundary layer over-mixing, and it is the main reason for the too large surface fluxes simulated (in absolute value) by COSMO under stable stratification, independently of the transfer scheme applied. Indeed, the model error due to the combined effect of the two circumstances previously described is visible only under very stable regime, where the operational unmodified scheme causes a larger overestimation of the surface fluxes with respect to LTG. In terms of near surface variables, the LTG approach produces worse wind speed at 10m and better dry bulb and dew point temperatures than the operational transfer scheme, partially due to the flux-gradient feedback and partially due to the specific diagnostics algorithm.
Finally, it should be stressed that the modified inertial resistance formulation for stable stratification can (and should) be implemented in the official COSMO code, but the consequent improvements will be fully visible in a 3D COSMO simulation only when the turbulence enhancing measures will be removed.

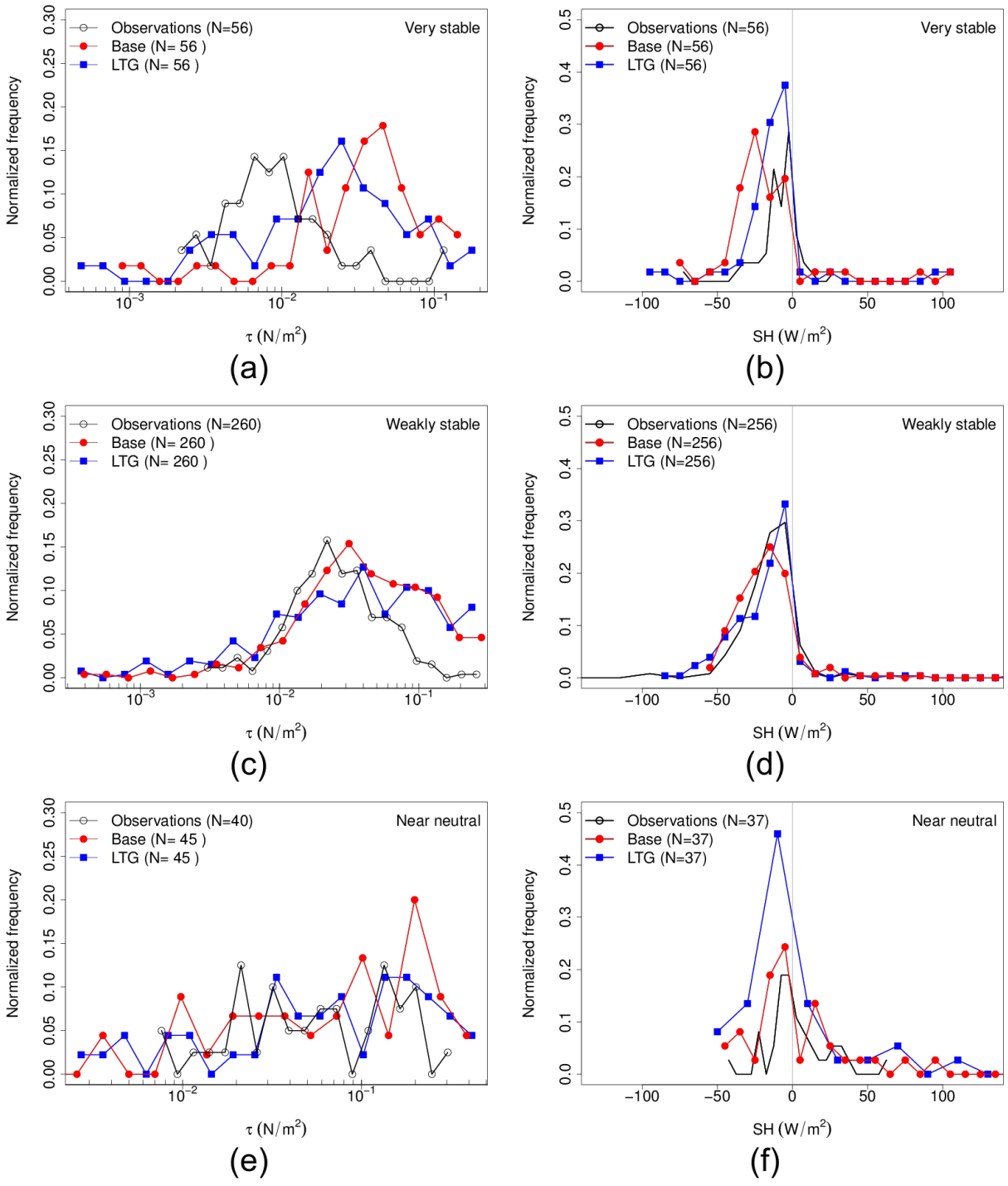

Figure 4.9: Normalized frequency distribution of the observed and simulated τ (left) and SH (right) employing the operational transfer scheme (labelled 'Base') or the LTG scheme, both evaluated for the model grid point closest to the station of San Pietro Capofiume. Data are gathered according to the observed stability intensity. Three regimes are considered: very stable stratification (top), weak stratification(center) and near neutral stratification (bottom) observed, identified respectively by the intervals $\xi \geq 0.6$, $0.02 \leq \xi \leq 0.6$, $-0.02 \leq \xi \leq 0.02$

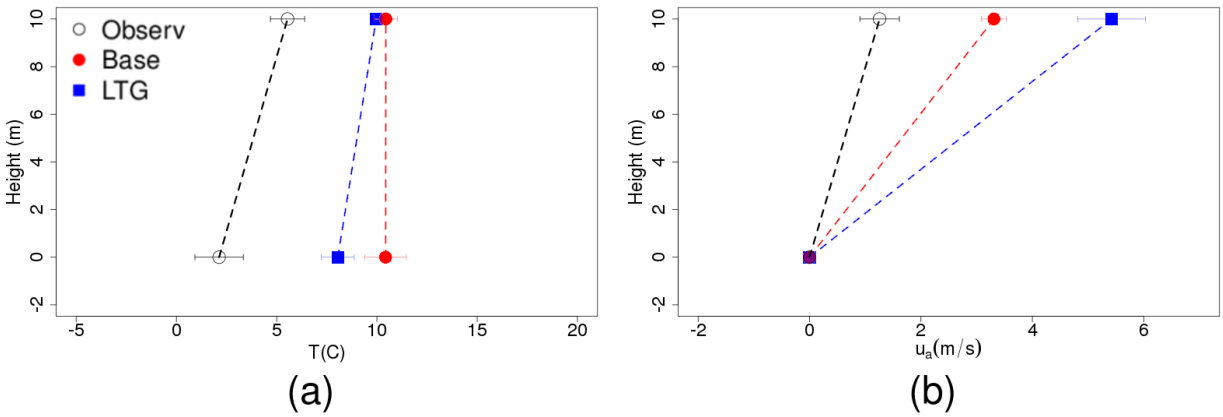

Figure 4.10: Averaged temperature (a) and wind speed (b) vertical profiles between the surface and the lowest model level (10m height) observed and simulated by COSMO using the operational transfer scheme ('Base') and LTG scheme. Only model data at the time of the radio-sounding launch are considered (31 data). Error bars express the standard error of the mean.

Chapter 5

Stable boundary layer and unresolved orography

5.1 Introduction

Mesoscale motions in the SBL include a variety of processes like cold drainage, meandering flow (i.e. the flopping around of the wind vector), internal gravity waves, horizontal roll vortices and others (a review in Mahrt, 2007). Their generation mechanisms are diverse and they can affect simultaneously the local SBL, yielding to a superimposition of several modes. Mesoscale motions extend from spatial scales just larger than turbulent eddies (for stable conditions on the order of 10m) to several kilometres (e.g. for horizontal meandering flow), with time-scales from less than a minute to one hour (Mahrt, 2007). Their spectral features show a strongly site dependency (Mahrt, 2009), as a result of the sensitivity to the surface peculiarity: small topographic features, gentle slope, roughness transitions, thermal contrast. All these issues precluded the development of a universal theory. Nevertheless, these motions are relevant in the SBL, due to the turbulence weakness.

As introduced in section 1.4.2, mesoscale processes that occur at unresolved scales require specific treatments. State-of-the-art operational NWP models attempt different approaches dealing with some orography-related and thermal heterogeneity-related processes (see section 1.4.2), which however only partially represent the real complexity. This neglect is one of the most accounted hypothesis for the operational NWP model needs for additional drag, which is currently compensated with turbulence-enhancing (long-term) measures.

In the present chapter, the focus is on the treatment of mesoscale processes associated to the Subgrid Scale Orography (SSO) in term of their effect on the turbulence in the SBL. Mainly three processes are relevant: at first, the presence of unresolved orography induces additional pressure forces to the mean flow, with a consequent increase of the drag along the orography flanks that slows down the flow and dissipates in turbulence. When the boundary layer is stably stratified, the vertical motions are suppressed, thus air sticks to the surface, enhancing this blocking effect. Under stable stratification,

a second (and secondary) mechanism is associated with the excitement of vertically propagating gravity waves. They transport momentum stress upward and can release it to the mean flow when they break. This causes a disturbance of the mean flow that decelerates, with the production of turbulence at levels where it is not expected (Nappo, 2004). A third mechanism is based on the evidence that gravity wave drag can be dissipated to about 20% of its surface value in the SBL without reaching the wave breaking point, only due to the interaction with turbulence (Grisogono et al., 1993). The drag dissipation is enhanced for gravity waves excited by narrow ridges ($\approx 100m$), a scale closer to the typical size of turbulent eddies. In fact a significant transfer of wave kinetic energy to turbulent kinetic energy is found in SBL is found experimentally (Finnigan, 1988; Finnigan et al., 1984).
In the COSMO model, the consequences on the mean flow of the first and second processes are managed by the SSO parametrization based on Lott and Miller (1997), while the third one is neglected, since a universally accepted treatment is not yet available (despite some attempts are under development, e.g. Steeneveld et al., 2008). In general in the NWP models, SSO is defined as the unresolved orography that is on horizontal scales larger than 5km (Beljaars et al., 2004), leaving aside all the smaller scales, whose impact on the mean flow are either treated by specific parametrizations (e.g. turbulent form drag from Beljaars et al., 2004) or implicitly described by an increase of the roughness length (which increments the surface stress), as in COSMO. In addition to the representation of the impact of SSO-associated processes on the mean flow, the COSMO model includes a specific treatment of their interaction with turbulence. This is a unique feature of COSMO. It is part of the STIC (Separated Turbulence interacting with Circulation) approach (Raschendorfer, 2007), which is based on the assumption that kinetic energy produced at the mesoscale by unresolved non-turbulent processes is transferred to the turbulence scale and can be considered as a source of turbulent kinetic energy. The option runs operationally at some weather services, following the results of a verification over a 2 months parallel run over the European domain (Raschendorfer, 2011). The main differences were on biases of near surface temperature, wind speed and pressure. The root mean square errors (rmse) of the three variables remained almost unchanged or improved slightly. This chapter aims at investigating the behaviour of this parametrization on the whole troposphere when the conditions are favourable to the development of stable stratification in the boundary layer, since these are the cases potentially more sensitive to the turbulence mixing increase. In particular, regions at high and low SSO are considered. The purpose is to evidence the potential capability to compensate the lack of drag in SBL, as an alternative to long-term approach. Section 5.2 gives a description of the parametrization. Two case studies are selected and described in section 5.3, while the results are reported in section 5.4.

5.2 Parameterization

The drag increment and consequent dissipation in turbulence due to the mechanisms of flow blocking and gravity wave breaking involves the transformation of mean kinetic energy in kinetic energy at the mesoscale, and subsequently in turbulent kinetic energy: at this scale it is dissipated in heat. In the COSMO model, the hypothesis from Raschendorfer (2007) of mesoscale and turbulence scale separation and interaction provides the framework for such energy transport (see section 2.2.1), as explained in the following.
The sink terms of the mean horizontal momentum related to SSO are provided by the SSO parametrization (Lott and Miller, 1997) in the following form:

$$\left.\frac{\partial \overline{\rho} u_i}{\partial t}\right|_{SSO} = \left.\frac{\partial \tau_i}{\partial z}\right|_{SSO}, i = x, y \tag{5.1}$$

In eq. 5.1, $\tau_i|_{SSO}$ is a virtual vertical flux density of horizontal momentum, which includes both the stress by the gravity-wave breaking and the flow blocking. The SSO scheme further provides a local dissipation heating term to be considered in the temperature equation. The parametrization under investigation represents the energy transport from the mean flow to the dissipation in heat. It is based on the consideration that all sink terms in the budget of the mean momentum vector are always associated to sink terms in the budget of the Mean Kinetic Energy (MKE), which in turn correspond to source terms in the budget of mesoscale circulation Kinetic Energy (CKE) according to the following formula (Raschendorfer, 2007):

$$\frac{\partial MKE_{SSO}}{\partial t} = \overline{u}\frac{\partial \tau_{SSO}}{\partial z} = -\frac{\partial CKE_{SSO}}{\partial t} \tag{5.2}$$

Formally, $\partial_t CKE_{SSO}$ contains also the energy production by the gravity waves, which takes place below the SSO effective height together with the blocking and which is then transformed in drag where the waves break. Neglecting the remote character of this part of CKE release, $\partial_t CKE_{SSO}$ describes the direct conversion of MKE into CKE, as wake production. As those motions typically are not in accordance with the closure assumptions of a turbulence scheme, they cannot be treated as a part of the latter. In the framework of STIC approach, the $\partial_t CKE_{SSO}$ can be treated as an additional production term of TKE, which intensifies the vertical turbulent mixing for all prognostic variables whenever the SSO scheme is active. The additional term in TKE equation (eq. 2.1) is one additive component of f^C forcing and it is formulated at every k model level (indicated as subscript) as:

$$f^C_{SSO} = \frac{1}{q}\frac{g_k \Delta p_k + g_{k-1}\Delta p_{k-1}}{\Delta p_k + \Delta p_{k-1}} \tag{5.3}$$

where $q = \sqrt{2TKE}$, Δp_k is the atmospheric pressure difference between the top and bottom of k level and the function g_k:

$$g_k = -\overline{u}\frac{\partial \tau_{SSO}}{\partial z} \tag{5.4}$$

Only positive values of f^C_{SSO} are introduced in the TKE equation. Therefore, the additional forcing term is considered only if the wind tendency due to SSO ($\partial_z \tau_{SSO}$) is opposed in sign to the total wind (for each component), i.e. cases in which the SSO scheme slows down the mean flow. Moreover, the more intense the total wind and the SSO related wind tendency are, the more TKE forcing is produced.

5.3 Data and methods

The parametrization behaviour is investigated by comparing a COSMO 3D simulation repeated respectively enabling and disabling the summation of f^C_{SSO} term in the TKE equation. Since the term depends on the wind tendency associated to SSO, it is computed only with model horizontal resolution coarser than 5km. The horizontal grid spacing chosen is 7km. The vertical dimension is discretized in 40 model level. The integration domain is in Figure 2.1. Initial and boundary conditions come from ECMWF analysis, with boundary conditions one-way nested and updated every 6 hours. The simulated case study is the winter three-day period characterized by anticyclonic conditions over Northern Italy described in section 2.4.1 in which the meteorological conditions were favourable to the development of SBL in the Po Valley.

5.4 Results

5.4.1 Effect on the atmospheric profiles

In the case study, the geostrophic flow comes from North-North-West and passes over the Alps. Figure 5.1 shows a vertical cross section approximately aligned with the geostrophic wind of the simulated wind speed and potential temperature. In the simulation without the additional TKE source term enabled, there is an intense wind above the mountain chain, with a maximum between 4 and $6km$ (Figure 5.1). Aloft, particularly on the lee of the highest ridge, a region of strong shear, with largest perturbations at about the top of the troposphere ($\approx 9-13km$ height) and in the stratosphere in the range $\approx 17km - 20km$, indicates the propagation of a non-hydrostatic gravity wave [1]. At the same levels, also the potential temperature is perturbed. In particular, the disturbance is close to convective instability (iso-theta lines are almost vertically oriented) at the first level of wave steepening (i.e. $9-13km$). In the lee of the Alps, the down flow along the slope weakly interacts with the stable boundary layer extending over the Po valley.

[1] A non-hydrostatic gravity wave differs from a hydrostatic gravity wave by the propagation downstream to the mountain instead being localized vertically above the surface flow perturbation

Figure 5.1: Vertical cross section of potential temperature (solid lines, contour interval $5°C$) and horizontal wind speed (colours) in the run without the SSO-related source of TKE enabled. Bottom plot is a zoom in the lee of the Alps. The section is parallel to the geostrophic flow (from North-NorthWest), in the plot from left to right. Time: 08/01 01:00. The two dotted lines correspond to the profiles plotted in Fig. 5.3

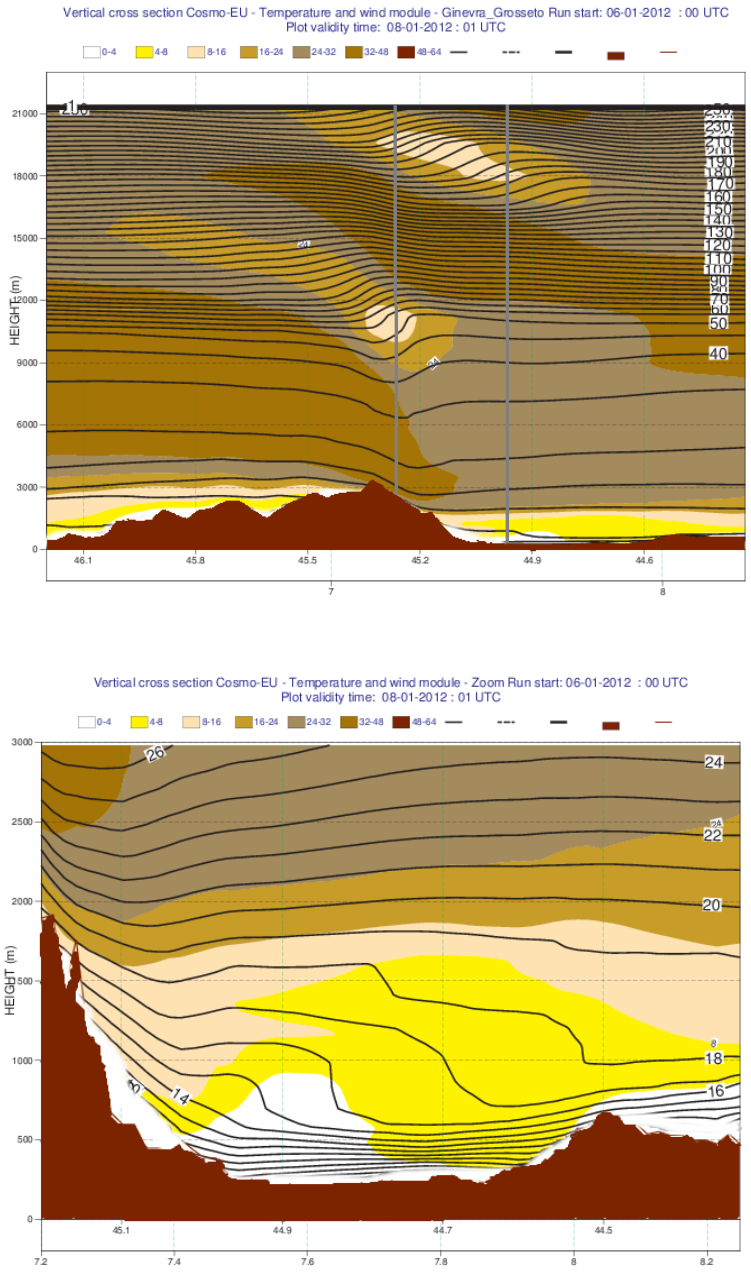

Figure 5.2: Cross vertical sections of the difference in TKE generated by the term activation (difference between the two simulations). Flow is from left to right

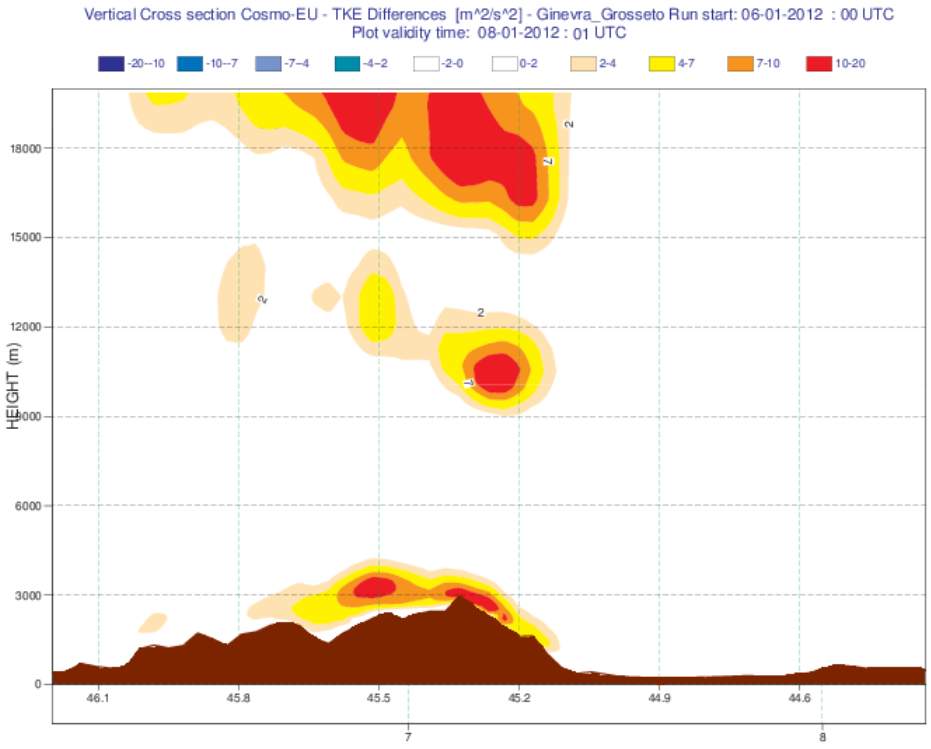

The activation of the SSO-related source of TKE produces in the second simulation a direct increment of TKE, with the highest increase (more than $10 m^2/s^2$) above the mountain chain (see the difference between the simulation with the term less the control in Figure 5.2), where SSO is largest. Indeed generally, regions characterized by high resolved orography present also elevated SSO. TKE increments are localized at the lowest model levels and at the two levels of wave perturbation, as shown in Figure 5.2. At the lowest model levels, the TKE modification refers to the blocking component of $\tau_i|_{SSO}$, while the other two regions refer to the gravity wave component. Despite non visible in Figure 5.2, TKE increases of about 30% also over points at low SSO, in the surface vicinity. It is shown by the vertical profile of TKE plotted in Figure 5.3,d above a point featuring low SSO in the lee of the mountain (identified by a gray line in Figure 5.1). This indicates that the additional contribute of the SSO-related term is relevant, despite being small, when compared to the scarcely turbulent SBL.

In general, the increase of TKE is associated to an increment of turbulent drag and a reduction of wind shear and thermal stratification due to the enhanced vertical mixing. Indeed at the point at high SSO:

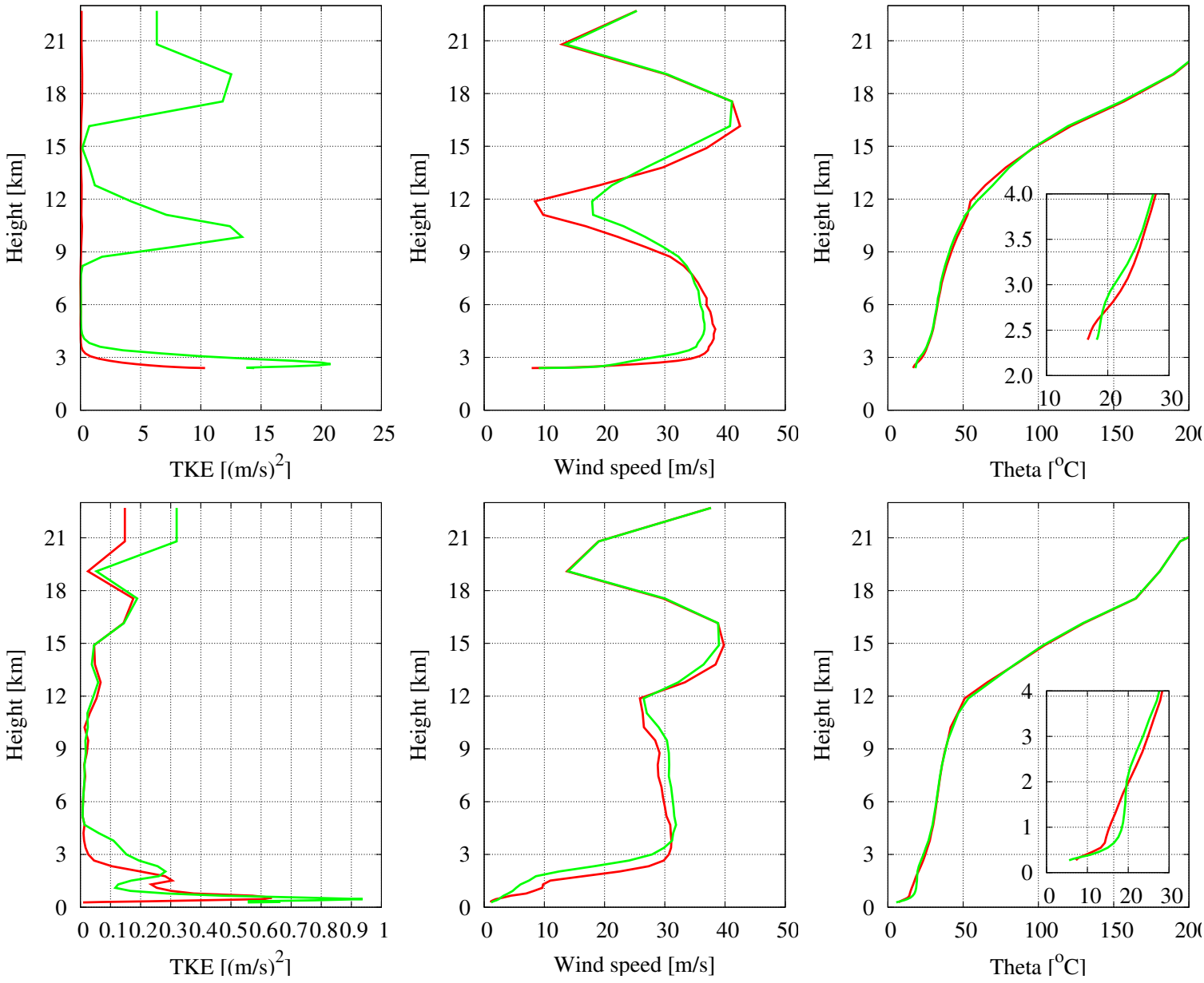

Figure 5.3: Simulated vertical profiles of TKE (left), horizontal wind speed (middle) and θ (right) in a model grid point with high SSO (lat=45.3, lon=7.2; top) and in a point downflow (lat=45.0, lon=7.5; bottom) simulated enabling and disabling the SSO-related term in TKE eq. (respectively indicated by a green and a red line). Time: 08/01 01:00

- in the range surface-4km, a weaker stable stratification manifests, with weaker shear (stronger wind speed and warmer temperature in the surface vicinity and weaker wind and cooler temperature aloft, see Figure 5.3),
- in the range $9-13km$, a smaller perturbation of wind and θ fields is visible at the first level of wave steepening: the wind shear is reduced and the θ disturbance is further from the convective instability. In this sense, the TKE term reduces the non-linear component of the gravity wave,
- above $17km$ the impact on horizontal wind and θ is marginal, likely due to the low air density that reduces the impact of TKE on the dynamics.

At point above low SSO, down flow to the high-SSO region, the advection yields a layer of colder air with weaker horizontal wind speed and higher TKE between 2 and $4km$ in the run with the the SSO-related term activated (Figure 5.3). Beneath, in the PBL, the small increase of TKE contrasts with the more intense thermal gradient, shown in Figure 5.3. This is likely a local effect occurring at the mountain feet associated to the reduction of the down slope flow (compare Figure 5.1 and Figure 5.4), likely caused by the surface warming over the mountain. Indeed, at a proper distance from the mountain slope, the vertical temperature profile in the PBL is only marginally affected by the term introduction (e.g. compare Figure 5.1 and Figure 5.4 at the right edge of the plot). On the whole, in this case favourable to SBL establishment, the option appears mainly active above high SSO regions, while above low SSO regions only small (but non-negligible in proportion to the scarce SBL diffusion) modifications occurs.

Figure 5.4: As in Figure 5.1 but with the SSO-related term of TKE equation enabled

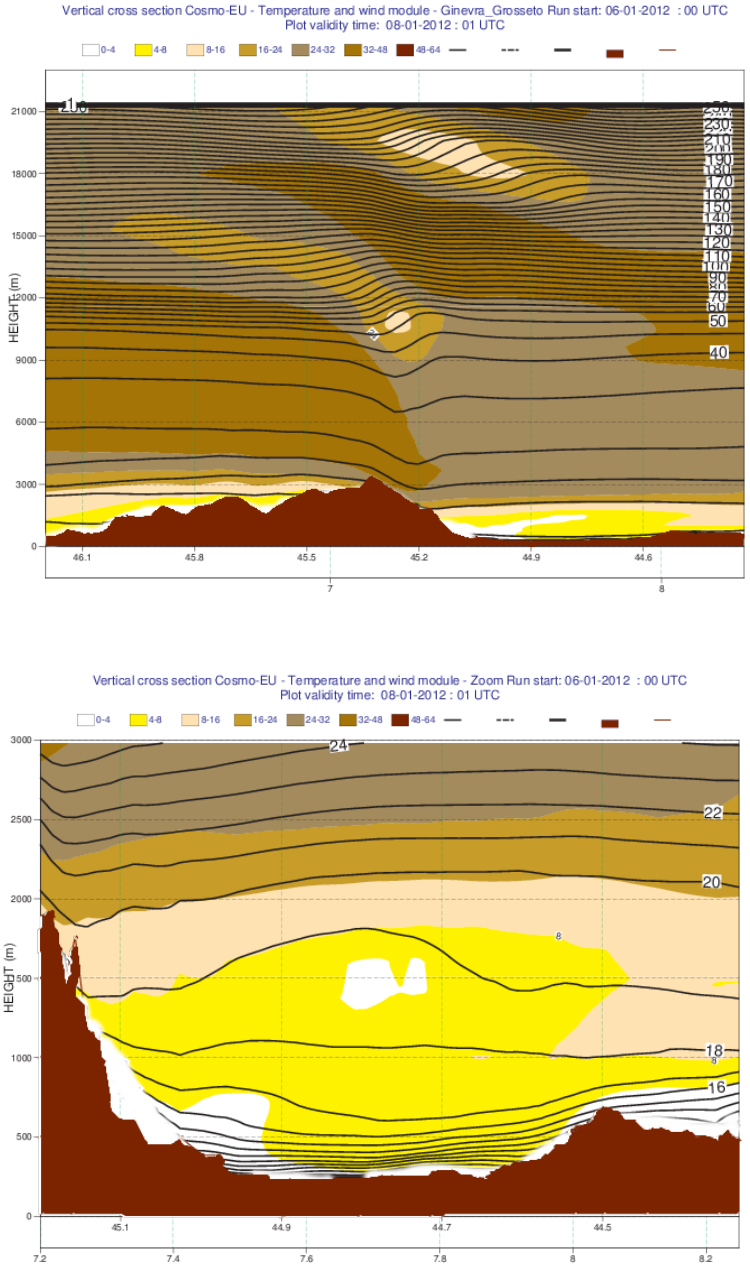

Figure 5.5: Meteorological stations aggregated on the base of the value SSO in the closer model gridpoint (red indicates standard variation of SSO $\leq 25m$ while blue indicates standard variation of SSO $\geq 25m$) on the top of the resolved orography map

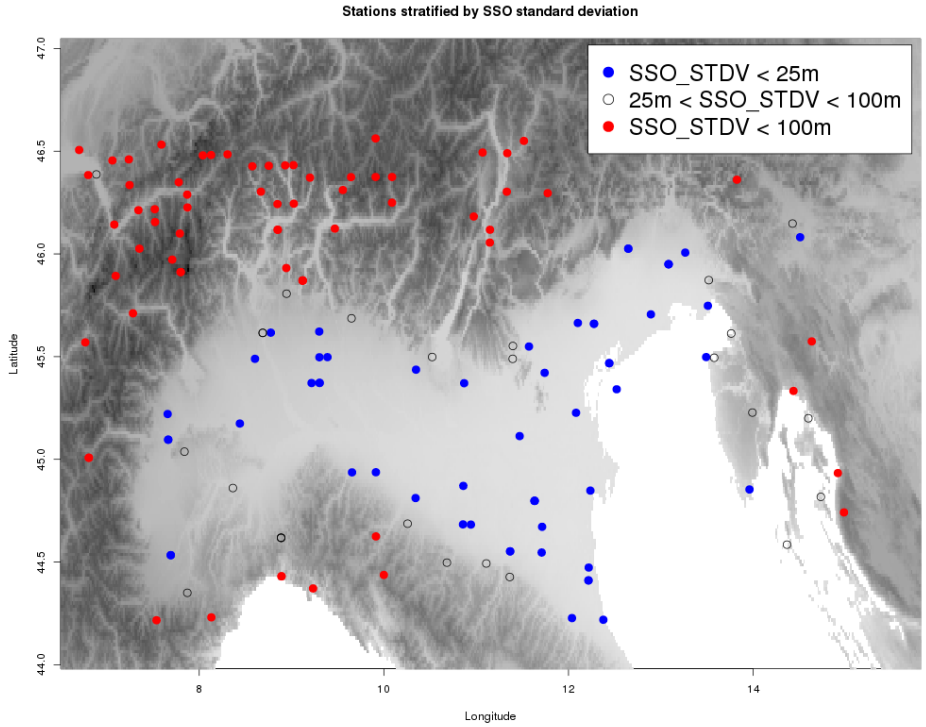

5.4.2 Effect at the near surface

A more general visualization of the near-surface effects of the SS0-related term of TKE equation in regions with high and low SSO is performed by aggregating over Northern Italy area the model grid points with similar standard deviation of SSO, as an indication of the presence of SSO. The temperature at 2m and the wind speed at 10m simulated by COSMO using the two configurations are then compared with the observations available from the ground station networks. Two categories are considered: stations which the nearest model grid point has SSO-standard deviation values below 25m in the first category, and above 100m in the second one. Figure 5.5 visualizes the stations considered in the present analysis.

The aggregated results are reported in Figure 5.6. The results for the 2m temperature at high SSO points confirms the near-surface warming up effect associated with the SSO-related term of TKE equation that has been evidenced in the vertical profile analysis. This warming is beneficial, as it mitigates the negative bias of $1 - 1.5°C$ and improves of the same quantity the rmse. At the same points, the aggregated wind speed at 10m results intensified by about $0.5m/s$, again coherently with the outcome of the profile study. This signal improves the bias and rmse.

At low SSO points, a light warming up of about $0.5°C$ is visible. This confirms the

hypothesis that the direct contribute of the SSO-related term to the TKE production has the dominant effect over low SSO points, while the strengthening of the SBL stratification observed in the profile analysis was a local feature occurring in the lee of the mountains. Given that the warming signal is constant at every hour, during the day it mitigates the negative bias, while during night it enlarges the positive bias. Hence, this SSO-related term promotes the mixing also in strongly stable boundary layers in Po Valley, which is detrimental if the long tail recipes are enabled. The signal of wind speed at 10m at the same points is very small.

5.4.3 Impact of the term in other atmospheric conditions

The aggregated analysis performed using long tail COSMO formulation is repeated also for another case study less favourable to the SBL development: a two-day case in May 2012 characterized by unstable conditions over the same area, due to a cold frontal passage and associated precipitation. The signals reported in Figure 5.7 are the same in sign to the one featured in the previous case study (compare with Figure 5.6), but much smaller in amplitude. This indicates that the SBL is more sensitive to the SSO-related term under investigation. Indeed, the mixing enhancement produced by the SSO-related TKE term is larger in proportion in the scarcely mixed SBL, than in a well mixed PBL.

5.5 Can this term be an alternative to long tail formulation?

In order to answer the question about the role of SSO-related term of TKE equation in substituting long tail formulation, the parameterization is tested in a COSMO version in which all the long tail options are disabled and it is compared to both the COSMO simulations with the long tail on and off. All the long tail recipes described in chapters 3 and 4 are reduced/removed in order to get a short tail version of the COSMO model [2] in which:

- the minimum limit for the diffusion coefficients of momentum and scalar are lowered to the more physical values $K_{min}^{M,H} = 0.01 m^2/s$,
- the additional term of TKE budget equation accounting for the subgrid thermal circulations, parameterized independently from any subgrid surface feature, is set equal to 0,
- the limit on the TKE forcing sum is removed,

[2] It is here referred to a short tail version of the COSMO model because the dismissal of several long tail recipes requires hard code modification and new code introduction

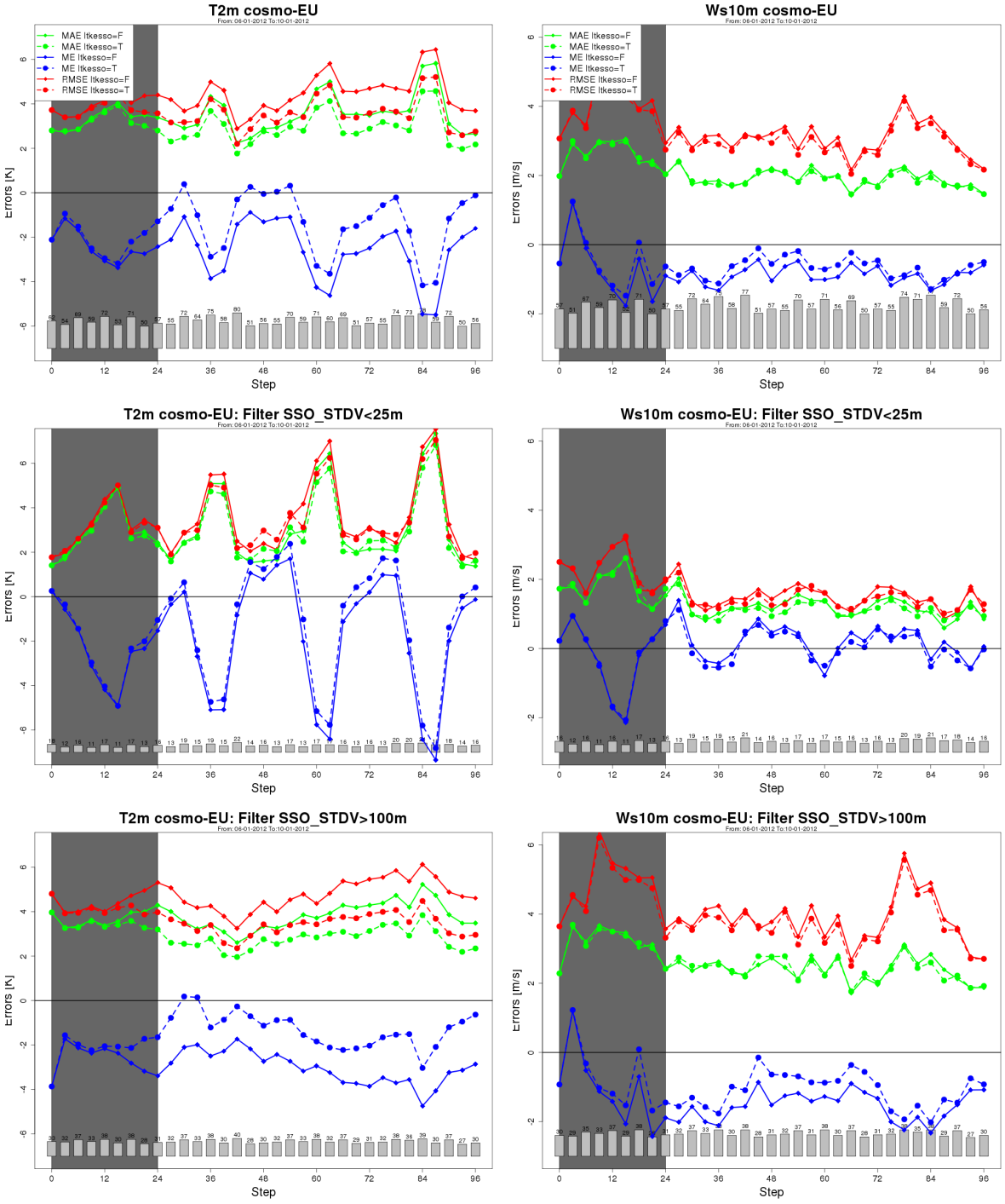

Figure 5.6: Verification of temperature at 2m and wind speed at 10m simulated by run with the term enabled (labelled 'LTKESSO=T') and the control (labelled 'LTKESSO=F'), by considering all North Italian stations (top), only North Italian stations which nearest model grid point with low SSO (middle) and only North Italian stations which nearest model grid point has high SSO (bottom). The histograms represent the sample size for each time range. The grey shaded area is considered as warming-up time and it is not involved in the analysis.

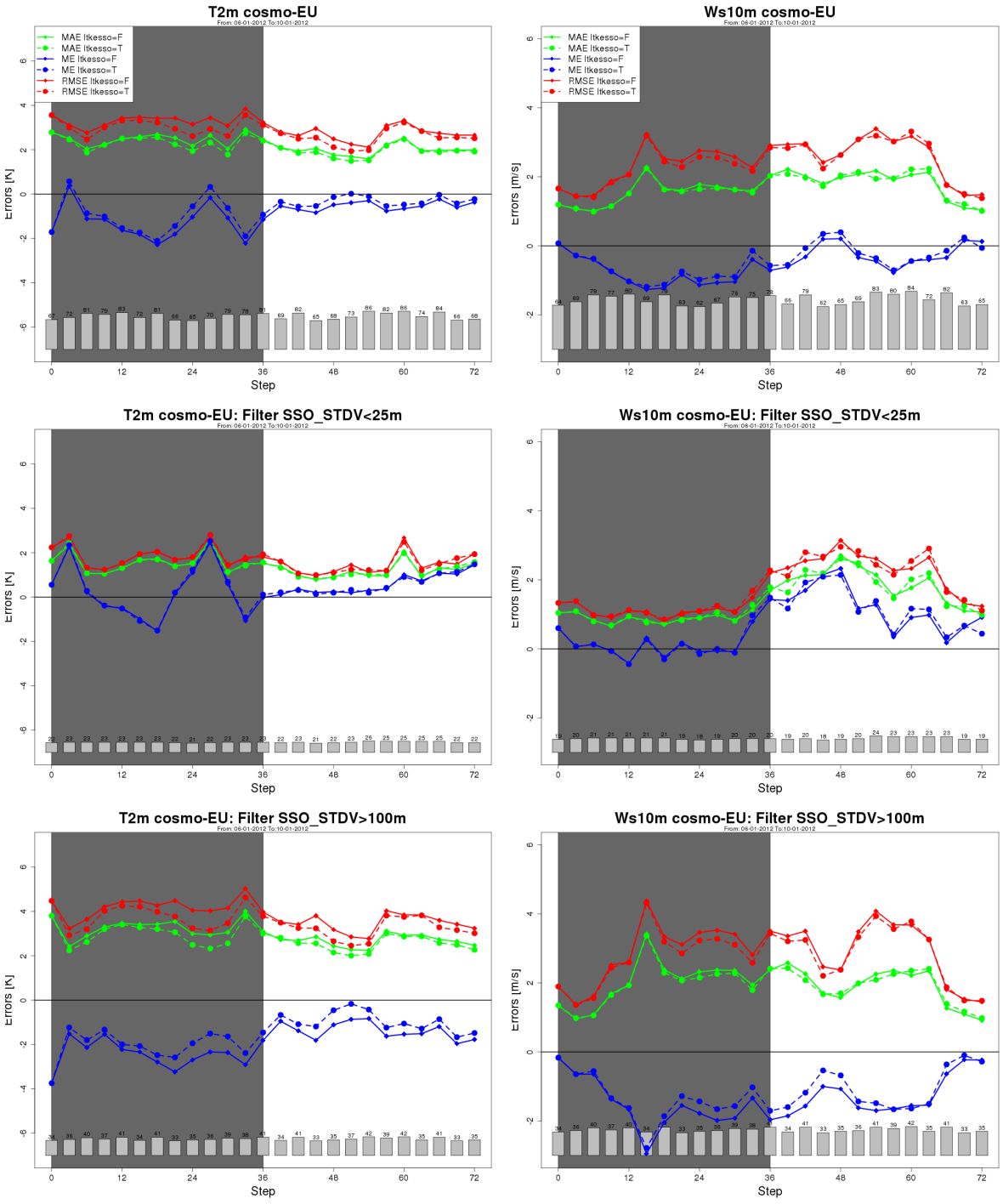

Figure 5.7: As in Fig. 5.6 but for the case of May.

- the minimum limit on q associated to the Mellor and Yamada (1982) scheme inconsistency at Level 2.5 is removed. This action is made possible through the use of stability functions for momentum and scalar derived from Mellor and Yamada (1982) scheme at Level 2.0 in case of unstable stratification,
- the hyperbolic interpolation function is used in spite of the linear option in the surface layer scheme,
- the limit on γ function in the surface layer scheme is removed

The experiment is performed using the case study of January 2012, in which the SSO-related term of TKE eq. resulted most active. The cross isobaric flow (as a measure of cyclone filling) is computed for each of the three simulations (long tail, short tail and short tail with SSO-related term of TKE equation), according to eq. 1.1 as $f \int_0^{z_{top}} v(z)dz$ with f the Coriolis parameter and $v(z)$ the wind component orthogonal to the geostrofic wind direction. Figure 5.8 shows the cross isobaric flow accumulated over the simulation time above four random grid points belonging to the integration domain. From Figure 5.8 it appears clearly that in all the points the introduction of the parameterization partially (with a smaller or larger extent) reduces the low cross-isobaric flow evidenced by the short tail simulation compared to the long tail one. Consequently, this experiment shows as the SSO-related additional term of TKE equation can respond to the request of larger cross isobaric flow, currently attained by long tail formulation. The parametrization results unable to fully cover the gap between short and long tail in terms of cross isobaric flow. It can be concluded that the option should be complemented by other actions (e.g. parameterization of other neglected processes) acting to enhance the cyclone filling tendency in short tail NWP models.

5.6 Conclusions

The effect of the additional source for TKE derived from the sink term of momentum generated by the SSO presence is studied. The parametrization is based on the hypothesis that subgrid scale motions induced by SSO produce kinetic energy, that can be treated by the turbulence scheme. By this extension, the kinetic energy extracted from the mean flow by the action of SSO is not immediately dissipated into inner energy. In spite, it is transported through all subgrid scale motions until it is finally dissipated. This hypothesis belongs to the framework of the Separated Turbulence Interacting with (non-turbulent and still unresolved) Circulations (STIC), developed by M. Raschendorfer (DWD). The approach is particularly interesting in term of SBL simulation, as it parametrizes a source of turbulent mixing in association with subgrid scale features of the surface. The neglect of the effects induced by this scale of motions are one of the most supported hypothesis for the necessity of artificial turbulence enhancement by long tail formulation (see references in chapter 1.4.2). Therefore, a critical question is on the capability of this additional parametrization as an alternative

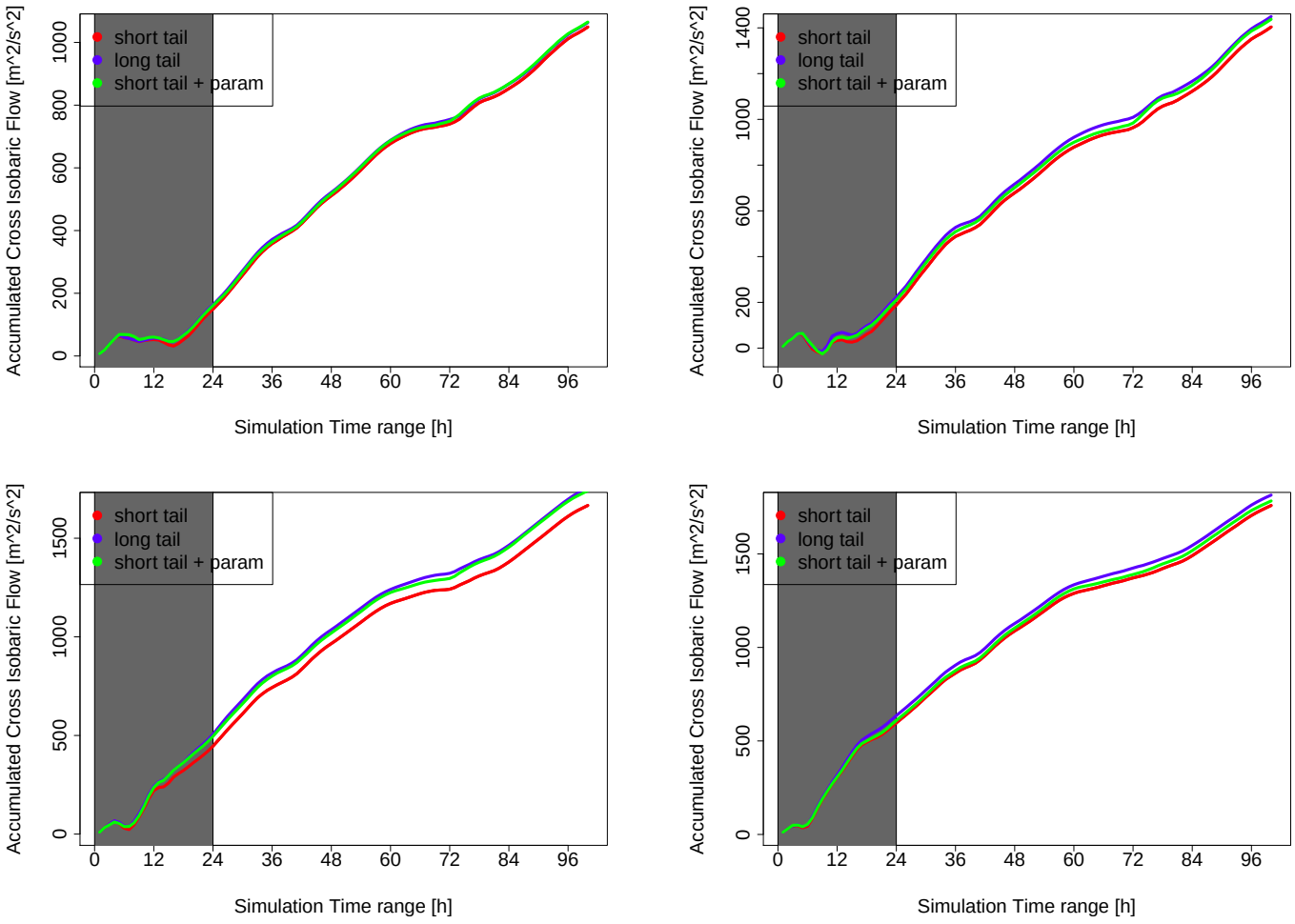

Figure 5.8: Cross-Isobaric flow accumulated along the simulation time over four random grid-points using the three COSMO simulations: applying the long tail options ("long tail"), switching them off ("short tail") and keeping them off together with introducing the SSO-related additional TKE term ("short tail +param"). Grey shaded area indicates the warming up time to neglect in the present analysis

to long tail practice. At first, the parametrization is studied in terms of its impact on top of the current long tail formulation of COSMO. The analysis of a case study featuring conditions favourable to the SBL development underlines that a large additional amount of TKE is generated due to the additional TKE source, mainly above areas of pronounced SSO at the lowest model levels (due to the blocking influence of SSO), at the top of the troposphere and within the stratosphere in the regions of orographic gravity wave steepening. Moreover, a non-negligible increment of TKE is observed also over low SSO regions within the SBL. The primary effects of the increment of turbulent vertical mixing at every level are: an increase of turbulent drag, a reduction of the vertical wind shear and a weakening of the thermal stratification. The consequences of these modifications, verified at the near surface in term of temperature and wind speed, shows a general improvement over high-topography regions. On the other side, at low SSO points (not directly involved in down slope flow in the lee of mountains) this additional term results detrimental during nocturnal SBL, since the already positive bias of temperature increases. This can be associated to the fact that the SBL is already over-mixed, due to the use of long tail limits. In a case study less favourable to the SBL development, the term introduction results less relevant, since in this case the relative increment of TKE is smaller.
In a second test, the critical point of the potential role of this parametrization as an alternative to long tail formulations is tackled. An experimental COSMO model version in which all the long tail recipes (detected and analysed in chapters 3 and 4) are removed is tested against the same with the option introduction and against the long-tailed previous run. The SSO-related term of TKE equation shows the ability to cover a relevant part of the cross-isobaric flow gap existing between short and long tail formulations. The largest benefit likely derives from the increment of turbulent drag at different levels (both at the surface vicinity and in correspondence to gravity wave steepening or breaking). Thus, the incorporation of this parametrization in short tail formulation gives a more physical but still partial answer to the operational need to large cyclone filling tendency, with respect to long tail approach. Possibly the representation of other neglected processes in the SBL, as for example the gravity wave induced by small scale terrain disturbances (Steeneveld et al., 2008), the low level drag induced by trapped lee waves (Teixeira et al., 2013), subgrid scale thermal heterogeneity effects (see chapter 6) might be able to complement it.

Chapter 6

Stable boundary layer and unresolved thermal heterogeneity of the surface

6.1 Introduction

This chapter deals with the representation of the effects on the SBL structure and turbulent transport caused by the horizontal temperature heterogeneities of the underlying surface. When the length scale of the surface heterogeneities is lower than the model resolution, the involved processes are not directly represented in NWP models and need to be parametrized. Whereas in the convective PBL it has been demonstrated that only temperature patches of scales larger than 5-10 km can affect the convective PBL structure and dynamics (Chen and Avissar, 1994; Lynn et al., 1995; Avissar and Schmidt, 1998; Stirling and Petch, 2004; Patton et al., 2005), the stable PBL can be influenced by heterogeneity of scales of 100m (Stoll and Porté-Agel, 2009; Mironov and Sullivan, 2016). In state-of-the-art mesoscale NWP models, the horizontal resolution is approaching lengths of 1-2km, thus only the SBL effects will need specific description. Large Eddy Simulations (LES) of weakly stable PBL over thermally homogeneous and heterogeneous surfaces evidenced that the thermal patchiness increases vertical mixing with respect to mean potential temperature and produces deeper SBL (Stoll and Porté-Agel, 2009; Mironov and Sullivan, 2016). In cases of weak stratification, advection of cold air over a warm surface can develop (locally) convective instability associated with convective rotors (Stoll and Porté-Agel, 2009). Under more stable stratification, where vertical motions are intensively dumped, likely less energetic processes as non-closed motions (e.g. internal gravity waves) can arise due to horizontal surface temperature contrasts (Mironov and Sullivan, 2016).

Several approaches have been developed to represent the effects of subgrid scale thermal inhomogeneities in NWP models. The most relevant ones are described in section 1.4.2. Among them, the flux aggregation technique of the tile approach is widely used in NWP models (Avissar and Pielke, 1989; Giorgi and Avissar, 1997; Ament and Sim-

mer, 2006), and it resulted in idealized experimentation (Stoll and Porté-Agel, 2009) the most efficient in weakly stable PBL applications, especially in its extension to the blending height (Blyth et al., 1993). The tile approach considers homogeneous sub-cell fractions of any size aggregated according to the main surface features, for which the vertical fluxes are separately computed. Subsequently they are aggregated for every cell at the lowermost model level, where they furnish the lower boundary condition to the turbulence scheme. The implicit hypothesis of the tile approach is that horizontal advection between patches is smaller than vertical exchange, and can thus be neglected. This is a main shortcoming of the approach. Another assumption consists in the occurrence of vertical homogeneity exactly at the model lowermost level (typically ranging between 10 and 20 m above the surface in current NWP models). This hypothesis is made milder by using the extension to the blending height (Blyth et al., 1993), which treats cases in which the vertical homogeneity occurs below the model lowermost level. Vice versa in the other cases (i.e. when the vertical homogeneity occurs above the model lowermost level, for example due to high thermal contrast between the patches), the tile solution can not be adequate. Finally, questions arise from the coupling of a tiled surface layer with the turbulence scheme (Mironov and Sullivan, 2016). A first question regards the order of turbulence scheme to apply: since temperature variance equation is very important, a scheme including its prognostic solution may be more suitable with respect to a scheme only including a diagnostic equation. A second point is about the lower boundary conditions to apply at the temperature variance equation, as both Neumann and Dirichelet conditions are potentially valid (Mironov and Sullivan, 2016). Despite its shortcomings and still open questions, the tile approach is a practical solution for NWP models, due to its simplicity and computational efficiency.
The present chapter aims at evaluating the benefit/limit of the tile approach in describing the SBL over thermally heterogeneous surfaces. Idealized simulations of a single column version of COSMO are compared with COSMO-LES simulations in order to assess the tile performance in cases of different stratification intensities, thermal contrast between the patches and horizontal advection strength. In order to tackle the questions about the coupling with the turbulence scheme, the tiled surface layer is either coupled with the COSMO first-order turbulence scheme, or with a second order scheme or, finally, with a second order scheme applying a lower boundary condition for the temperature variance equation. In the next section, few concepts on the implications on second-order moment equations of a thermal heterogeneous surface are reported (from Mironov and Sullivan, 2016). In section 6.3, the idealized experimental set up and the configurations of the COSMO-LES and COSMO models employed are described. Section 6.4 reports the results, while in section 6.5 the implications for operational applications in terms of substitution of long-tail formulations are discussed.

6.2 Thermal heterogeneity and turbulence equations

Mironov and Sullivan (2016) recently illustrated the turbulent mixing increment in SBL in presence of a thermally heterogeneous surface, stemming from second-moment budget equations (decomposed in resolved and subgrid scale component with respect to a LES simulation). The logical steps are herein reported.
The key role is played by the temperature variance budget equation (here reported after boundary layer approximation and neglect of secondary terms):

$$\frac{1}{2}\left(\frac{\partial}{\partial t}+\overline{w}\frac{\partial}{\partial z}\right)\overline{\theta'^2}=-\overline{w'\theta'}\frac{\partial\overline{\theta}}{\partial z}-\frac{1}{2}\frac{\partial}{\partial z}\overline{\theta'^2 w'}-\epsilon_\theta \tag{6.1}$$

where the terms r.h.s are respectively the mean gradient production/destruction term, the turbulent transport of resolved scale $\overline{\theta'^2}$ and the specific dissipation. When the surface is thermally heterogeneous, the non-zero temperature variance causes an increment in the term of turbulent transport of $\overline{\theta'^2}$ in the surface vicinity, which not only redistributes $\overline{\theta'^2}$ along the vertical, but induces a net gain of $\overline{\theta'^2}$ near the surface (see Figure 6.1,a). The temperature variance is included in the equation for the vertical temperature flux $\overline{w'\theta'}$, expressed in its simplified version (boundary layer approximation, assumption of stationariety, neglect of third-order term and dissipation, decomposition of pressure term):

$$\overline{w'\theta'}=-\frac{1}{C_t^\theta}\tau_\epsilon\overline{w'^2}\frac{\partial\theta}{\partial z}+(1+C_b^\theta)\frac{\tau_\epsilon}{C_t^\theta}\frac{g}{\theta}\overline{\theta'^2} \tag{6.2}$$

where the terms r.h.s are respectively the down-gradient term and the counter-gradient terms, in which C_t^θ and C_b^θ are dimensionless coefficients and τ_ϵ is a time scale. As shown in eq. 6.2, the temperature variance belongs to the counter-gradient term. Since $\overline{w'\theta'}$ is negative under stable stratification, the more $\overline{\theta'^2}$ increases, the more the downward $\overline{w'\theta'}$ is reduced (Figure 6.1,b). Finally, $\overline{w'\theta'}$ belongs to the buoyancy forcing in the TKE budget equation ($TKE=0.5\sqrt{\overline{u'}+\overline{v'}+\overline{w'}}$):

$$\frac{dTKE}{dt}=-\overline{u'w'}\frac{\partial\overline{u}}{\partial z}+\frac{g}{\theta}\overline{w'\theta'}-\epsilon-\frac{1}{2}\frac{\partial\overline{u'u'w'}}{\partial z}-\frac{1}{\rho}\frac{\partial\overline{w'p'}}{\partial z} \tag{6.3}$$

where the first and second terms r.h.s are respectively the wind shear production and the buoyancy terms, the third term is dissipation, the fourth vertical turbulent transport and the last is pressure diffusion. Under stable stratification, the buoyancy is a sink to TKE, thus a reduced $\overline{w'\theta'}$ augments TKE (Figure 6.1,c). On the whole, the processes induces an increment of vertical turbulent mixing and a deeper, more vertically homogeneous and less stable PBL (Figure 6.1,d).

6.3 Data and methods

The experimentation consists of a set idealized simulations of SBL, with prescribed initial and boundary conditions (a description in section 6.3.1), performed with both a

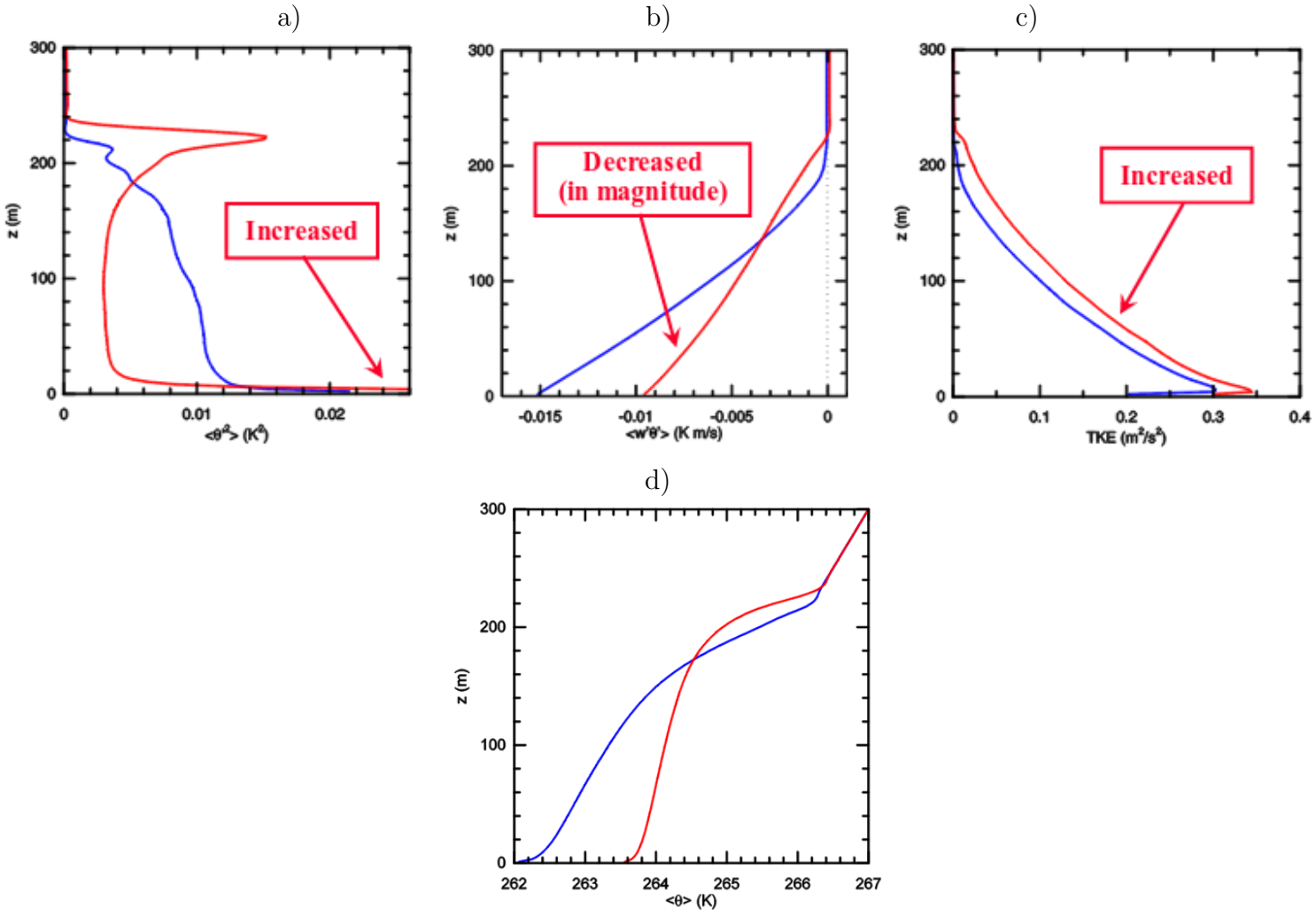

Figure 6.1: LES simulated vertical profiles of potential temperature variance (a), vertical temperature flux (b), TKE (c) and potential temperature (d) in weakly stratified PBL over thermally homogeneous (blue line) and heterogeneous terrain (red line). From Mironov and Sullivan (2016)

single column version of the COSMO model, in which the tile approach is additionally implemented as well as a second-order turbulence scheme, and a LES version of the COSMO model (COSMO-LES, i.e. the COSMO model configured to run as a LES model). The set up of COSMO-LES is presented in section 6.3.2, while the configuration of the 1D version of the COSMO model is reported in section 6.3.3. Notice that COSMO-LES has never been tested for SBL representation, thus preliminary tests are also performed to ensure the correct performance in the present experiments.

6.3.1 Idealized experiment

The idealized experiments are based on a case of nocturnal cooling of a dry weakly stable PBL over flat and thermally homogeneous surface, documented in Kosović and Curry (2000). The case has been often employed for idealized studies. Indeed the case was adopted in the GABLS1 inter-comparison study, in which the performances of numerous LES models and several NWP models in 1D mode were assessed in the shear-driven SBL over homogeneous terrain (e.g. Beare et al., 2006; Cuxart, 2006). On the same case, Stoll and Porté-Agel (2009) and Mironov and Sullivan (2016) based (with few modifications) their idealized tests over thermally heterogeneous terrain. The selection of this case in the present experimentation was aimed at dealing with a well known situation, for which also LES optimal configuration is available.
The idealized simulations are inspired to the ones of Stoll and Porté-Agel (2009), who investigated the sensitivity to the patches size and thermal contrast using a specific mean cooling rate ($-0.25K/h$). They found low sensitivity to the patches size while high sensitivity to thermal contrast. However, Mironov and Sullivan (2016) discussed the possibility of a diverse outcome in case of a stronger mean stratification. Therefore, this experimentation includes simulations with three different mean surface cooling rate (and consequently different mean environmental stratification within the PBL), equal or more stable than the cases in Stoll and Porté-Agel (2009). The sensitivity to the thermal contrast between the patches is investigated in the more stable configuration, in which, possibly, the SBL response is taken to extremes. Moreover, the sensitivity to mean horizontal advection is tested in the case of medium stratification. In total, the experimentation includes 7 simulations. Their specificities in terms of mean environment stratification intensity, mean wind horizontal advection and thermal contrast between the surface patches are summarized in Table 6.1. Cases are identified by the following codes: 'SPA' is the closest case to Stoll and Porté-Agel (2009), 'NSPA' and 'SSPA' feature stronger mean surface cooling, 'NSPA-lowU' and 'NSPA-highU' feature 'NSPA' mean surface cooling and respectively lower and higher initial horizontal advection, while 'SSPA-lowTC' and 'SSPA-highTC' feature the strongest mean surface cooling 'SSPA' and respectively low and high thermal transition between patches. Prescribed surface temperature temporal rates for the cases are represented in Figure 6.2.

In all the tests, the initial potential temperature profile consists of a mixed layer with potential temperature 265K up to 100m with an overlying inversion of strength

Case	$\overline{u}(m/s)$	Mean surface cooling $[K/h]$	Thermal contrast $[K]$
SPA	8	-0.25	6
NSPA	8	-0.375	6
SSPA	8	-0.666	6
NSPA-lowU	2	-0.375	6
NSPA-highU	14	-0.375	6
SSPA-lowTC	8	-0.666	4
SSPA-highTC	8	-0.666	8

Table 6.1: Prescribed conditions for the different simulations characterized by varying mean surface cooling, mean zonal wind intensity (while meriodional component is always 0) at the initial time step, and temperature jump between the patches after 8 hours of simulation.

$0.01K/m$. The mean surface cooling is prescribed and the rate adopted in each simulation are reported in Table 6.1. The geostrophic wind is initially prescribed in East-West direction, while initial meridional component is set to 0. The values of $\overline{u}$ used in each simulation are reported in Table 6.1. The surface heterogeneity consists of abrupt transitions in surface temperature in the streamwise direction. This forms a series of spanwise homogeneous surface temperature patches 100m-long that alternate between two temperature values equally distant from the mean surface temperature. The thermal contrast values obtained after 8 hours of simulation in each configurations are reported in Table 6.1. Results are averaged over the last 2 hours of simulation, along which all the patches cool at the mean surface cooling rate. The simulation site is flat and covered by short grass. Differently from Kosović and Curry (2000) and all the other studies, in the present test the site is located at the Equator (in spite of being at 65N), for reasons explained in the following section 6.3.2.

6.3.2 COSMO-LES

COSMO-LES is an interface of the COSMO model available in the official code, which allows idealized simulations in 1D, 2D or 3D mode also at very high resolution and which offers several options to set orography, other external parameters, initial (thermo)-dynamic profiles, surface fluxes, model boundary conditions, artificial convection triggers, etc.. (Blahak, 2015). COSMO-LES was demonstrated being comparable to LES simulations in neutral and convective PBLs at horizontal resolutions ranging from 50 to 25m (Langhans et al., 2012). However, it has never been tested in stable PBL cases. Therefore, several preliminary checks and sensitivity tests to the horizontal grid spacing, to model domain size in both x and y direction are performed in order to ensure the correct module performance. The results are reported in Appendix C.
The final selected configuration of COSMO-LES for the current experimentation are in 2D with y-direction neglected, since no relevant features are expected in this direction

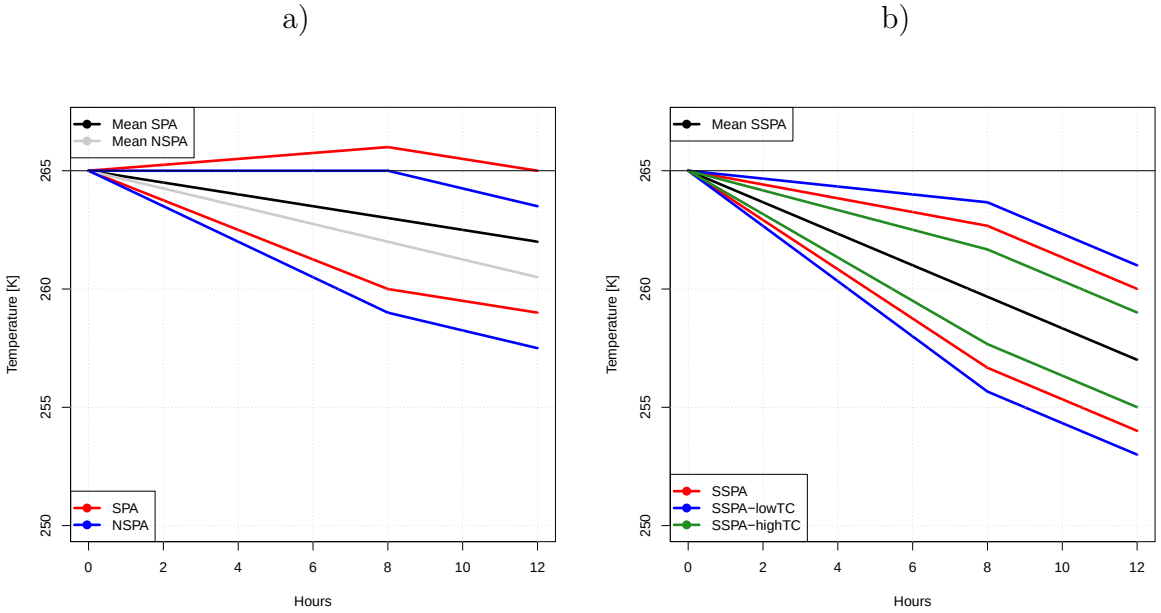

Figure 6.2: Prescribed cooling/warming rates at the surface patches in the COSMO-LES idealized simulations. Plot a) reports cases 'SPA', 'NSPA', 'NSPA-lowU', 'NSPA-highU' (the last two are equal to 'NSPA'), whereas plot b) reports cases 'SSPA', 'SSPA-lowTC', 'SSPA-highTC'

(wind initial direction does not rotate because Coriolis force is null at the Equator, the prescribed temperature transition is in streamwise direction, as well as the consequent advection between patches). Periodic boundary conditions are imposed along zonal and meridional directions, coherently with Stoll and Porté-Agel (2009). The horizontal resolution is $\Delta x = \Delta y = 3.125m$, which is at higher resolution to what prescribed by Stoll and Porté-Agel (2009) in order to resolve the smaller turbulent eddies developing in cases of stronger mean surface cooling (and thus stronger environmental stability, e.g. cases 'NSPA' and 'SSPA'), see sensitivity study to the horizontal grid spacing in Appendix C. The vertical resolution is $\Delta z = 3.125m$ in agreement with Stoll and Porté-Agel (2009). The flow is simulated with a grid of 128x1x128 points in x,y and z direction respectively in a box of 400m x 3.125m x 400m (broader domains do not induce relevant changes, see sensitivity test in Appendix C). The integration time step is $dt = 0.01s$. In contrast with Stoll and Porté-Agel (2009), Coriolis parameter is set equal to 0 (i.e. simulation site at the Equator), since otherwise, an inertial oscillation develops with a time period of $2\pi/f \approx 13h$, due to the unbalance between Coriolis force and pressure horizontal gradient, initialized from the prescribed wind speed at the first time step. The steady-state can not be reached during the 12 hours of simulation time, thus the inertial oscillation is a disturbing feature and should be avoided.
The turbulence scheme applied is based on Smagorinsky-Lilly scheme (implementation in the COSMO model described in Langhans et al., 2012). It is important to

remove any long-tail formulation implemented in the scheme, since the vertical mixing would be highly perturbed. The minimum diffusion coefficients for momentum and heat is hard-coded and equal to $K_{min}^{M,H} = 1m^2/s$. It is lowered to the value $K_{min}^{M,H} = 0.01m^2/s$, allowing for non-constrained SBL representation. The surface layer scheme used is the Louis et al. (1982) scheme implemented in the COSMO model, based on Monin-Obukhov similarity theory (description in section 4.2.2). While the subgrid component of the variances/covariances is computed by the turbulence scheme, the resolved component is derived by computing in every grid cell the deviation of each variance/covariance element ($\overline{u}$, $\overline{w}$ and $\overline{\theta}$) from the horizontal average and averaging over the domain their square (obtaining the variances) or their combination (obtaining the covariances). Moreover, such derived resolved components of variances/covariances are averaged over the last 2h of simulation, in order to approximate the ensemble-mean quantities (output every 6-min).

6.3.3 COSMO

The single column version of COSMO is configured to run at 2km of horizontal grid spacing, a nowadays typical mesoscale model resolution. The vertical axis is linearly discretized in 64 levels, 6.25m thick, thus the vertical domain corresponds to the one of COSMO-LES. Initial conditions are the same ones imposed in COSMO-LES simulations, as well as the prescription of the surface mean cooling rate. Periodic boundary conditions are applied in both x and y directions. The surface layer scheme applied is Louis et al. (1982), coherently with the option applied in COSMO-LES. Three different turbulence schemes are alternatively applied:

1. the truncated second-order closurebased on Mellor and Yamada (1982) at Level 2.5, i.e. with prognostic TKE budget equation and diagnostic budget equations for the other second-order moments, which is operational in COSMO (description in section 2.2.1). The additional forcing term to TKE budget equation associated with subgrid scale orography (description in chapter 5) is switched off, as the experiments are performed in flat terrain. The term of TKE budget equation accounting for the sub grid circulations caused by surface thermal heterogeneity (description in chapter 2.2.1) is switched off too. Indeed this term is meant to deal only with thermal circulations induced by subgrid orography [1]. In the following this closure is referred to as 'TKE scheme'

2. the second-order closure based on Mellor and Yamada (1982) at Level 3.0, i.e. with prognostic TKE and scalar variances ($\overline{\theta'^2}$ and $\overline{q'^2}$) budget equations (e.g. eqs. 6.3 and 6.1) and diagnostic equations (including counter-gradient term) for covariances (e.g. eq. 6.2). The Mellor and Yamada (1982) singularity for the scheme at Level 3.0, described in section 3.3, is treated using Helfand and Labraga

[1] At the current state, this is not yet the case

(1988) correction. The scheme was implemented in COSMO by E. Machulskaya as an external branch to the official code. In the following this closure is referred to as 'TKESV scheme'

3. the same as point 2), but a Dirichelet lower boundary condition is applied to $\overline{\theta'^2}$ budget equation. In particular, $\overline{\theta'^2}$ at the lowest model level is set equal to the potential temperature variance at the surface. It would have been more correct to introduce the lower boundary condition for $\overline{\theta'^2}$ at z_0 level (i.e. the bottom boundary of the lowest model level), since it comes from the surface variance, but this would imply solving $\overline{\theta'^2}$ equation from z_0 level (while at the moment it is solved only from the upper boundary of lowest model level). In the following this closure is referred to as 'TKESV+LBC scheme'

The single column version of COSMO using the TKE-scheme has been already tested in the idealized case considered in the present analysis, but with homogeneous surface and with Coriolis force enabled, by Buzzi (2008). In particular, Buzzi (2008) found an optimal configuration of the TKE-scheme for the representation of this weakly SBL. This includes:

- the minimum limit for $K^{M,H}$ set to $0.01m^2/s$ instead of the long-tail larger values
- the coefficient l_{max}, a parameter controlling the asymptotic mixing length (see eq. 2.2.1), is set equal to 40m instead of larger values (usually values ranging between 150m-500m for COSMO operational applications). In this way, the maximum eddies size is reduced
- the diffusion coefficient for momentum K^M is vertically filtered at the end of turbulence scheme by a 5-point smoothing function:

$$f_k^{new} = 0.5f_k + 0.2(f_{k+1} + f_{k-1}) + 0.05(f_{k+2} + f_{k-2}) \tag{6.4}$$

  where the subscript k is the vertical grid index. This solution is adapted from one of the options investigated by Buzzi (2008) in order to cure a numerical oscillation [2] that manifests in the simulated diffusion coefficients along the vertical when the long-tail $K_{min}^{M,H}$ is lowered from a value of $1m^2/s$, and which causes unrealistic stepwise profiles of temperature and wind. Whereas in Buzzi (2008) the filtering was applied to both K^M and K^H, in the present work only the filtering of K^M was sufficient to cure the oscillation onset (shown in Appendix D).

[2] Burchard and Deleersnijder (2001) suggested that the issue originates in a physical inconsistency of the stability function in Mellor and Yamada (1982) model, leading to a non-monotone normalized stress function (defined as $\frac{K^M}{q^2}|\frac{\partial \overline{u}}{\partial z} = S^M(G^M)^{0.5}$) in a plane $G^M x G^H$ (the functions S^M, G^M, G^H are defined in section 3.3). Moreover, Mellor (2003) evidenced that the issue is only associated to staggered grid (whereby the mean variables like temperature and wind components are staggered relative to the turbulence variables like q and turbulent fluxes), thus suggesting that the problem is related to the model numerics.

These mentioned settings are adopted in the single column simulations performed in this study, in all the alternatively associated turbulence schemes.
Additionally, a sensitivity test to the mixing length formulation (shown in Appendix D) revealed that the COSMO simulation is extremely sensitive to the reduction of the parameter controlling the asymptotic mixing length (l_{max}) to very small value (on the order of 1 meter). In particular using such small values, the SBL height halves and a secondary maximum close to the PBL top in the turbulence variances/covariances is smoothed out. Despite this setting improves the agreement between COSMO and COSMO-LES (Appendix D), such small values of mixing length are far from the potential values of a 2km-resolution model. Therefore, the optimized setting of l_{max} from Buzzi (2008) is kept. The same sensitivity study evidenced also a small sensitivity to the stability correction to the Blackadar formulation. This correction limits the mixing length for increasing static stability (see eq. 2.2.1 Deardorff, 1976)and its application is reasonable in the study of SBL. Therefore, it is enabled in the present experimentation.
The tile approach is implemented in a simplified manner: only two tiles equally large are considered, both sited over grass, and for which the surface temperature is prescribed to evolve with a different rate. The surface layer scheme is run for each tile and the surface fluxes of momentum and sensible heat are averaged at the lowest model level. Since the COSMO surface layer scheme outputs the transfer coefficients C^M and C^H instead of the surface fluxes, the average is computed in term of the transfer coefficients according the following derivation (in which the bulk flux formulation in eqs. 2.6-2.7 are applied):

$$SH_1 + SH_2 = \overline{SH} \quad \rightarrow \quad C_1^H(\bar{t} - t_{g,1}) + C_2^H(\bar{t} - t_{g,2}) = \overline{C^H}(\bar{t} - \overline{t_g}) \tag{6.5}$$

$$\tau_1 + \tau_2 = \overline{\tau} \quad \rightarrow \quad C_1^M + C_2^M = \overline{C^M} \tag{6.6}$$

where the subscript 1,2 identify respectively the first and second tile, while the over line the mean grid cell variables.

6.3.4 COSMO-LES vs COSMO SCM short-tailed

COSMO-LES and COSMO single column model should be regarded as different tools, the first one giving the best representation of nature, the second one giving the best representation of nature provided by a mesoscale NWP model in short tail version.
A first test to check the agreement between these two models is performed over homogeneous terrain. Results evidenced that COSMO single column is over-diffusive compared to the COSMO-LES (see appendix D). Indeed, the SBL is deeper in COSMO single column, with more mixed wind and potential temperature, and with a secondary maximum of TKE at the SBL top.These outcomes agree with Buzzi (2008)'s reproduction of the very similar GABLS1 case study [3]. Given that the version of COSMO single column

[3]The few differences with Buzzi (2008)'s experiment are that in his test the location site was at 73N (while the present experimentation is at the Equator), the COSMO single column model used the operational surface layer scheme (while in the present experimentation it uses the Louis et al. (1982)

used is short tailed, the divergences between COSMO single column and COSMO-LES are intrinsically associated to the different nature of the two models. Possibly the different resolutions and/or turbulence descriptions explain them.
The situation is more complex over heterogeneous terrain, condition that can be represented by COSMO-LES, but not in the reference COSMO single column model (not applying the tile technique), in which the grid cell surface temperature is homogeneous by definition. Figure 6.3 shows the vertical profiles of θ, wind speed, turbulent variances and covariances simulated by COSMO-LES and COSMO single column model in the 'NSPA' idealized case study (outcomes are similar in all the cases considered). The COSMO single column version is labelled to as 'COSMO TKE' (where 'TKE' indicates the used turbulence scheme, which solves prognostically the TKE budget equation only). COSMO TKE shows an over-diffusive tendency with respect to COSMO-LES: it overestimates the SBL height and the turbulent second order moments at the SBL top (where it is visible a secondary maximum, in particular for the variances), and it underestimates the wind speed. In analogy with the homogeneous terrain case, these issues are reasonably associated with the intrinsic different nature of the two models. In confirmation of this consideration, a sensitivity study to the setting of the master length scale in COSMO TKE (presented in appendix D) evidenced that the divergences between COSMO TKE and COSMO-LES reduce if the former uses a shorter asymptotic mixing length, i.e. if in COSMO TKE it is assumed that the maximum size of turbulent eddies is smaller. However, this selection is not suggested in a mesoscale NWP model (because it should be able to adapt to different turbulence situations, including also large convective eddies). The differences in the mixing lengths are an example of the intrinsic different nature of COSMO single column and COSMO-LES.
The more stratified θ vertical profile in COSMO TKE with respect to COSMO-LES derives instead from the lack of a description of the surface thermal heterogeneity in COSMO TKE, as it will be shown in the next section.

6.4 Results

6.4.1 Tile approach and sensible heat fluxes

In the COSMO model, the grid cell surface temperature is homogeneous by definition, unless the tile approach is enabled. If so, the thermal heterogeneity is described by averaging the surface fluxes of the two tiles considered (and for which the surface temperature is prescribed). While in COSMO-LES the surface heterogeneity firstly affects the θ variance (see section 6.2), in the tiled COSMO the heterogeneity passes through the surface fluxes, and mainly the sensible heat flux SH, as the tiles have different vertical thermal delta. The use of a different SH in the tiled COSMO model influences the surface-atmosphere coupling within the model surface layer and the vertical tem-

scheme), and finally the LES ensemble mean and its standard deviation were from Cuxart (2006) (while in the present experimentation are from COSMO-LES)

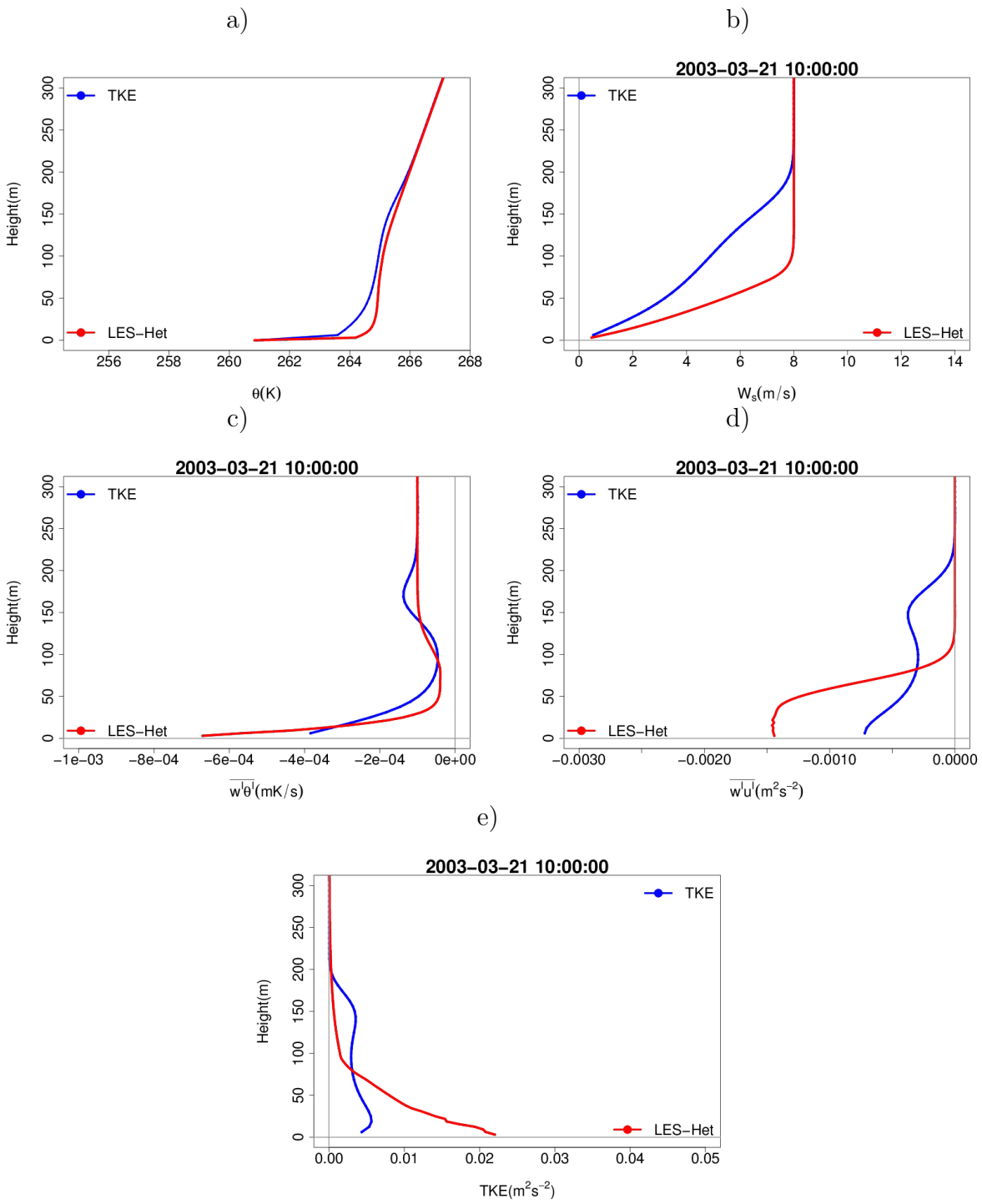

Figure 6.3: Domain mean of the vertical profiles of potential temperature (a), wind speed (b), buoyancy flux (c), shear stress (d) and TKE (e) simulated by COSMO-LES and by COSMO TKE and averaged over the last 2 hours of simulation in NSPA case study

Cases	ξ	SH COSMO 'TKE' $[W/m^2]$		SH COSMO 'TKE-2Tiles' $[W/m^2]$	
		BIAS	RMSE	BIAS	RMSE
SPA	0.2	-0.66	0.66	-0.16	0.23
NSPA	0.7	-0.34	0.35	-0.13	0.2
SSPA	1.4	-0.78	0.78	-0.76	0.76
NSPA-lowU	2.4	-0.25	0.25	-0.26	0.26
NSPA-highU	0.3	-2.4	2.40	-0.9	1.20
SSPA-lowTC	1.5	-1.62	1.62	-1.58	1.58
SSPA-highTC	1.0	-0.46	0.46	-0.43	0.43

Table 6.2: RMSE of COSMO 'TKE' and 'TKE-2Tiles' in simulating the grid cell sensible heat flux (RMSE SH) over the last 2 hours of simulation (hours 10-12) in the idealized experiments. Grid cell stability parameter (ξ) averaged over the same period is also reported.

perature profile aloft. Therefore, a first assessment of the tile approach performance under stable stratification regards the simulation of SH and its consequences on the lapse rate.

Table 6.2 reports the statistical scores over the last two hours of simulation of the grid cell SH og the COSMO single column runs, both without and with tiled surface layer and both coupled with TKE turbulence scheme (they will be later referred to as 'COSMO TKE' and 'COSMO TKE-2Tiles'), compared to the domain averaged fluxes of COSMO-LES. In any conditions, the COSMO single column model underestimates SH. Given that COSMO-LES and COSMO use the same surface layer scheme (and therefore the same algorithm for the computation of the transfer coefficients), the origin of the underestimation can lay in a systematically too small vertical temperature gradient within the surface layer or too small wind speed at the lowest model level. Later in this section, it will be showed that the second one is the main source of the SH systematic underestimation. By comparing the SH scores in COSMO TKE and COSMO TKE-2Tiles, it is clear as the introduction of the tile approach reduces the BIAS and the RMSE, especially in the less stable cases. Figure 6.4 shows the relative improvement of using a tiled surface layer in COSMO (in term of ratio between the COSMO simulation respective RMSEs, therefore the lower the better) as a function of the grid cell stability parameter ξ.

The tile approach manifests the larger improvements in cases from weak to moderate stability, while at $\xi \geq 1$ the benefit is marginal. This functionality takes origin from the bell shape of the SH for positive ξ (e.g. Luhar et al., 2009, , see also section 1.2.1): SH is weak near neutrality, at increasing stability it reaches a maximum and finally decreases to weak values. Depending on the stability in each thermal patch, the benefit of using the tile method to represent the cell average can be small or large. Figure 6.5 shows an example of a case in which the tile approach can give a large benefit (assuming that the tile fluxes perfectly match the ones of the LES thermal patches). In

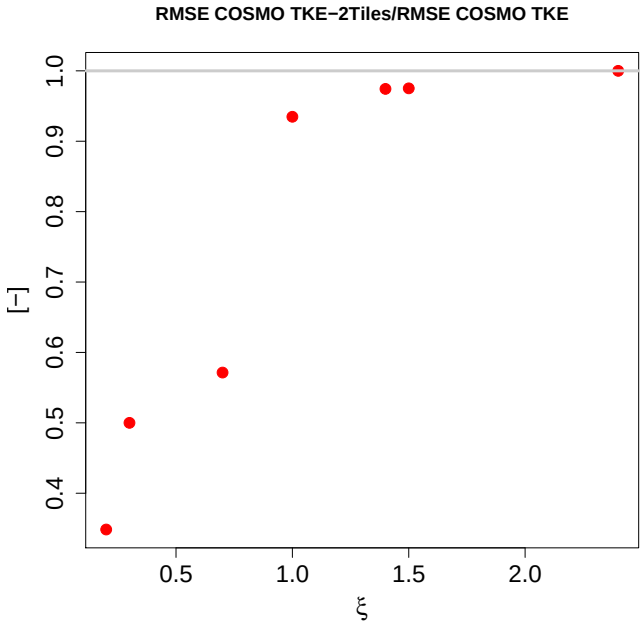

Figure 6.4: RMSE of COSMO TKE-2Tiles normalized over the RMSE of COSMO TKE plotted as a function of the cell average stability parameter ξ

this example (corresponding to 'NSPA' case) the patches falls respectively on the two sides of the bell, and their average is lower than the homogeneous terrain SH, which is instead close to the flux maximum. Vice versa, a case with a null benefit is when both the patches falls on the right side of the bell and their sensible fluxes are weak: their average will approximate the homogeneous terrain value, as the latter will be in more stable condition with similarly weak SH flux.

Following this consideration, it is possible to explain the benefit/neutrality on the vertical lapse rate in using the tile method in COSMO. Figure 6.6 shows the θ profiles simulated by COSMO-LES and COSMO in both the TKE and TKE-2Tiles version in three cases characterized by different stability conditions, i.e. in cases 'SPA', 'NSPA' and 'SSPA'. In the less stable cases 'SPA' and 'NSPA', the tile method produces a benefit on the thermal profile, leading to more mixed PBL. In the most stable case, 'SSPA', the tile use is neutral in term of thermal profile, since this case falls in the weak SH fluxes situation previously described.

Figure 6.6,a requires some more considerations since it presents an unstable air layer between 25m-80m above a weakly stable PBL. In SPA case, the surface temperature is prescribed to slightly increase in the warm patches along the first 8 hours of simulation, (Figure 6.2). This is a quite rare situation in nature compared to the mostly common case of differential cooling (an example are the breaking of sea ice leaving open water areas, polynyas, warmer than the ice surface). The unstable stratification in the internal boundary layer over the warm patch can cause non-linear dependencies

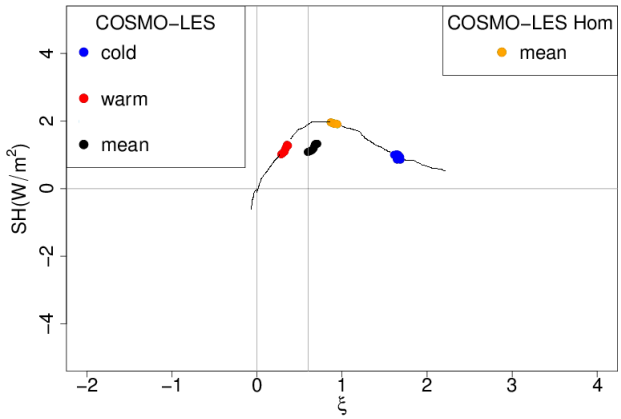

Figure 6.5: Surface sensible heat fluxes in several points of the COSMO-LES domain in 'NSPA' case over the last 2 hours of simulation. Points site over the warm patch in condition of minimum effect of advection (warm) and over the cold patch in condition of minimum effect of advection (cold). For comparison the average surface sensible heat flux in COSMO-LES simulation of the same case over homogeneous terrain is also reported. Moreover, a sketch of the bell shape of SH is added.

and can finally lead to an average convective boundary layer. This is exactly what occurs in the COSMO-LES idealized experiment along the hours 1-8 (not shown). In the following 4 hours, the surface temperature cools at the average rate of $-0.25K/h$ over the full domain. In this period, on average, a stable boundary layer develops underneath the residual unstable layer, explaining Figure 6.6,a. In this elaborate situation, COSMO using the tile approach approximates the well mixed COSMO-LES simulation but can not produces the unstable residual layer. Evidently, COSMO TKE-2Tiles did not manage to represent in the previous hours the average convective regime.

6.4.2 Tile approach: non-fulfillment of the assumptions

In the introduction, the hypothesis on which the tile approach is based are already mentioned. They are:

- the advection between patches is smaller than vertical exchange, and can thus be neglected,
- the horizontal homogeneity is reached within the lowest model level

The idealized cases are herein considered in terms of the degree of fulfillment of these hypothesis, in order to pinpoint the role of these assumption breakouts in the tile performance. Again, sensible heat fluxes are used as first indicators of the tile performance.

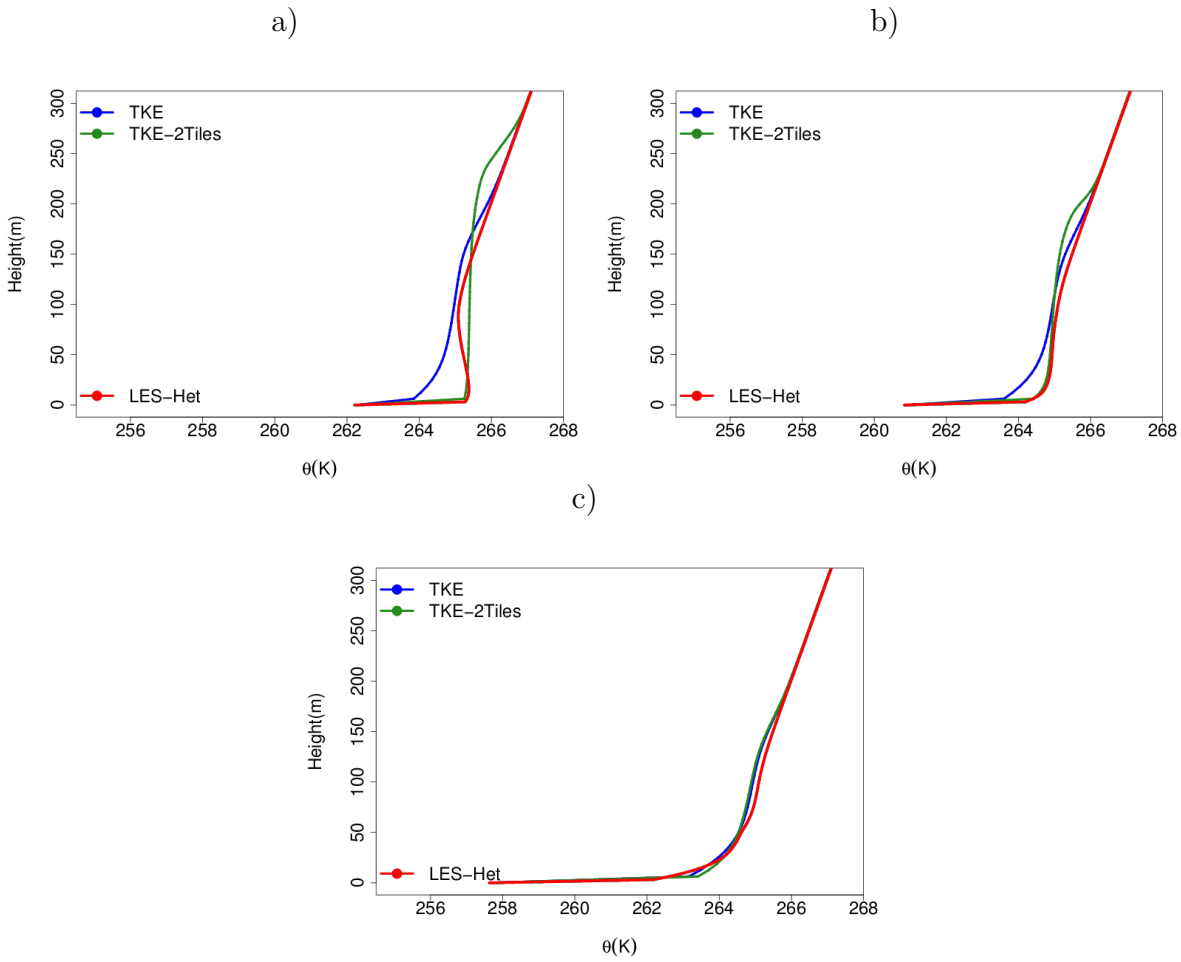

Figure 6.6: Mean vertical profiles of potential temperature in 'SPA' (a), 'NSPA' (b) and 'SSPA' case (c) simulated by COSMO-LES and by COSMO single column in 'TKE' and 'TKE-2Tiles' version

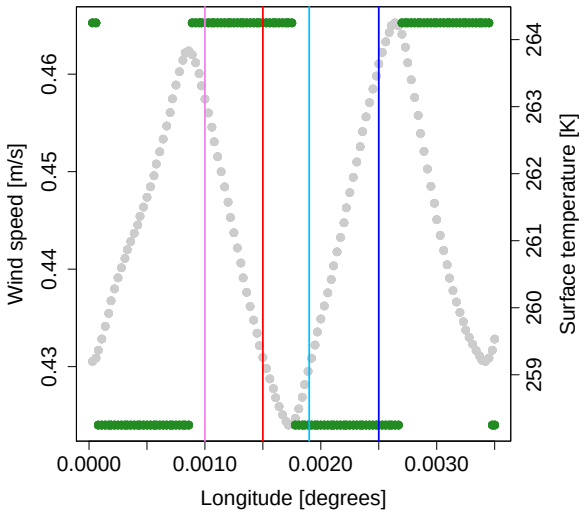

Figure 6.7: Modulation of wind horizontal advection at the lowest model level (grey dots) and prescribed surface temperature (green dots) over the domain in 'NSPA' case after +10h of simulation performed by COSMO-LES. Color vertical lines indcates grid points used in the analysis for minimum and maximum advection effect over the warm and cold patches (wind blows from left to right)

Thermal circulation

The inter-patches advection (or thermal circulation) is the response to the local convergence/divergence over the warm/cold patch in the surface vicinity. Figure 6.7 evidences the thermal circulation as a modulation of the horizontal advection at the lowest model level ($z = 3.125m$) over the thermal patches in 'NSPA' case after +10h of simulation performed by COSMO-LES. The wind speed blows from left to right in the plot. It is maximum in the transition between the cold and warm patches and minimum in the transition between the warm and the cold patches, as a consequence of the local convergence over the warm patch. In the 'NSPA' case, the convergence/divergence are associated to a weak vertical upward/downward flow over the warm/cold patch (not shown).

Table 6.3 reports the amplitude of the wind modulation $\Delta u = u_{max} - u_{min}$ and of its ratio to the domain average value $\overline{u}$. They are generally proportional, as the strongest circulation is associated to the strongest mean wind, and vice versa (as evidenced in Figure 6.8,a). Indeed in the windiest cases, more kinetic energy is available for secondary motions, while the opposite is valid in less windy cases. Based on the same kinetic energy availability consideration, it can explained the observed inverse proportionality between the amplitude of the wind modulation and the mean atmospheric stability (as evidenced in Figure 6.8,b). Moreover, from Table 6.3, it can be evidenced a direct proportionality between the thermal circulation and the thermal con-

Cases	ξ	Δu	$\Delta\overline{u}/\overline{u} * 100$	ΔT
SPA	0.2	0.11	11.45%	0.026
NSPA	0.7	0.11	12.1%	0.018
SSPA	1.4	0.07	6.4%	0.027
NSPA-lowU	2.4	0.02	3%	0.005
NSPA-highU	0.3	0.16	12.8%	0.047
SSPA-lowTC	1.5	0.01	2.5%	0.020
SSPA-highTC	1.0	0.05	9.5%	0.031

Table 6.3: RMSE of COSMO 'TKE' and 'TKE-2Tiles' in simulating the grid cell sensible heat flux (RMSE SH) over the last 2 hours of simulation (hours 10-12) in the idealized experiments. Grid cell stability parameter (ξ) averaged over the same period is also reported, as well as the intensity of secondary advection ($\Delta u = u_{max} - u_{min}$), the same normalized on $\overline{u}$ and the amplitude of temperature variation at level $z = 3.125m$

trast between the patches (compare cases 'SSPA-lowTC','SSPA' and 'SSPA-highTC'): the larger the contrast, the stronger the secondary advection. This dependency follows a flux-gradient relation, but the few amount of cases considered in this idealized experimentation precludes a meaningful definition of the proportionality.

In principle, the thermal circulation impacts on the patch surface SH fluxes, due to the modulation of wind and of temperature (due to the advection of the patch internal PBLs) at the lowest model level (remember bulk flux formulation in eq. 2.7). While the temperature modulation at this level (z=3.125m) is quite small (on the order of $10^{-2}K$, as shown in Table 6.3), a larger impact can be associated to the wind modulation, which can be on the order of $\approx 10\%$ of the mean wind. Therefore, a first estimate of the inter-patch advection effect on SH can be done neglecting the variation of thermal vertical delta. In this case, the cold advection over the warm patch would lead to more intense SH flux, with respect to grid points for which the cold advection is marginal, because the secondary advection is maximum (see Figure 6.7). Similarly, the advection of warm air over the cold patch would lead to weaker SH flux, with respect to grid points for which the advection of warm air is less intense, because the secondary advection is minimum (see Figure 6.7). Figure 6.9 reports the sensible heat fluxes simulated by COSMO-LES in different grid points of the model domain that are more or less affected by advection. Cases 'SPA', 'NSPA' and 'NSPA-highU' are considered, as they present the largest amplitude of the wind speed. In all these cases, the effect of warm air advection over the cold patch is indeed to weaken the SH flux. Instead, the effect of cold air advection over the warm patch is not always to strengthening SH. Rather, in the less stable cases ('SPA' and 'NSPA-highU'), the SH decreases due to the cold advection effect. Therefore, in these two cases, the consequences of the temperature modulation in term of variation of thermal vertical delta and transfer coefficient computation are not negligible. Moreover, the inter-patch advection in these less stable cases is relevant in term of breakout of the tile assumption for two reasons:

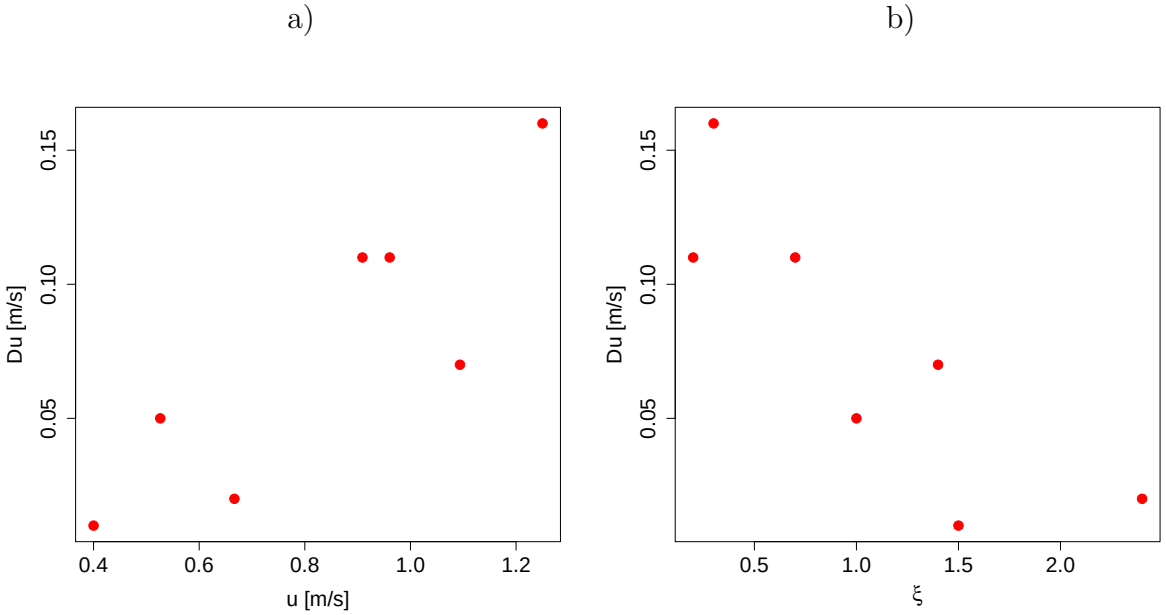

Figure 6.8: Amplitude of wind speed modulation ($\Delta u = u_{max} - u_{min}$) as a function of the domain mean wind speed (a) and stability parameter (b) in the different idealized cases

- the consideration of the cold advection over the warm patch can make the difference between a stable or an unstable warm patch (this is valid in particular for case 'SPA' in Figure 6.9,a). Indeed, in the hypothesis of a tile approach perfectly simulating the SH over the warm patch, but by definition not considering the inter-patch advection, the warm patch will be wrongly seen as stable

- the advection effects over both the cold and warm patches is to reduce the downward sensible heat flux. Therefore, their impacts is not counterbalanced on the computation of the domain average SH. Indeed, in the hypothesis of a tile approach perfectly simulating the SH over the warm patch, but by definition not considering the inter-patch advection, the averaged SH will be too downward.

Away from these less stable situations, the effects of inter-patch advection on the warm/cold patches SH fluxes is smaller and tends to be counterbalanced (advection increases downward flux over the warm patch and reduces it over the cold patch) when averaging over the domain. Therefore, in the hypothesis of a tile approach perfectly simulating the SH over the warm patch, but by definition not considering the inter-patch advection, this neglection will results in marginal effect on the averaged SH.

Finally, the impact of the secondary advection on the performance of the tile approach as it is implemented in COSMO single column is considered. In Figure 6.10, the ratio between the RMSE of COSMO TKE-2Tiles and of COSMO TKE for the SH

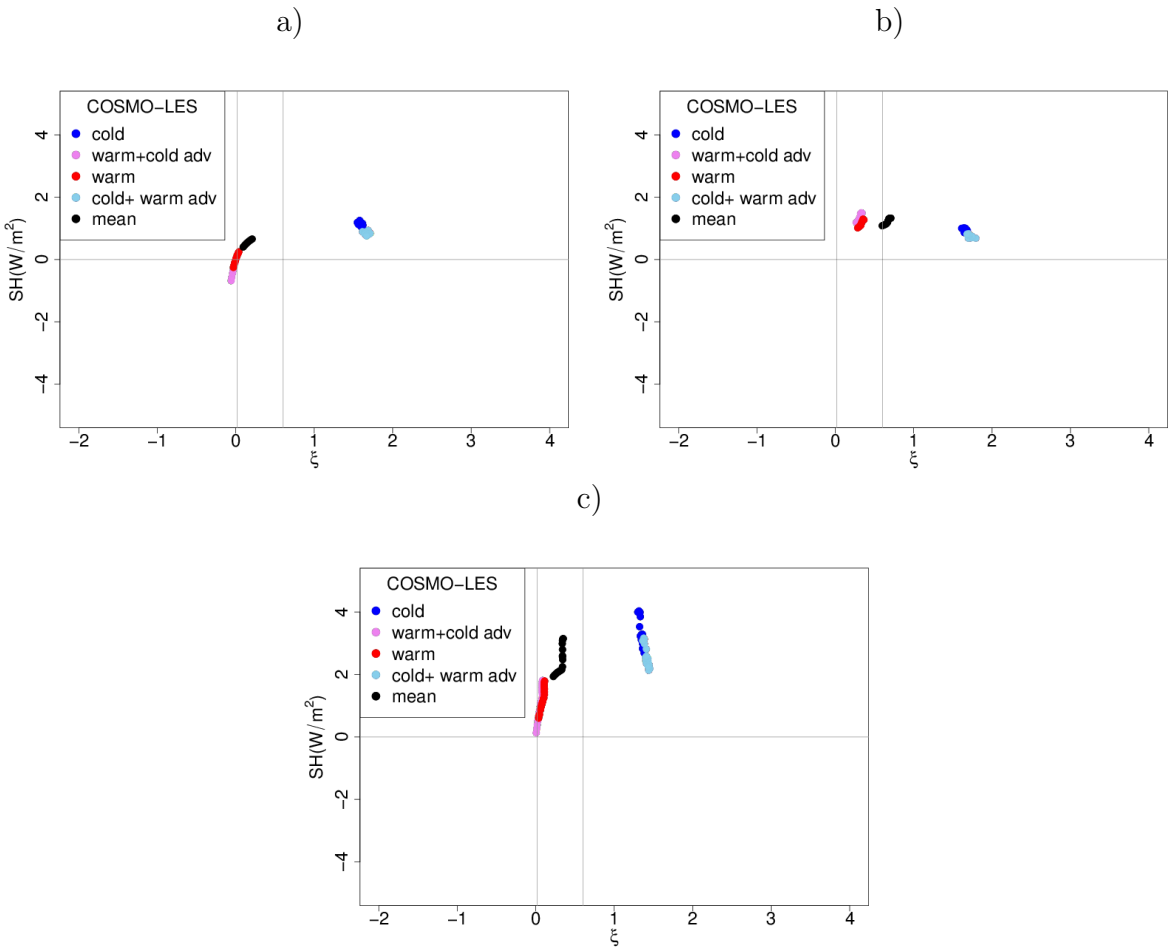

Figure 6.9: Surface sensible heat fluxes in several points of the COSMO-LES domain over the last 2 hours of simulation in 'SPA' case (a), 'NSPA' case (b) and 'NSPA-highU' case. Points site over the warm patch in condition of minimum or maximum effect of advection (respectively labelled 'warm' and ' warm+adv') and over the cold patch in condition of minimum or maximum effect of advection ((respectively labelled 'cold' and ' cold+adv'). The selected grid points are indicated by color lines in Figure 6.7

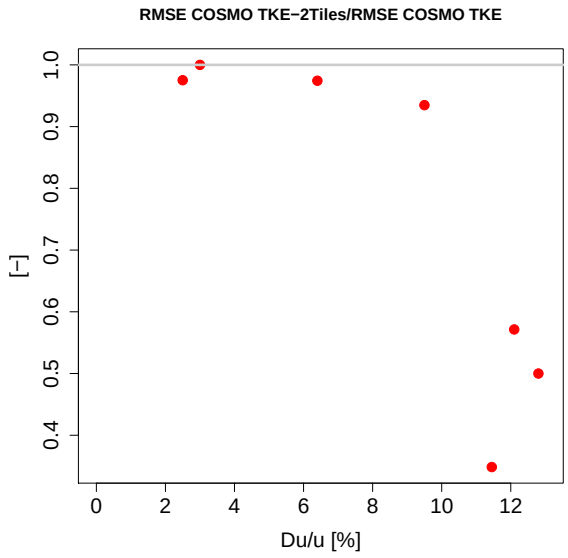

Figure 6.10: RMSE of COSMO TKE-2Tiles normalized over the RMSE of COSMO TKE plotted as a function of the cell average circulation normalized on the mean wind speed

flux in the idealized experiments are plotted as a function of the normalized secondary advection. The smaller the ratio is, the larger is the improvement due to the tile introduction. The plot shows that the larger improvements are exactly for the cases with larger secondary advection. This contrasting result can be understood as a consequence of the thermal circulation dependency on stability (Figure 6.8). Since the largest circulations develop in less stable cases and since the tile approach is particularly effective in these cases, thus the tile method improves these cases, independently on the circulation intensity. It appears therefore that the tile method in its implementation in COSMO in the studied cases does not suffer for the neglect of thermal circulation. Clearly, the studied cases represent only a subset of real situations, and negative consequences due to the neglect of thermal circulation can arise. As demonstrated, less stable cases are the most vulnerable to such occurrences.

Homogeneity assumption

The lowest model level of COSMO single column model is located at $z = 6.25m$. The tile method assumes that at this level the atmosphere is horizontally blended. In Table 6.4, they are reported the amplitude of modulation of wind and temperature at $z = 6.25m$ in COSMO-LES simulation. Compared to the modulation of the same variables at level $z = 3.125m$ (reported in Table 6.4), they are one order of magnitude smaller. Therefore, it is reasonable to consider that homogeneity assumption is fulfilled in all the cases in the present experimentation. An additional confirmation comes from the fact that the tile performance does not depends on the amplitude of these modulations, as depicted

Cases	ξ	$\Delta u(z = 6.25m)$	$\Delta T(z = 6.25m)$
SPA	0.2	0.013	0.004
NSPA	0.7	0.026	0.015
SSPA	1.4	0.017	0.007
NSPA-lowU	2.4	0.001	0.002
NSPA-highU	0.3	0.09	0.113
SSPA-lowTC	1.5	0.001	0.006
SSPA-highTC	1.0	0.033	0.012

Table 6.4: RMSE of COSMO 'TKE' and 'TKE-2Tiles' in simulating the grid cell sensible heat flux (RMSE SH) over the last 2 hours of simulation (hours 10-12) in the idealized experiments. Grid cell stability parameter (ξ) averaged over the same period is also reported, as well as the intensity of secondary advection ($\Delta u = u_{max} - u_{min}$) and the intensity normalized on $\overline{u}$.

in Figure 6.11.

6.4.3 Tile approach interaction with turbulence equations

This section deals with the consequences of the tile introduction on the representation of the SBL turbulence. The focus is on the ability of the turbulence scheme, when associated to a tiled surface layer, to mimic the structure of the SBL over heterogeneous terrain. Three different options are considered: 1) the TKE turbulence scheme operational in COSMO, 2) the full second order TKESV scheme and 3) the same but introducing Dirichelet lower boundary condition to the θ variance equation.
The reference is COSMO-LES, which represents the consequences of the surface heterogeneity on the SBL in agreement with the theory: the increment of the potential temperature variance near the surface decreases the negative buoyancy flux, which in turn allows TKE to rise and the SBL to be more mixed (see Figure C.3 in Appendix C). While in COSMO-LES the surface heterogeneity firstly affects the θ variance, in COSMO applying the tile approach the heterogeneity information is conveyed through the surface fluxes, and mainly the sensible heat flux SH, as the tiles have different vertical thermal delta. The variation of SH influences the surface-atmosphere coupling within the model surface layer and the vertical temperature profile aloft, as shown in Figure 6.6. These changes interact with the turbulence equations in two manners: at first via the buoyancy flux $\overline{w'\theta'}$ (which is proportional to the vertical θ gradient) as it is a sink in the TKE budget equation, and secondly via the eddy diffusion coefficients (which as well depend on stratification). Via the diffusion coefficients, also $\overline{w'u'}$ changes and thereupon the vertical wind profile. These logical steps are recognisable in Figures 6.12 and 6.13, where the profiles of the different mentioned variables are shown for the case NSPA (these logical steps are detectable in all the idealized cases considered). As already shown in Figure 6.6, COSMO TKE-2Tiles presents a more mixed and deeper

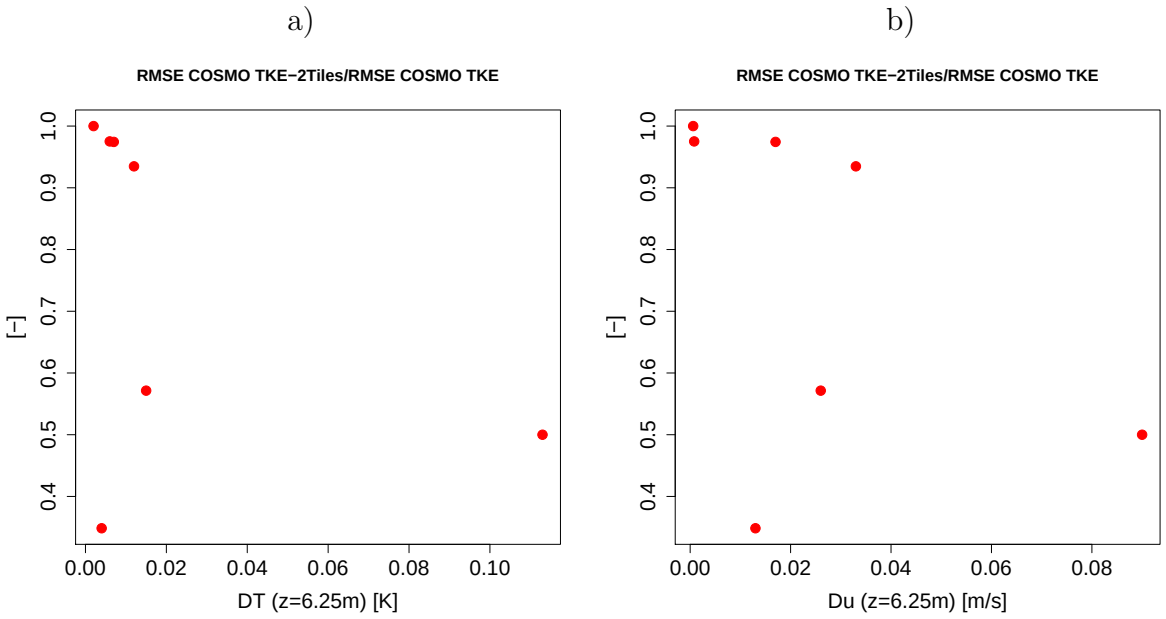

Figure 6.11: RMSE of COSMO TKE-2Tiles normalized over the RMSE of COSMO TKE plotted as a function of temperature variation ($\Delta t = t_{max} - t_{min}$) and wind speed variation ($\Delta u = u_{max} - u_{min}$) at level $z = 6.25m$ corresponding to the lowest model level in COSMO. Results are averaged over the last two hours of simulation

SBL, especially in the upper half of the SBL. In the surface vicinity, a thin layer of strong stratification develops as a consequence of the surface temperature cooling. The largest impacts on SBL turbulence in the 'NSPA' case are induced in the middle of the SBL, where the less stable stratification yields to more intense K^M and K^H (Figure 6.13). They in turn causes stronger turbulent fluxes and TKE in the upper half of SBL, as well as more homogeneous wind profile. Moreover it is also visible the direct reaction of the buoyancy flux to the reduction of vertical lapse rate in the surface vicinity when the tile approach is applied.

The use of a full second order turbulent scheme, in spite of the truncated version operational in COSMO, has two main actions: at first the prognostic solution of the θ variance equation yields to modified diffusion coefficient for heat K^H and momentum K^M, and secondly, the counter gradient term in $\overline{\theta' w'}$ reduces the negative buoyancy. The former effect is well recognisable in Figure 6.13 when comparing the COSMO TKE-2Tiles with the COSMO run applying the tile and the TKESV turbulence scheme (later referred to as 'COSMO TKESV-2Tiles'): the prognostic solution of the potential variance leads to larger K^M and smaller K^H, which respectively produce larger $\overline{u' w'}$ and smaller $\overline{\theta' w'}$. In conclusion, both these secondary effects increase TKE, as they are part of the TKE forcing terms. Vice versa, the expected reduction of $\overline{\theta' w'}$ caused by the TKESV scheme via the counter gradient term of $\overline{\theta' w'}$ in not visible, not even if the lower boundary condition for the potential temperature variance is enabled. Indeed, even in this case (labelled 'COSMO TKESV-LBC-2Tiles'), the more relevant effect is caused by a further increment of K^M and K^H, which yields to a strengthening of the turbulent flux and consequently of TKE.

6.4.4 Representation of the vertical SBL structure

The assessment of the performance of the different COSMO configurations compared to COSMO-LES is not easy, since divergences between COSMO and COSMO-LES are quite relevant already in the reference COSMO TKE, especially in terms of wind speed (which is underestimated) and in the upper half of the SBL in terms of turbulent variance/covariances (which are overestimated). Therefore, a realistic evaluation can be done only considering the lower half of the SBL, i.e. approximately the lowest 50m. In this sense, it is possible to assess the COSMO performances compared to COSMO-LES in the different environmental conditions described by the idealized case studies. The vertical profiles in the lowest 50m of θ, wind speed, turbulence variances and covariances are here considered in their domain average and temporal average over the last two hours of simulation. Vertical profiles of these variables in the various COSMO configuration and in COSMO-LES are visualized in appendix E. The statistical scores bias and RMSE are computed comparing COSMO configurations with COSMO-LES along the vertical profiles in the lowest 50m. Full results are reported in Table E.1 in appendix E. Figure 6.14 shows the relative improvement/deterioration associated with the tile method coupled with different turbulence schemes with respect to COSMO

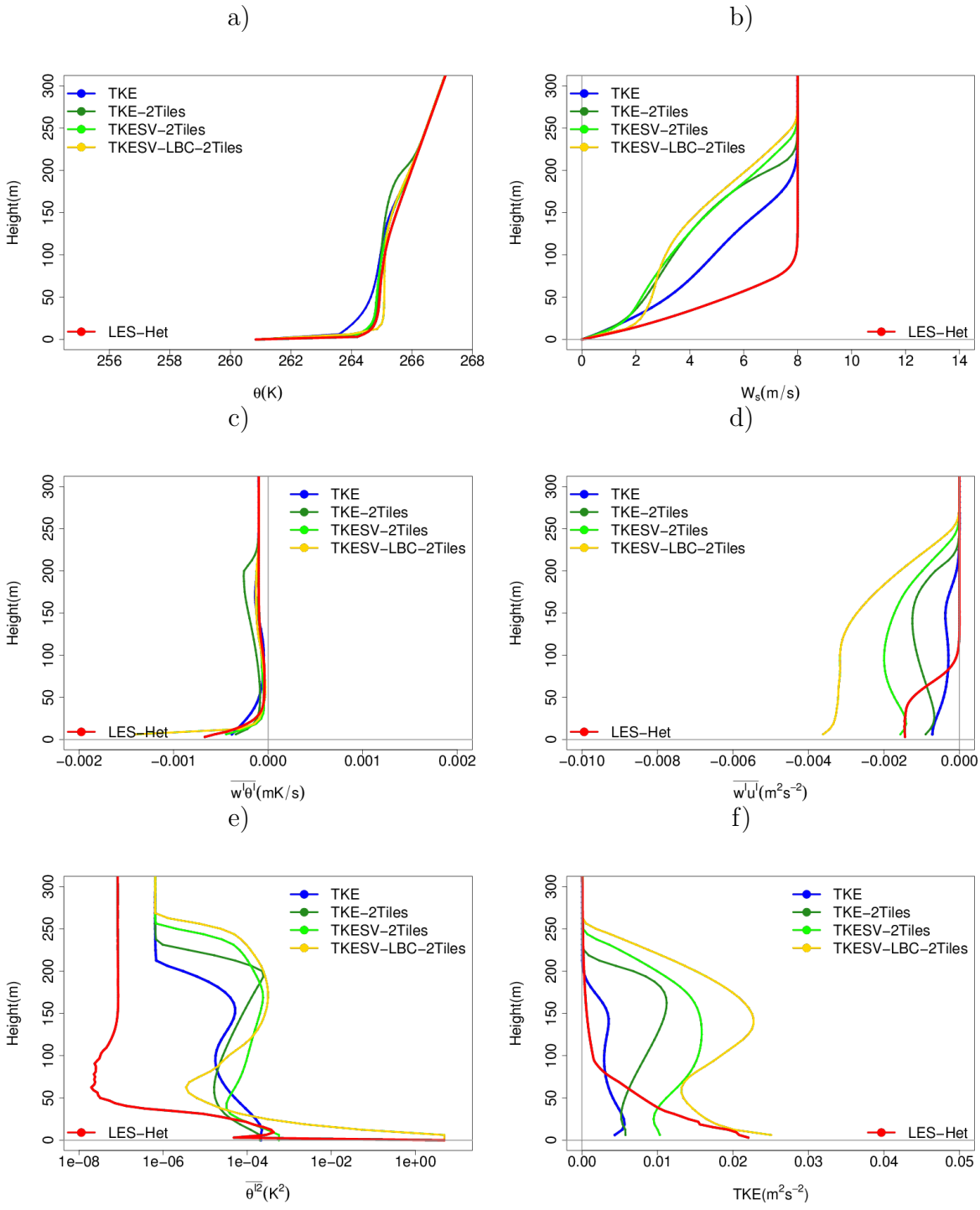

Figure 6.12: Domain average of the vertical profiles of potential temperature(a), wind speed(b), vertical temperature flux (c), vertical momentum stress (d), variance of potential temperature (e) and TKE (f) averaged over the last 2 hours of simulation as simulated by COSMO-LES and by COSMO single column applying different configurations, as in legend

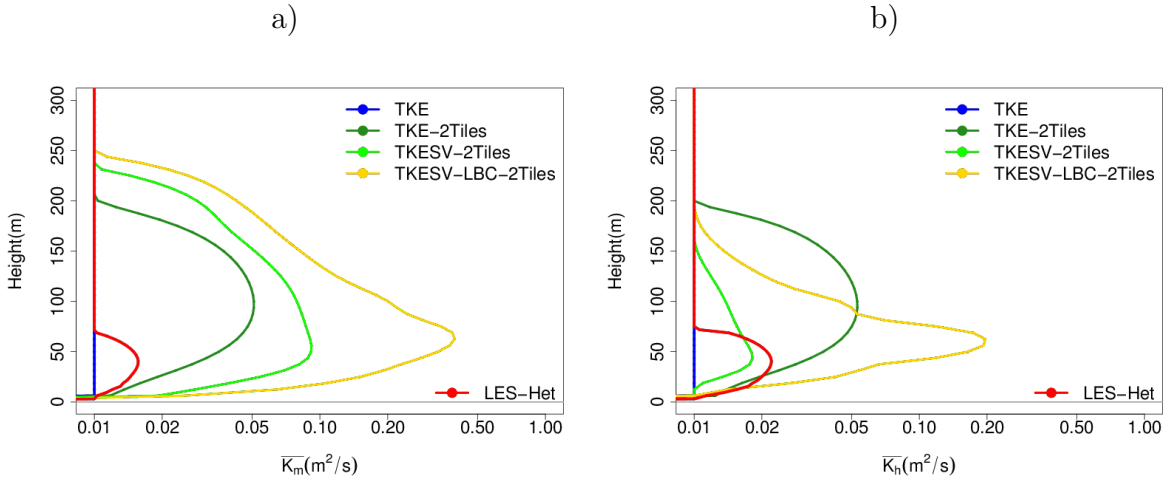

Figure 6.13: As in Figure 6.12, but for the momentum (a) and heat (b) diffusion coefficients

TKE, for the previously mentioned variables. In practice, the plots show the ratio between the RMSEs of the tiled COSMO versions and of COSMO TKE. In this way, values lower/greater than 1 indicate a improvement/deterioration produced by the use of tile, and the values close to 0 pinpoints the best performing combination. The ratios are plotted as a function of the domain average stability parameter in order to evidence a possible dependency on this factor. The values of ξ in each idealized case are reported in Table 6.2. The plots evidence that:

- the introduction of the tile approach is beneficial for the vertical profiles of θ and of $\overline{w'\theta'}$ (but only if the TKESV turbulence scheme is applied), it is neutral for the vertical profiles of TKE and of $\overline{w'u'}$, while it is detrimental for the wind speed. This latter point is due to the strong wind speed underestimation that COSMO single column shows in any configuration: the use of tiling increments this already present feature of COSMO.

- the use of TKESV turbulence scheme associated to the tile method improves the representation of the buoyancy flux, which would be otherwise deteriorated by the use of the tile approach coupled with the lower order turbulent scheme TKE. The selection of a specific turbulent scheme in combination with the tile method is neutral for the other considered variables

- the introduction of the lower boundary condition into the θ variance equation deteriorates the representation of the profiles of θ and the covariances, is neutral for TKE and improves the wind speed

- the improvement associated to the tile approach introduction shows a dependency of the average stability only in the potential temperature profile, as already observed in Figure 6.6.

In conclusion, the tile approach is either beneficial or neutral for the representation of the vertical structure of the SBL over heterogeneous terrain (the only exception is wind speed, which is nevertheless affected by large error already in the COSMO reference version). In terms of turbulence scheme, there is small difference between using TKE or TKESV scheme. Nevertheless, it is suggested the application of the second one to improve the buoyancy flux simulation. Moreover, the consideration of the Dirichelet lower boundary conditions in the scalar variance equation is not beneficial. Possible reasons of this failure include the applied method (Neumann or mixed boundary conditions could be more appropriate in the present application, E. Machulskaya pers. comm.) and the implementation in the COSMO code (currently the boundary condition is described in the manner that θ variance at the lowest model level is set equal to the surface value).

6.5 Conclusions

The present chapter dealt with the open questions regarding the introduction and the performance of the tile approach in a mesoscale NWP model in order to describe the SBL structure over thermally heterogeneous terrain. Through idealized experiments, SBL cases in different stratification, advection and surface thermal contrast conditions have been considered. The COSMO model has been used in two different configurations both as the best representation of nature (COSMO-LES) and as the best representation that a mesoscale NWP model in short tail version can do of nature (COSMO in single column version at 2km of resolution).
The tile approach significantly improves the representation of the grid cell surface sensible heat flux for SBL cases up to weak/moderate stability regimes ($\xi \leq 1$), while the improvement is marginal for more stable PBL. The explanation is related to the non-linear behaviour of the sensible heat flux at increasing stability and to the respective local stability regime over the thermal patches. As a consequence of the surface fluxes enhancement, in the same stability conditions ($\xi \leq 1$), also the vertical profiles of potential temperature experience a net improvement, well representing the larger vertical homogeneity associated to surface thermal patchiness (Mironov and Sullivan, 2016). The magnitude of the buoyancy flux in the lowest layers is also better represented by applying the tile approach, but only in combination with a full second order turbulence scheme. With respect to other variables related to turbulence (TKE, $\overline{u'w'}$), the tile introduction is neutral. Detrimental effect has been found for wind speed, which resulted more homogeneous in an already too homogeneous SBL with respect to wind (this issue is associated to an intrinsic difference between a 2km resolution model and a LES model and the tile approach magnifies divergences). The benefit of the use of a full second order turbulence scheme in spite to a truncated version of it (solving θ'^2 equation diagnostically only) resulted limited to the buoyancy flux. However, this scheme version does not consider the pivotal surface value of θ'^2 in its implementation. A scheme version in which this information is conveyed via Dirichelet lower boundary condition has been also tested, but with negative outcome. It is possible that the development

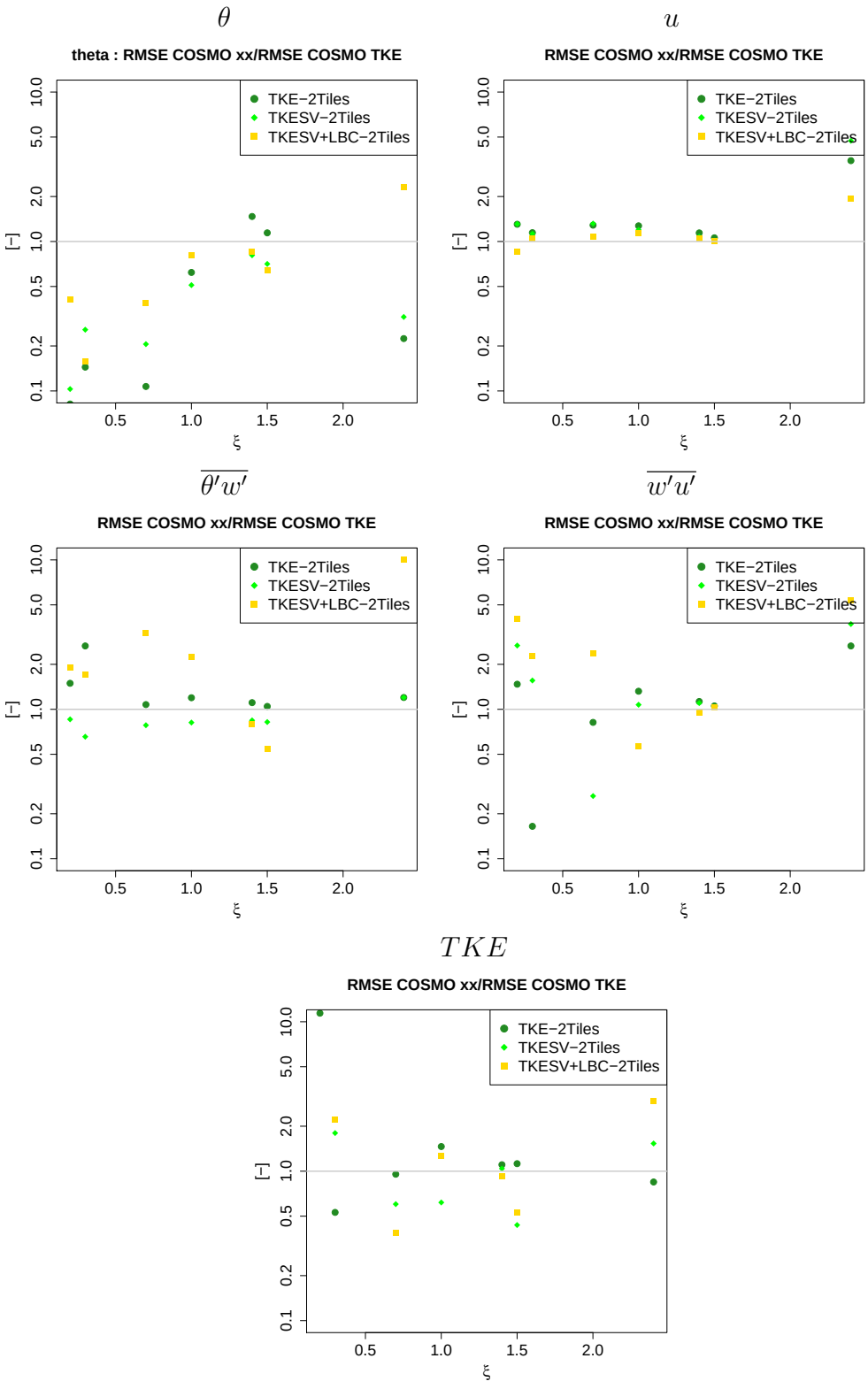

Figure 6.14: Ratio between the RMSEs of the tiled COSMO versions (TKE-2Tiles, TKESV-2Tiles, TKESV+LBC-2Tiles) and of COSMO TKE plotted as a function of the domain average stability parameter

of a specific lower boundary condition for the θ'^2 equation extends the improvement associated to surface flux, lapse rate and buoyancy flux in a tiled model also to the other turbulence variances/covariances.
Moreover, the behaviour of thermal circulation (inter-patches advection) has been considered, as well as the weight of its neglect by the tile approach. This secondary circulation showed a dependency with the average stability, resulting stronger in less stable PBLs (when more kinetic energy is available and vertical motions are less suppressed). Its neglect is particularly dangerous in these cases, where it yields to an overestimation of the downward sensible heat fluxes. In more stable cases ($\xi \geq 0.7$), the inter-patch advection is less intense and its effects on the sensible heat fluxes over the warm and cold patches counterbalances in the averaging operation. Consequently, a specific parametrization of the thermal circulation that considers all these findings is suggested as an addendum to the tile method.
Finally, the last open question regards the possibility that the introduction of the tile approach could help in describing an increment of cross-isobaric flow, which at the current state is accomplished by the long-tail formulations. The present analysis evidenced that the description of surface thermal heterogeneity by the tile approach has the potential to significantly modify the vertical structure of the SBL in mesoscale NWP model, producing more homogeneous and more mixed SBL. Therefore, it is reasonable to expect that such approach would improve the simulation of the cross-isobaric large scale flow that a short-tail model can provide. In order to verify this hypothesis, it will be necessary to test the tile method, optionally coupled the TKESV scheme (and with a well studied lower boundary condition to the θ'^2 equation), in real case studies, over thermally heterogeneous terrain, and to investigate the consequences both at the local SBL scale and at the large synoptic scale.

Chapter 7

Conclusions

In the introduction, the main aim of the thesis was stated as being:

to investigate the critical points in the SBL representation in specific long-tailed turbulence and transfer schemes operationally applied in a numerical weather prediction model, and to formulate and evaluate potential solutions to them

The use of long-tail formulations (i.e. low limit to turbulent diffusivity, Beare et al., 2006) is a common practice in operational NWP since the 90's (e.g., Beljaars and Viterbo, 1998; Sandu et al., 2013; Holtslag et al., 2013). It is motivated by the link between small scale turbulent diffusivity and synoptic scale processes, since it prevents a decay of the large scale scores (e.g. cyclone filling). Conditions of scarce diffusivity in the PBL, as in the case of stable stratification, are particularly sensitive to the use of long-tail. Among the several open challenges in SBL modelling, the need for a more accurate representation of the complexity within grid boxes (i.e. flow patterns generated by subgrid scale heterogeneities) in SBL is developed in the thesis.
The question has been explored using the COSMO (Consortium for Small-Scale Modelling) model, the reference model for the limited area numerical weather prediction in Italy. The COSMO operational turbulence scheme is a truncated second order scheme adapted from Mellor and Yamada (1982) at Level 2.5 (Raschendorfer, 2001; Wacker et al., 2005). The operational transfer scheme is based on the decomposition of the surface layer in sub-layers treated in terms of aerodynamic resistances and infers the turbulence state from the turbulence scheme.

The specific aims indicated in the introduction are reported in the following, together with the results from the thesis investigation. **1) To evaluate the performance of a specific operational NWP model in simulating real SBL conditions, compared to a short tail NWP model**
This first aim is addressed in section 2.4, in which the simulation performed by the COSMO model in its long tail (operational-like) version has been compared to the one performed by the WRF model using a short tail turbulence scheme and to observations

collected in the horizontally homogeneous site in the Po Valley (Italy) over a three-day period characterized by conditions favourable to the SBL development (clear sky, weak wind). The COSMO simulation shows in all the different types of the observed SBL (i.e. intermittent, transient, radiative):

- a too deep SBL, which is also too close to neutral stratification
- an overestimation of surface fluxes with increasing stability

The first point is intimately related to the several long-tail formulations introduced in the turbulence scheme, and consequently they induce too intense turbulent mixing in the scarcely diffusive SBL. The second point is partially caused by the mentioned long-tail over-mixing in the SBL, and by a theoretical inconsistency in the applied surface layer scheme. The same experiment performed with the short tailed configuration of WRF model shows:

- a SBL too close to neutrality and too deep in the radiative night and a SBL too stable and too shallow in the intermittent nights
- a lapse rate in agreement with observations in the surface vicinity in all the nights
- an underestimation of the surface fluxes of sensible heat and momentum under stable stratification (unrelated to the stability regime)
- better results in term of surface fluxes and near surface diagnostics (with the exception of wind speed at 10m) compared to COSMO under stable stratification

The first point confirms that the over-mixing of the SBL, in any kind of stability, observed in COSMO is associated to the use of long-tail formulation. In general the WRF simulation gives a better representation of reality than COSMO. However, it also appears that the long-tail removal does not produce by itself a perfect simulation. As stated in the Introduction, several open challenges affects the SBL description and other efforts will be required to cure other minor errors once the long tail necessity will be accounted in a different way.

2) To identify the turbulence-enhancing (or long-tail) formulations applied in the turbulence and transfer scheme, focusing on their impacts in different atmospheric and topographic conditions, to consider the consequences of their weakening/removal, and to propose alternatives to the specific cases in which the limit to low diffusivity is an unmeant side effect

Aim 2 is addressed in chapter 3 regarding the formulations of the operational COSMO turbulent scheme, and in chapter 4 for the part related to the operational transfer scheme. The four turbulence enhancing recipes, found in the turbulence scheme, are listed in the following:

1. the lower limit of the diffusion coefficients for momentum and scalars $K^{M,H}$ is the most known turbulence enhancing option introduced in COSMO (Buzzi, 2008; Volker et al., 2009; Heise, 2006; Köhler et al., 2011). It is set equal to a value higher than observational evidence ($K^{M,H}_{min} = 0.4m^2/s$ in the operational COSMO code at SIMC). In the present study, the reduction to a value non-influencing the turbulence scheme computation ($K^{M,H}_{min} = 0.01m^2/s$) over a 3D domain evidences a weak cooling of the near surface temperature and an intensification of the thermal inversion over flat terrain (where stable stratification is stronger), confirming the results from Volker et al. (2009). Despite the near surface simulation being on average weakly improved compared to observations over these areas, the forecast uncertainties grow via a numerical oscillation, which is associated to the parametrization of the subgrid surface thermal heterogeneity as a term of TKE equation.

2. the current scale interaction term introduced in the TKE equation, in order to account for the influence of the subgrid surface thermal heterogeneity on TKE, does not include any dependence on subgrid surface features (in absence of subgrid clouds). Moreover, it has a strong turbulent mixing effect at the lowest model levels (besides causing the deep oscillations previously mentioned). For these reasons, it is considered as a long-tail formulation. Its deactivation, associated with the reduced diffusivity limit ($K^{M,H}_{min} = 0.01m^2/s$), leads to a strong cooling at 2m, being beneficial over flat regions and deleterious over rough terrain regions (where thermal heterogeneity are most likely present). Therefore, the introduction of a modulation of this term with a subgrid scale feature (e.g. orography variance, as included in the ICON global model, G. Zängl, pers. communication) is suggested to improve the physical meaning of the interaction term and to reduce its long tail action.

3. the limit of the sum of the forcing term in the TKE equation is a less known long-tail formulation. It avoids the turbulence scheme to describe cases in which the stratification exceeds the very stable threshold $Ri_f \geq 0.19$, and in these cases the negative sink of TKE due to the buoyancy forcing is limited. The removal of such limit in a real case study yields to lower near surface temperature over mountains (stressing the model deficiencies in these areas), while the impact on very SBL in flat regions is very weak (likely because the presence of large $K^{M,H}_{min}$ hides it).

4. the limit to TKE associated to the treatment of the singularities and realizability constrains of the Mellor and Yamada (1982) scheme at Level 2.5 (see a description of the application in the COSMO model in Wacker et al., 2005) is a less known long-tail formulation. It prevents the turbulence scheme to describe cases of strongly growing turbulence under stable stratification (e.g. at the sunset). Several alternatives to the COSMO treatment of the singularities and realizability constraints were tested in order to remove/reduce the limit for stable

stratification. The only working option in 1D simulations consists in a merge of the Mellor and Yamada (1982) scheme at Level 2.0 (i.e. only in terms of stability function computations) and the Level 2.5 scheme, for $Ri \leq 0$.

Chapter 4 demonstrates that these long-tail formulations influence the operational transfer scheme as well, producing a transfer enhancement at high stability (i.e. detected as an overestimation of the surface fluxes). Indeed, the COSMO transfer scheme infers the turbulence state within the surface layer from the turbulence scheme, instead of using an empirically based stability dependency as in the Monin-Obukhov based transfer schemes. Additionally, a limit in the transfer scheme and, mainly a physical inconsistency in the selection of the interpolation function between the two nodes at which the turbulence equations are solved within the surface layer prevent the correct decay of transfer with increasing stratification, even when the long tail formulations are removed. In conclusion, only the combination of i) short-tailed turbulence scheme, ii) solved inconsistency in the interpolation function within the surface layer by using a hyperbolic function instead of a linear function and iii) use of a less strict limit to γ function, permits to avoid the transfer enhancing behaviour under strongly stable stratification of the operational COSMO model.

3) To assess the potential role of the neglected subgrid scale processes to overcome the operational need of turbulence-enhancing formulations in the SBL, and in particular considering a parametrization of two unresolved processes:
A) the parametrization of the kinetic energy transfer from circulations induced by subgrid scale orography to turbulence.
The parametrization is based on the hypothesis that subgrid scale motions, induced by subgrid scale orography (SSO), produce kinetic energy that can be accounted for by the turbulence scheme. By this extension, the kinetic energy extracted from the mean flow, by the action of SSO, is not immediately dissipated into inner energy, but is transported through all subgrid scale motions until it is finally dissipated. This hypothesis belongs to the framework of the Separated Turbulence Interacting with (non-turbulent and still unresolved) Circulations (STIC), developed by M. Raschendorfer, and it is already implemented in the operational COSMO code.
The parametrization applied on top of the long tail COSMO formulations, in conditions favourable to the development of stable stratification in the PBL, generates a large additional TKE above areas of pronounced SSO i) at the lowest model levels (due to the blocking influence of SSO), ii) at the top of the troposphere and iii) within the stratosphere in the regions of orographic gravity wave steepening. The consequences of these modifications, verified at the near surface in term of temperature and wind speed, imply a general improvement over high-topography regions. Over low SSO areas, a non-negligible increment of TKE is also observed within the SBL, yielding to a weak (but detrimental) increment of the already present positive bias of temperature (likely related to long-tail over-mixing).

The potential role of this parametrization, as an alternative to long tail formulations, is investigated through an inter-comparison in a real case study performed by three versions of COSMO: i) its long-tailed version, ii) its short-tailed version and iii) its short-tailed version plus this parametrization. This SSO-related term of the TKE equation shows the ability to cover a relevant part of the cross-isobaric flow gap existing between short and long tail formulations. The largest benefit likely derives from the increment of turbulent drag at different levels (both at the surface vicinity and in correspondence to gravity wave steepening or breaking). Thus, the incorporation of this parametrization in short tail formulation gives a more physical, but still partial answer, to the operational need to large cyclone filling tendency, with respect to teh long tail approach.

B) the parametrizations of the modification on the SBL structure induced by subgrid thermal heterogeneity of the surface.

The COSMO model already includes a parametrization attempting to describe the effects of a thermally heterogeneous terrain on the PBL, as a part of the turbulence scheme. However, as described in section 3.1, it does not achieve its aim, since it does not include on any surface subgrid features, and it is not suitable for the present purpose. Vice versa chapter 6 considers the use of an alternative approach, the "tiling" technique (Avissar and Pielke, 1989), by which the cell fluxes are aggregated from dishomogeneous sub-cell fluxes. The coupling of a tiled transfer scheme with a turbulence scheme under SBL rises a number of issues, including the fulfillment of the tile method assumptions, which order of turbulence scheme to use and which lower boundary conditions to pass to the turbulence equations. All these points are investigated through idealized simulations of different SBL cases over thermally heterogeneous terrain (with varying mean advection intensities, thermal contrast between the patches and mean surface cooling) performed by the COSMO model in 1D, and using COSMO-LES as a reference. The outcome is that the tile technique can represent the modification of the surface sensible heat fluxes and the reduction of vertically stratification induced by a subgrid scale thermal heterogeneity of the surface, being in fair agreement with the reference. The tile approach appears particularly beneficial for stability going from near neutral up to weak/moderate. Cases with weaker stability are more sensitive to the neglect of the horizontal advection between the subgrid thermal patches (assumed by the tile approach), which suggests the development of a specific parametrization to account for it. None of the turbulence schemes (second order truncated and second order schemes), when coupled to the tiled surface scheme, manage to fully describe the influence of the thermally heterogeneous terrain on the turbulent variances/covariances. This point will need further investigation.

In conclusion, the analysis evidenced that the description of surface thermal heterogeneity by the tile approach has the potential to significantly modify the vertical structure of the SBL in a mesoscale NWP model, producing less stable SBL. In particular, the action on the SBL mixing influences the cross-isobaric large scale flow, as described in section 1.3. Therefore, it is reasonable to expect a positive outcome from a tile implementation in these cases. The original question about the potential role of such parametrization

in substituting the long-tail formulations has been only partly addressed, and more experimentation is required to fully answer this point. Suggestions are presented in the following section.

7.0.1 Future work

This research suggests that at least part of the cross-isobaric filling effect, achieved by the long-tail formulations, can be represented by processes occurring at the subgrid scale currently neglected in NWP models. In particular, the analysis of the parametrization considering the kinetic energy transfer to the turbulence scheme induced by unresolved orography (chapter 5) confirms the previous statement. More effort will be necessary to fully confirm if the same is valid for the description of thermally heterogeneous terrain at the subgrid scale. In order to verify this hypothesis, it will be necessary to test the tile method, optionally coupled with the full second order scheme (and with a well studied lower boundary condition to the θ'^2 equation), in real case studies, over thermally heterogeneous surface, and to investigate the consequences both at the local SBL scale and at the large synoptic scale.
Moreover, several other neglected processes can be significant: i) gravity waves induced by small scale terrain disturbances, whose parametrization was demonstrated able to supply almost the same amount of cross-isobaric mass flux generated by the long-tail formulations (Steeneveld et al., 2008), ii) turbulent orographic form drag, which represents drag associated with subgrid orography elements with horizontal scales less than 5 km such as hills or individual mountains (Beljaars et al., 2004), iii) low level drag induced by trapped lee waves (Teixeira et al., 2013), etc..
Given that the use of long-tail formulations is a first order issue for SBL representation in operational NWP model, several other unresolved questions regarding SBL modeling are partly hidden by it and more work will be required to bring them to light in the future.

Chapter 8

Acknowledgements

I'm grateful to the several people that contributed in different forms to the development of this thesis. M. Raschendorder is particularly thanked for the several afternoons of discussion about the operational turbulence and transfer schemes of the COSMO model, for the technical help and for the original suggestions. E. Machulskaya gave as well a fundamental contribution in terms of theoretical support, stimulating conversations and brilliant ideas. I'm very grateful to all the members of the Numerical Modelling group at ARPAE-Emilia Romagna for their always helpful presence, to the whole SIMC group for their kind hospitality and for having funded part of this PhD research. Another thanks goes to the members of the COSMO community and to the Modelling group of ECMWF, whose interest for this work was a motivation to the effort. Finally, the theses Tutor, Prof. R. Rizzi, is thanked for the nice helpfulness also in critical situations, and of course the thesis Supervisor, Doct. T. Paccagnella is thanked for the continuous support, the firm trust, the positive and constructive exchanges from the very first day of this research.

Appendix A

Complements to the COSMO turbulence scheme

Vertical q diffusion term From eq. (2.1), it is:

$$q_{diff} = -\frac{1}{q\overline{\rho}}\frac{\partial}{\partial z}\left[\frac{1}{2}\overline{\rho q^2 w'}\right] \tag{A.1}$$

The vertical flux of q^2 is parametrized in the code following the K-theory :

$$\overline{q^2 w'} = -K_q \frac{\partial q^2}{\partial z}, \;\; K_q = MIN\left(securi \cdot \frac{(\Delta z)^2}{dt}, c_{diff} \cdot \overline{q} \cdot \overline{l}\right) \tag{A.2}$$

where $\overline{q}$ and $\overline{l}$ are the mean vertical values of respectively q and the mixing length between the level k at which the computation is done and the level below $k+1$ (e.g. $\overline{q} = 1/2(q_k + q_{k+1})$). Δz is half of the thickness between levels k+1 and k-1, c_{diff} is a factor for turbulent diffusion set equal to 0.2 and modifiable in the namelist and *securi* is a coefficient added in order to achieve numerical stability in the explicit solution (modifiable in namelist as well).
Substituting the flux parametrization (eq. (A.2)) in eq. (A.1) and making some further manipulations, the parametrization of q_{diff} applied in the model is obtained:

$$q_{diff} = -\frac{1}{\overline{\rho} \cdot q}\frac{\partial}{\partial z}\left(-\frac{\overline{\rho}}{2} K_q \frac{\partial q^2}{\partial z}\right) \tag{A.3}$$

$$= -\frac{1}{\overline{\rho} \cdot q}\frac{\partial}{\partial z}\left(-\overline{\rho}\, K_q\, q \frac{\partial q}{\partial z}\right) \tag{A.4}$$

$$= \frac{1}{\overline{\rho} \cdot q}\left[q\,\frac{\partial}{\partial z}\left(\overline{\rho} K_q \frac{\partial q}{\partial z}\right) + \overline{\rho}\, K_q \left(\frac{\partial q}{\partial z}\right)^2\right] \tag{A.5}$$

$$= \frac{1}{\overline{\rho}}\frac{\partial}{\partial z}\left(\overline{\rho} \cdot K_q \frac{\partial q}{\partial z}\right) + \frac{K_q}{q}\left(\frac{\partial q}{\partial z}\right)^2 \tag{A.6}$$

Appendix B

Complements to the COSMO transfer scheme

B.1 Derivation of the aerodynamics resistances

The transfer scheme applied in the COSMO model represents the surface layer (extending from the top of the canopy up to the center of the lowermost model level z_A) as the superimposition of two sub-layers (as depicted in the sketch in Figure B.1):

- the inertial or free atmosphere sub-layer, in which the fluxes are constant
- the roughness sub-layer, i.e. the atmospheric layer immediately above the canopy (roughness elements) in which the fluxes are affected by the canopy presence. A laminar component is included, in which the molecular diffusion is the dominant process

B.1.1 Inertial sub-layer

The inertial resistance represents the opposition to the transfer offered by air within the constant-flux layer, thus it can be expressed in the integral form between the roughness length z_0 and z_A:

$$r_{0A}^{\varphi} = \int_{z_0}^{z_A} \frac{dz}{K_{0A}^{\varphi}(z)} \tag{B.1}$$

where the specific turbulent coefficient $K_{0A}^{\varphi}(z)$ is assumed as the product of a turbulent length scale $l(z)$ and a turbulent velocity scale $u^{\varphi}(z)$:

$$K_{0A}^{\varphi}(z) = l(z)u^{\varphi}(z) \tag{B.2}$$

The turbulent length scale is defined as $l(z) = \kappa z$, while $u^{\varphi}(z)$ derives from the turbulence scheme, under provision of its functional dependence on z. Since the full turbulence scheme is applied at the upper boundary level $z = z_P$ of the lowest model

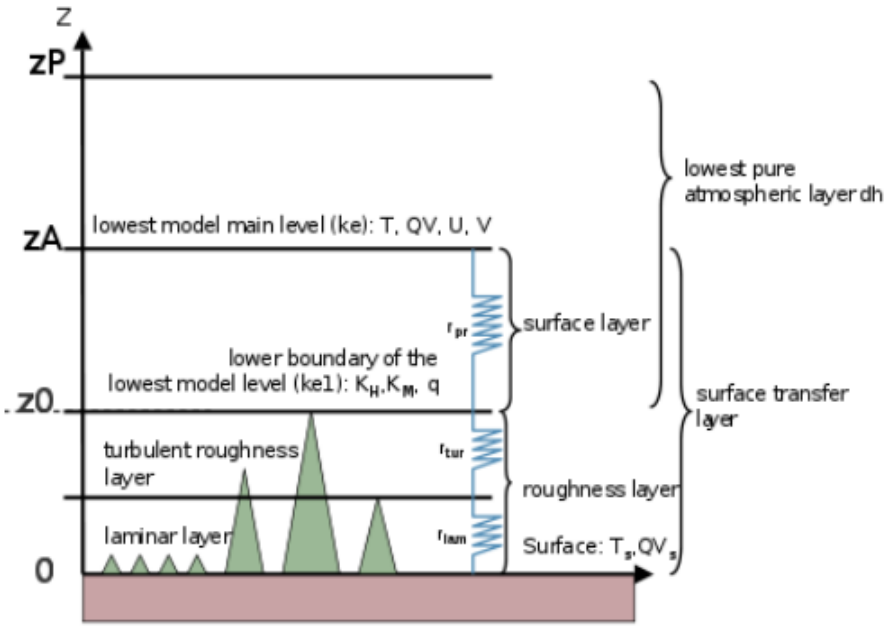

Figure B.1: Schematic representation of the vertical levels in the transfer scheme of the COSMO model (the labelled "laminar and roughness sub-layers" correspond in their associated form to the roughness sub-layer, while the labelled "surface layer" corresponds to the inertial sub-layer). Sketch modified from Buzzi (2008)

layer and additionally (in a reduced mode) at level $z = z_0$, the turbulent velocity scale u^{φ} is provided at these two levels of the vertical profile and the resistance integrals can be solved via an interpolation function for u^{φ} between those two nodes.

$$\begin{aligned} K^{\varphi}_{0A}(z = z_P) &= K^{\varphi}_P \\ K^{\varphi}_{0A}(z = z_0) &= K^{\varphi}_0 \end{aligned}$$

wherein K^{φ}_P and K^{φ}_0 are the turbulent diffusion coefficients derived at level z_P and z_0 respectively. The interpolation function for u^{φ} between those two nodes is assumed linear with z, in order to ensure the accordance with the MOST based formulations at least in the specific case of neutral stratification. The final formula applied in COSMO code can be derived integrating eq. B.1 in the following way.

$$r^{OA}_{M,H} = \int_{z_0}^{z_A} \frac{1}{l(z)u^{\varphi}(z)} dz \tag{B.3}$$

$$= \frac{1}{k} \int_{z_0}^{z_A} \frac{1}{zu^{\varphi}(z)} dz \tag{B.4}$$

Introducing the linear vertical dependency of $u^{\varphi}(z)$:

$$u^{\varphi}(z) = Az + B \tag{B.5}$$

where the coefficients A and B should represent the turbulence diffusivity within the surface layer. They can be expressed as a function of u_p^φ and u_0^φ by solving the system:

$$\begin{aligned} u_p^\varphi &= Az_P + B \\ u_0^\varphi &= Az_0 + B \end{aligned}$$

leading to:

$$A = \frac{u_P^\varphi - u_0^\varphi}{z_P - z_0} = \frac{\Delta u^\varphi}{\Delta z} \tag{B.6}$$

$$B = u_0^\varphi - \frac{\Delta u^\varphi}{\Delta z} z_0 = u_P^\varphi - \frac{\Delta u^\varphi}{\Delta z} z_P \tag{B.7}$$

Introducing them in the inertial resistance:

$$\begin{aligned} r_{OA}^\varphi &= \frac{1}{k}\int_{z_0}^{z_A} \frac{1}{z(Az+B)} dz = \\ &= \frac{1}{kA}\int_{z_0}^{z_A} \frac{1}{z^2 + B/Az} dz \end{aligned}$$

The term inside the integral can be treated transforming it into the form:

$$\frac{1}{z^2 + B/Az} = \frac{1}{z^2 + Dz + C - C} = \frac{1}{(z+\sqrt{C})^2 - C} \tag{B.8}$$

with $D = B/A = 2\sqrt{C}$. Substituting $(z+\sqrt{C}) = t$, the previous equation can be recast in :

$$\frac{1}{t^2 - C} = \frac{1}{(t+\sqrt{C})(t-\sqrt{C})} \tag{B.9}$$

The coefficients α and β that verify the previous equation are found through:

$$\frac{\alpha}{t+\sqrt{C}} \frac{\beta}{t-\sqrt{C}} \tag{B.10}$$

which are:

$$\alpha = -\beta = -\frac{1}{2\sqrt{C}} \tag{B.11}$$

Reintroducing the variables z, B and A, the inertial resistance can be recast in the subsequent form and solved:

$$\begin{aligned} r_{OA}^\varphi &= \frac{1}{kA}\int_{z_0}^{z_A} \frac{1}{B/A}\left(\frac{1}{z} - \frac{1}{z+B/A}\right) dz = \\ &= \frac{1}{kB}\left(\int_{z_0}^{z_A} \frac{1}{z} dz - \int_{z_0}^{z_A} \frac{1}{z+B/A}\right) = \\ &= \frac{1}{kB}\left(\ln\frac{z_A}{z_0} - \ln\frac{|z_A + B/A|}{|z_0 + B/A|}\right) \end{aligned}$$

Finally using the value of A and B expressed as in eq. B.6-B.7, the inertial resistance is expressed as:

$$r_{OA}^{\varphi} = \frac{1}{k(u_0^{\varphi} - \frac{\Delta u^{\varphi}}{\Delta z} z_0)} \left(\ln \frac{z_A}{z_0} - \ln \frac{|z_A + \frac{\Delta z}{\Delta u^{\varphi}} u_0 - z_0|}{|z_0 + \frac{\Delta z}{\Delta u^{\varphi}} u_0^{\varphi} - z_0|} \right) \tag{B.12}$$

In the COSMO code, the absolute value functions are not used. In spite the limit to $\frac{u_P^{\varphi}}{u_0^{\varphi}}$ ratio: $0.5 \leq \frac{u_P^{\varphi}}{u_0^{\varphi}} \leq 2$ is used, through the function $\gamma = \frac{z_0}{u_0^{\varphi}} \frac{\Delta u^{\varphi}}{\Delta z} = \frac{z_0}{\Delta z} \left(\frac{u_P^{\varphi}}{u_0^{\varphi}} - 1 \right)$, which can vary then between $\gamma = [-\frac{z_0}{2\Delta z} : 2\frac{z_0}{\Delta z}]$.
In the neutral case, in which $\Delta u \to 0$, the inertial resistance results:

$$r_{0A}^{\varphi} = \frac{1}{k u_0^{\varphi}} \ln \frac{z_A}{z_0} \tag{B.13}$$

In all the other cases the equation can be simplified by defining $\gamma = \frac{z_0}{u_0} \frac{\Delta u}{\Delta z}$:

$$r_{0A}^{\varphi} = \frac{1}{k u_0^{\varphi} (1 - \gamma)} \ln \frac{z_A}{|z_0 + \gamma(z_A - z_0)|} = \tag{B.14}$$

$$= \frac{z_0}{K_P^{\varphi} (1 - \gamma)} \ln \frac{z_A}{|z_0 + \gamma(z_A - z_0)|} \tag{B.15}$$

In case $\gamma = 1$, r_{OA}^{φ} formulation presents a singularity. The following equation is applied in this case:

$$r_{OA}^{\varphi} = \frac{z_0}{z_A} (z_A - z_0) \tag{B.16}$$

B.1.2 Roughness sub-layer

This sub-layer is considered only for scalar variables (T and q), an approximation valid only in case of dense canopy, where the skimming of wind between vegetation is negligible (the momentum transfer coefficient into the roughness sub-layer depends on the elements spacing Fazu and Schwerdtfeger, 1989). Similarly to the integral formulation of the inertial resistance (eq. B.1), also the roughness resistance is assumed a function of a specific conductivity coefficient K_{S0}^H in the following way:

$$r_{S0}^H = \int_{z_S}^{z_0} \frac{dz}{K_{S0}^H(z)} = \int_{z_S}^{z_0} \frac{dz}{l(z) u_0^H(z)} = \tag{B.17}$$

where z_S is a non-rigid surface following the canopy top.
The length scale $l(z)$ is dependent on the height z and on the surface area index $\sqrt{\Gamma}$ as follow:

$$\frac{dl}{dz} = \frac{k}{\sqrt{\Gamma}} \to l(z) = \int_{z_s}^{z_0} \frac{k}{\sqrt{\Gamma}} dz \tag{B.18}$$

The surface area index $\sqrt{\Gamma}$ should range from its maximum value at the rigid surface S_0 to 1 at the upper boundary of the roughness sub-layer. However, for simplicity, it is

assumed constant along the whole the layer and equal to its value at the surface S_0. The velocity scale is constant and equal to the velocity scale value at the bottom of the inertial sub-layer $u_0^H = \frac{K_0^H}{kz_0}$. Introducing the lenght scale and the velocity turbulent scale formula in eq. B.1.2, the integral can be solved. The passages are reported in the following.

$$
\begin{aligned}
r_{S0}^H &= \int_{z_s}^{z_0} \frac{1}{l(z) S_0^2 u_0^H} dz && \text{(B.19)} \\
&= \frac{1}{S_0^2 u_0^H} \int_{z_s}^{z_0} \frac{dz}{l(z)} && \text{(B.20)} \\
&= \frac{1}{S_0^2 u_0^H} \frac{S_0}{k} \int_{l_s}^{l_0} \frac{dl}{l(z)} && \text{(B.21)} \\
&= \frac{1}{k S_0 u_0^H} [\ln(l_0) - \ln(l_s)] && \text{(B.22)}
\end{aligned}
$$

At the surface, it is assumed $l(z_S) = \nu u_0^{-1}$, with ν the kinematic viscosity. By this, the roughness sub-layer resistance for heat exchange is:

$$
r_{S0}^H = \frac{1}{k S_0 u_0^H} \ln \frac{K_0^M}{\nu} \tag{B.23}
$$

Moreover, another contribution is introduced in eq. 4.8, in order to account for the laminar heat transfer. Thus the roughness sub-layer resistance becomes:

$$
r_{S0}^H = \frac{1}{k S_0 u_0^H} \ln \frac{K_0^M}{\nu} + \frac{\varsigma}{k S_0 u_0^M} \frac{\nu}{\mu} \tag{B.24}
$$

with ς a function of the land/water coverage ratio in the grid box, meant to increase the laminar contribute over water surface, and μ the kinematic conductivity.

B.2 Variables at the diagnostic level

The variables at the diagnostic level (in the following generally indicated as ϕ_d), i.e. temperature and humidity at 2m and wind components at 10m, are obtained by the proportion:

$$
\frac{\phi_d - \phi_g}{r_{gd}} = \frac{\phi_A - \phi_g}{r_{gA}} \tag{B.25}
$$

where the under script g and A stay for level z_g, which represents the rigid surface and z_A, which is the center of the lowermost model level. The resistances are computed as:

$$
\begin{aligned}
r_{gd} &= r_{gS} + r_{S0} + r_{0o} + r_{od} && \text{(B.26)} \\
r_{gA} &= r_{gS} + r_{S0} + r_{0o} + r_{od} + r_{dA} && \text{(B.27)}
\end{aligned}
$$

where the under script S, o and 0 represent respectively z_S, i.e. the level of the non-rigid surface at the canopy top, z_o, i.e. the reference roughness length for a SYNOP station site (set to $0.2m$) and z_0, i.e. the roughness length characterizing the grid point surface.
In the system of eq. B.26-B.27, the resistance r_{gS} is neglected, since the scheme does not consider canopy, the resistance r_{S0} is eq. B.24, the resistance $r_{0o} = \int_{z_0}^{z_o} \frac{1}{l(z)u} dz = \frac{1}{ku} \int_{z_0}^{z_o} \frac{1}{z} dz = \frac{1}{ku} ln(\frac{z_o}{z_0})$ and finally the resistance r_{dA} is obtained using the same derivation as for the inertial resistance in which z_o is used in spite of z_0 and $z_d = 0.5\Delta h_A + z_o$ in spite of z_A *double-check*.

Appendix C

COSMO-LES: preliminary tests in heterogeneous stable boundary layer

When not differently mentioned, the following sensitivity tests are performed using the 'NSPA' test configuration (Table 6.1).

C.0.1 Sensitivity to resolution

Figure C.1 shows the differences along the vertical between the simulations performed with different horizontal resolutions ($\Delta x = \Delta y = 12.5m, 6.25m, 3.125m$ and $1.56m$) using a domain 400m extended in x-direction, 1 grid length extended in y-direction and $400m$ hight, with a vertical resolution of $3.125m$. With increased resolution from 12.5m to 3.125m, there is a general decrease of boundary layer depth, coherently with the results of the terrain homogeneous simulations from Beare et al. (2006). The big increment in the resolved component of the variances (indicated by thin dashed curves in Figure C.1,e,f) at $3.125m$ resolution compared with the coarser resolution cases evidences that the largest part of the turbulent eddies is resolved only at grid space of $3.125m$. Thus, it is recommended the use of a $\Delta x = \Delta y = 3.125m$ or lower. The finer resolution simulation considered ($\Delta x = \Delta y = 1.56m$) produces non realistic profiles, anomalous with respect to the coarser cases. COSMO-LES is an spin-off of the mesoscale the COSMO model, which was not originally developed to run at such extremely high resolution. Likely, such grid space overcomes model capability. In conclusion, a $\Delta x = \Delta y = 3.125m$ is recommended for weakly-to-moderate SBL simulation.

C.0.2 Sensitivity to model domain

The 'NSPA' original domain size is increased in y-direction from 1 to 16 points, thus allowing the third dimension. Horizontal periodic boundary conditions are kept in both the cases. The test is performed to verify if the turbulent eddies need some spanwise

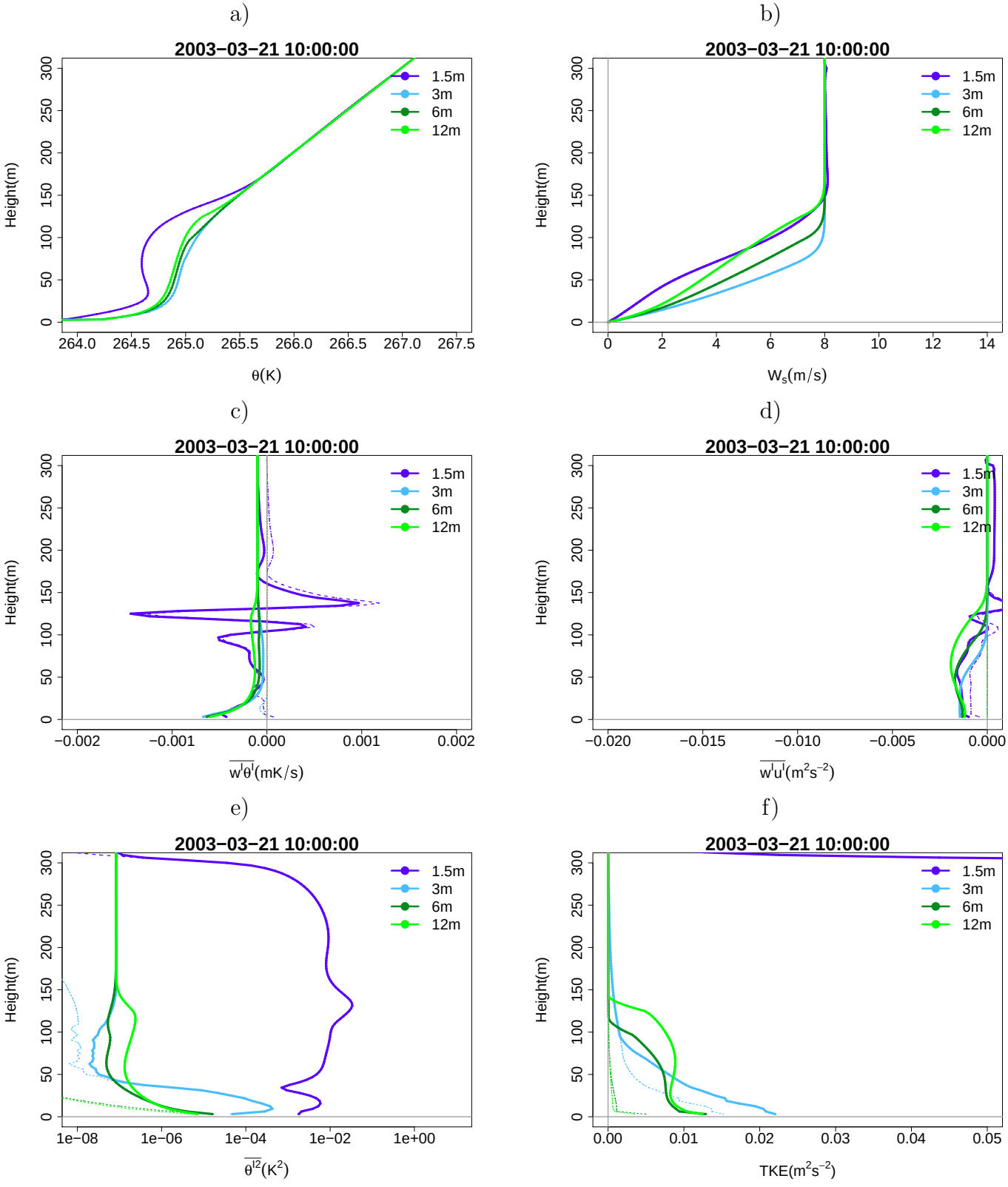

Figure C.1: Vertical profiles of potential temperature variance, vertical temperature flux (b),potential temperature variance (c), mean wind speed (d), momentum flux (e), TKE (f) simulated by COSMO-LES in 'NSPA' test over thermally heterogeneous terrain using different horizontal grid lengths: 12.5m, 6.25m, 3.125m and 1.56m. Resolved components of variances/covariances are evidenced by dashed thin curves

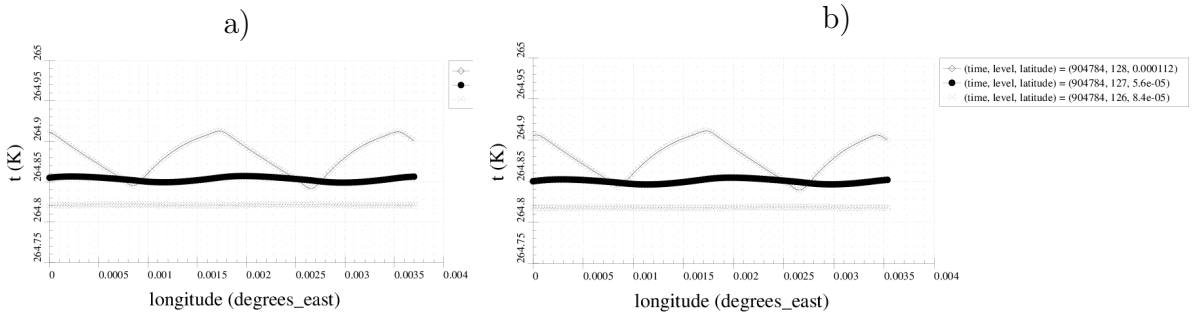

Figure C.2: Streamwise section of temperature at the three lowermost model levels in the simulation using 128x16x128 grid points (a) and in the one using 128x1x128 grid points (b) in respectively x,y and z direction

space to develop. The simulation appears not sensitive to the enlarged domain. Indeed the behaviour of the unique point in the 2D simulation is repeated in any point in y-direction in the 3D case. As an example, the streamwise section of temperature at the three lowermost model levels in the two simulations is shown in Figure C.2.

C.0.3 Comparison of simulations over thermally homogeneous and heterogeneous surfaces

The neglect of Coriolis force in COSMO-LES impedes the apple-to-apple comparison with previous LES simulations available in literature (e.g. Beare et al., 2006; Cuxart, 2006; Stoll and Porté-Agel, 2009; Mironov and Sullivan, 2016). Indeed the lack of Coriolis term in momentum budget equation prevents the reproduction of the LLJ, leading to lower shear at this level, and consequently lower mixing, stronger stability and lower PBL height. In order to verify the correct case reproduction by COSMO-LES two points are considered: 1) the simulation should be realistic and the introduction of thermal heterogeneity at the surface should behave consistently with the theory (section 6.2), 2) the resolved components of the variances/covariances should be larger than the parametrized one.
In Figure C.3 they are presented the vertical profiles of several variables in a simulation over thermally homogeneous surface and in another simulation over thermally heterogeneous surface. The domain used in this test consists of $64x1x128$ points in x, y, and z directions in a box of 200mx3.125mx400m. In this configuration only two patches 100m-long of different temperature are used. This configuration was a first set-up used for COSMO-LES experimentation, which was later substituted by the configuration using a larger domain in x-direction [1]. For the full experimentation, it was decided to

[1]Despite periodic boundary conditions ensure the infinite repetition of thermal transition in x-direction, few marginal differences appears due to the domain size in x-direction, regarding mainly the potential temperature variance and TKE (compare the heterogeneous terrain curve in Figure C.3, with the simulation at 3.125m of horizontal resolution in Figure C.1)

apply a larger domain size in x-direction, but, for the purpose of the present COSMO-LES assessment, also this smaller domain is suitable (as deviations are marginal). The terrain heterogeneity causes an increases of temperature variance close to the surface, which leads to a reduced temperature flux that in turn causes an increment of TKE and of vertical mixing. This is also reflected in higher PBL height in the heterogeneous case. All these points agree with the expectation from the theory, confirming the good performance of COSMO-LES. The resolved component of the variances is larger than the subgrid scale part, confirming that COSMO-LES is filtering out only a small portion of the full turbulent spectrum. Temperature and momentum fluxes show a different proportion of the two components, with the parametrized one being the largest. *why?*.

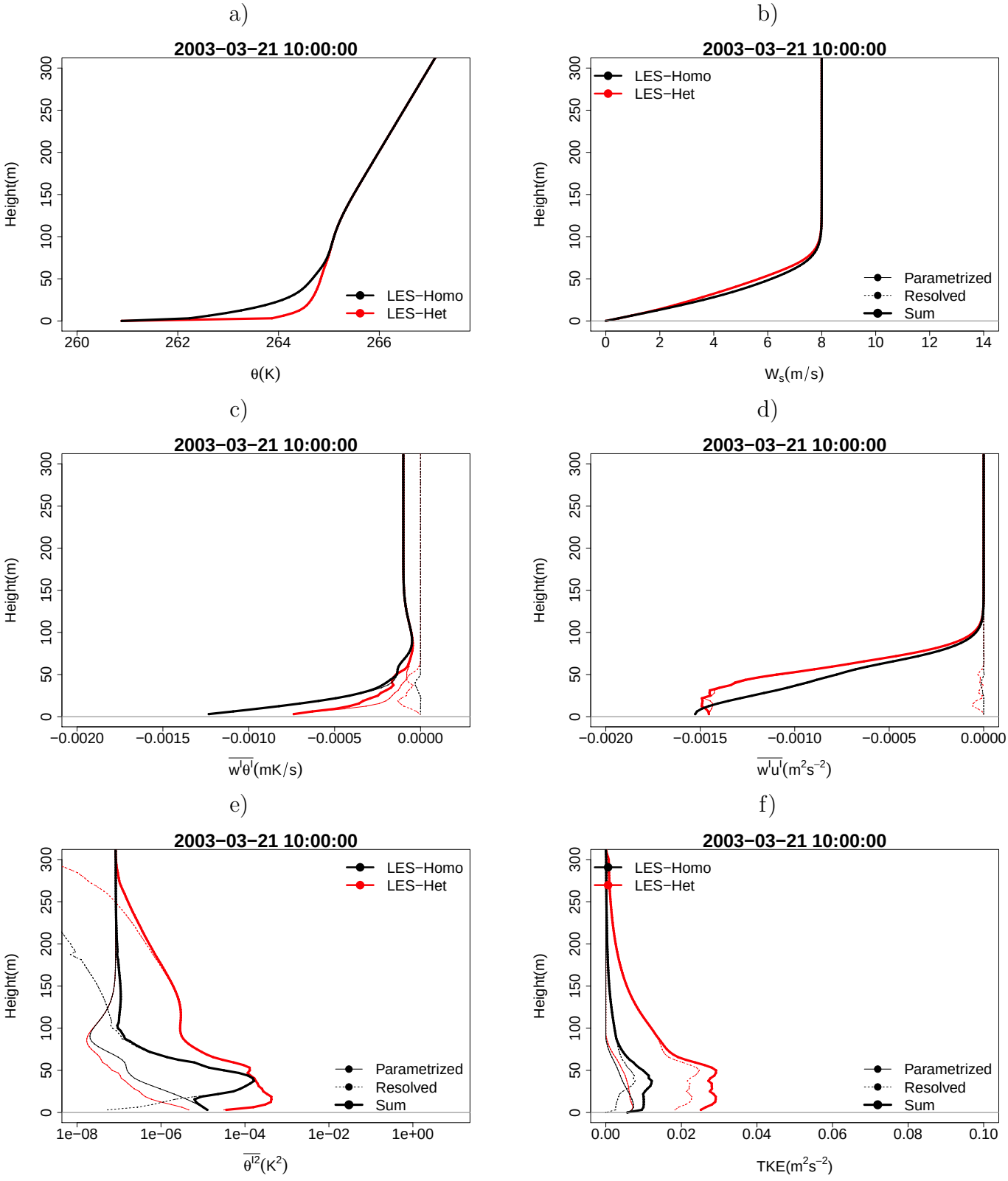

Figure C.3: Vertical profiles of potential temperature variance, vertical temperature flux (b),potential temperature variance (c), mean wind speed (d), momentum flux (e), TKE (f) simulated by COSMO-LES in 'NSPA' test over thermally homogeneous and heterogeneous terrain. Subgrid and resolved component of the turbulent moments are evidenced with dashed and point-dashed curves respectively.

Appendix D

COSMO single column: preliminary tests in heterogeneous stable boundary layer

D.0.4 Curing the vertical oscillations

Since the focus is on SBL representation, it is important to remove from the COSMO single column model the most relevant long-tail options. Therefore, the minimum limit to the turbulent eddy diffusivity for heat and momentum $K^{M,H}$ are lowered to the non-influencing value $0.01m^2/s$(Buzzi, 2008). However, this action causes the onset of oscillations and anomalous behaviour in the vertical profiles of wind speed, θ and turbulent variables (Figure D.1). A similar issues was detected by Buzzi (2008) in testing the COSMO single column performance in the idealized simulation of a weakly stable PBL over homogeneous surface. He argued that the problem originates from a physical inconsistency of the stability function of Mellor and Yamada (1982) scheme, already detected by Burchard and Deleersnijder (2001), leading to a non-monotone normalized stress function (defined as $\frac{K^M}{q^2}|\frac{\partial \overline{u}}{\partial z} = S^M(G^M)^{0.5}$) in a plane $G^M x G^H$ (the functions S^M, G^M, G^H are defined in section 3.3). Buzzi (2008) moreover explained the numerical-like kind of this issue, reporting the previous evidence from Mellor (2003) that the problem manifests only in staggered grid (whereby the mean variables like temperature and wind components are staggered relative to the turbulence variables like q and turbulent fluxes), thus indicating a relation with the model numerics. Whereas in Buzzi (2008) the filtering was applied to both K^M and K^H, in the present work only the filtering of K^M was sufficient to cure the oscillation onset (Figure D.1)[1]. The filtering applied is a 5-point smoothing function:

$$f_k^{new} = 0.5f_k + 0.2(f_{k+1} + f_{k-1}) + 0.05(f_{k+2} + f_{k-2} \tag{D.1}$$

[1]notice that in the present experiment, Louis et al. (1982) surface layer scheme is used instead of the operational COSMO scheme and Coriolis force is set to 0

where the subscript k is the vertical grid index.
The reduction of the coefficient l_{max}, a parameter controlling the asymptotic mixing length (see eq. 2.2.1), from values ranging between 150m-500m (usually applied in COSMO operational applications) to a value of 40m is the another point of the Buzzi (2008)'s optimized configuration, which is applicable in the present experiment [2]. In this way, the maximum eddies size is reduced. Consequently, TKE reduces and the vertical profiles of wind speed and θ are less homogeneous (Figure D.1).
Such configured COSMO simulation still deviates from COSMO-LES in the same points evidenced by Buzzi (2008):

- underestimation of TKE below 150m and overestimation above
- overestimation of θ below 100m and overestimation between 100m and 200m
- underestimation of the wind speed below 150m and overestimation above

All these points suggest that COSMO has a larger vertical diffusion within this weakly SBL over homogeneous terrain with respect to COSMO-LES.

D.0.5 Sensitivity to the mixing length

Some sensitivity tests are performed in COSMO single column to the mixing length setting. The master length scale (or mixing length) is based in COSMO on Blackadar (1962)'s formulation, using the equation:

$$\frac{1}{l(z)} = \frac{1}{\kappa z} + \frac{1}{l_{scal}} + a_{stab}\frac{\sqrt{f_h}}{q} \tag{D.2}$$

where z is the geometric distance from the rigid surface detracted from a certain displacement height of the roughness layer, $\kappa = 0.4$ is von Karman constant and the parameter l_{scal} is the ratio between the asymptotic length scale from Blackadar (1962) ($l_{\inf}$, i.e. the maximum size of turbulent eddies) and κ. a_{stab} is a switching parameter enabling the correction for stability from Deardorff (1976). The sensitivity study considered the introduction of Deardorff (1976) correction and the reduction of l_{scal} from the optimal value found by Buzzi (2008) $l_{scal} = 40m$ to smaller values: 14m and 3m [3].
Figure D.2 reports the vertical profiles simulated by the COSMO single column model using $K^{M,H}_{min} = 0.01m^2/s$, the vertical filtering of K^M and the mentioned different settings of the mixing length formulation. The COSMO simulation results very sensitive to the reduction of the asymptotic length scale via l_{scal} (or l_{max}). In particular, the SBL height is reduced by decreasing l_{scal} and a secondary maximum in TKE (but also in

[2] configuration regarding the surface layer scheme not applicable as Louis et al. (1982) surface layer scheme is used in the present experimentation

[3] Actually the test is performed by playing with the another parameter named l_{max}. l_{scal} is defined as the minimum between the horizontal grid scale Δ_g and l_{max}. Given that Δ_g is 2km, it is always larger than l_{max} and l_{max} corresponds to l_{scal}

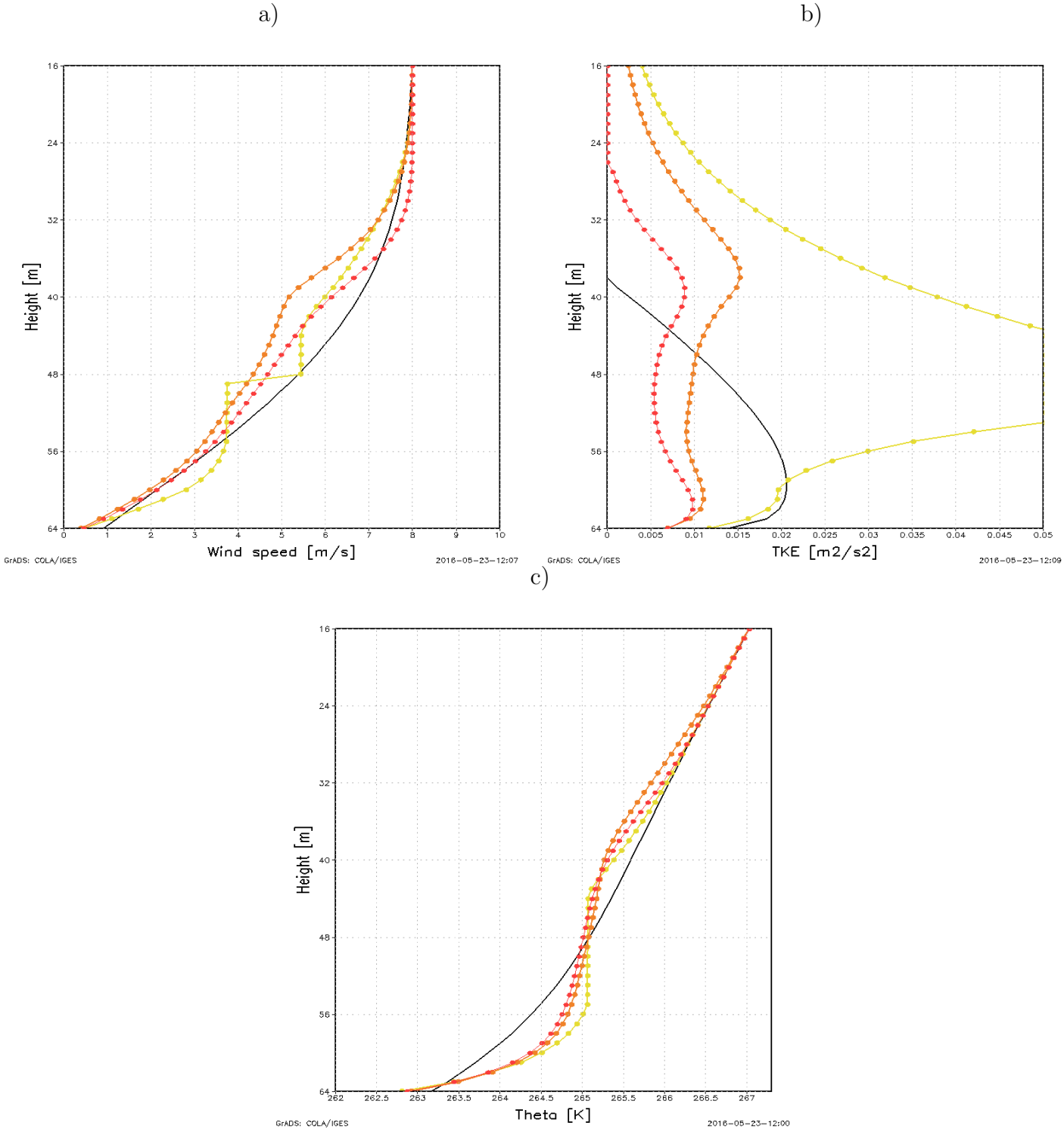

Figure D.1: Vertical profiles of wind speed (a), TKE (b) and potential temperature (c) simulated by COSMO-LES in test case over thermally homogeneous terrain (black line) and simulated by COSMO single column using different configuration: operational-like but with $K^{M,H}_{min} = 0.01m^2/s$ (yellow), the same but vertical filtering of K^M (orange) and latter introducing the optimization options suggested by Buzzi (2008). Notice that the vertical axis indicates the vertical model levels, which are 6.25m thick

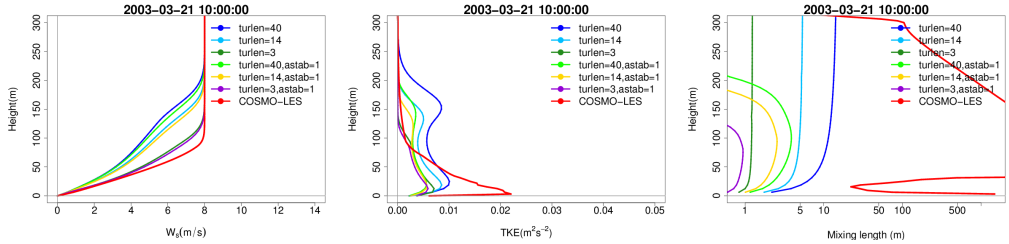

Figure D.2: Vertical profiles of wind speed(left), TKE (middle) and mixing length (right) simulated by COSMO single column using different setting of the mixing length formulation

other variance/covariances) are reduced. Indeed, smaller turbulent eddies reduce turbulence mixing activity. The activation of the stability correction has a smaller impact, again reducing SBL height and the secondary maximum in TKE. The mixing length vertical profile (Figure D.2,right) evidences that both the decrement of l_{scal} and the stability correction reduce the mixing length, the former acting along the whole z-axis, while the latter mainly acting at the SBL top.
The setting using $l_{scal} = 3m$ and the stability correction is the closest to the COSMO-LES simulation. However, while it is reasonable to use a correction for stable stability, the use of $l_{scal} = 3m$ is not justifiable, as a 2km-resolution model should describe also larger eddy size. Therefore, the Buzzi' optimal value $l_{scal} = 40m$ is kept for this experimentation.

Appendix E

The tile performance

The following Table E.1 and the following Figures reports the results of the simulation of the vertical SBL structure over thermally heterogeneous terrain as performed by COSMO single column model using the reference version (no tile and TKE turbulence scheme, labelled COSMO TKE) and the versions applying tile method in association with different turbulence schemes (they are labelled respectively 'COSMO TKE-2Tiles', 'COSMO TKESV-2Tiles' and 'COSMO TKESV+LBC-2Tiles', representing the turbulence schemes: truncated 2.0 order, full 2.0 order and full 2.0 order plus lower boundary condition for scalar variance)

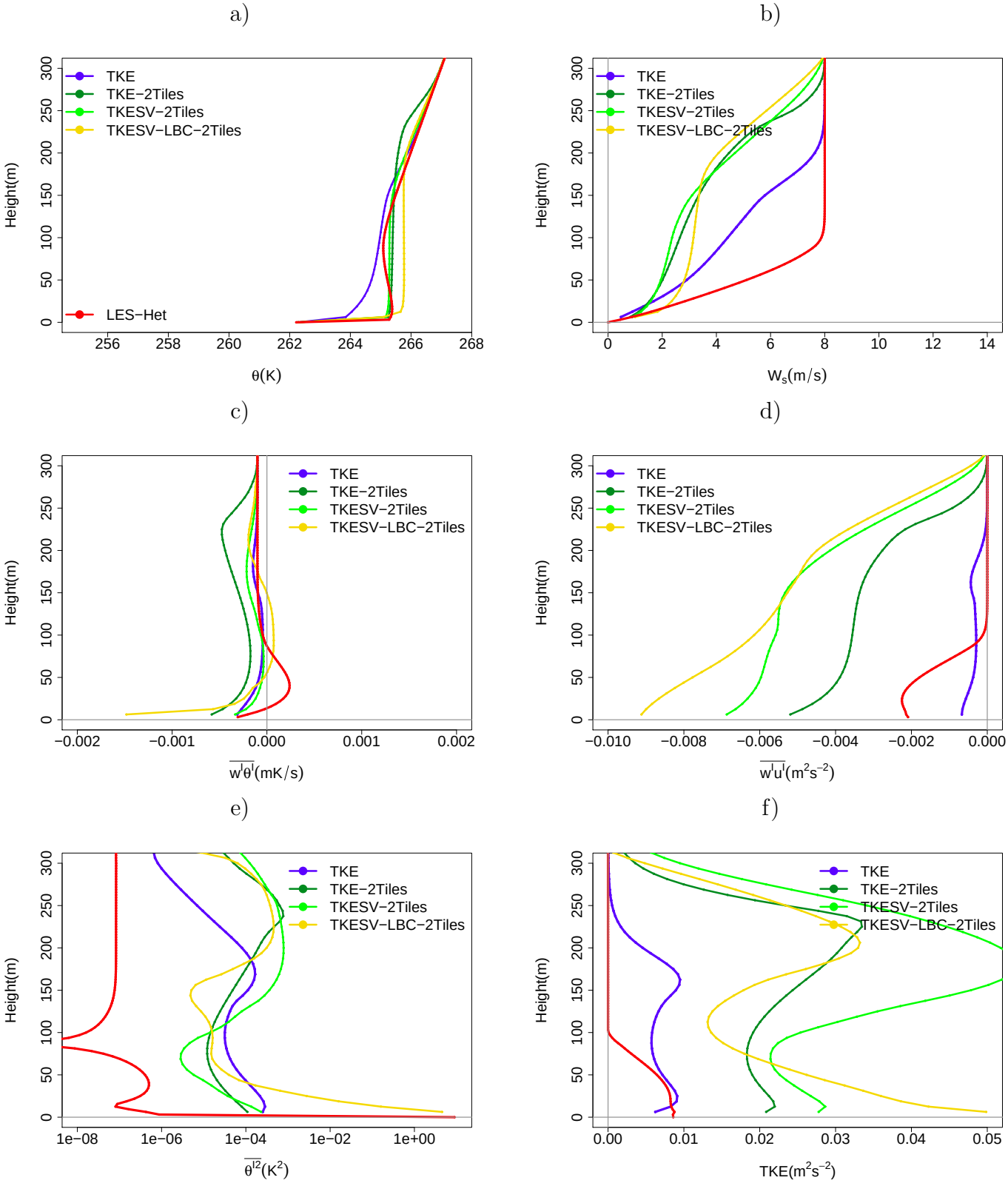

Figure E.1: Domain average of the vertical profiles of potential temperature(a), wind speed(b), vertical temperature flux (c), vertical momentum stress (d), variance of potential temperature (e) and TKE (f) averaged over the last 2 hours of simulation as simulated by COSMO-LES and by COSMO single column applying different configurations, as in legend, in SPA idealized case study

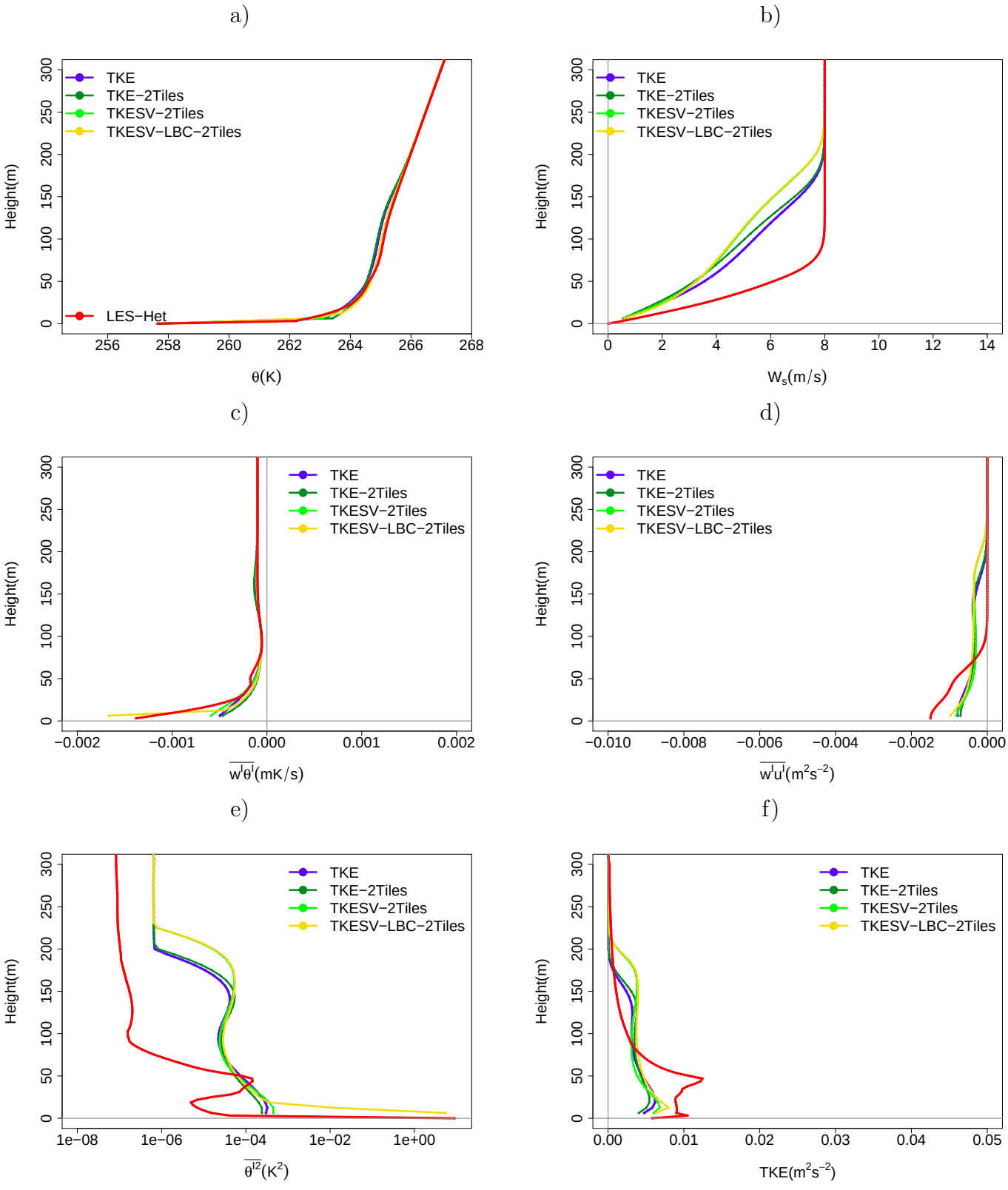

Figure E.2: As in Figure E.1, but simulation of the SSPA case

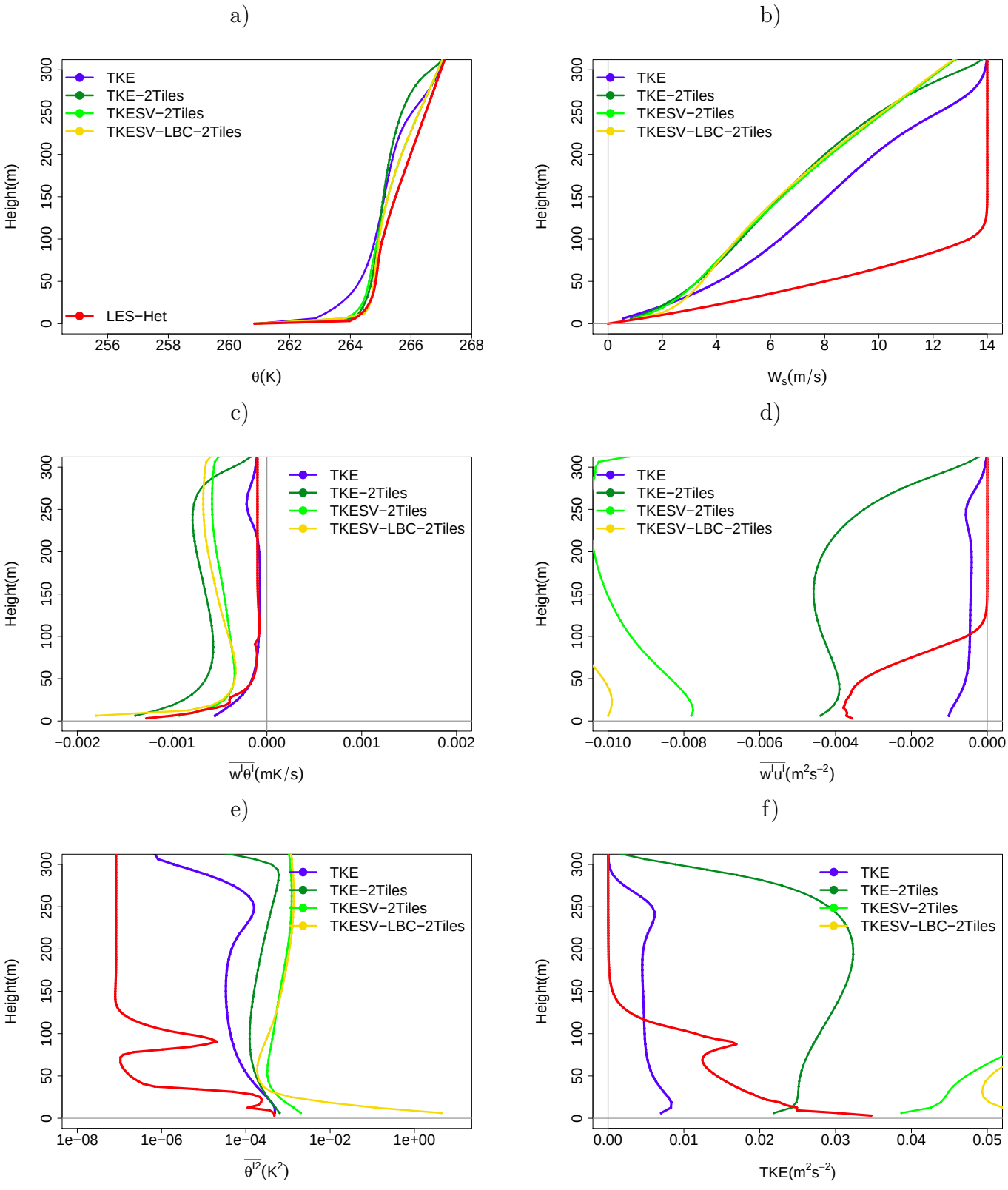

Figure E.3: As in Figure E.1, but simulation of the NSPA-highU case

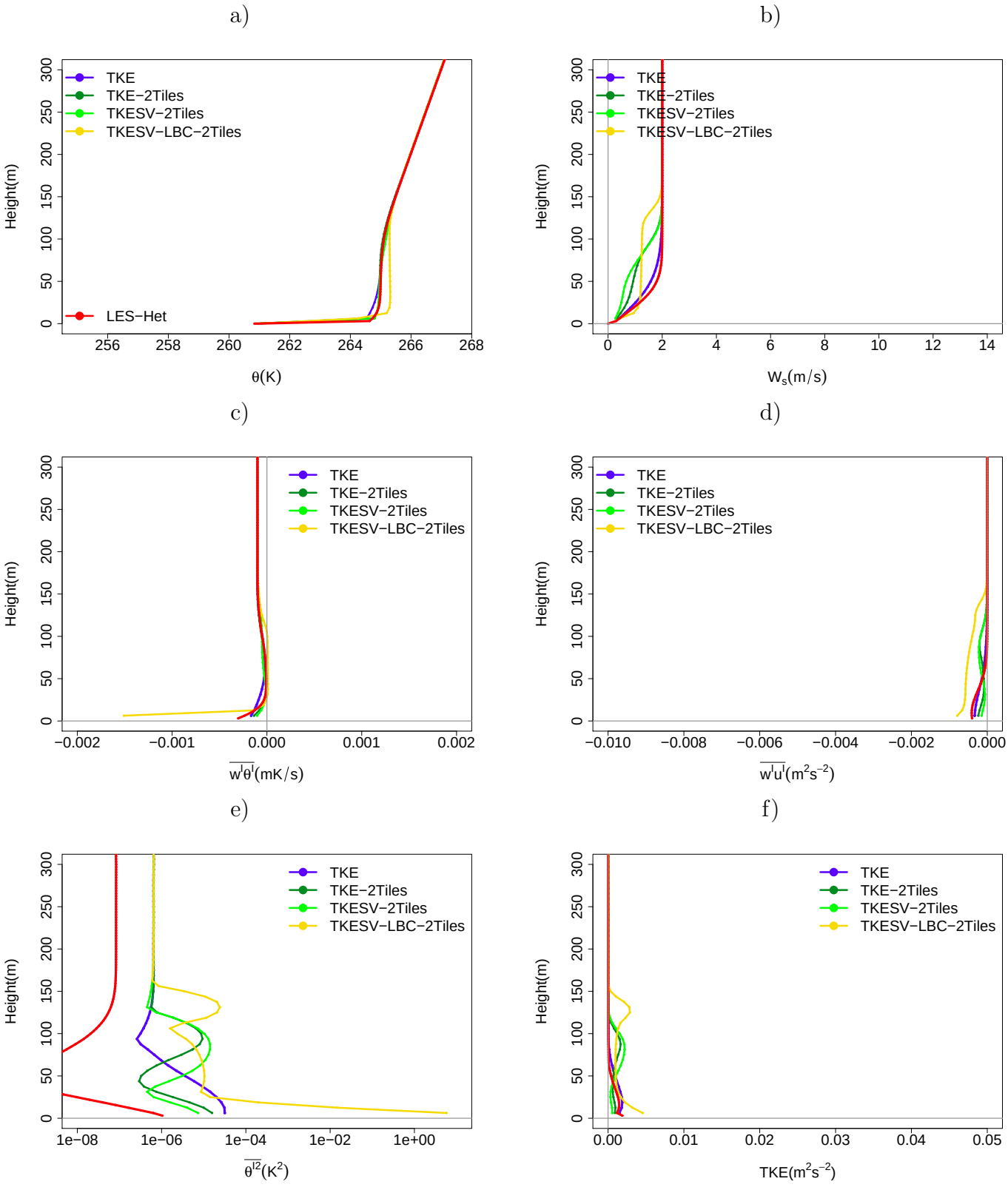

Figure E.4: As in Figure E.1, but simulation of the NSPA-lowU case

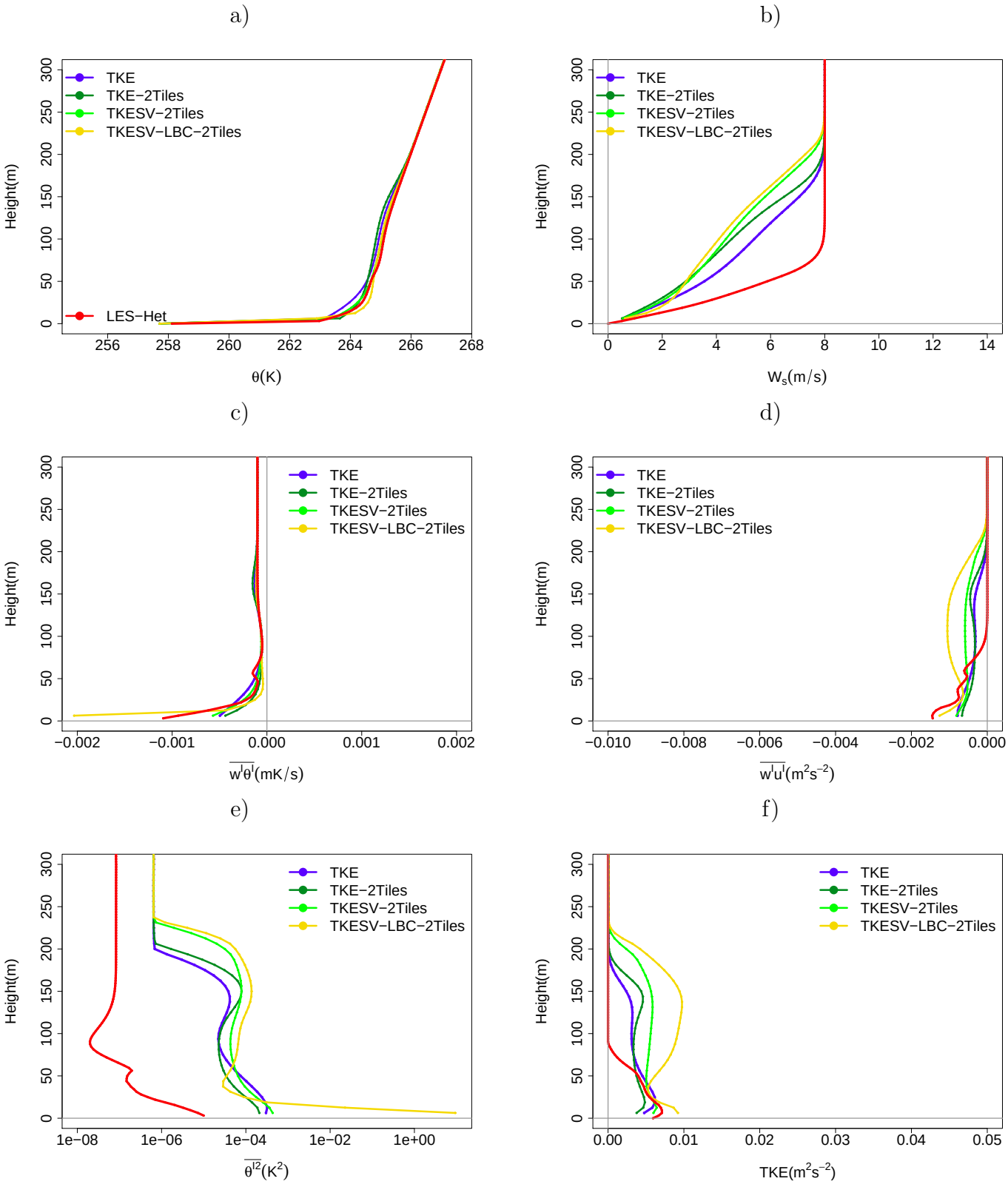

Figure E.5: As in Figure E.1, but simulation of the SSPA-highTC case

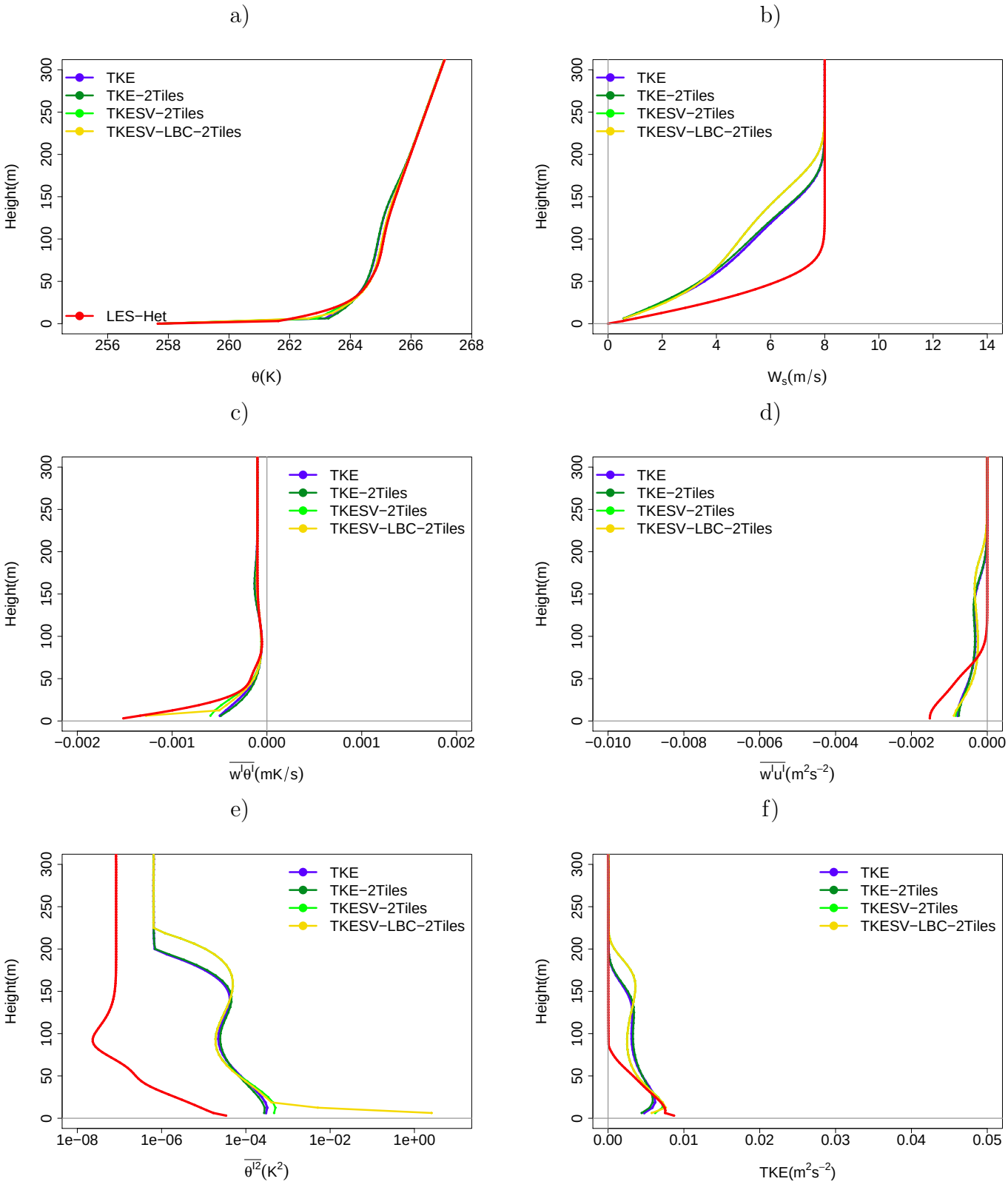

Figure E.6: As in Figure E.1, but simulation of the SSPA-lowTC case

	COSMO TKE		COSMO TKE-2Tiles		COSMO TKESV-2Tiles		COSMO TKESV+LBC-2Tiles	
SPA								
$\overline{\theta}$	-0.850480	0.958190	0.013356	0.078339	-0.052135	0.098665	0.311380	0.390935
$\overline{u}$	-1.297114	1.421365	-1.558978	1.862177	-1.533939	1.862177	-0.835351	1.214555
$\overline{w'\theta'}$	-0.000298	0.000308	-0.000458	0.000264	-0.000257	0.000264	-0.000503	0.000588
$\overline{w'u'}$	0.001577	0.001580	-0.002299	0.004222	-0.004215	0.004222	-0.006402	0.006411
TKE	0.000244	0.001120	0.012772	0.018129	0.018073	0.018129	0.027956	0.028722
$\overline{\theta'^2}$	0.000185	0.000199	0.000048	0.000099	0.000065	0.000099	0.588974	1.603222
NSPA								
$\overline{\theta}$	-0.500571	0.568810	-0.042109	0.060947	-0.098433	0.116989	0.104280	0.221162
$\overline{u}$	-1.370327	1.489189	-1.704038	1.962164	-1.710431	1.962164	-1.281806	1.597137
$\overline{w'\theta'}$	-0.000029	0.000092	0.000041	0.000072	0.000056	0.000072	-0.000079	0.000298
$\overline{w'u'}$	0.000816	0.000818	0.000661	0.000215	-0.000137	0.000215	-0.001929	0.001932
TKE	-0.008735	0.009711	-0.008206	0.005847	-0.003586	0.005847	0.003460	0.003760
$\overline{\theta'^2}$	0.000036	0.000095	-0.000040	0.000108	0.000047	0.000108	0.619432	1.732837
SSPA								
$\overline{\theta}$	0.025928	0.208862	0.135146	0.307182	0.073140	0.168959	0.136179	0.178012
$\overline{u}$	-1.604688	1.750537	-1.831014	1.888149	-1.715713	1.888149	-1.648954	1.842249
$\overline{w'\theta'}$	0.000176	0.000294	0.000232	0.000248	0.000139	0.000248	0.000055	0.000235
$\overline{w'u'}$	0.000509	0.000522	0.000574	0.000575	0.000571	0.000575	0.000492	0.000497
TKE	-0.004411	0.004671	-0.004979	0.004859	-0.004405	0.004859	-0.003829	0.004333
$\overline{\theta'^2}$	0.000152	0.000203	0.000092	0.000271	0.000193	0.000271	0.692658	1.954923
NSPA-lowU								
$\overline{\theta}$	-0.115709	0.144346	0.004548	0.032353	-0.008836	0.045150	0.212992	0.334343
$\overline{u}$	-0.147609	0.166667	-0.516019	0.787073	-0.711260	0.787073	-0.148399	0.321389
$\overline{w'\theta'}$	-0.000024	0.000045	0.000024	0.000054	0.000028	0.000054	-0.000145	0.000450
$\overline{w'u'}$	0.000049	0.000061	0.000162	0.000227	0.000202	0.000227	-0.000319	0.000327
TKE	0.000476	0.000483	-0.000285	0.000740	-0.000494	0.000740	0.000999	0.001424
$\overline{\theta'^2}$	0.000018	0.000020	0.000004	0.000003	0.000002	0.000003	0.718852	2.027891
NSPA-highU								
$\overline{\theta}$	-0.781987	0.872105	-0.104151	0.125923	-0.202446	0.224071	-0.031312	0.137627
$\overline{u}$	-2.306273	2.535592	-2.539259	2.858971	-2.446819	2.858971	-2.181525	2.647622
$\overline{w'\theta'}$	0.000111	0.000183	-0.000484	0.000120	-0.000083	0.000120	-0.000220	0.000314
$\overline{w'u'}$	0.002818	0.002820	-0.000437	0.004398	-0.004382	0.004398	-0.006384	0.006388
TKE	-0.013094	0.013885	0.004245	0.024987	0.023846	0.024987	0.030513	0.030703
$\overline{\theta'^2}$	0.000163	0.000188	0.000209	0.000797	0.000664	0.000797	0.562563	1.545113
SSPA-lowTC								
$\overline{\theta}$	0.212249	0.419577	0.262181	0.479496	0.159301	0.296997	0.184112	0.269791
$\overline{u}$	-1.702438	1.863793	-1.803538	1.887017	-1.713236	1.887017	-1.689738	1.868718
$\overline{w'\theta'}$	0.000274	0.000388	0.000300	0.000319	0.000198	0.000319	0.000143	0.000212
$\overline{w'u'}$	0.000520	0.000539	0.000546	0.000560	0.000551	0.000560	0.000549	0.000556
TKE	-0.000260	0.001309	-0.000467	0.000571	0.000061	0.000571	0.000056	0.000694
$\overline{\theta'^2}$	0.000203	0.000220	0.000174	0.000326	0.000287	0.000326	0.319808	0.902325
SSPA-highTC								
$\overline{\theta}$	-0.300741	0.321800	-0.069870	0.199840	-0.102301	0.164384	0.045078	0.260021
$\overline{u}$	-1.465527	1.593830	-1.855110	1.908328	-1.725132	1.908328	-1.549581	1.801291
$\overline{w'\theta'}$	0.000035	0.000179	0.000138	0.000146	0.000061	0.000146	-0.000052	0.000401
$\overline{w'u'}$	0.000270	0.000342	0.000400	0.000367	0.000306	0.000367	0.000109	0.000194
TKE	-0.000005	0.001067	-0.001172	0.000659	0.000107	0.000659	0.001125	0.001356
$\overline{\theta'^2}$	0.000205	0.000223	0.000102	0.000234	0.000197	0.000234	1.168198	3.296002

Table E.1: Bias and RMSE of COSMO 'TKE', 'TKE-2Tiles', 'TKESV-2Tiles' and 'TKESV+LBC-2Tiles' in simulating the domain averaged profiles of θ, wind speed, turbulence variances and covariances over the last 2 hours of simulation (hours 10-12) in the various idealized experiments.

Appendix F

Bibliography

Bibliography

Acevedo, O. C., and D. R. Fitzjarrald, 2003: In the core of the night-effects of intermittent mixing on a horizontally heterogeneous surface. *Boundary-Layer Meteorol.*, **106**, 1–33.

Ament, F., and C. Simmer, 2006: Improved representation of land-surface heterogeneity in a non-hydrostatic numerical weather prediction model. *Bound.-Layer Meteor.*, **121**, 153–174, doi:10.1007/s10546-006-9066-4.

Anderson, P. S., 2009: Measurement of prandtl number as a function of richardson number avoiding self-correlation. *Boundary-Layer Meteorol.*, **131**, 345–362, doi:10.1007/s10546-009-9376-4.

Ansorge, C., and J. P. Mellado, 2014: Global intermittency and collapsing turbulence in the stratified planetary boundary layer. *Boundary-Layer Meteorol.*, **153**, 89–116, doi:10.1007/s10546-014-9941-3.

Arola, A., 1999: Parameterization of turbulent and mesoscale fluxes for heterogeneous surfaces. *J. Atmos. Sci.*, **56**, 584–598.

Atlaskin, E., and T. Vihma, 2012: Evaluation of nwp results for wintertime nocturnal boundary-layer temperatures over europe and finland. *Quarterly Journal of the Royal Meteorological Society*, **138 (667)**, 1440–1451, doi:10.1002/qj.1885, URL http://dx.doi.org/10.1002/qj.1885.

Avissar, R., and R. A. Pielke, 1989: A parameterization of heterogeneous land surfaces for atmospheric numerical models and its impact on regional meteorology. *Mon. Wea. Rev*, **117**, 2113–2136.

Avissar, R., and T. Schmidt, 1998: An evaluation of the scale at which ground-surface heat flux patchiness affects the convective boundary layer using large-eddy simulations. *Journal of the Atmospheric Sciences*, **55 (16)**, 2666–2689.

Baas, P., G. J. Steeneveld, B. J. H. van de Wiel, and A. A. M. Holtslag, 2006: Exploring self-correlation in flux-gradient relationships for stably stratified conditions. *J. Atmos. Sci.*, **63**, 3045–3054, doi:10.1175/JAS3778.1.

Baldauf, M., A. Seifert, J. F´orstner, D. Majewski, M. Raschendorfer, and T. Reinhardt, 2011: perational convective-scale numerical weather prediction with the cosmo model: description and sensitivities. *Monthly Weather Review*, **139**, 3887–3905.

Basu, S., and A. A. M. Holtslag, 2012: Why do stable boundary layer simulations over land sometimes crash? *Proc. 20th Symposium on Boundary Layers and Turbulence/18th Conference on Air-Sea Interaction*, Boston, American Meteorological Society.

Beare, R., and Coauthors, 2006: An intercomparison of large-eddy simulations of the stable boundary layer. *Boundary-Layer Meteorol*, **118**, 247–272.

Beare, R. J., 2007: Boundary layer mechanisms in extratropical cyclones. *Quarterly Journal of the Royal Meteorological Society*, **133**, 503–515, doi:10.1002/qj.30.

Bechtold, P., E. Bazile, F. Guichard, P. Mascart, and E. Richard, 2001: A mass-flux convection scheme for regional and global models. *Quarterly Journal of the Royal Meteorological Society*, **127 (573)**, 869–886, doi:10.1002/qj.49712757309.

Beljaars, A., 2011: The stable boundary layer in the ecmwf model. *Proc. ECMWF Workshop on Diurnal cycles and the stable boundary layer*, Reading, England, ECMWF, 1–10.

Beljaars, A., A. Brown, and N. Wood, 2004: A new parameterization of turbulent orographic form drag. *Q. J. R. Meteorol. Soc.*, **130**, 1327–1347.

Beljaars, A., and A. A. M. Holtslag, 1991: Flux parameterization over land surfaces for atmospheric models. *J. Appl. Meteorol.*, **30**, 327–341, doi:10.1175/JAS4002.1.

Beljaars, A., and P. Viterbo, 1998: The role of the boundary layer in a numerical weather prediction model. *Clear and Cloudy Boundary Layers*, Roy. Netherlands Acad. of Arts and Sci., North-Holland, Amsterdam, 287–304.

Blackadar, A. K., 1962: The vertical distribution of wind and turbulent exchange in a neutral atmosphere. *Journal of Geophysical Research*, **67 (8)**, 3095–3102, doi:10.1029/JZ067i008p03095, URL http://dx.doi.org/10.1029/JZ067i008p03095.

Blahak, U., 2015: Simulating idealized cases with the cosmo-model (draft version). Manual, Consortium for small scale modelling. URL http://www.cosmo-model.org/content/model/documentation/core/artif_docu.pdf.

Blyth, E. M., 1995: Using a simple svat scheme to describe the effect of scale on aggregation. *Bound.-Layer Meteor.*, **72**, 267–285.

Blyth, E. M., A. J. Dolman, and N. Wood, 1993: Effective resistance to sensible- and latent-heat flux in heterogeneous terrain. *Quart. J. Roy. Meteor. Soc.*, **119**, 423–442.

Bonafé, G., 2010: Srnwp data pool: the meteorological site of san pietro capofume,italy. Tech. rep., ARPAE - Emilia Romagna. [Available online at http://www.cosmo-model.org/srnwp/support/SanPietroCapofiume/stationInfo.pdf].

Bou-Zeid, E., C. Meneveau, and M. B. Parlange, 2004: Large-eddy simulation of neutral atmospheric boundary layer flow over heterogeneous surfaces: Blending height and effective surface roughness. *Water Resour. Res.*, **40**, W02 505.

Brown, A., and S. Webster, 2004: Orographic flowblocking scheme characteristics. *Q. J. R. Meteorol. Soc.*, **130**, 3015–3028.

Brown, A. R., A. C. M. Beljaars, H. Hersbach, A. HOLLINGSWORTH, M. MILLER, and D. VASILJEVIC, 2005: Wind turning across the marine atmospheric boundary layer. *Q. J. R. Meteorol. Soc.*, **131**, 1233–1250.

Burchard, H., and Deleersnijder, 2001: Stability of alegebraic non-equilibrium second order closure models. *Ocean Modelling*, **3**, 33–50.

Businger, J. A., J. C. Wyngaard, Y. Izumi, and E. F. Bradley, 1971: Flux–profile relationships in the atmospheric surface layer. *J. Atmos. Sci.*, **28**, 181–189.

Buzzi, M., 2008: Challenges in operational numerical weather prediction at high resolution in complex terrain. Ph.D. thesis, Swiss federal institute of technology (ETH), 185 pp., doi:10.3929/ethz-a-005698833.

Buzzi, M., M. W. Rotach, M. Raschendorfer, and A. Holtslag, 2011: Evaluation of the cosmo-sc turbulence scheme in a shear-driven stable boundary layer. *Met Z*, **20(3)**, 335–350, doi:10.1127/0941-2948/2011/0050.

Cerenzia, I., F. Tampieri, and M. Tesini, 2014: Diagnosis of turbulence schema in stable atmospheric conditions and sensitivity tests. *Proc. COSMO Newsletter*, Consortium for small scale modelling, Vol. 14, 28–36, [Available online at http://www.cosmo-model.org/content/model/documentation/newsLetters/newsLetter14/cnl14_04.pdf].

Chen, F., and R. Avissar, 1994: The impact of land-surface wetness heterogeneity on mesoscale heat fluxes. *Journal of the Applied Meteorology*, **33 (11)**, 1323–1340.

Chen, F., and J. Dudhia, 2001: Coupling an advanced land surface hydrology model with the penn state ncar mm5 modeling system. part i: Model implementation and sensitivity. *Mon. Wea. Rev.*, **129**, 569–585.

Cheng, Y., and W. Brutsaert, 2005: Flux-profile relationships for wind speed and temperature in the stable atmospheric boundary layer. *Boundary-Layer Meteorol.*, **114**, 519–538, doi:10.1007/s10546-004-1425-4.

Chimonas, G., and C. J. Nappo, 1989: Wave drag in the planetery boundary layer over complex terrain. *Bound. - Layer Meteor.*, **47**, 217–232.

Cuxart, J., 2006: Single-column model intercomparison for a stably stratified atmospheric boundary layer. *Boundary-Layer Meteorol*, **118**, 273–303.

de Wiel, B. J. H. V., A. F. Moene, O. K. Hartogensis, H. A. R. D. Bruin, and A. A. M. Holtslag, 2003: Intermittent turbulence in the stable boundary layer over land. part iii: A classification for observations during cases-99. *Journal of the Atmospheric Sciences*, **60 (20)**, 2509–2522, doi:10.1175/1520-0469(2003)060⟨2509:ITITSB⟩2.0.CO;2.

de Wiel, B. J. H. V., A. F. Moene, and H. J. J. Jonker, 2012a: The cessation of continuous turbulence as precursor of the very stable nocturnal boundary layer. *J. Atmos. Sci.*, **69**, 3097–3115, doi:10.1175/JAS-D-12-064.1.

de Wiel, B. J. H. V., A. F. Moene, H. J. J. Jonker, P. Baas, S. Basu, J. M. M. Donda, J. Sun, and A. A. M. Holtslag, 2012b: The minimum wind speed for sustainable turbulence in the nocturnal boundary layer. *J. Atmos. Sci.*, **69**, 3116–3127, doi: 10.1175/JAS-D-12-0107.1.

de Wiel, B. J. H. V., R. J. Ronda, A. F. Moene, H. A. R. de Bruin, and A. A. M. Holtslag, 2002: Intermittent turbulence and oscillations in the stable boundary layer over land. part i: A bulk model. *J. Atmos. Sci.*, **59**, 942–958.

Deardorff, J. W., 1976: On the entrainment rate of a stratocumulus-topped mixed layer. *Quarterly Journal of the Royal Meteorological Society*, **102 (433)**, 563–582, doi:10.1002/qj.49710243306, URL http://dx.doi.org/10.1002/qj.49710243306.

Doms, G., and Coauthors, 2011: A description of the nonhydrostatic regional cosmo model: physical parameterizations. User's guide, Consortium for small scale modelling, Deutscher Wetterdienst, Offenbach, 154 pp. [Available online at http://www.cosmo-model.org/content/model/documentation/core/cosmoPhysParamtr.pdf].

Donda, J., I. van Hooijdonk, A. Moene, G. van Heijst, H. Clercx, and B. van de Wiel, 2016: The maximum sustainable heat flux in stably stratified channel flows. *Quarterly Journal of the Royal Meteorological Society*, **142**, 781–792, doi:10.1002/qj.2680.

Edwards, J. M., 2011: Radiation and turbulence in the stable boundary layer. *Proc. ECMWF Workshop on Diurnal cycles and the stable boundary layer*, Reading, England, ECMWF, 1–10.

Fazu, C., and P. Schwerdtfeger, 1989: Flux-gradient relationships for momentum and heat over a rough natural surface. *Quarterly Journal of the Royal Meteorological Society*, **115 (486)**, 335–352, doi:10.1002/qj.49711548607.

Finnigan, J. J., 1988: Kinetic energy transfer between internal gravity waves and turbulence. *Journal of the Atmospheric Sciences*, **45 (3)**, 486–505, doi:10.1175/1520-0469(1988)045⟨0486:KETBIG⟩2.0.CO;2.

Finnigan, J. J., F. Einaudi, and D. Fua, 1984: The interaction between an internal gravity wave and turbulence in the stably-stratified nocturnal boundary layer. *Journal of the Atmospheric Sciences*, **41 (16)**, 2409–2436, doi:10.1175/1520-0469(1984)041⟨2409:TIBAIG⟩2.0.CO;2.

Gal-Chen, T., and R. Sommerville, 1975: On the use of a coordinate transformation for the solution of the navierstokes equations. *J. Comput. Phys.*, **17**, 209–228.

Giorgi, F., and R. Avissar, 1997: Representation of heterogeneity effects in earth system modeling: Experience from land surface modeling. *Reviews of Geophysics*, **35 (4)**, 413–437.

Grachev, A. A., E. L. Andreas, C. W. Fairall, P. S. Guest, and P. O. G. Persson, 2007: On the turbulent prandtl number in the stable atmospheric boundary layer. *Boundary-Layer Meteorol.*, **125**, 329–341, doi:10.1007/s10546-007-9192-7.

Grachev, A. A., C. W. Fairall, P. O. G. Persson, L. A. E, and P. S. Guest, 2005: Stable boundary-layer scaling regimes: The sheba data. *Boundary-Layer Meteorol.*, **116**, 201–235, doi:10.1007/s10546-004-2729-0.

Grasselt, R., D. Sch´uttemeyer, K. Warrach-Sagi, F. Ament, and C. Simmer, 2008: Validation of terra-ml with discharge measurements. *Meteorol. Z.*, **17**, 763–773.

Grisigono, B., 2011: The angle of the near-surface wind-turning in weakly stable boundary layers. *Quart. J. Roy. Meteor. Soc.*, **137**, 700–708, doi:10.1002/qj.638.

Grisogono, B., S. C. Pryor, and R. E. Keislar, 1993: Mountain wave drag over double bell-shaped orography. *Quarterly Journal of the Royal Meteorological Society*, **119 (509)**, 199–206, doi:10.1002/qj.49711950909, URL http://dx.doi.org/10.1002/qj.49711950909.

Ha, K. J., and L. Mahrt, 2003: Radiative and turbulent fluxes in the nocturnal boundary layer. *Tellus*, **55A**, 317–327.

Hassid, S., and B. Galperin, 1983: A turbulent energy model for geophysical flows. *Boundary-Layer Meteorology*, **26 (4)**, 397–412.

Heise, E., 2006: Validation of boundary layer clouds: Test results with the minimum vertical diffusion coefficient set equal to zero in lm. *Proc. COSMO Newsletter*, Consortium for small scale modelling, Vol. 06, 94–102, URL http://www.cosmo-model.org/content/model/documentation/newsLetters/newsLetter06/cnl6_heise_blc.pdf.

Helfand, H. M., and J. C. Labraga, 1988: Design of a non-singular level 2.5 second-order closure model for the prediction of atmospheric turbulence. *Journal of the Atmospheric Sciences*, **45 (2)**, 113–132, doi:10.1175/1520-0469(1988)045⟨0113:DOANLS⟩2.0.CO;2.

Hicks, B., 1978: Some limitations of dimensional analysis and power laws. *Bound.-Layer Meteor.*, **14**, 567–569.

Holdsworth, A. M., T. Rees, and A. H. Monahan, 2016: Parameterization sensitivity and instability characteristics of the maximum sustainable heat flux framework for predicting turbulent collapse. *Journal of the Atmospheric Sciences*, **73 (9)**, 3527–3540, doi:10.1175/JAS-D-16-0057.1.

Holtslag, A. A. M., and Coauthors, 2013: Stable atmospheric boundary layers and diurnal cycles: Challenges for weather and climate models. *Bull. Amer. Meteor. Soc.*, **94**, 1691–1706, doi:10.1175/BAMS-D-11-00187.1.

Hong, S., and H. L. Pan, 2006: Nonlocal boundary layer vertical diffusion in a medium-range forecast model. *Mon. Wea. Rev.*, **124**, 2322–2339.

Hong, S. Y., 2010: A new stable boundary-layer mixing scheme and its impact on the simulated east asian summer monsoon. *Quarterly Journal of the Royal Meteorological Society*, **136**, 1481–1496.

Hu, X.-M., D. C. Doughty, K. J. Sanchez, E. Joseph, and J. D. Fuentes, 2012: Ozone variability in the atmospheric boundary layer in maryland and its implications for vertical transport model. *Atmospheric Environment*, **46**, 354 – 364, doi:http://dx.doi.org/10.1016/j.atmosenv.2011.09.054.

Jacobsen, I., and E. Heise, 1982: A new economic method for the computation of the surface temperature in numerical models. *Contr. Atmos. Phys.*, **55**, 128–141.

Janjic, Z., 2002: Nonsingular implementation of the mellor-yamada level 2.5 scheme in the ncep meso model in national centers for environmental prediction. Tech. rep.

Jiménez, M. A., A. Mira, J. Cuxart, A. Luque, S. Alonso, and J. A. Guijarro, 2008: Verification of a clear-sky mesoscale simulation using satellite-derived surface temperatures. *Monthly Weather Review*, **136 (12)**, 5148–5161, doi:10.1175/2008MWR2461.1.

Jimenez, P., J. Dudhia, J. F. Gonzalez-Rouco, J. Navarro, J. Montavez, and E. Garcia-Bustamante, 2011: A revised scheme for the wrf surface layer formulation. *Mon. Wea. Rev.*, **140**, 898–918, doi:10.1175/MWR-D-11-00056.1.

Klipp, C. L., and L. Mahrt, 2004: Flux-gradient relationship, self-correlation and intermittency in the stable boundary layer. *Quart. J. Roy. Meteor. Soc.*, **130**, 2087–2103.

Koch, S. E., and Coauthors, 2005: Turbulence and gravity waves within an upper-level front. *J. Atmos. Sci.*, **62**, 3885–3908.

Köhler, M., M. Ahlgrimm, and A. Beljaars, 2011: Unified treatment of dry convective and stratocumulus-topped boundary layers in the ecmwf model. *Quarterly Journal of the Royal Meteorological Society*, **137**, 43–57.

Kosović, B., and J. A. Curry, 2000: A large eddy simulation study of a quasi-steady, stably stratified atmospheric boundary layer. *Journal of the atmospheric sciences*, **57 (8)**, 1052–1068.

Langhans, W., J. Schmidli, and B. Szintai, 2012: A smagorinsky-lilly turbulence closure for cosmo-les: Implementation and comparison to arps. *Proc. COSMO Newsletter*, Consortium for small scale modelling, Vol. 12, 20–31, URL http://www.cosmo-model.org/content/model/documentation/newsLetters/newsLetter12/2-langhans.pdf.

LeMone, M. A., M. Tewari, F. Chen, and J. Dudhia, 2014: Objectively determined fair-weather nbl features in arw-wrf and their comparison to cases-97 observations. *Monthly Weather Review*, **142 (8)**, 2709–2732, doi:10.1175/MWR-D-13-00358.1.

Lorente-Plazas, R., P. A. Jimenez, J. Dudhia, and J. P. Montávez, 2016: Evaluating and improving the impact of the atmospheric stability and orography on surface winds in the wrf model. *Mon. Weath. Rew.*, **144**, 2685–2693, doi:10.1175/MWR-D-15-0449.1.

Lott, F., and M. Miller, 1997: A new subgrid orographic drag parameterization: Its formulation and testing. *Q. J. R. Meteorol. Soc.*, **123**, 101–127.

Louis, J. F., 1979: A parametric model of vertical eddy fluxes in the atmosphere. *Boundary-Layer Meteorol.*, **17**, 187–202.

Louis, J. F., M. Tiedtke, and J. F. Geleyn, 1982: A short history of the operational pbl parameterization at ecmwf. *ECMWF Workshop on Planetary Boundary Layer Parameterization*, Reading, England, ECMWF, 59-80.

Luhar, A., P. Hurley, and K. Rayner, 2009: Modelling near-surface low winds over land under stable conditions: sensitivity tests, flux-gradient relationships, and stability parameters. *Boundary-Layer Meteorol*, **130**, 249–274, doi:10.1007/s10546-008-9341-7.

Lynn, B. H., D.Rind, and R.Avissar, 1995: The importance of mesoscale circulations generated by subgrid-scale landscape heterogeneities in general circulation models. *Journal of Climate*, **8 (2)**, 191–2005, doi:10.1175/1520-0442(1995)008⟨0191:TIOMCG⟩2.0.CO;2.

Mahfouf, J. F., 1991: Analysis of soil moisture from near-surface parameters: A feasibility study. *J. Appl. Meteor.*, **30**, 1534–1547.

Mahrt, L., 1982: Momentum balance of gravity flows. *Journal of the Atmospheric Sciences*, **39 (12)**, 2701–2711, doi:10.1175/1520-0469(1982)039⟨2701:MBOGF⟩2.0.CO;2.

Mahrt, L., 1987: Grid-averaged surface fluxes. *Mon. Wea. Rev.*, **115**, 1550–1560.

Mahrt, L., 1998: Stratified atmospheric boundary layers and breakdown of models. *Theoret. Comput. Fluid Dynamics*, **11**, 263–279, doi:10.1007/s001620050093.

Mahrt, L., 2007: Weak-wind mesoscale meandering in the nocturnal boundary layer. *Environ. Fluid Mech.*, **7**, 331–347, doi:10.1007/s10652-007-9024-9.

Mahrt, L., 2009: Characteristics of submeso winds in the stable boundary layer. *Tellus*, **60A**, 700–705.

Mahrt, L., 2010: Variability and maintenance of turbulence in the very stable boundary layer. *Boundary-Layer Meteorol.*, **135**, 1–18, doi:10.1007/s10546-009-9463-6.

Mahrt, L., and D. Vickers, 2006: Extremely weak mixing in stable conditions. *Bound. Layer Meteor.*, **119**, 19–39, doi:10.1007/s10546-005-9017-5.

Mason, P. J., 1988: The formation of areally averaged roughness lengths. *Quart. J. Roy. Meteor. Soc*, **114**, 399–420.

Mauritsen, T., and G. Svensson, 2007: Observatons of stably stratified shear-driven atmospheric turbulence at low and high richardson numbers. *J. Atmos. Sci.*, **64**, 645–655, doi:10.1175/JAS.3856.1.

McFarlane, N., 1987: The effect of orographically excited gravity wave drag on the general circulation of the lower stratosphere and troposphere. *J. Atmos. Sci.*, **44**, 1775–1800.

Mellor, G., 2003: The three-dimensional current and surface wave equations. *Journal of Physical Oceanography*, **33 (9)**, 1978–1989.

Mellor, G. L., 1973: Analytic prediction of the propertiers of stratified planetary surface layers. *J. Atmos. Sci.*, **31**, 1061–1806.

Mellor, G. L., and T. Yamada, 1982: Development of a turbulence closure model for geophysical fluid problems. *Rev. Geophys.*, **20**, 851–875.

Mironov, D., E. Heise, E. Kourzeneva, B. Ritter, N. Schneider, and A. Terzhevik, 2010: Implementation of the lake parameterisation scheme flake into the numerical weather prediction model cosmo. *Boreal Env. Res.*, **15**, 218–230.

Mironov, D., and B. Ritter, 2004: Testing the new ice model for the global nwp system gme of the german weather service. *Research Activities in Atmospheric and Oceanic Modelling*, J. Cote, Ed., Vol. Rep. 34, WMO/TD 1220, WMO, Geneve.4.21-4.22.

Mironov, D. V., and P. P. Sullivan, 2016: Second-moment budgets and mixing intensity in the stably stratified atmospheric boundary layer over thermally heterogeneous surfaces. *Journal of Atmospheric Sciences*, **73 (1)**, 449–464.

Mlawer, E. J., S. J. Taubman, P. D. Brown, M. J. Iacono, and S. A. Clough, 1997: Radiative transfer for inhomogeneous atmospheres: Rrtm, a validated correlated-k model for the longwave. *Journal of Geophysical Research*, **102**, 16 663–16 682.

Monin, A. S., and A. M. Obukhov, 1954: Basic laws of turbulent mixing in the surface layer of the atmosphere. *Tr. Geofiz. Inst. Akad. AN SSSR*, **24(151)**.

Nappo, C. J., 2002: *An introduction to atmospheric gravity waves*. Academic Press, London.

Nappo, C. J., 2004: A parameterization of wave stress in the planetary boundary layer for use in mesoscale models. *Atmospheric Environment*, **38 (17)**, 2665 – 2675, doi: http://dx.doi.org/10.1016/j.atmosenv.2004.02.019, URL //www.sciencedirect.com/science/article/pii/S1352231004001712.

Nieuwstadt, F., 1984: The turbulent structure of the stable, nocturnal boundary layer. *J. Atmos. Sci.*, **41**, 2202–2216.

Nieuwstadt, F. T. M., 1985: A model for the stationary, stable boundary layer. *Turbulence and Diffusion in Stable Environments*, J. C. R. Hunt, Ed., Oxford University Press, 149–179.

Palmer, T. N., G. J. Shutts, and R. Swinbank, 1986: Alleviation of a systematic westerly bias in general circulation and numerical weather prediction models through an orographic gravity wave drag parametrization. *Quarterly Journal of the Royal Meteorological Society*, **112 (474)**, 1001–1039, doi:10.1002/qj.49711247406.

Patton, E. G., P. P. Sullivan, and C. H. Moeng, 2005: The influence of idealized heterogeneity on wet and dry planetary boundary layers coupled to the land surface. *Journal of the Atmospheric Sciences*, **62 (7)**, 2078–2097, doi:10.1175/JAS3465.1.

Raschendorfer, M., 2001: The new turbulence parameterization of lm. *Proc. COSMO Newsletter*, Vol. 1, 89–997, [Available online at http://www.cosmo-model.org/content/model/documentation/newsLetters/newsLetter01/newsLetter_01.pdf].

Raschendorfer, M., 2007: A new source term in the parameterized tke equation being of relevance fot the stable boundary layer: the circulation term. Presentation at Workshop on Cloudy boundary layer, Toulose.

Raschendorfer, M., 2009: Parameterisation of turbulence in cosmo. Tech. rep., Offenbach, Germany.

Raschendorfer, M., 2011: Ergebnisse der experimente mit aktiver nachlaufwirbelturbulenz durch sso. DWD, Routine-Sitzungen.

Ritter, B., and J.-F. Geleyn, 1992: A comprehensive radiation scheme for numerical weather prediction models with potential applications in climate simulations. *Mon. Wea. Rev.,*, **120**, 303–325.

Sandu, I., A. Beljaars, P. Bechtold, T. Mauritsen, and G. Balsamo, 2013: Why is it so difficult to represent stably stratified conditions in numerical weather prediction (nwp) models? *Journal of Advances in Modeling Earth Systems*, **5**, 117–133, doi: 10.1002/jame.20013.

Schraff, C., 1997: Mesoscale data assimilation and prediction of low stratus in the alpine region. *Meteorol. Atmos. Phys.*, **64**, 21–50.

Schulz, J. P., G. Vogel, C. B. 3, S. Kothe, U. Rummel, and B. Ahrens, 2016: Evaluation of the ground heat flux simulated by a multi-layer land surface scheme using high-quality observations at grass land and bare soil. *Meteorologische Zeitschrift*, **25**, 607–620.

Schumann, U., 1977: Realizability of reynolds stress turbulence model. *Phys. Fluids*, **20**, 721–725.

Sellers, P. J., Y. Mintz, Y. C. Sud, and A. Dalcher, 1986: A simple biosphere model (sib) for use within general circulation models. *Journal of the Atmospheric Sciences*, **43 (6)**, 505–531, doi:10.1175/1520-0469(1986)043⟨0505:ASBMFU⟩2.0.CO;2.

Sinclair, V. A., S. E. Belcher, and S. L. Gray, 2010: Synoptic controls on boundary-layer characteristics. *Bound.-Layer Meteor.*, **134**, 387–409.

Sommeria, G., and J. W. Deardorff, 1977: Subgrid-scale condensation in models of non-precipitating clouds. *J. Atmos. Sci.*, **34**, 344–355.

Sorbjan, Z., 2006: Local structure of turbulence in stably stratified boundary layers. *J. Atmos. Sci.*, **63**, 1526–1537.

Sorbjan, Z., 2010: Gradient-based scales and similarity laws in the stable boundary layer. *Quart. J. Roy. Meteor. Soc.*, **136**, 1243–1254, doi:10.1002/qj.638.

Sorbjan, Z., and A. Grachev, 2010: Gradient-based scales and similarity laws in the stable boundary layer. *Quart. J. Roy. Meteor. Soc.*, **136**, 1243–1254, doi:10.1002/qj.638.

Steeneveld, G. J., A. A. M. Holtslag, C. J. Nappo, B. J. H. van de Wiel, and L. Mahrt, 2008: Exploring the possible role of small-scale terrain drag on stable boundary layers over land. *Journal of Applied Meteorology and Climatology*, **47 (10)**, 2518–2530, doi: 10.1175/2008JAMC1816.1.

Steeneveld, G. J., C. J. Nappo, and A. A. M. Holtslag, 2009: Estimation of orographically induced wave drag in the stable boundary layer during cases99. *Acta Geophys.*, **57**, 857–881.

Steeneveld, G. J., M. J. J. Wokke, C. D. G. Zwaaftink, S. Pijlman, B. G. Heusinkveld, A. F. G. Jacobs, , and A. A. M. Holtslag, 2010: Observations of the radiation divergence in the surface layer and its implication for its parameterization in numerical weather prediction models. *J. Geophys. Res.*, **115**, doi:10.1029/2009JD013074.

Stirling, A. J., and J. Petch, 2004: The impacts of spatial variability on the development of convection. *Quarterly Journal of the Royal Meteorological Society*, **130 (604)**, 3189–3206, doi:10.1256/qj.03.137.

Stoll, R., and F. Porté-Agel, 2009: Surface heterogeneity effects on regional-scale fluxes in stable boundary layers: Surface temperature transitions. *Journal of the Atmospheric Sciences*, **66 (2)**, 412–431, doi:10.1175/2008JAS2668.1.

Stull, R. B., 1988: *An Introduction to Boundary Layer Meteorology*. Kluwer Academic Publishers.

Sun, J., S. P. Burns, D. H. Lenschow, R. Banta, and R. Newsom, 2002: Intermittent turbulence associated with a density current passage in the stable boundary layer. *Boundary Layer Meteorol.*, **105**, 199–219.

Sun, J., L. Mahrt, R. M. Banta, and Y. L. Pichugina, 2012: Turbulence regimes and turbulence intermittency in the stable boundary layer during cases-99. *J. Atmos. Sci.*, **69**, 338–351.

Sun, J., and Coauthors, 2004: Atmospheric disturbances that generate intermittent turbulence in nocturnal boundary layers. *Boundary Layer Meteorol.*, **110**, 255–279, doi:10.1023/A:1026097926169.

Sun, J., and Coauthors, 2015: Review of wave-turbulence interactions in the stable atmospheric boundary layer. *Reviews of Geophysics*, **53**, 956–993, doi:10.1002/2015RG000487.

Survey, U. G., 2016: National water information system data available on the world wide web (usgs water data for the nation). Tech. rep. URL http://waterdata.usgs.gov/nwis/.

Svensson, G., and A. Holtslag, 2009: Analysis of model results for the turning of the wind and related momentum fluxes in the stable boundary layer. *Boundary-layer Meteorology*, **132**, 261–277, doi:10.1007/s10546-009-9395-1.

Teixeira, M. A. C., J. L. Argan, and P. M. A. Miranda, 2013: Orographic drag associated with lee waves trapped at an inversion. *Journal of the Atmospheric Sciences*, **70 (9)**, 2930–2947, doi:10.1175/JAS-D-12-0350.1.

Tiedtke, M., 1989: A comprehensive mass flux scheme for cumulus parameterization in large-scale models. *Mon. Wea. Rev.,*, **117**, 1179–1799.

Tsiringakis, A., G. Steeneveld, and A. Holtslag, 2016: Small-scale orographic gravity wave drag in stable boundary layers and its impacts on synoptic systems and near surface meteorology. *Quarterly Journal of the Royal Meteorological Society*, **0**, 1–15.

Vickers, D., and L. Mahrt, 2007: Observations of the cross wind velocity variance in the stable boundary layer. *Environ Fluid Mech*, **7**, 55–71.

Viterbo, P., A. Beljaars, J.-F. Mahfouf, and J. Teixeira, 1999: The representation of soil moisture freezing and its impact on the stable boundary layer. *Q. J. R. Meteorol. Soc.*, **125**, 2401–2426, doi:10.1002/qj.49712555904.

Volker, P. D., D. V. Mironov, and M.Raschendorfer, 2009: On the performance of the cosmo model regarding the pbl structure and pbl clouds. URL http://www.cosmo-model.org/content/consortium/generalMeetings/general2009/plenary/volker_pbl.pdf.

Wacker, U., K. J. Potty, C. Lupkes, J. Hartmann, and M. Raschendorfer, 2005: A case study on a polar cold air outbreak over fram strait using a mesoscale weather prediction model. *Boundary-Layer Meteorology*, **117 (2)**, 301–336, doi:10.1007/s10546-005-2189-1.

Webster, S., A. Brown, D. Cameron, and C. Jones, 2003: Improvements to the representation of orography in the met office unified model. *Q. J. R. Meteorol. Soc.*, **129**, 1989–2010.

Wicker, L., and W. Skamarock, 2002: Time–splitting methods for elastic models using forward time schemes. *Mon. Wea. Rev.*, **130**, 2088–2097.

X.-M.Hu, P. M. Klein, and M. Xue, 2013: Evaluation of the updated ysu planetary boundary layer scheme within wrf for wind resource and air quality assessments. *Journal of Geophysical Research: Atmospheres*, **118 (18)**, 10,490–10,505, doi:10.1002/jgrd.50823, URL http://dx.doi.org/10.1002/jgrd.50823.

Yagüe, C., S. Viana, G. Maqueda, and J. M. Redondo, 2006: Influence of stability on the flux-profile relationships for wind speed, ϕ_m, and temperature, ϕ_h, for the stable atmospheric boundary layer. *Nonlinear Proc. Geoph.*, **13**, 185–203.

Yamada, T., 1979: Prediction of the nocturnal surface inversion height. *Journal of Applied Meteorology*, **18 (4)**, 526–531, doi:10.1175/1520-0450(1979)018⟨0526:POTNSI⟩2.0.CO;2.

Zilitinkevich, S. S., T. Elperin, N. Kleeorin, and I. R. I, 2007: Energy– and flux–budget (efb) turbulence closure model for stably stratified flows. part i: steady-state, homogeneous regimes. *Boundary-Layer Meteorol.*, **125**, 167–191, doi:10.1007/s10546-007-9189-2.